

# Microporous Polymers Tailored For Applications in Solution and Sustainability



The  
University  
Of  
Sheffield.

Alex James

A thesis submitted to the University of Sheffield in partial fulfilment to the requirements for  
the degree of Doctor of Philosophy

November 2019



# Contents

---

<b>CONTENTS</b> .....	<b>I</b>
<b>THESIS PREFACE</b> .....	<b>V</b>
<b>ABSTRACT</b> .....	<b>VI</b>
<b>AUTHORS DECLARATION</b> .....	<b>VIII</b>
<b>PUBLICATIONS</b> .....	<b>IX</b>
<b>ACKNOWLEDGMENTS</b> .....	<b>X</b>
<b>CHAPTER 1 - INTRODUCTION</b> .....	<b>1</b>
1.1    POROUS MATERIALS .....	2
1.2    INORGANIC MICROPOROUS MATERIALS .....	3
1.2.1    Zeolites .....	3
1.3    HYBRID INORGANIC-ORGANIC MATERIALS .....	3
1.3.1    Metal-Organic Frameworks (MOFs) .....	3
1.4    MICROPOROUS ORGANIC POLYMERS .....	4
1.4.1    Covalent Organic Frameworks (COFs) .....	5
1.4.2    Covalent Triazine Frameworks (CTFs) .....	9
1.4.3    Conjugated Microporous Polymers (CMPs) .....	12
1.4.4    Hyperscrosslinked Polymers (HCPs) .....	16
1.4.5    MOPs via Free Radical Polymerisation .....	18
1.4.6    Polymers of Intrinsic Microporosity (PIMs) .....	20
1.5    SOLUBLE MICROPOROUS POLYMERS .....	23
1.6    POROUS POLYMERS FOR SUSTAINABILITY .....	29
1.6.1    Hydrogen Storage .....	29
1.6.2    Carbon Dioxide Storage .....	29
1.6.3    Wastewater Treatment .....	31
1.7    THESIS AIMS .....	34
1.8    REFERENCES .....	35
<b>CHAPTER 2 - METHODS</b> .....	<b>47</b>
2.1. EXPERIMENTAL TECHNIQUES .....	48
2.1.1. Infra-Red Spectroscopy .....	48
2.1.2. Gas Sorption .....	48
2.1.3. Solid State NMR .....	48
2.1.4. Solution NMR .....	48

2.1.5. Gel Permeation Chromatography (GPC) .....	48
2.1.6. Dynamic Light Scattering (DLS) .....	49
2.1.7. Small Angle X-ray Scattering (SAXS).....	49
2.1.8. UV-Vis Spectroscopy.....	49
2.1.9. Steady-State Fluorescence Spectroscopy .....	49
2.1.10. Scanning Electron Microscopy (SEM) .....	50
2.1.11. Transmission Electron Microscopy (TEM) .....	50
2.1.12 Elemental analysis .....	50
2.2. GAS SORPTION THEORY.....	50
2.2.1 Langmuir Model.....	51
2.2.2 BET Theory .....	53
2.2.3 Isotherm Shapes.....	55
2.2.3 Adsorption Hysteresis .....	57
2.3 REFERENCES .....	59
<b>PART A – TOWARDS APPLICATIONS IN SOLUTION.....</b>	<b>60</b>
<b>Chapter 3 - Synthesis of PEG-<i>b</i>-DVB-co-FN Porous Polymeric Dispersions.....</b>	<b>61</b>
3.1 INTRODUCTION .....	62
3.2 CHAPTER AIMS .....	65
3.3 OPTIMISING REACTION CONDITIONS .....	66
3.3.1 Divinylbenzene:Fumaronitrile Ratio.....	66
3.3.2 Varying Solvent Composition .....	66
3.3.3 Varying Reaction Concentration .....	69
3.4 MODIFYING CORE DP .....	69
3.5 SOLID STATE CHARACTERISATION .....	71
3.5.1 Infrared Spectroscopy .....	72
3.5.2 Solid State NMR Spectroscopy .....	73
3.5.3 Elemental Analysis .....	75
3.6 SURFACE AREA AND POROSITY .....	76
3.7 DISPERSIBILITY AND SOLUTION STABILITY .....	79
3.7.1 Solution Stability .....	79
3.7.2 Dynamic Light Scattering .....	81
3.8 SMALL ANGLE X-RAY SCATTERING (SAXS) STUDIES .....	83
3.9 HYPOTHESIS OF AGGREGATE FORMATION .....	86
3.9.1 Synthesis of Analogous Poly(styrene) Samples .....	86
3.10 SWELLING OF SAMPLE IN VARIOUS SOLVENTS .....	88
3.11 LUMINESCENT PROPERTIES.....	90
3.11.1 UV-Vis Spectroscopy.....	91

3.11.2 Fluorescence Spectroscopy .....	92
3.12 VARYING CROSSLINKING MONOMER .....	93
3.12.1 Free Radical Polymerisation .....	93
3.12.2 RAFT-PISA of FN and crosslinker .....	96
3.12.3 Solution-Phase Characterisation .....	98
3.13 CONCLUSION .....	101
3.14 EXPERIMENTAL .....	102
3.14.1 Materials.....	102
3.14.2 Synthesis of PEG <sub>113</sub> -Br .....	102
3.14.3 Synthesis of PEG-based macro-chain transfer agent (CTA).....	102
3.14.4 Synthesis of HCPN-0.75 .....	103
3.14.5 PEG <sub>113</sub> -b-DVB <sub>300</sub> -co-FN <sub>225</sub> (RAFT only) via RAFT polymerisation .....	103
3.14.5 PEG <sub>113</sub> -b-DVB <sub>150</sub> -co-FN <sub>113</sub> via RAFT mediated PISA .....	103
3.14.6 PEG <sub>113</sub> -b-DVB <sub>300</sub> -co-FN <sub>225</sub> via RAFT mediated PISA .....	104
3.14.7 PEG <sub>113</sub> -b-DVB <sub>600</sub> -co-FN <sub>450</sub> via RAFT mediated PISA .....	104
3.14.8 PEG <sub>113</sub> -b-DVB <sub>1200</sub> -co-FN <sub>900</sub> via RAFT mediated PISA.....	104
3.14.9 Synthesis of insoluble FN/EGD Polymer via Free Radical Polymerisation .....	104
3.14.10 Synthesis of insoluble FN/THT Polymer via Free Radical Polymerisation.....	105
3.14.11 Synthesis of PEG <sub>113</sub> -b-EGD <sub>600</sub> -co-FN <sub>450</sub> via RAFT mediated PISA .....	105
3.14.12 Synthesis of PEG <sub>113</sub> -b-THT <sub>600</sub> -co-FN <sub>450</sub> via RAFT mediated PISA.....	105
3.15 APPENDIX .....	106
3.16 REFERENCES .....	109
<b>CHAPTER 4 - APPLICATIONS OF PEG-<i>b</i>-DVB-<i>co</i>-FN POROUS POLYMERIC DISPERSIONS .....</b>	<b>111</b>
4.1 CHAPTER AIMS .....	112
4.2 CHEMOSENSING OF NITROAROMATICS.....	113
4.3 GAS UPTAKE AND SELECTIVITY .....	120
4.3.1 Carbon Dioxide Uptake and Selectivity .....	120
4.3.2 Methane Uptake .....	124
4.4 CONCLUSION .....	126
4.5 EXPERIMENTAL .....	127
4.5.1 Materials.....	127
4.5.2 Fluorescence Quenching Studies.....	127
4.6 REFERENCES .....	128
<b>CHAPTER 5 - WHITE LIGHT EMISSION USING DVB/AA POROUS POLYMERIC DISPERSIONS .....</b>	<b>131</b>
5.1 CHAPTER AIMS .....	132
5.2 RADICAL POLYMERISATION OF DVB AND AA .....	133
5.3 RAFT-PISA OF DVB AND AA.....	135

5.3.1 Synthesis of Dispersible Porous Polymers .....	135
5.3.2 Solid State Characterisation .....	136
5.3.3 Nitrogen Gas Sorption isotherms .....	138
5.3.4 Dynamic Light Scattering .....	139
5.4 POST-SYNTHETIC MODIFICATION OF DVB/AA PPDS .....	140
5.5 WHITE LIGHT EMISSION .....	145
5.5.1 White Light Parameters .....	146
5.5.2 CIE Plots of An-PPDs and Rhodamine B .....	146
5.5.3 Addition of Fluorescein to An-PPD:Rhodamine B suspension .....	149
5.5.4 CCT and CRI of White Light Suspensions .....	150
5.5.5 Quantum Yield .....	151
5.5.6 Literature Comparison .....	152
5.6 CONCLUSION .....	153
5.7 EXPERIMENTAL .....	154
5.7.1 Materials .....	154
5.7.2 Free Radical Polymerisation of Divinylbenzene and Acrylic Acid .....	154
5.7.3 RAFT-PISA of DVB and AA using a PEG macro-CTA .....	154
5.7.3 Esterification of PEG <sub>113</sub> -b-DVB <sub>800</sub> -co-AA <sub>200</sub> Using 9-Anthracenemethanol .....	155
5.7.4 Esterification of PEG <sub>113</sub> -b-DVB <sub>900</sub> -co-AA <sub>100</sub> using 9-Anthracenemethanol .....	155
5.7.5 Synthesis of 9-Anthracenemethyl Acrylate Monomer .....	155
5.8 APPENDIX .....	156
5.9 REFERENCES .....	159
<b>PART B – APPLICATIONS IN SUSTAINABILITY .....</b>	<b>160</b>
<b>CHAPTER 6 - REMEDIATION OF Sr AND Cs USING SULFONATED HYPERCROSSLINKED POLYMERS .....</b>	<b>161</b>
<b>CHAPTER 7 – PRESSURE SWING CO<sub>2</sub> ADSORPTION USING FUNCTIONAL HYPERCROSSLINKED POLYMERS ...</b>	<b>188</b>
<b>CHAPTER 8 - CONCLUSIONS .....</b>	<b>210</b>
8.1 CONCLUSIONS .....	211
8.2 FUTURE WORK .....	213

# Thesis Preface

---

This thesis is split into two parts in which Part A is presented as full research chapters and Part B is presented in the format of journal manuscripts. Part A introduces a novel class of solution dispersible porous polymer based on the synthesis of core-shell type block co-polymers synthesised *via* a RAFT-PISA approach. Part B investigates the applications of hypercrosslinked polymers in the area of sustainability.

The overall layout of this thesis is as follows:

- Chapter 1 is an introduction covering porous materials with a focus on the few soluble and porous materials which exist and how porous materials have been applied towards sustainable applications. Chapter 2 lays out the methods used throughout this thesis.

## *Part A – Applications in Solution*

- Research chapters 3, 4 and 5 discuss the design and applications of porous materials in solution.

## *Part B – Applications in Sustainability*

- Chapters 6 and 7, presented in the form of research manuscripts describe how microporous polymers can be designed and utilised towards applications in sustainability.
- Chapter 8 lays out the conclusions of the thesis and describes the proposed future work.

# Abstract

---

Microporous organic polymers are typically insoluble materials possessing high surface areas alongside a chemically and thermally stable low density framework. As such they have been intensively studied over the past two decades towards applications in removal of pollutants from water, gas capture and storage, catalysis and more. Part B demonstrates the design and application of functionalised microporous materials applied towards sustainable applications. A sulfonated microporous polymer, synthesised using metal-free synthesis conditions is reported and applied towards the removal of heavy metals from aqueous solution. The material, SHCP-1, has a BET surface area in excess of 800 m<sup>2</sup>/g and is capable of removing over 95 mg/g of Sr and 273 mg/g of Cs in the presence of large amounts of other competing ions. In other work, a series of monomers are hypercrosslinked to yield microporous materials containing different chemical moieties and applied towards the capture of CO<sub>2</sub> using a pressure-swing methodology. Initially the CO<sub>2</sub> uptake of each network was measured at high pressure (20 bar) before a pressure-swing approach was applied to separate industrially relevant mixes of CO<sub>2</sub> and N<sub>2</sub>. Networks based on carbazole, triphenylmethanol and triphenylamine were capable of converting a dilute CO<sub>2</sub> stream (> 20 %) into a concentrated stream (> 85 %) after only two pressure swing cycles from 20 bar (adsorption) to 1 bar (desorption).

Though microporous materials can be applied towards a diverse range of applications they are not without their drawbacks. The main disadvantage of most microporous polymers is their insolubility in all common organic solvents which limits their processability and scalability. Part A of this thesis discusses work carried out on the design, synthesis and characterisation of a new class of microporous *and* solution-processable polymer. These materials are synthesised through the controlled radical polymerisation of a bifunctional crosslinking monomer alongside a second co-monomer. A Reversible Addition Fragmentation Transfer Polymerisation Induced Self-Assembly (RAFT-PISA) approach was applied to yield polymer nanoparticles comprised of a porous insoluble core dispersed in solution by long hydrophilic polymer chains (Figure A1.1). This allows for the design of porous colloidal suspensions that can be applied towards applications in solution.

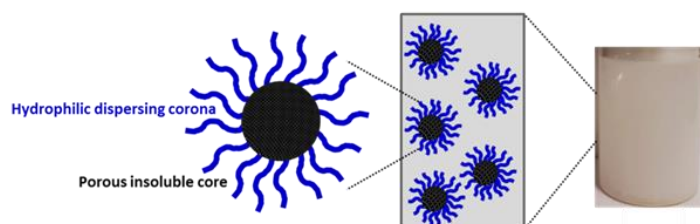


**Figure A1.1** Design concept of solution-processable microporous polymeric dispersions

This synthesis is reported for the first time using the monomers divinylbenzene and fumaronitrile. Fine-tuning of the reaction resulted in the synthesis of microporous materials with surface areas ranging from 270 – 409 m<sup>2</sup>/g that were capable of forming stable dispersions in various solvents. As a result of their fluorescent properties they are able to act as selective chemosensors towards nitroaromatic compounds in solution. A fluorescent quenching effect is observed when the electron-rich porous core interacts with the electron-deficient nitroaromatic compounds with a limit of detection of 170 ppb being observed. The versatile nature of this synthetic approach is demonstrated by swapping the fumaronitrile monomer for acrylic acid which still results in the formation of a porous material. The resulting material can be post-synthetically modified through exploiting the carboxylic acid moieties within the core to yield anthracene-incorporated porous materials. These porous polymers demonstrate blue fluorescence emission under UV irradiation in the visible region of light. This fluorescence alongside the porosity of the material can be exploited and used to encapsulate other fluorophores which when irradiated by UV-light give rise to a white-light emitting solution.

# Authors Declaration

---

The work presented in this thesis, with the exception of the SAXS and TEM data is the original work of the author. Both SAXS data along with TEM images were collected by Dr. Matthew Derry and associated credit is given at the start of each chapter when relevant. In the sections where the chapter are presented as manuscripts the chapter foreword describes in detail the contribution of each author. All work described in this thesis was carried out at the University of Sheffield between the period of October 2016 and October 2019. The views expressed in this thesis are the views of the author and not necessarily those of the University of Sheffield.

# Publications

---

This thesis contains research published in the following articles:

- 1 **A. M. James**, M. J. Derry, J. S. Train and R. Dawson, *Polym. Chem.*, 2019, **10**, 3879–3886.
- 2 **A. M. James**, S. Harding, T. Robshaw, N. Bramall, M. D. Ogden and R. Dawson, *ACS Appl. Mater. Interfaces*, 2019, **11**, 22464–22473.
- 3 **A. M. James**, D. Reed, P. Styring and R. Dawson, A Pressure Swing Approach Towards Selective CO<sub>2</sub> Sequestration Using Functionalised Hypercrosslinked Polymers (HCPs), 2019, (submitted)
- 4 **A. M. James** and R. Dawson, Efficient and Tuneable White-Light Emission Using a Dispersible Porous Polymer, 2019, (Submitted)

Other publications resulting from work carried out during PhD:

- 5 T. J. Robshaw, **A. M. James**, D. B. Hammond, J. Reynolds, R. Dawson and M. D. Ogden, Calcium-loaded hydrophilic hypercrosslinked polymers for extremely high defluoridation capacity *via* multiple uptake mechanisms, 2019, (submitted)
- 6 S. A. Ivko, **A. M. James**, J. Wilson, R. Dawson and T. Haynes, Heterogenisation of a Carbonylation Catalyst on Dispersible Microporous Polymer Nanoparticles, 2019, (in preparation)

# Acknowledgments

---

I would like to thank my supervisor Dr. Rob Dawson for giving me the opportunity to undertake this project. Being the first student of a supervisor has been equally challenging and rewarding but overall enjoyable and I would not wish for a different experience. I also want to thank all past and present group members for all of your support.

Dr. Sandra Van Meurs, Dr. Craig Robertson I am very grateful to you for running my very many solid state NMR samples.

Undertaking a PhD is something that cannot be done without belief, hard-work, determination but most of all a group of friends who you can rely on always. Fortunately for me I have had the latter in abundance! I could not have gotten to where I am without my friends who have continually motivated me and inspired me to never give up especially in the harder times. Magda, Peter and Lydia you have always been there for me and I definitely would not even be doing a PhD if were not for you all.

The lunch bunch crew, JTrain, the big DA, Geordie James, Shannon and Joe have been a solid support throughout and I could not think of a better group to take to an all-you-can-eat buffet! Jenny has been a huge source of encouragement and I know I would not be where I am if it was not for her constant pep-talks. Dave, you may be from Manchester and now live in Leeds but you're still alright I guess. James you have been a great housemate and friend and I now understand 20 % of what you say. Jannon you always believe what I say and you think I am hilarious (half of you does anyway).

Samuel Ulysees Ivako I and Liam Woodhead you have both provided me with much needed humour and relief. Although I am 110 % sure I would have handed in months earlier had it not been for you both roping me into making Halloween costumes, going to tea and generally not doing work I would not have had it any other way! I am really going to miss working in a workplace where my sunny quotes are not only understood *but* encouraged.

JSB and Sally you have both been two great friends and I think I have probably spent more time at your house than I have my own over the past two years. I am going to miss our market and coffee trips, see Instagram, and most of all the karaoke! I also want to say a huge thank you to everyone at tea who welcomed me, made me laugh and inspired me. Heather, Matt, Tom, Andy, Eren, Dave, Stephen and everyone else past and present.

Lastly, I want to thank my parents and brother for all of your support both financially and emotionally, I could not have done this without you. Also my dog Chip!

# List of Abbreviations

---

AA – Acrylic Acid

AIBN - Azobisisobutyronitrile

ATR – Attenuated Total Reflectance

ATRP – Atom Transfer Radical Polymerisation

BAM - Bisacrylamide

BET – Brunauer-Emmett-Teller

CCT – Correlated Colour Temperature

CIE - Commission internationale de l'éclairage

CMP – Conjugated Microporous Polymer

COF – Covalent Organic Framework

CP – Cross-Polarisation

CRI – Colour Rendering Index

CTA – Chain Transfer Agent

CTF – Covalent Triazine Framework

DCE – 1,2-Dichloroethane

DCM – Dichloromethane

DLS – Dynamic Light Scattering

DMF – Dimethylformamide

DP – Degree of Polymerisation

DVB - Divinylbenzene

EGD – Ethylene glycol dimethacrylate

eq. – Equivalentents

FDA – Formaldehyde dimethyl acetal

FN – Fumaronitrile

FTIR – Fourier-Transform Infrared

g – Grams

GPC – Gel Permeation Chromatography

h – Hours

HCP – Hypercrosslinked Polymer

IUPAC – International Union of Pure and Applied Chemistry

K – Kelvin

KPS – Potassium persulfate

MAS – Magic Angle Spinning

MeCN – Acetonitrile

mg – Milligram

min – Minutes

mL – Millilitres

$M_n$  – Average number molecular mass

MOF – Metal-Organic Framework

mol – Moles

MOP – Microporous Organic Polymer

ms – Milliseconds

$M_w$  – Weight average molecular mass

nm – Nanometres

NMRP – Nitroxide-Mediated Radical Polymerisation

NMR – Nuclear Magnetic Resonance

PDI – Polydispersity Index

PEG – Poly(ethylene glycol)

PIM – Polymers of Intrinsic Microporosity

PISA – Polymerisation-Induced Self-Assembly

PPD – Porous Polymeric Dispersions

PVA – Poly(vinyl alcohol)

PXRD – Powder X-ray Diffraction

QY – Quantum Yield

RAFT – Reversible Addition Fragmentation Polymerisation

RDRP – Reversible-deactivation radical polymerisation

RT – Room Temperature

s – Seconds

SA<sub>BET</sub> – BET Surface Area

SAXS – Small Angle X-ray Scattering

SEM – Scanning Electron Microscopy

ssNMR – Solid-state Nuclear Magnetic Resonance

TEM – Transmission Electron Microscopy

TGA – Thermogravimetric Analysis

THF – Tetrahydrofuran

THT – 1,3,5-triacrylhexanhydro-1,3,5-triazine

V<sub>0.1</sub> – Micropore Volume

V<sub>TOT</sub> – Total Pore Volume

WLE – White-Light Emission



# **Chapter 1 - Introduction**

## Chapter 1. Introduction

### 1.1 Porous Materials

Porous materials can be broadly categorised into three different classes, as defined by IUPAC, in accordance to their pore size. Macroporous materials have pore widths greater than 50 nm, mesoporous materials have pore widths between 2 – 50 nm and microporous materials have pore widths less than 2 nm.<sup>1</sup> Microporous materials can be further split into three broad categories – namely organic, inorganic and hybrid inorganic–organic materials. This introduction focuses predominantly on the former with a brief discussion relating to some of the different types of inorganic and hybrid microporous materials.

It seems appropriate to mention the role activated carbon has taken on as one of the first porous materials adopted industrially over the past 50 years. Activated carbon is a form of microporous material comprised solely of carbon and synthesised from carbonaceous source materials such as coal or petroleum pitch but also from sustainable sources such as wood, bamboo and other sources of biomass.<sup>2,3</sup> The synthesis involves the activation of the material which is achievable either physically, through pyrolysis at very high temperatures (> 800 °C) or chemically which sees the precursor mixed with a chemical activating agent (KOH or ZnCl<sub>2</sub>) before being combusted at lower temperatures (400 – 700 °C).<sup>4</sup> The end result is a cheap and stable material with a high surface area and small pores which can be exploited for numerous applications.<sup>5</sup> Industrially, activated carbon is primarily used to remove organic and metallic impurities as a purification measure where their high surface areas and small pores aid rapid uptake of these contaminants.<sup>6,7</sup> An example of this is the hydrocarbon sweetening process in which activated carbon is used to remove H<sub>2</sub>S and CO<sub>2</sub> from natural gas so it can be more safely transported and sold.<sup>8</sup> Activated carbons are also applied in the treatment of industrial wastewater so as not to pollute clean drinking water given their abundant microporous structure, low cost and ease of regeneration.<sup>7</sup> This application is particularly poignant given the rising levels in water pollution and scarcity of clean drinking water in many countries. Finally, activated carbon has been applied as a catalyst in many industrial processes either as the direct catalyst<sup>9,10</sup> or as a catalytic support for metal catalysts<sup>11,12</sup>. In the case of the former the activity of the materials stems from the functionality imparted during synthesis and surface heterogeneity whereas the ability to act as a support stems from the high surface area, abundance of micropores, ease of surface modification and stability of the material.<sup>13</sup>

## Chapter 1. Introduction

### 1.2 Inorganic Microporous Materials

#### 1.2.1 Zeolites

Zeolites are a class of natural and synthetic hydrated aluminosilicates which possess complex three-dimensional structures with cavities.<sup>14</sup> Zeolites are ordered materials characterised by a framework of silica and alumina tetrahedra, each consisting of four oxygen atoms.<sup>15</sup> These Si-O or Al-O bonds stretch out in three dimensions leading to the presence of open cavities which can accommodate alkaline earth metals, rare-earth metals, positively charged clusters, water and small organic molecules. Furthermore, these ions/molecules can be removed or exchanged whilst leaving the aluminosilicate framework intact. The different ways in which the three-dimensional network can form gives rise to the wide variety of zeolitic frameworks reported in the literature. Natural zeolites are often formed as a result of volcanic activity, which is represented in the word zeolite, from the Greek words “zeo” meaning to boil and “lithos” meaning stone. Synthetic zeolites are synthesised using templates which results in a porous structure upon removal of the template, usually achieved *via* pyrolysis. The unique properties of zeolites such as their high thermal stability, ability to withstand high pressures and ability to exchange the metal ion(s) present in the cavity has seen these materials used in a range of applications from selective gas capture and storage<sup>16,17</sup> to catalysis<sup>18</sup> and wastewater treatment.<sup>19</sup> Industrially, zeolites are applied to the oil refinery process where they are used in processes such as cracking (producing shorter alkanes from long ones) and reforming (turning cyclohexane’s into aromatics).<sup>20</sup> Zeolites have been employed for a number of years in the petrochemical industry mainly owed to their abundant nature, low costs, stability and high catalytic activity.<sup>21</sup>

### 1.3 Hybrid Inorganic-Organic Materials

#### 1.3.1 Metal-Organic Frameworks (MOFs)

Metal-organic frameworks are hybrid inorganic-organic crystalline materials comprised of metal ions or small metal clusters linked together by multitopic organic linkers.<sup>22</sup> These materials have received widespread attention over the last two decades due to the versatility of different metals and ligands which can be used and the ease by which a crystalline product can be attained and characterised. This has led to over 60 000 MOF structures to be reported on the Cambridge Structural Database (CSD) to date (not including amorphous materials),<sup>23</sup> making MOFs one of the fastest growing fields in chemistry. Owed in part to their crystalline structure, MOFs have well defined and tuneable pore sizes which can give rise to very high surface areas (> 7000 m<sup>2</sup>/g).<sup>24,25</sup>

## Chapter 1. Introduction

Due to their tuneable nature and high surface areas MOFs have been applied to many diverse research applications such as gas separation and storage,<sup>26,27</sup> catalysis,<sup>22</sup> chemosensing<sup>28,29</sup>, removal of toxic metals or organic pollutants from aqueous solution<sup>30,31</sup> and more.<sup>32</sup> It is also possible to use computational methods to predict the final structure of a certain MOF which allows for some prediction of the material properties.<sup>23,27</sup> This feature is much more difficult for amorphous organic microporous materials.

The two main issues with MOFs are their stability and the difficulty faced when attempting to scale-up their synthesis to the proportions required for industrial/commercial viability. Through the generation of the MIL and UIO systems the stability issues have somewhat being alleviated though issues with scalability remain persistent. The most typical way of synthesising MOFs is through solvothermal synthesis which involves mixing solutions of the inorganic salt and organic linker in a sealed vessel before heating the reaction mixture and synthesise the insoluble frameworks which eventually forms fine crystals.<sup>33</sup> Though this method is effective on a laboratory scale it is not feasible when the desire is to scale up the synthesis and target real world applications. There have been other methods of synthesis investigated towards the scale-up of MOF materials such as electrochemical approaches, microwave assisted approaches and mechanochemical methods which lend themselves more to scalability.<sup>33,34</sup> These advances in synthesis have led to the commercialisation of some MOF systems, for example six different MOF systems are commercially available to purchase from Sigma-Aldrich and a number of different spin-out companies are designing MOF products for various uses such as expanding the shelf life of fresh fruit and vegetables.<sup>34</sup>

### 1.4 Microporous Organic Polymers

Microporous organic polymers (MOPs) are materials comprised of solely the lighter elements of the periodic table (i.e. B, C, N, O) connected through strong covalent bonds.<sup>35</sup> As with other microporous materials they have high surface areas, typically between 500 – 2000 m<sup>2</sup>/g but some surpass 6000 m<sup>2</sup>/g (PPN-4)<sup>36</sup>. Most are air and moisture stable, even retaining their structure and porosity after boiling in acid<sup>37</sup> (unlike most MOFs which would decompose under these conditions). Furthermore, the lack of any heavy metals in these frameworks results in a low density network which is advantageous for applications such as gas capture and storage. A key advantage of MOPs is the numerous and diverse chemical reactions which can be employed to synthesise these materials.<sup>38</sup> For example, one can form crystalline organic materials such as covalent organic frameworks (1.4.1) by employing dynamic and reversible condensation reactions. However, it is also possible to carry out non-reversible reactions to yield amorphous materials such as hypercrosslinked polymers (section 1.4.4). This diversity

## Chapter 1. Introduction

has yielded many different types of microporous organic materials being reported over the past two decades.

### 1.4.1 Covalent Organic Frameworks (COFs)

Covalent organic frameworks (COFs) are a class of microporous polymer that is distinguished by their crystallinity. They are synthesised by linking together organic building blocks through dynamic covalent bond formation. Crystallinity in these materials is a result of the reversible nature of these reactions which allows for some structural correction during synthesis resulting in the lower energy thermodynamic product, not too dissimilar to MOF synthesis. This is in contrast to most other types of MOPs, which are the kinetic product of non-reversible covalent bond formation and as such are predominantly amorphous.

The first COF synthesis was reported in 2005 by Yaghi and co-workers<sup>39</sup>, the result of the reversible formation of strong B-O bonds to form boroxine rings which can be seen as analogous to the metal centres found in MOFs. The first COFs synthesised were named COF-1 and COF-5 with both being synthesised under solvothermal conditions in a dioxane/mesitylene solvent mixture. COF-1 is the simplest material in the series and is synthesised through the self-condensation of diboronic acid which results in the formation of B<sub>3</sub>O<sub>3</sub> rings connected by benzene rings in a hexagonal array. COF-5 is formed in a similar way but, instead of a self-condensation reaction, sees diboronic acid react with hexahydroxytriphenylene (HHTP) to form a five membered BC<sub>2</sub>O<sub>2</sub> ring bridged by benzene rings. In 2007 the COF family of materials was further extended by varying the strut length of the diboronic acid reagent (Figure 1.1) to yield COF-6 (1,3,5-benzenetriboronic acid), COF-8 (1,3,5-benzenetris(4-phenylboronic acid)), and COF-10 (4,4'-biphenyldiboronic acid).<sup>40</sup>

## Chapter 1. Introduction

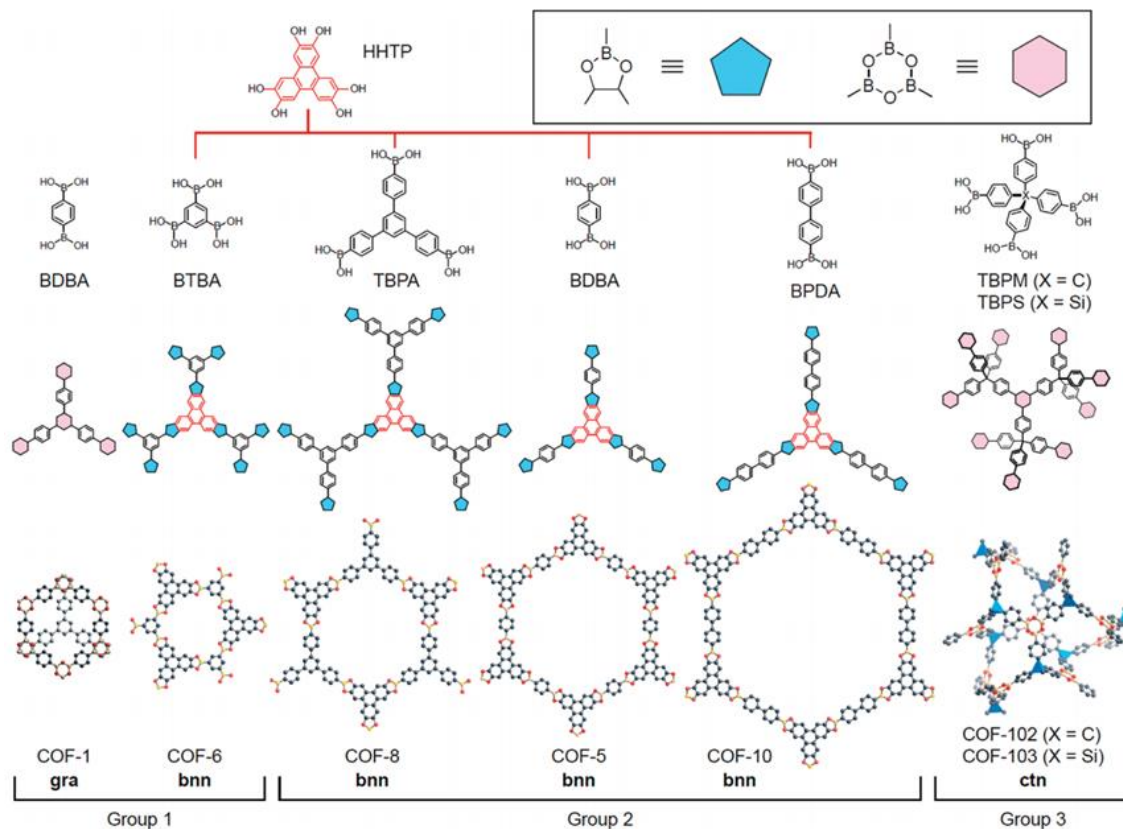


**Figure 1.1** Selected COFs synthesised by the Yaghi group<sup>41</sup>

All COF samples synthesised were expected to form planar 2D organic sheets in which two distinct packing arrangements would form. A staggered AB arrangement where three-connected vertices lie over the centre of the six-membered rings of neighbouring layers, similar to that observed in graphite,<sup>42</sup> or an eclipsed arrangement in which the sheets lay over one another as observed in boron nitride.<sup>43</sup> Powder X-ray diffraction (PXRD) studies revealed distinct peaks directly related to each packing configuration which confirmed COF-1 adopts the graphite-like configuration and each of the other COFs adopt the boron nitride packing arrangement.

Up until 2007, all reported COFs were 2D due to their synthesis involving the use of planar monomers. This changed in 2007 when Yaghi and co-workers reported the first examples of 3D COFs.<sup>44</sup> These materials still involved reversible B-O bond formation to yield a crystalline product but employed 3D reagents in the form of *tetra*(4-dihydroxyborylphenyl)methane and its silicon analogue to yield COF-102 and COF-103 respectively. Likewise, COF-105 and COF-108 could be formed by reacting *tetra*(4-dihydroxyborylphenyl)methane and its silicon analogue *via* co-condensation with HHTP respectively. All these materials were found to be crystalline.



## Chapter 1. Introduction

Up until 2009, all literature on COF synthesis involved the use of boronic acid based monomers that formed a crystalline network as a result of reversible boroxine ring formation. However, this changed in 2009 when Yaghi and co-workers reported the first COF synthesised using imine linkages (Figure 1.3) named COF-300.<sup>48</sup> This 3D network was synthesised as a result of the dehydration reaction between the tetrahedral building block tetra(4-aminyl)methane and linear linker terephthalaldehyde. COF-300 was found to be crystalline, possessing a diamond-like structure. Gas sorption analysis revealed the sample had a BET surface area of 1360 m<sup>2</sup>/g with pore size distribution analysis confirming the sample was microporous with a pore size centred around 7.2 Å, close to the 7.8 Å observed in the crystal model.

Over the last decade there have been many more COF syntheses reported which have used a variety of chemical linkages to yield crystalline and porous COF materials. These include imine linkages, hydrazone linkages, enamine linkages, azine linkages as well as the traditional B-O and B-C-O bond forming reactions. These different synthetic procedures have allowed the incorporation of different functionalities to be present within the final material allowing these materials applied towards many different applications. For example, in 2013 Jiang and co-workers synthesised Py-Azine-COF which is an azine linked COF capable of detecting trace amounts of the explosive compound picric acid.<sup>49</sup> In 2018 Ma and co-workers reported the synthesis of PyVg-COF which included viologen units within the structure that ensures the 2D material does not stack upon itself meaning this material is very solution stable and can be applied towards optoelectronic device fabrication.<sup>50</sup> Further to this, COFs have been investigated for their applications in gas separation,<sup>41</sup> wastewater treatment,<sup>51</sup> chemosensing<sup>52</sup> and more.<sup>53</sup>

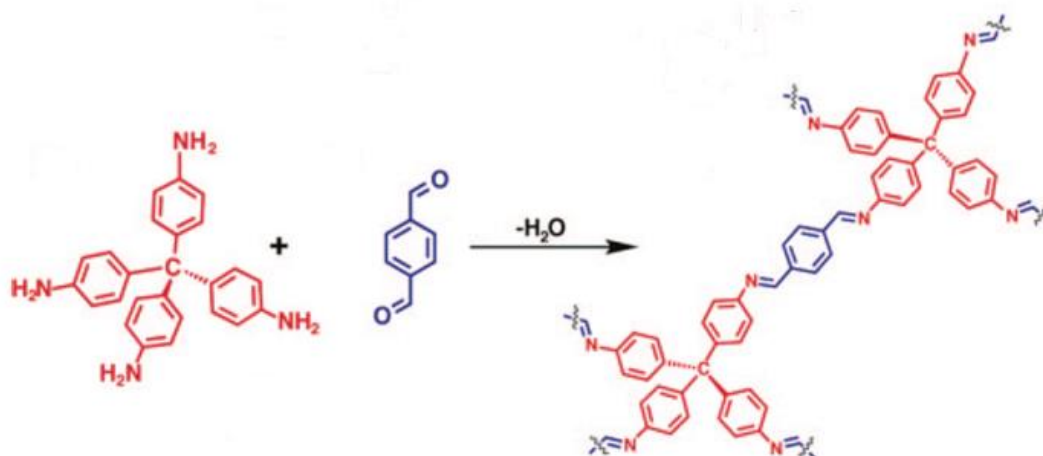


**Figure 1.3** Synthesis of imine-linked COF-300 as reported by the Yaghi group<sup>48</sup>

## Chapter 1. Introduction

Despite the fact there has been much research in the field of COFs over almost two decades there are still numerous issues with these materials, which has limited their industrial applicability despite their excellent properties. Two main factors limiting COFs from realising their potential are; difficulties in synthesising large amounts of material and poor processability. COFs require long reaction times (2-5 days) and are predominantly synthesised through solvothermal reactions carried out in sealed tubes with low internal pressures. These two conditions are vital to ensure the final product is crystalline. There have recently been some reports of synthesising COFs *via* other means which could allow for scalability such as microwave assisted<sup>54</sup> and mechanochemical<sup>55</sup> synthesis methods. However, these too have their own drawbacks and usually form materials which are less crystalline or have lower surface areas than their solvothermal analogues.<sup>56</sup> Likewise, even if it were possible to synthesise large quantities of a COF that met industrial requirements processability issues are still present and need to be overcome. The first COF thin film was not fabricated until 2017<sup>57</sup> highlighting that much research needs to be carried out before COFs can realise their potential and be applied both industrially and commercially.

### 1.4.2 Covalent Triazine Frameworks (CTFs)

In 2008 Thomas *et al.* reported the first synthesis of covalent triazine frameworks (CTFs) which are the product of the condensation of nitrile containing organic monomer units synthesised through ionothermal conditions.<sup>58</sup> In these reactions, molten  $\text{ZnCl}_2$  acts as both the solvent and catalyst for the reaction thereby requiring very high reaction temperatures ( $> 400\text{ }^\circ\text{C}$ ). However, the resulting material is stable, porous and even semi-crystalline in nature. The crystallinity of the final product is a result of dynamic covalent bond formation resulting in the thermodynamic product and not the kinetic product, similar in some ways to COF synthesis. One may expect the starting materials, being organic, to decompose at the high temperatures required for the reaction to take place but organic aromatic nitriles are somewhat thermally stable showing little to no decomposition at the desired reaction temperature.

CTF-1 was the first reported CTF published by Thomas and co-workers and was synthesised by heating mixtures of dicyanobenzene and zinc chloride at  $400\text{ }^\circ\text{C}$  for 40 h (Figure 1.4). This reaction afforded a porous material with a specific BET surface area of  $791\text{ m}^2/\text{g}$ , though this could be increased to  $1123\text{ m}^2/\text{g}$  by varying the equivalents of  $\text{ZnCl}_2$  used in the reaction. Upon further increasing the  $\text{ZnCl}_2$ :monomer ratio it was found that the surface area did increase though this was at the expense of crystallinity as the materials became increasingly amorphous. PXRD analysis revealed that, though CTF-1 exhibited rather broad diffraction peaks, displayed a structure somewhat similar to that of COF-1.<sup>39</sup>

## Chapter 1. Introduction

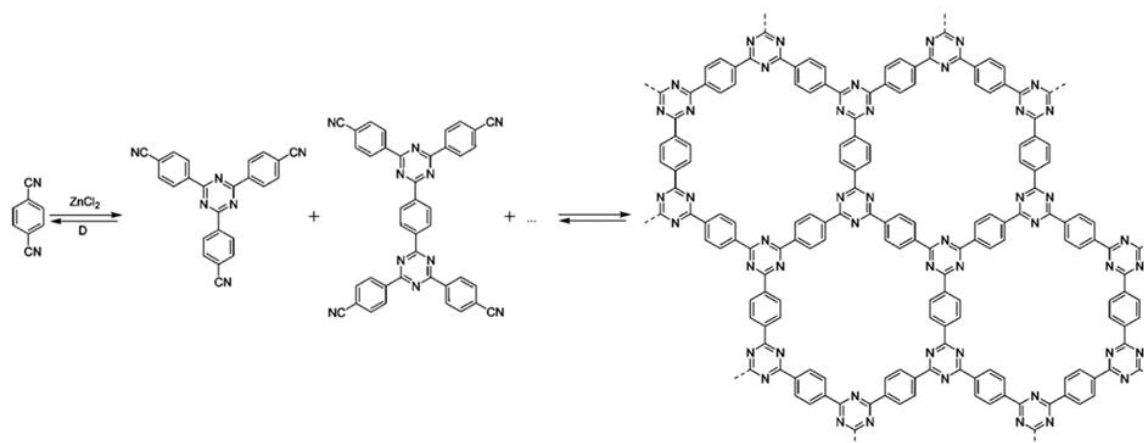


**Figure 1.4** Synthetic route towards of CTF-1 as reported by Thomas *et al.*<sup>58</sup>

Building on the success of CTF-1 a more comprehensive study of the reaction using a variety of different thermally stable organic nitriles were applied to synthesise new CTFs.<sup>59</sup> In this work a range of commercially available aromatic nitrile monomers (Figure 1.5) were applied towards the dynamic salt melt condensation reaction in the hope of yielding porous crystalline networks. Monomers with different geometries and different numbers of nitrile groups were studied as it would be expected that these factors would influence the arrangement formed by the final product. This work also reported that the reaction conditions, i.e. the temperature of reaction, ratio of  $ZnCl_2$ :monomer and reaction time were all found to be very important parameters which could be tuned to vary the pore size and surface area of the final material. For example, increasing the quantity of  $ZnCl_2$  generally led to an increase in surface area though only to a point. After this, increasing this ratio became detrimental to both surface area and crystallinity. Likewise, higher reaction temperatures also proved beneficial towards synthesising higher surface area materials but after a point increased temperatures became problematic and reduced the surface area. The best surface areas were attained for samples which were heated first at 400 °C before then being ramped up to 600 °C as in the case of pDCB which had the highest reported surface area of 3270 m<sup>2</sup>/g. This was also the case for CTF-0, a network which was reported in 2013 by Thomas and co-workers using tricyanobenzene and had a BET surface area of 2011 m<sup>2</sup>/g.<sup>60</sup>

## Chapter 1. Introduction

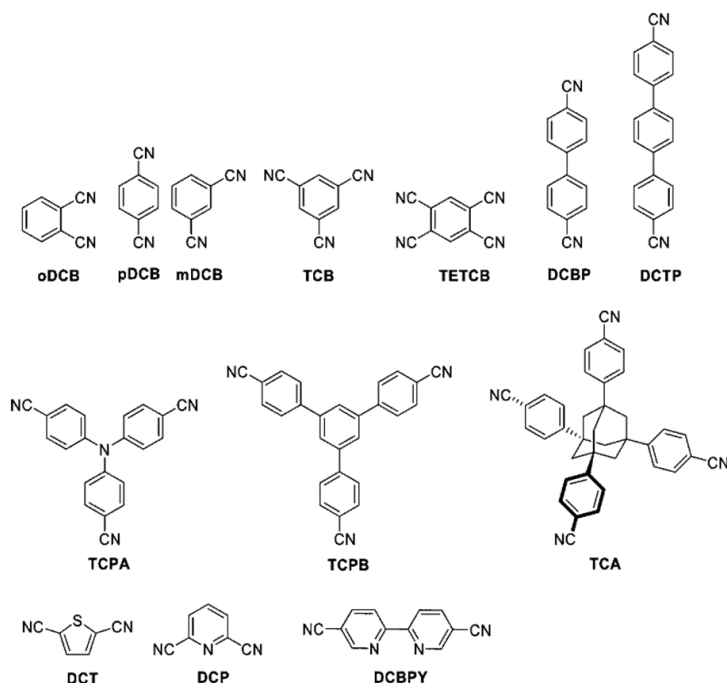


**Figure 1.5** Different nitrile monomers used to synthesise CTFs<sup>59</sup>

The major drawback of CTFs are the high temperatures and long reaction times required for their synthesis which hinders scalability. Unfortunately, the high temperatures required for the reaction also mean that chemical functionalities present on the chosen monomers often do not survive the reaction hence no functional CTFs have been reported when synthesised using this approach. There have been some reports of synthesising CTFs through other means rather than the typical ionothermal synthesis. In 2012, the Cooper group reported the synthesis of CTFs at both room temperature and by using microwave assisted methods through application of a trifluoromethanesulfonic acid (TFMS) catalyst.<sup>61</sup> Unlike conventional CTFs, these materials were not black but instead were shown to be fluorescent powders with absorption and luminescence spectra dependent on monomer choice. Furthermore, it was found that the materials synthesised at room temperature were amorphous yet those synthesised using a microwave had some degree of crystallinity. This report was closely followed by another from the Dai group who also reported the use of TFMS acid but were able to form CTF membranes.<sup>62</sup> In this work TFM-1 was synthesised at 100 °C for around 20 mins and done so in a flat glass dish to induce film formation in a manner synonymous to both sol-gel synthesis and typical solvent casting membrane formation processes (*i.e.* polymerisation is coupled with solvent evaporation). This method was particularly useful as it not only alleviated issues with the reaction temperature but also yielded a functional thin film porous material, which could be applied towards selective gas separation.

## Chapter 1. Introduction

In 2017 Cooper *et al.* reported the synthesis of CTFs by the condensation reaction of aldehydes and amidines.<sup>63</sup> This reaction involved no harsh acids or high temperatures and as such it was possible to scale the reaction up to yield multi-gram quantities. However, these materials were found to be amorphous though they did retain their optical bandgap resulting in applications in photocatalytic water splitting with CTF-HUST-2 showing hydrogen evolution rates exceeding  $2600 \mu\text{mol h}^{-1} \text{g}^{-1}$ .

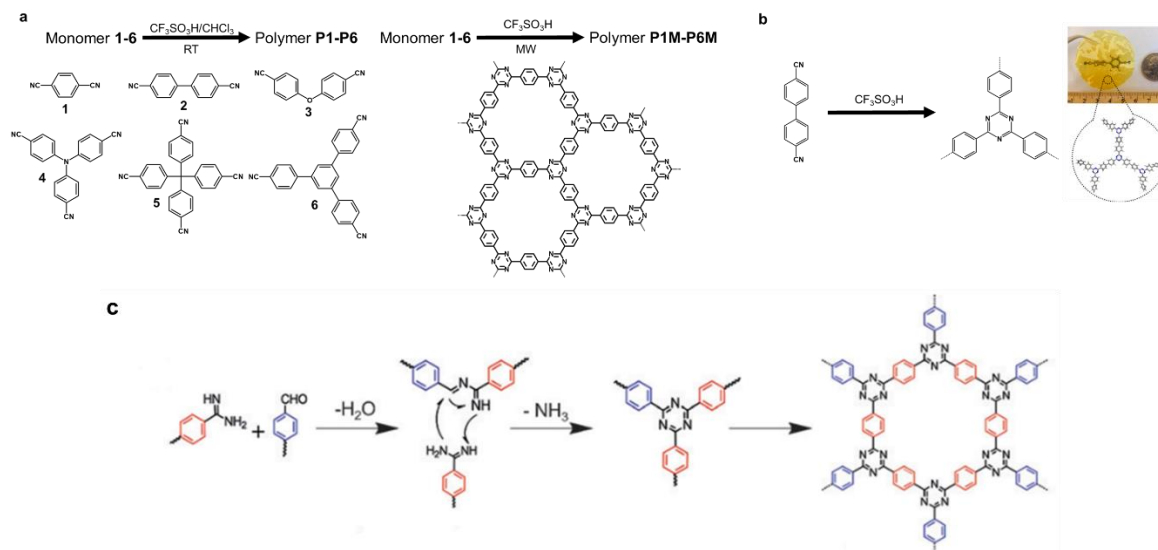


**Figure 1.6** Different synthetic approaches towards CTF other than the traditional ionothermal method. (a) Ren *et al.*,<sup>61</sup> (b) Zhu *et al.*<sup>62</sup> and (c) Wang *et al.*<sup>63</sup>

### 1.4.3 Conjugated Microporous Polymers (CMPs)

Conjugated microporous polymers (CMPs) are the only class of MOP to combine both a permanently porous structure alongside an extended fully  $\pi$ -conjugated network. Unlike COFs and to some extent CTFs, these materials are completely amorphous and show no crystallinity. The first CMP was reported in 2007 by the Cooper group and was the result of the palladium catalysed Sonogashira-Hagihara cross-coupling reaction between alkyne and halogen aromatic building blocks (Figure 1.7).<sup>64</sup> CMP-1 was synthesised through the cross-coupling reaction of 1,3,5-triethynylbenzene and 1,4-diiodobenzene and was found to have a BET surface area of  $834 \text{ m}^2/\text{g}$ . Though amorphous, the pore size and surface area of CMPs can be tuned by varying the length of the organic linker, also known as the strut length. For example, CMP-3 possessed the longest strut length and consequently had the lowest BET surface area ( $522 \text{ m}^2/\text{g}$ ). This is due to the increased strut length imparting more flexibility into the material thereby lowering the free volume of the network. This was further corroborated in 2008 when the Cooper group reported CMP-0, which had the shortest strut length and as a result the highest BET surface area ( $1018 \text{ m}^2/\text{g}$ ).<sup>65</sup>

## Chapter 1. Introduction

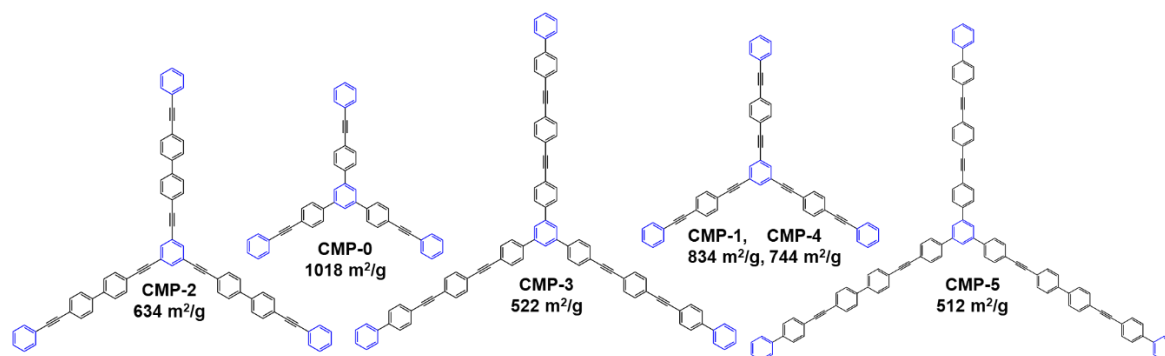


**Figure 1.7** Schematic structures for a series of CMP networks

Homocoupled CMP networks were reported in 2008 by Jiang *et al.* who successfully homocoupled 1,3,5-triethynylbenzene and 1,4-diethynylbenzene to yield HCMP-1 and HCMP-2 respectively.<sup>66</sup> Both HCMP-1 and HCMP-2 were porous and had apparent BET surface areas of 842 m<sup>2</sup>/g and 827 m<sup>2</sup>/g respectively. A later report by Li *et al.* showed how lithium ions could be incorporated into the framework and used to increase the capacity of the materials towards hydrogen gas storage.<sup>67</sup> Incorporating 0.5 wt. % Li<sup>+</sup> ions into the HCMP-1 network leads to a 4 fold increase in the hydrogen capacity of the material compared to the unmodified HCMP-1. Such high uptake is owed in part to both the porous nature of the material as well as the charge-induced dipole interaction between the Li<sup>+</sup> ions and H<sub>2</sub>.

A key advantage CMP synthesis has over other MOP syntheses, e.g. CTF synthesis, is that functional groups present on the monomers are present in the final material. As such, this is a very convenient way to design materials, which can be tuned towards specific applications through judicious choice of starting materials. This was exploited by Dawson *et al.* in 2011 who synthesised a series of CMP networks using monomers containing a range of different chemical moieties.<sup>68</sup> These functional groups survived the network formation, as confirmed by solid-state NMR, which resulted in an increased affinity between CO<sub>2</sub> and the porous network compared to the non-functional analogue (CMP-1). The incorporation of functional groups can also modify the physical properties of the material such as the hydrophobicity. Notably, most MOP networks are insoluble and often hydrophobic yet the inclusion of hydrophilic groups within the final product was proven by Dawson *et al.* to impart a degree of hydrophilicity into the final material.<sup>69</sup> Incorporation of hydroxyl groups into the CMP material leads to an increase in the network hydrophilicity with inclusion of fluoride inducing the opposite effect (Figure 1.8). Inclusion of different chemical moieties can also allow for further post-synthetic modification of the network, as shown in 2011 by Jiang *et al.* who synthesised metal-containing CMP networks by cross-coupling 1,3,5-triethynylbenzene with 5,5-dibromo-2,2'-bipyridine.<sup>70</sup> Upon synthesis, these materials were mixed with a Re metal salt to incorporate a metal

## Chapter 1. Introduction

complex into the network bound by chelation to the bipyridine units. This material was able to act as a catalyst in the reductive amination of some disubstituted ketones.

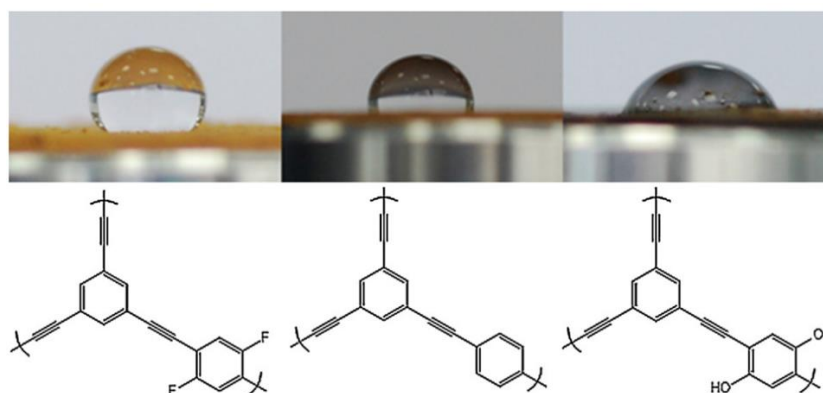


**Figure 1.8** (above) Water-contact angle study of the different CMP materials (below) showing the effect of imparting different functionalities has on the hydrophilicity of the final material<sup>71</sup>

Though Sonogashira-Hagihara coupling reactions are the most prominent reactions used to yield CMP networks they are not the only reaction capable of forming CMPs. There have been publications reporting the synthesis of CMP networks using a variety of different coupling reactions such as Suzuki,<sup>72,73</sup> Yamamoto,<sup>74</sup> oxidative coupling,<sup>75</sup> Schiff-base reactions<sup>76,77</sup> and more<sup>78,79</sup>. This variety has led to the synthesis of a wide range of different networks containing a plethora of diverse chemical functionalities which can help tune the final material towards the desired end application (Figure 1.9).

Due to the extended conjugated network which results from CMP synthesis these materials can be applied towards applications which exploit both their porosity but also the properties which arise from the fully conjugated network. For example, CMPs have been applied towards photocatalytic hydrogen evolution,<sup>80–82</sup> chemosensing,<sup>83–85</sup> catalysis,<sup>70,86,87</sup> light emission<sup>73,88</sup> and more<sup>75,78,89</sup> with most applications exploiting the low band gap and optical properties of these materials. Though the scope for variation in CMP synthesis is wide and numerous functionalities can be introduced into the final material leading to a number of applications, the final product is still completely insoluble which limits the processability of the material.

Chapter 1. Introduction

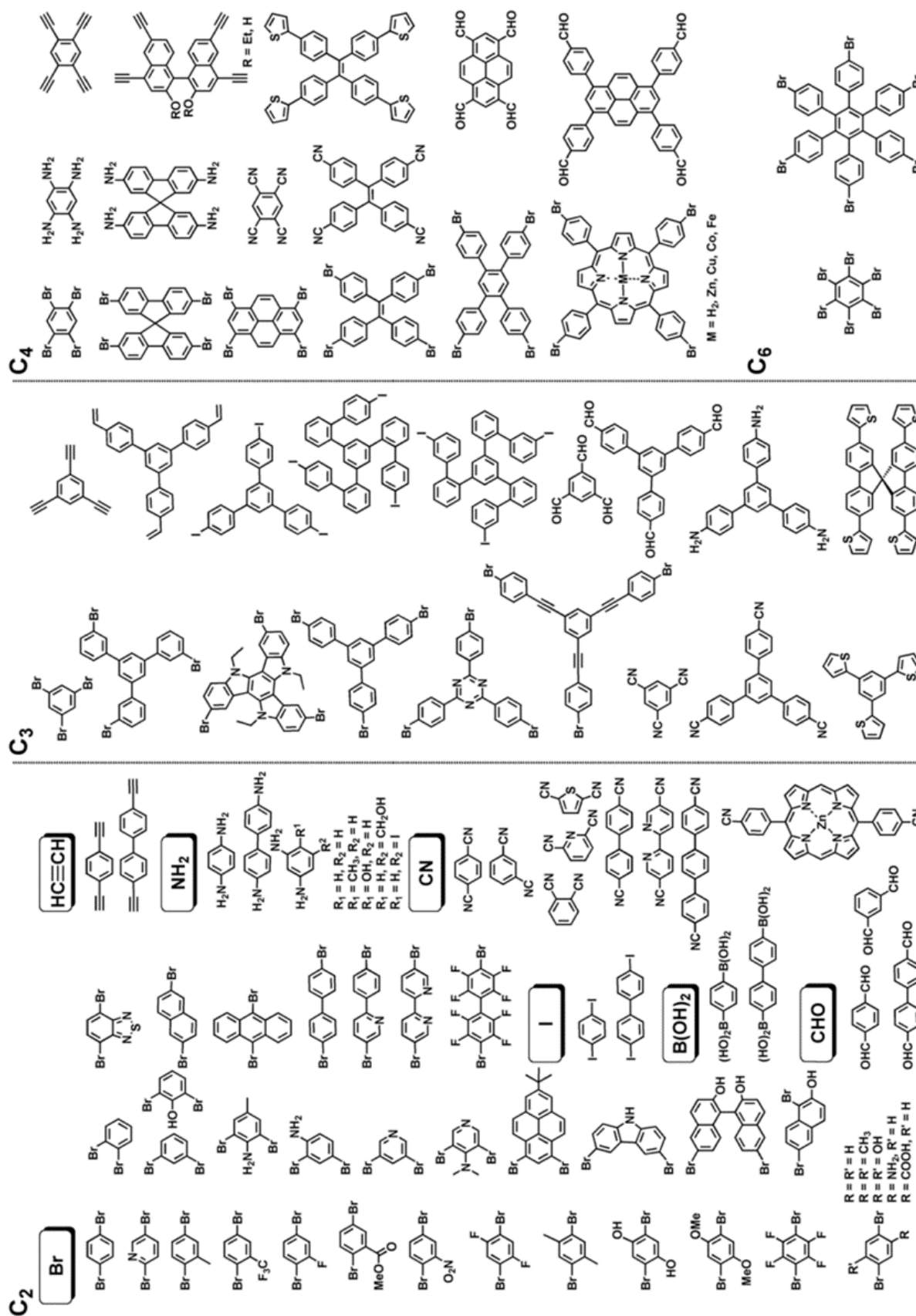
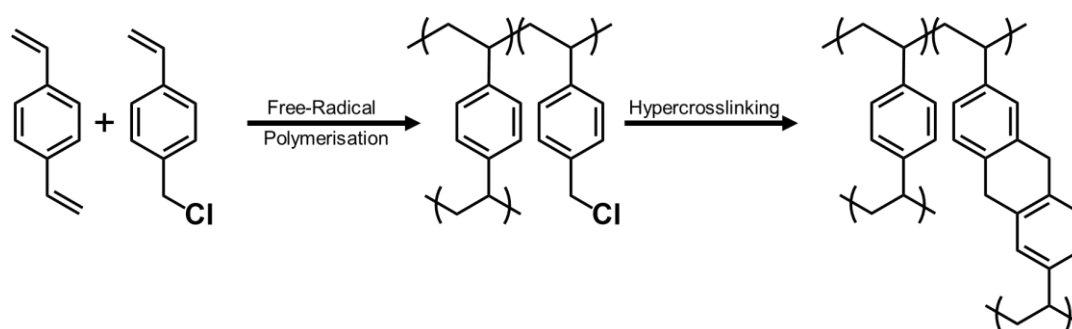


Figure 1.9 A selection of the different organic building blocks used in CMP synthesis<sup>79</sup>

## Chapter 1. Introduction

### 1.4.4 Hypercrosslinked Polymers (HCPs)

Hypercrosslinked polymers are a class of MOP which date back significantly further than most others. HCPs can be traced back to the 1970s where they were first reported by Russian chemist Vadim A. Davankov.<sup>90</sup> The design principle behind these materials was to build on the concepts used for designing macroporous resins but extend the crosslinking even further (Figure 1.10). This results in the formation of a highly rigid and crosslinked network which is microporous and thus possesses a high BET surface area. HCPs based on crosslinked poly(styrene) are commonly referred to as Davankov resins and can be designed to have surface areas exceeding 2000 m<sup>2</sup>/g.<sup>91</sup>



**Figure 1.10** Synthesis towards Davankov type resins *via* Friedel-Crafts alkylation

The hypercrosslinking reaction is the result of a Friedel-Crafts alkylation reaction that employs a Lewis acid catalyst which reacts with the methyl halogen groups. This group displaces a proton on the aromatic ring which result in the formation of a methylene bridge. This occurs numerous times resulting in a highly crosslinked network. It is possible to prepare HCPs without first synthesising a crosslinked precursor and instead use aromatic monomers that contain these crosslinking groups. Predominantly, these monomers are usually disubstituted monomers such as *α,α'*-dichloroxylene (DCX), bis(chloromethyl)biphenyl (BCMBP), and bis(chloromethyl)anthracene (BCMA) because they can give rise to an extended network. Using these pure monomers during HCP synthesis, in a polycondensation reaction, has seen materials synthesised with surface areas close to 2000 m<sup>2</sup>/g.<sup>92</sup> This method is also much more efficient and keeps costs low due to eliminating a previously key synthetic step.

Using crosslinkable monomers over first having to create a crosslinked precursor network allows for the incorporation of different aromatic monomers into the final network. For example, Schwab *et al.* were able to incorporate dibenzofuran and other monomers (Figure 1.11) into a porous network through statistical co-polymerisation with BCMBP which resulted in a dibenzofuran-BCMBP co-polymer with a surface area of 1800 m<sup>2</sup>/g.<sup>93</sup> This approach is a simple and convenient way to easily incorporate functionality into these materials which

## Chapter 1. Introduction

improves performance in certain applications. This route may also allow for further post-synthetic modification of the final material depending on which chemical moieties are present.

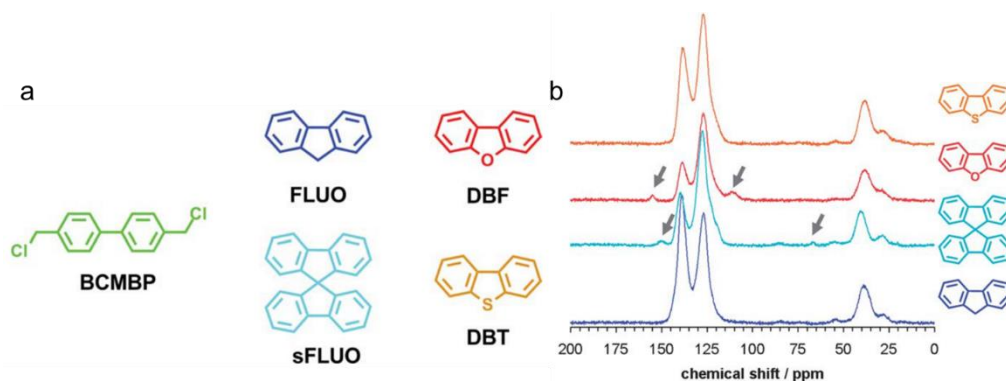


**Figure 1.11** (a) monomers co-polymerised with BCMBP to produce functional networks and (b) solid-state  $^{13}\text{C}$  NMR spectra showing successful incorporation of co-monomer into final product

Despite the demonstration that co-condensation of BCMBP alongside other rigid aromatic monomers allows for incorporation of different monomers into the final product, characterisation of these co-networks is difficult given that there is no way of knowing how much, if any, of the co-monomer had been incorporated into the final product. In 2011, Tan and co-workers transformed HCP synthesis by reporting the “knitting method” as an alternative route towards the synthesis of HCPs.<sup>94</sup> Unlike prior syntheses, this method allows potentially any rigid aromatic monomer to be hypercrosslinked by the use of an external crosslinker, in this case, formaldehyde dimethylacetal (FDA). The chemistry is based on that of Friedel-Crafts alkylation, however the external crosslinker acts in place of a crosslinkable monomer and introduces a methylene bridge into the material (Figure 1.12). This method radically altered the way by which HCPs were synthesised and led to many new reports based on monomers previously thought to be “non-crosslinkable” being published.<sup>95–98</sup>

The main advantage of the knitting method is its versatility, one merely has to only vary the monomer to yield a new product containing new functional groups. However, it also allows other variables to be changed which can have huge effects on the porosity of the final product. For example, when creating a benzene network it was noted that the highest surface area of  $1391\text{ m}^2/\text{g}$  was obtained for a material with a benzene:FDA ratio of 1:3. When using an equimolar ratio, the surface area dramatically reduced to less than  $900\text{ m}^2/\text{g}$ .<sup>94</sup>

## Chapter 1. Introduction

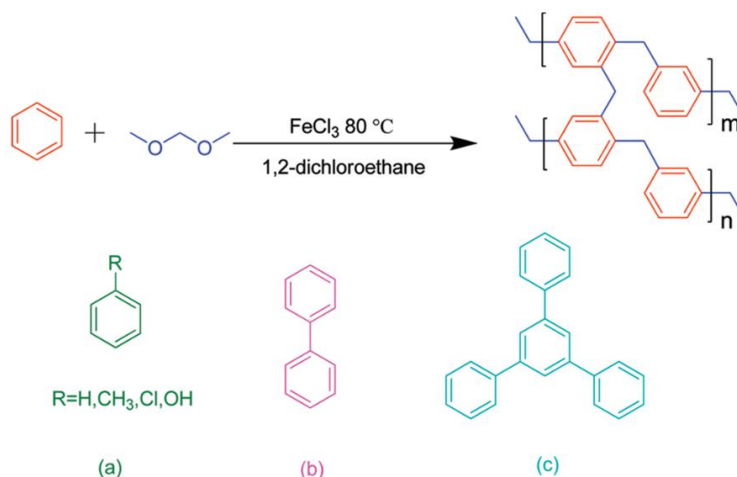


**Figure 1.12** Schematic representation of the knitting method used to synthesise HCP networks<sup>94</sup>

Of the numerous types of microporous polymers, HCPs lend themselves best to scalability. This is mainly a result of the synthesis being simple, involving cheap and abundant starting materials and offers short reaction times (~12 h). The ease of which functionality can be incorporated into the final material has led to exploration of numerous applications such as gas storage,<sup>99–103</sup> wastewater purification,<sup>104–106</sup> catalysis<sup>107–110</sup> and more<sup>98,111–114</sup>. Nevertheless, there are still disadvantages such as the fact that most HCPs can only be synthesised in dichloroethane, the reaction produces corrosive by-products and large quantities of heat are generated due to the exothermic nature of the reaction. Furthermore, the use of stoichiometric amounts of metal catalyst is also problematic, both in synthesis and in purification. There have been efforts to alleviate this, Schute and Rose reported the synthesis of HCPs using sulphuric acid in place of traditional  $\text{FeCl}_3$  though this route did result in materials with lower surface areas and was especially poor when applied towards the knitting method.<sup>115</sup> Nevertheless, HCPs represent a class of porous materials that can be easily and cost-effectively synthesised, lend themselves to scale-up and can be applied towards numerous applications.

### 1.4.5 MOPs *via* Free Radical Polymerisation

The main drawbacks of HCP synthesis is the stoichiometric quantities of metal catalyst and the necessity of the toxic DCE solvent. These drawbacks affect both conventional HCP synthesis and the knitting method. In 2016 the Li group reported the design of a HCP like network synthesised using conventional free radical polymerisation.<sup>116</sup> Here, the result of a porous network arises from the alternating radical polymerisation of DVB and bismaleimides (Figure 1.13). This method does not suffer from the same drawbacks as conventional HCP synthesis as it involves no metal catalyst, less harmful solvents, produces no harsh by-products and offers high atom economy.

## Chapter 1. Introduction

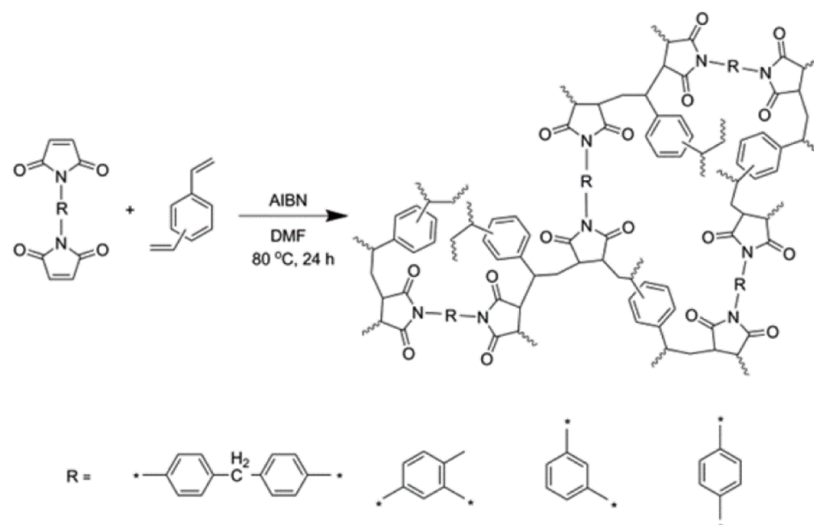


**Figure 1.13** Synthesis of HCP based on free radical polymerisation as reported by Gao *et al.*<sup>116</sup>

The networks synthesised by this method were found to have BET surface areas ranging from 695 – 841 m<sup>2</sup>/g depending on which bismaleimide monomer was polymerised. The materials contained a mixture of both micro- and mesopores (2 – 20 nm) as indicated by the presence of a prominent hysteresis loop in the nitrogen gas sorption isotherm and confirmed by pore size analysis. The highest surface area material *p*-PDM-DVB (841 m<sup>2</sup>/g) displayed excellent CO<sub>2</sub> capacity, adsorbing 11.22 wt. % at 1 bar and 273 K. This high performance is attributed to both the microporous network as well as the inclusion of heteroatoms in the final material.

In 2017 Li and co-workers reported the same synthetic approach towards porous materials by substituting fumaronitrile (FN) in place of the bismaleimides, thereby demonstrating the versatility of this method.<sup>117</sup> Surface areas exceeding 800 m<sup>2</sup>/g were achieved by varying the ratio of DVB:FN. The final material could also be carbonised to yield a nitrogen rich and highly porous material (1450 m<sup>2</sup>/g) capable of acting as a supercapacitor with a capacitance of 330 F/g. It was also shown, in 2018, by Zhu *et al.*<sup>118</sup> how this approach can be UV initiated as opposed to conventional thermal initiation. The advantage UV initiation holds over thermal initiation is the increased rate of reaction, polymerisation is possible at room temperature and reactions are much faster.

## Chapter 1. Introduction

### 1.4.6 Polymers of Intrinsic Microporosity (PIMs)

Polymers of intrinsic microporosity (PIMs) represent the only class of microporous polymer that are both porous *and* soluble, thereby offering numerous processability advantages over all other MOPs. First reported in 2004 by McKeown and Budd,<sup>119</sup> the porosity in PIMs is a result of the polymerisation of rigid and contorted monomers that possess a tetrahedral spiro centre referred to as a site of contortion. This is essentially a bond about which there is restricted rotation and as such promotes space inefficient packing within the polymer chain resulting in the creation of free volume and hence microporosity upon removal of the solvent (Figure 1.14). One key difference between PIMs and other MOPs is the fact that the porosity in the former is intrinsic, *i.e.* solely rising from the materials molecular structure, whereas the porosity in the latter is a result of the creation of a porous network *via* covalent bond formation.

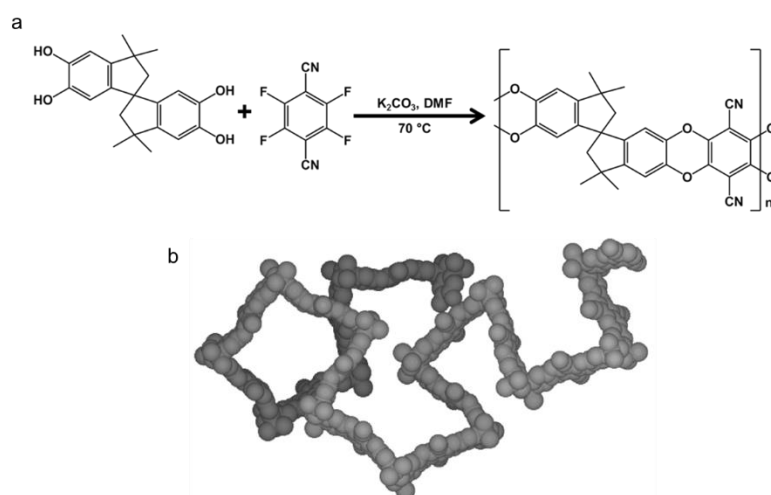


**Figure 1.14** (a) Synthetic route to PIM-1 and (b) space-filling model of PIM-1

The first PIM was based on a porphyrin network which included metal centres with surface areas ranging from 900 – 1000 m<sup>2</sup>/g.<sup>120</sup> However, these networks were all completely insoluble and it was not until 2004 that soluble porous polymers were first reported. In this work a series of linear and intrinsically porous materials were synthesised by the formation of dibenzodioxane linkages. The most studied of these materials, PIM-1, had the highest BET surface area of 850 m<sup>2</sup>/g while others ranged from 430 – 600 m<sup>2</sup>/g. Given that these materials are soluble it is possible to determine their molecular mass *via* GPC which was found to be 270 000 g/mol for PIM-1.

Dibenzodioxane formation was the reaction mechanism predominantly used to synthesis many early PIM materials, including PIM-1. This reaction involves the nucleophilic aromatic substitution mechanism between a biscatechol alongside a tetrahalide monomer, in the case of PIM-1 this was; 5,5',6,6'-tetrahydroxy-3,3',3',3'-tetramethyl-1,1'-spirobisindane and

## Chapter 1. Introduction

2,3,5,6-tetrafluoroterephthalonitrile. This synthesis has also led to the design of other PIMs by varying the monomers used in the reaction (Figure 1.15). However, the research interest in this area has led to the development of PIMs by a number of different routes such as imide<sup>121–123</sup> and amide<sup>123</sup> formation as well as Tröger's base formation<sup>124,125</sup>. All these routes lead to materials which are porous and soluble though their surface areas and molecular weights vary dramatically. Further to this, PIMs can also be post-synthetically modified which, in the case of PIM-1, typically involves modifying the CN group. For example, Patel and Yavuz reported the synthesis of amidoxime-PIM-1 by modification of the nitrile group of PIM-1 using a hydroxyl amine.<sup>126</sup> Though this material had a lower surface area than PIM-1 it was able to uptake more CO<sub>2</sub> as a result of the introduction of this amine moiety. Song *et al.* were able to introduce oxidative crosslinks into PIM-1 by heating the material in the presence of oxygen, with these crosslinks improving the CO<sub>2</sub>:CH<sub>4</sub> selectivity of the material.<sup>127</sup>

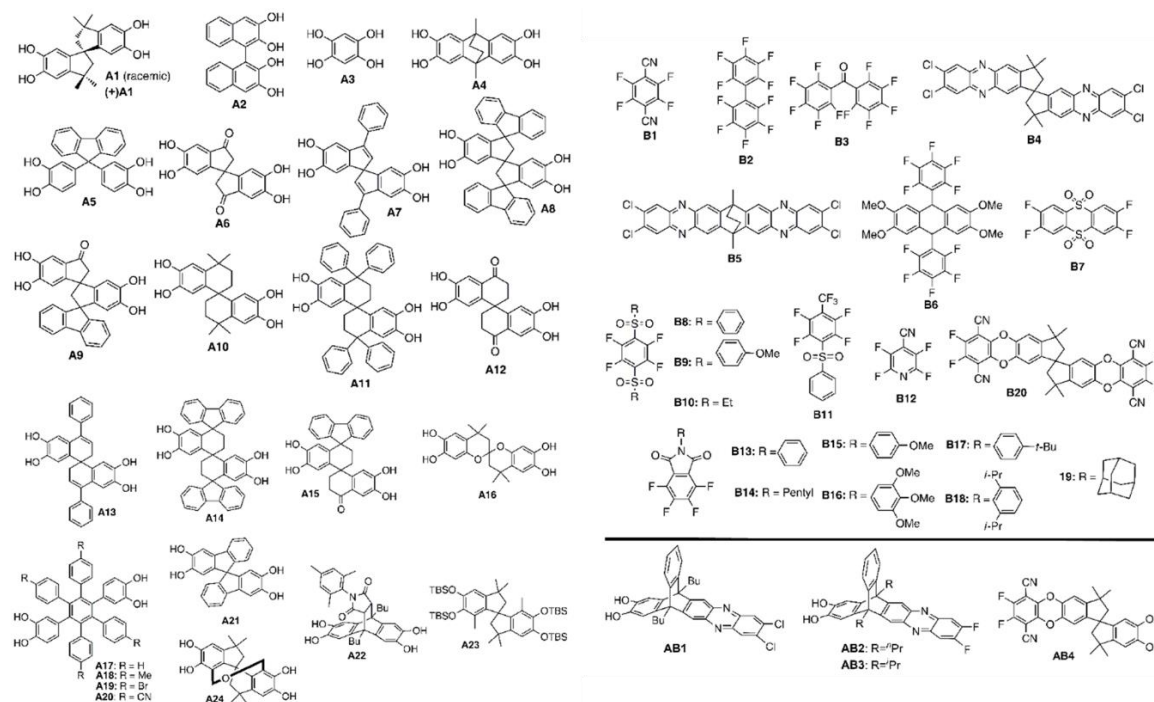


**Figure 1.15** Examples of monomers used towards PIM synthesis *via* dibenzodioxane formation<sup>128</sup>

Conventional polymers have been extensively researched as gas separation membranes for the last 50 or so years.<sup>129</sup> Polymer membranes for gas separation is a very energy-efficient process given that they require no thermal regeneration barrier and involves no phase change.<sup>130</sup> Polymer membranes achieve separation based on a diffusion mechanism in which some gas molecules can diffuse through the membrane but others are excluded. Of the polymers studied as membranes for gas separation those which possess rigid molecular structures give the best permeance and selectivity values, owed to the larger amounts of free volume within the material.<sup>131</sup> Membrane behaviour is characterised by two main features,

## Chapter 1. Introduction

permeability and selectivity. Quite often, it is the case that a material which demonstrates good permeability suffers from poor selectivity and vice-versa with this balance being the key challenge in membrane technology. In 1991 Robeson extensively analysed the literature for certain gas mixtures and reported the first upper bound, a log plot of permeability against selectivity representing state-of-the-art performance.<sup>132</sup> At the time, no material rested above the upper limit, though eventually some materials began to surpass this bound and so in 2008 this was revisited.<sup>133</sup>

PIMs represent great potential in the field of gas separation membranes given that they are porous materials capable of being cast into freestanding films. As such, since the first report of PIM-1 there has been extensive research into the use of PIMs as gas separation membranes for a wide variety of different gas mixtures. PIM-1 and PIM-7 were studied for their ability to separate mixes of O<sub>2</sub>/N<sub>2</sub> and CO<sub>2</sub>/CH<sub>4</sub> and it was found that the results exceed the 1991 upper bound.<sup>134</sup> Further treatment of the film with methanol led to even greater performance and this effect was attributed to the methanol removing any residual solvent and relaxing the polymer chains.<sup>135</sup> Since then many different PIMs have been reported towards the separation of a variety of different gas mixtures.<sup>122,130,136–138</sup>



**Figure 1.16** (left) Pure PIM-1 film<sup>137</sup> and (right) MMM of PIM-1 and MIL-101<sup>139</sup>

Over time the polymer chains are able to relax which has the effect of narrowing the pores resulting in improved selectivity however with the disadvantage of a decrease in permeability. One way to slow this aging effect whilst still maintaining the permeability of the material is by designing mixed-matrix membranes (MMMs). These materials are synthesised by mixing a porous material with a solution of PIM before forming a membrane through solvent evaporation (Figure 1.16). This has been reported for a variety of porous materials including MOFs,<sup>139–141</sup> HCPs,<sup>142</sup> zeolites<sup>143</sup> and others<sup>144–146</sup>. The inclusion of a second material into the network provides the dual advantage of minimising the aging effect of the PIM material as well as imparting new properties into the material which aids either selectivity or permeability. For example, inclusion of PAF-1 into a PIM-1 membrane, as reported by Lau *et al.*,<sup>147</sup> increases

## Chapter 1. Introduction

the hydrogen permeability of the material by 375 % as well as increasing the H<sub>2</sub>:N<sub>2</sub> selectivity from 4:1 to 13:1.

PIMs represent the only class of MOP to be both porous and soluble which allows for easier processability leading to real world applications. In 2015, 3M and the University of Manchester developed a visible sensor based on PIMs for use in industrial respirators. The fabricated PIM film sits in the respirator and changes colour when organic vapours are adsorbed onto the membrane thereby alerting the user that the respirator needs to be changed. This commercial application of PIMs over other MOPs was predominantly driven by their ease of processability that allowed them to be cast into a membrane and applied to a device. Other MOPs have been designed to detect organic vapours yet cannot be easily processed hence are not yet suitable for real world applications.

### 1.5 Soluble Microporous Polymers

Despite MOPs being intensively researched for over two decades, resulting in thousands of publications, there are very few reports on the design of soluble MOPs. Most obviously, this is due to the fact that microporosity in MOPs is driven by the formation of a rigid network built by irreversible covalent bonds and this results in complete insolubility of the network. Therefore, designing materials that are both solution processable and porous is a very difficult task. Nevertheless, there have been a small number of reports on this topic over the past few years and this section summarises these findings.

In 2012 Cooper and co-workers reported the first ever synthesis of a soluble CMP, dubbed SCMP-1.<sup>148</sup> This material was synthesised *via* a two-step (A<sub>4</sub> + B<sub>2</sub>)-type Suzuki-catalysed aryl-aryl coupling reaction (Figure 1.17). In the first step the arylboronates of both A<sub>4</sub> and B<sub>2</sub> were generated, through the addition of Pd(OAc)<sub>2</sub>, before the statistical polymerisation of the two monomers was carried out in the same flask through the addition of Pd(PPh<sub>3</sub>)<sub>4</sub> and K<sub>2</sub>CO<sub>3</sub>.

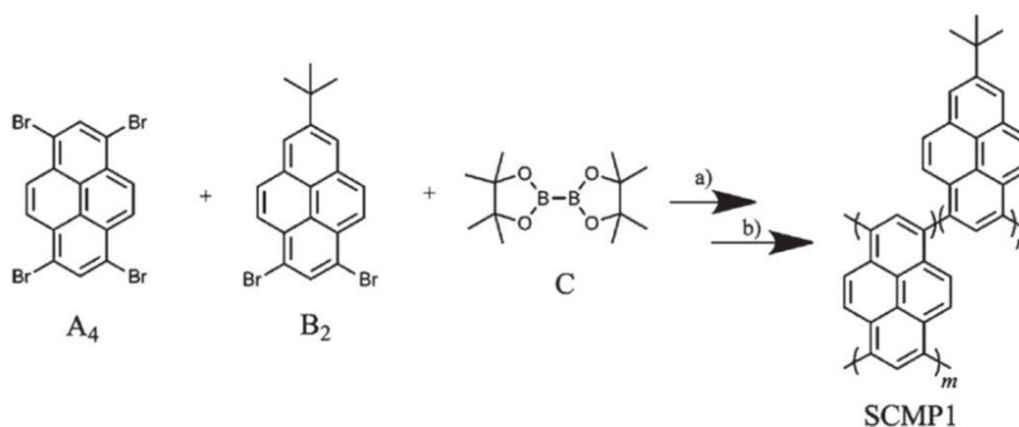


**Figure 1.17** Synthesis of SCMP-1 *via* a two-step synthetic procedure<sup>148</sup>

## Chapter 1. Introduction

Solubility of the final product is due to the incorporation of the bulky *tert*-butyl groups present on monomer B<sub>2</sub>. The presence of these groups helps to limit the molecular weight of the material as well as aiding solubility by incorporating solubilising alkyl groups. Interestingly, the porosity of the material is very dependant on the way in which it is isolated from solution. Rapid precipitation of the material using an anti-solvent yields a porous material yet slow solvent evaporation yields a non-porous film. Hence, dissolving the material in DCM followed by reprecipitation into petroleum ether gave a material with a BET surface area of 505 m<sup>2</sup>/g yet allowing the DCM to slowly evaporate yielded a non-porous sample (12 m<sup>2</sup>/g), though interestingly both materials reported similar hydrogen adsorption capacities (~4 mmol/g). GPC analysis revealed SCMP-1 had a relatively low molecular weight (M<sub>n</sub>) of 4340 g/mol with a PDI of 1.22, which may explain why the film formed from this material was not mechanically stable enough to be handled (Figure 1.18).

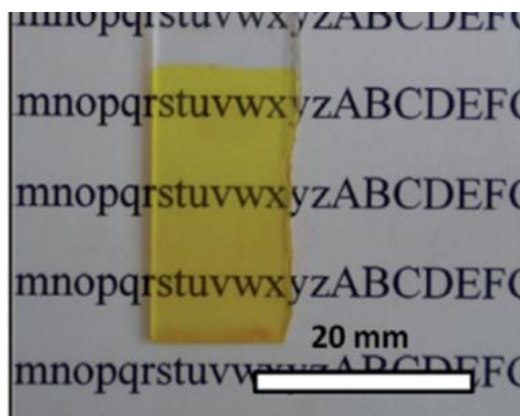


**Figure 1.18** Solvent cast film of SCMP-1 supported on a glass slide

In 2015, Patra and co-workers reported the synthesis of a porous CMP synthesised from the Sonogashira coupling of tetraphenyl-5,5-dioctylcyclopentadiene and 1,4-diethynylbenzene.<sup>83</sup> Fine-tuning of the reaction conditions resulted in the formation of an insoluble powder, solution and nanoparticles. A solid powder (P1) was the result of a conventional Sonogashira cross-coupling reaction whereas P2 (solution) was synthesised by altering the catalyst and reaction time (to inhibit extended coupling and form an insoluble network). P3 (nanoparticles) were the result of an emulsion-type Sonogashira cross-coupling reaction using water as the solvent and SDS as the surfactant stabiliser (Figure 1.19).

## Chapter 1. Introduction

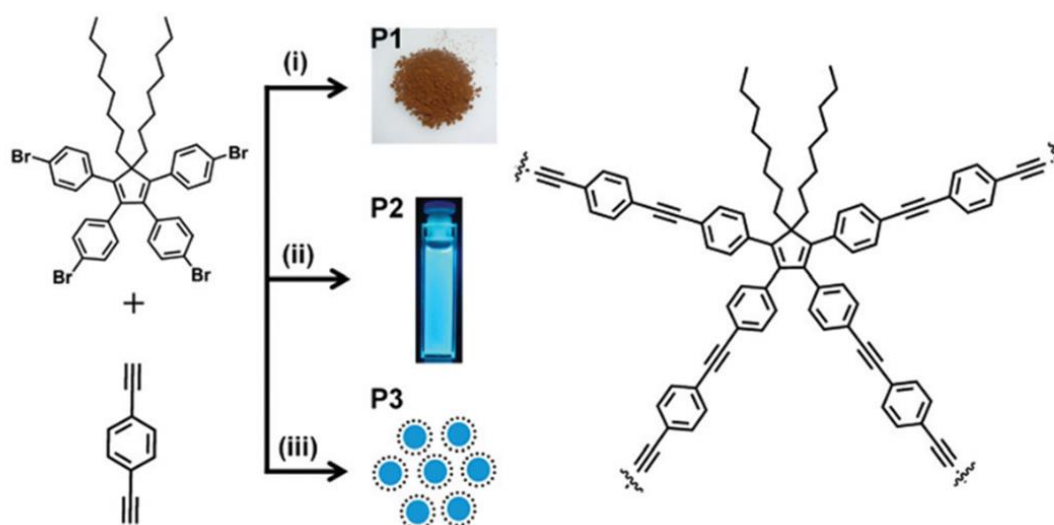


**Figure 1.19** Synthesis of soluble CMP as reported by Patra and co-workers.<sup>83</sup> Reaction conditions: P1 (i)  $[\text{Pd}(\text{PPh}_3)_4]$ , CuI, diisopropylamine, toluene, 80 °C, 48 h, P2 (ii)  $[\text{Pd}(\text{PPh}_3)_2\text{Cl}_2]$ , CuI, diisopropylamine, toluene, 80 °C, 12 h and P3 (iii)  $[\text{Pd}(\text{PPh}_3)_4]$ , CuI, SDS, water, toluene, 50 °C, 48 h,

The long alkyl chains present in these materials imparts a degree of flexibility into the final product as well as limiting any  $\pi$ - $\pi$  stacking interactions between aromatic rings which aids the solubility of these samples. The solution is a result of a less extensive crosslinked network owed to the shorter reaction time and different catalyst. GPC analysis of the solution (P2) revealed a molecular weight ( $M_w$ ) of 16 kDa with a PDI of 1.2, much higher than that reported for SCMP-1 yet less than PIM-1. Film formation was not reported for this material so it is unknown if this material would form a mechanically stable film, though a separate report in 2016 did show film formation, though on a support.<sup>149</sup> Both the solution and nanoparticles could be obtained in the form of powders through reprecipitation into cold methanol with both capable of re-dispersion into THF, DMF and chlorinated solvents.

The surface areas of the materials varied radically despite being comprised of the same monomers. The insoluble powder had a BET surface area of 405  $\text{m}^2/\text{g}$  yet the solution and nanoparticles were much lower, 39  $\text{m}^2/\text{g}$  and 143  $\text{m}^2/\text{g}$  respectively. This is perhaps expected given that solubility is owed to a less crosslinked network, especially for the solution, hence this would result in a lower surface area. Furthermore, gas sorption analysis also reveals a huge drop in micropore volume compared to P1 (0.14  $\text{cm}^3/\text{g}$ ) lowering to 0.037  $\text{cm}^3/\text{g}$  for P3 and 0.0068  $\text{cm}^3/\text{g}$  for P2. Despite its lower surface area, P3 actually demonstrated a much larger total pore volume of 0.93  $\text{cm}^3/\text{g}$  compared to P1 (0.68  $\text{cm}^3/\text{g}$ ) which may be a result of condensation between spherical particles due to the packing arrangement in the solid state. Though this work is a great example of a soluble microporous polymer the surface area of the

## Chapter 1. Introduction

final materials is poor, with virtually no micropores present, and the reaction involved three synthetic steps to synthesise the monomer prior to polymerisation which employs expensive metal catalysts.

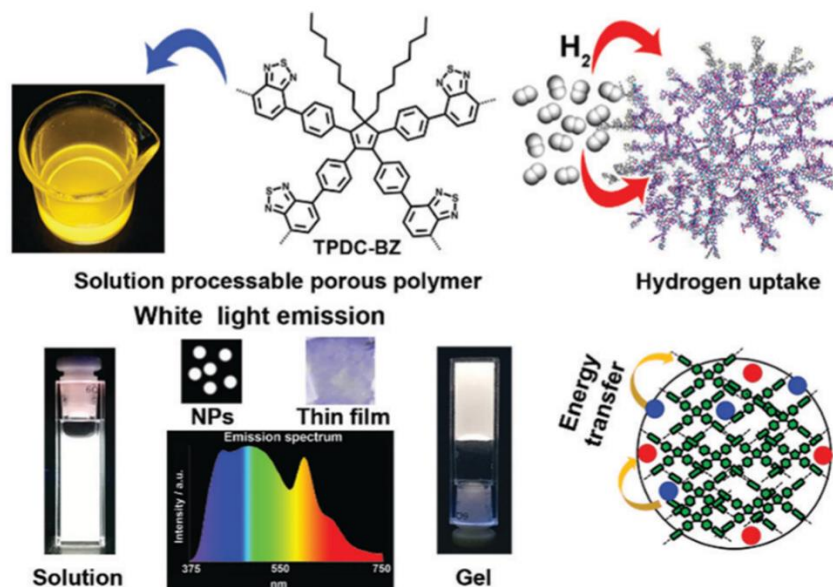


**Figure 1.20** Structure of TPDC-BZ and a schematic illustrating its various forms and applications

A year later, in 2016, the same group reported the synthesis of a structurally similar soluble CMP, synthesised *via* a  $A_4 + B_2$  type Suzuki–Miyaura polycondensation reaction, which could in turn be used to fabricate thin films, gels and nanoparticles.<sup>150</sup> This material, named TPDC-BZ was exploited for its yellow fluorescence and mixed with organic fluorophores to generate white-light (Figure 1.20). TPDC-BZ, has a specific BET surface area of  $610 \text{ m}^2/\text{g}$  with micropore and external surface area determined to be  $330 \text{ m}^2/\text{g}$  and  $280 \text{ m}^2/\text{g}$  respectively by the t-plot method. This material was found to be ultramicroporous ( $< 0.7 \text{ nm}$ ) which gave rise to prominent hydrogen uptake of  $6.4 \text{ mmol/g}$  (1 bar and 77 K), comparable to insoluble porous polymers<sup>78,92,93,96,151</sup> and some PIMs<sup>136</sup>.

In the same year, Wood and co-workers reported the synthesis of solution-processable HCPs, named SHCPs.<sup>152</sup> In this work, conventional hypercrosslinking chemistry was carried out on linear poly(styrene) but at very high dilutions in order to introduce intramolecular crosslinks within individual chains as opposed to intermolecular crosslinks between different chains (Figure 1.21). This is similar in nature to the work carried out by Davankov who synthesised poly(styrene) and crosslinked it high dilution using monochlorodimethyl ether.<sup>153</sup> This resulted in soluble and porous materials with the most porous material, SHCP-5 having a BET surface area of  $724 \text{ m}^2/\text{g}$ . However, after centrifugation and filtration of the solution the BET surface area of the “purely soluble material” was actually  $530 \text{ m}^2/\text{g}$

## Chapter 1. Introduction

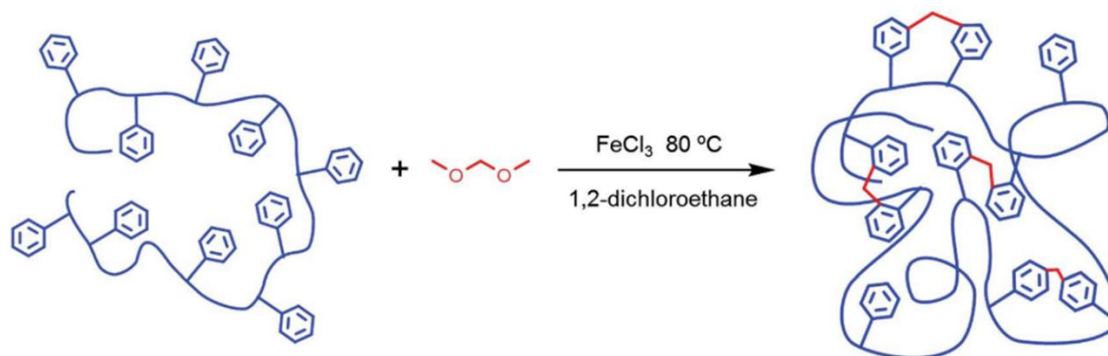


**Figure 1.21** Synthetic approach towards SHCPs<sup>152</sup>

Though this method proved effective in synthesising soluble porous materials the high dilutions (0.005 mol of poly(styrene)/450 mL of DCE) coupled with the fact that the FDA had to be continuously added limits scalability and significantly raises costs. When the FDA was added at once in a batch process the resulting material was found to be brittle and insoluble. Film formation was attempted using SHCP-4 and though this material did form a film, it was too fragile to be handled and had to remain on the support. Finally, these porous materials were also applied towards uptake of different gases and achieved uptakes of between 1.23 mmol/g to 1.84 mmol/g for CO<sub>2</sub> at 1 bar, 273 K. H<sub>2</sub> and CH<sub>4</sub> uptake was also tested for these materials with uptakes of 0.69 to 1.01 wt. % (1 bar, 77 K) and 0.08 to 0.14 wt. % respectively.

In 2015, Matyjaszewski and co-workers reported the synthesis of water-dispersible microporous polymeric nanospheres.<sup>154</sup> Unlike the conventional soluble materials discussed in this section, this work reports the synthesis of hypercrosslinked particles, which are dispersible in solvent media through the presence of long hydrophilic polymer chains. First, divinylbenzene-co-vinylbenzyl chloride nanoparticles are formed before hypercrosslinking these particles to yield porous insoluble spherical particles. Afterwards, SI-ATRP is used to graft long hydrophilic polymer chains onto the material resulting in the formation of “hairy” polymeric nanospheres which are solvent dispersible (Figure 1.22). Though these materials are not typically soluble, they are solution-processable.

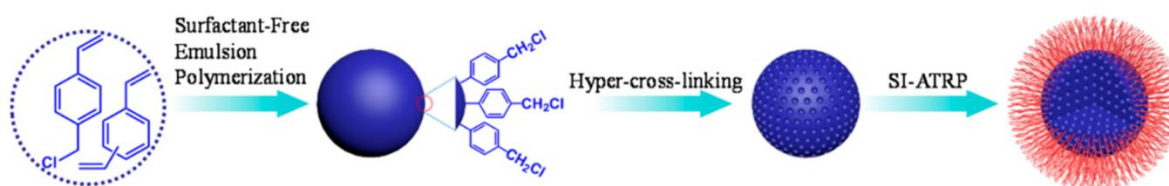


**Figure 1.22** Synthesis of hairy microporous polymeric nanospheres<sup>154</sup>

## Chapter 1. Introduction

This work was the first reported case of synthesising porous and solution-processable porous materials through the union of controlled radical polymerisation and conventional hypercrosslinking chemistry. The synthesis exploits that fact that methyl chloride groups survive the hypercrosslinking procedure and can be used as an initiation site to grow hydrophilic polymers *via* ATRP. Prior to hypercrosslinking the DVB-co-VBC emulsion droplets were essentially non-porous ( $11 \text{ m}^2/\text{g}$ ). Upon hypercrosslinking the surface area increased dramatically to  $1323 \text{ m}^2/\text{g}$  as would be expected due to the extensive crosslinking. Finally, grafting of the hydrophilic polymer, poly(2-dimethylaminoethyl methacrylate) (PDMAEMA) reduced the surface area to  $562 \text{ m}^2/\text{g}$  though it is worth mentioning this did not affect the diameter of the micropores which remained at around 1.3 nm.

The hydrophilicity introduced into the material was aptly demonstrated by both dispersing in water and water contact angle measurements compared to the hypercrosslinked precursor. The highly porous and insoluble HCP emulsion droplets had a water contact angle of  $142^\circ$  which highlighted the inherent hydrophobicity of the sample. Though, upon grafting of the hydrophilic polymer the water contact angle dropped to  $< 5^\circ$  which demonstrates good mixing with the solvent. The inherent hydrophilicity of this material allows for superior removal of the water soluble organic dye alizarin red. After 20 h the dispersible porous polymer was able to adsorb  $1.03 \text{ mg}/\text{m}^2$  compared to the  $0.28 \text{ mg}/\text{m}^2$  which is attributed to the better mixing of the material in solution resulting in better access to the porous core for the dye. The total capacity of the material was found to be  $580 \text{ mg}/\text{g}$ .

Finally these material were also found to be both pH and temperature responsive and could change their size upon modifying these conditions. For example, at pH 10 and  $25^\circ\text{C}$  the diameter of the material, as measured by DLS, was 837 nm yet upon heating to  $50^\circ\text{C}$  this lowered to 661 nm, a result of the LCST of the polymer chain. The size could be increased by lowering the pH and this was a result of protonating the polymer chains caused swelling of the chains (pH 2,  $50^\circ\text{C}$  = 1237 nm). This work demonstrated an alternative synthesis route towards solution-processable porous materials which, though not conventionally soluble, can be synthesised quicker and cheaper than the other materials discussed in this section. The main drawback of this approach is that it is not generic and as such cannot be applied towards a variety of different monomer. Furthermore, numerous synthetic steps and the use of metal catalysts increases costs and is environmentally harmful.

## Chapter 1. Introduction

### 1.6 Porous Polymers for Sustainability

In recent years there have been a number of reports on the use of MOPs for sustainable applications such as wastewater treatment and gas capture and storage. MOPs are ideal materials for these applications as they combine a low density frameworks with ease of functionality and the ability to fine tune physical properties such as pore volume and surface area. Furthermore, they are often much cheaper and more stable than alternative porous materials such as zeolites and MOFs.

#### 1.6.1 Hydrogen Storage

The need to reduce air pollution and keep up with the energy demands of the modern world have led to hydrogen being considered as an alternative fuel. Hydrogen gas produces clean energy with the only by-product produced being water which makes it a clean source of energy. However, to be considered a realistic fuel source it is imperative that it is stored in both a safe and efficient way. As such, MOPs have been explored as materials towards the storage of hydrogen gas.

COFs can be designed to be highly microporous and as such give rise to very large surface area which aids hydrogen uptake. For example, COF-102 and COF-103 both possess BET surface areas exceeding 3000 m<sup>2</sup>/g and demonstrate hydrogen uptake at 77 K of over 7 wt. %, double that of COF-8 (3.50 wt. %) which has a BET surface area of 1350 m<sup>2</sup>/g thereby demonstrating the impact of surface area on uptake.<sup>155</sup> Though surface area is an important factor when designing porous materials for gas uptake so is chemical functionality. This was demonstrated in the design of CMPs for hydrogen storage by Deng *et al.* who showed that the addition of a small amount of Li ions (0.5 wt. %) dramatically increase the hydrogen uptake of CMP-0 from 1.6 wt. % to 6.1 wt. %.<sup>67</sup> Though these numbers seem promising they are skewed somewhat by the fact that the uptakes were recorded at 77 K, which is not a viable operating temperature for commercial application. In 2009 Smit *et al.* designed Li decorated COFs which showed high hydrogen uptake of nearly 7 wt. % at 298 K and 100 bar which surpasses the US department of energy targets of 6 wt. % under the same conditions.<sup>156</sup>

#### 1.6.2 Carbon Dioxide Storage

The capture of CO<sub>2</sub> has become an intensively researched area over the last decade owed much to the issues of global warming and climate change resulting from the release of CO<sub>2</sub> into the atmosphere from anthropogenic point sources. As such CO<sub>2</sub> capture and storage from these large point sources is now considered the most viable medium term solution to mitigate further irreversible changes to the climate. MOPs represent a class of materials well suited towards the capture of CO<sub>2</sub> from these sources. In the same way MOPs can be tailored

## Chapter 1. Introduction

towards hydrogen uptake so too can they be designed in such a way to maximise CO<sub>2</sub> capture. This was shown by Dawson and co-workers in 2011 when designing functionalised CMP networks to maximise CO<sub>2</sub> sorption capacity.<sup>157</sup> It was found that networks containing functionality showed a much greater affinity towards CO<sub>2</sub> and therefore demonstrated much higher uptake than non-functional materials with much higher surface areas (Figure 1.23). This shows how judicious choice of starting material can lead to enhanced performance capabilities even when the surface area is lower than non-functional analogues.

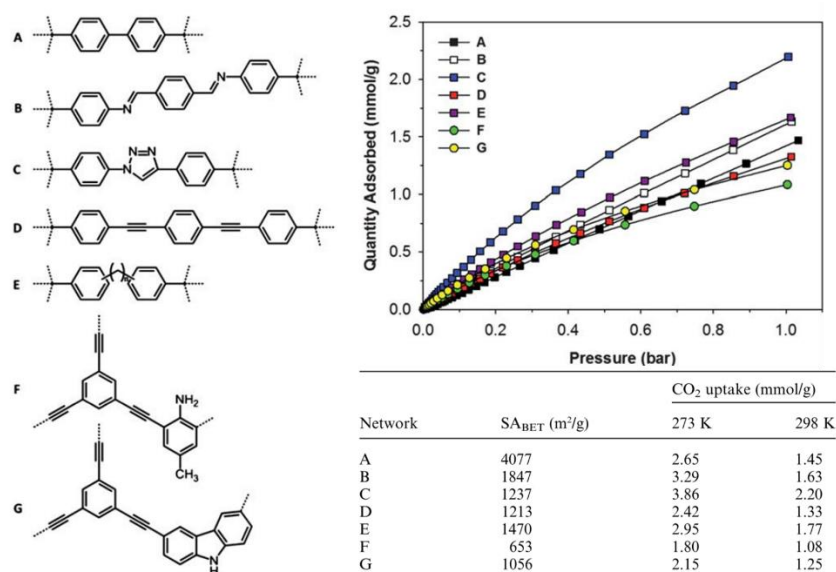


**Figure 1.23** Structure of different functional CMP networks alongside their CO<sub>2</sub> uptake abilities

To be considered a viable candidate for CO<sub>2</sub> capture it is also imperative that the material can be synthesised in high yields and at low costs. These factors mean that materials such as COFs and CMPs are not suitable candidates given the cost of their synthesis. One class of MOP which do meet these requirements are HCPs. HCPs can be synthesised on larger scales than other types of MOPs at low costs and can incorporate different chemical functionality into the final material. For example it is possible to apply the knitting method and crosslink functional monomers together using an external crosslinker. This was done successfully by Jiang *et al.* who synthesised a 1,1,2,2-tetraphenylethane-1,2-diol (TPD) co-polymer network which demonstrated CO<sub>2</sub> uptake exceeding 4 mmol/g at 273 K.<sup>97</sup> Likewise, it is also possible to apply crosslinkable monomers to yield HCPs. This has been demonstrated by Martin and co-workers who designed HCPs using BCMBP which showed uptake exceeding 13 mmol/g at 30 bar thereby demonstrating the excellent stability and applications of these materials.<sup>158</sup> As such there have been numerous more reports on the use of HCPs as candidates for CO<sub>2</sub> uptake.<sup>111,159</sup>

## Chapter 1. Introduction

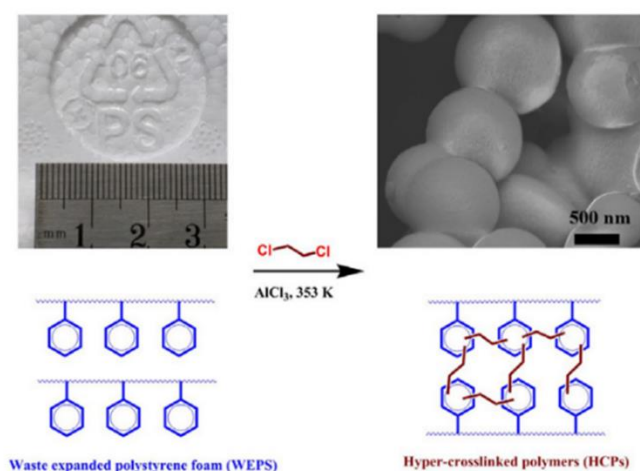


**Figure 1.24** Design of HCP using waste poly(styrene) foam as shown by Liu *et al.*<sup>160</sup>

One particular advantage of HCP synthesis is the versatility of the crosslinking reaction in that it is compatible with a wide range of different starting materials. These starting materials are predominantly either pre-crosslinked resins or simple aromatic monomers. However, in 2017 Liu and co-workers demonstrated that it is even possible to apply a waste material towards HCP synthesis when they successfully hypercrosslinked waste expanded poly(styrene) foam (Figure 1.24).<sup>160</sup> In this work, poly(styrene) foam, commonly seen in packaging, was dissolved in DCE which was applied as both the solvent and crosslinker for the reaction. This resulted in porous materials with BET surface areas ranging from 179 – 573 m<sup>2</sup>/g and CO<sub>2</sub> uptake of between 0.9 – 2 mmol/g. In 2019, the same authors applied the same approach but used different crosslinkers which led to enhanced CO<sub>2</sub> uptake of over 2.5 mmol/g.<sup>161</sup> Though this uptake is lower than most, this work represents a way in which a plentiful and non-decomposable waste material can be applied towards a sustainable application. Furthermore, many papers which report CO<sub>2</sub> uptake capacity do so using single component gases at unrealistic temperature. These conditions are unrepresentative of actual conditions and as such provides no real evidence that said material would make a viable candidate when applied to real world conditions.

### 1.6.3 Wastewater Treatment

In addition to gas uptake, porous materials can also be applied to other sustainable applications such as the treatment of wastewater. The high surface areas, chemical stability and tuneable functionality most MOPs possess make them desirable candidates for the removal of pollutants from wastewater. As with gas capture, MOPs can be tailored specifically towards the capture of certain pollutants. For example, He *et al.* designed a sulphur-rich HCP network by hypercrosslinking the monomer 2,4,6-trithiophen-1,3,5-triazine using an external

## Chapter 1. Introduction

crosslinker.<sup>162</sup> This material had a BET surface area of 255 m<sup>2</sup>/g and was capable of removing Cu(II) from aqueous solution with a maximum adsorption capacity of 98.33 mg/g. Likewise, in 2018 Fu *et al.* reported another sulphur-rich HCP, named NOP-28, which was capable of both selectively detecting and removing mercury ions from water.<sup>163</sup> In this work the fluorescence emission of the material is quenched when in the presence of Hg(II) ions with an exceptional limit of detection of 12 ppb (Figure 1.25). The uptake of Hg(II) ions is very high showing a maximum adsorption capacity of 658 mg/g from aqueous solution despite a modest BET surface area of 144 m<sup>2</sup>/g.

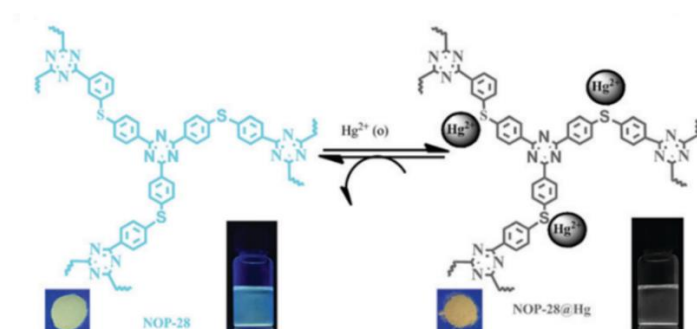


**Figure 1.25** Chemosensing ability of NOP-28 towards Hg(II) ions<sup>163</sup>

In addition to metal ions, it is also possible to design MOP networks to remove organic pollutants. In particular, when applied towards the removal of aromatic and aliphatic compounds from aqueous solutions the hydrophobicity of the polymer network is very beneficial. In 2014, Yang *et al.* reported the synthesis of a triphenylamine-based HCP network by applying BCMBP as the crosslinking monomer. Both powders and monoliths were synthesised depending on the nature of the reaction. The powder, PBP-N-25 had a surface area of 1362 m<sup>2</sup>/g and showed benzene and cyclohexane vapour uptakes of 94.1 wt. % and 95.3 wt. % respectively. These values far outperformed that of water (1.7 wt. %) thereby highlighting the hydrophobic nature of the material and how this would be beneficial for removal of these pollutants in aqueous solution. The monolith, M-PBP-N-25, had a surface area of 551 m<sup>2</sup>/g yet, due to its structure, could be applied towards the removal of cyclohexane from solution where it was found the material was capable of removing 348 wt. % after 10 minutes.

In 2011 Li *et al.* demonstrated how HCMP-1 and HCMP-2 can be used to coat a sponge which can then be applied towards the removal of a variety of chemical contaminants such as organic solvents and oils. The HCMP-1 treated sponge was found to show exceptional uptake abilities towards octane and nitrobenzene, 2300 wt. % and 3300 wt. % respectively. In 2015 Yang *et al.* synthesised a superhydrophobic material by employing fluorinated monomers to yield

## Chapter 1. Introduction

PFCMP-0.<sup>164</sup> This material was capable of simultaneously adsorbing an organic pollutant (toluene), a dye (congo red) and lead ions all in the same solution. For all three pollutants, the material was capable of removing over 99 % from solution and was the first material capable of this simultaneous removal.

## Chapter 1. Introduction

### 1.7 Thesis Aims

This thesis is presented in two parts, which describe the work carried out on designing porous polymers for applications in solution (Part A) and for applications in sustainability (Part B). As such, it is necessary to lay out these aims accordingly by each section.

#### Part A

The aim of this thesis is to investigate microporous polymers and their applications using both traditional insoluble materials and novel solution-processable materials which could lead to applications in the solution phase. The majority of microporous materials are completely insoluble in all common organic solvents, a feature that limits both their applications and processability. As such, these materials are often used as the insoluble powders they form during synthesis.

The main objectives of Part A are to:

- Design a versatile synthetic route towards the design of microporous polymers which can be applied to a range of different monomers
- Fully characterise the new materials both as solids and in the solution phase
- Apply the synthesised materials towards new applications in the solution phase

#### Part B

Part B of this thesis describes work carried out on the design of more traditional porous polymers towards applications in sustainability. Namely, these materials were designed specifically to have applications that try to mitigate the environmental issues the planet is currently facing. This includes a chapter on the removal of contaminants from aqueous solution and a chapter on the capture and storage of CO<sub>2</sub>. These chapters appear in paper format and have either been published or submitted.

The main objectives of Part B are to:

- Design functional porous materials which can be applied to sustainable applications
- Test these materials in a way which mimics the working conditions of their potential applications
- Try to mitigate or even eliminate any environmentally harmful or unsustainable synthetic methods and only use harsh chemicals if necessary

## Chapter 1. Introduction

### 1.8 References

- 1 R. A. W. Sing, K.S.W., Everet, D. H., Haul, *Pure Appl. Chem.*, 1985, **57**, 603–619.
- 2 O. Ioannidou and A. Zabaniotou, *Renew. Sustain. Energy Rev.*, 2007, 11, 1966–2005.
- 3 E. Haffner-Staton, N. Balahmar and R. Mokaya, *J. Mater. Chem. A*, 2016, **4**, 13324–13335.
- 4 M. S. Shamsuddin, N. R. N. Yusoff and M. A. Sulaiman, *Procedia Chem.*, 2016, **19**, 558–565.
- 5 N. Balahmar, A. S. Al-Jumialy and R. Mokaya, *J. Mater. Chem. A*, 2017, **5**, 12330–12339.
- 6 A. R. Khan, T. A. Al-Bahri and A. Al-Haddad, *Water Res.*, 1997, **31**, 2102–2112.
- 7 S. Babel and T. A. Kurniawan, *J. Hazard. Mater.*, 2003, 97, 219–243.
- 8 Z. C. Kampouraki, D. A. Giannakoudakis, K. S. Triantafyllidis and E. A. Deliyanni, *Green Chem.*, 2019, **21**, 6685–6698.
- 9 K. Malins, V. Kampars, J. Brinks, I. Neibolte and R. Murnieks, *Appl. Catal. B Environ.*, 2015, **176–177**, 553–558.
- 10 A. Korus, A. Samson, A. Szlęk, A. Katelbach-Woźniak and S. Sładek, *Fuel*, 2017, **207**, 283–292.
- 11 H. Li, D. Yu, Y. Hu, P. Sun, J. Xia and H. Huang, *Carbon N. Y.*, 2010, **48**, 4547–4555.
- 12 E. Auer, A. Freund, J. Pietsch and T. Tacke, *Appl. Catal. A Gen.*, 1998, **173**, 259–271.
- 13 F. Rodríguez-Reinoso, *Carbon N. Y.*, 1998, **36**, 159–175.
- 14 A. Feliczak-Guzik, *Microporous Mesoporous Mater.*, 2018, **259**, 33–45.
- 15 Y. Li, L. Li and J. Yu, *Chem*, 2017, 3, 928–949.
- 16 C. Chen, D. W. Park and W. S. Ahn, *Appl. Surf. Sci.*, 2014, **292**, 63–67.
- 17 S. J. Chen, M. Zhu, Y. Fu, Y. X. Huang, Z. C. Tao and W. L. Li, *Appl. Energy*, 2017, **191**, 87–98.
- 18 J. Weitkamp, *Solid State Ionics*, 2000, **131**, 175–188.

## Chapter 1. Introduction

- 19 S. Wang and Y. Peng, *Chem. Eng. J.*, 2010, 156, 11–24.
- 20 V. Blay, B. Louis, R. Miravalles, T. Yokoi, K. A. Peccatiello, M. Clough and B. Yilmaz, *ACS Catal.*, 2017, 7, 6542–6566.
- 21 A. Primo and H. Garcia, *Chem. Soc. Rev.*, 2014, 43, 7548–7561.
- 22 H. Furukawa, K. E. Cordova, M. O’Keeffe and O. M. Yaghi, *Science (80-. )*, 2013, 341.
- 23 C. Altintas, G. Avci, H. Daglar, A. Nemati Vesali Azar, I. Erucar, S. Velioglu and S. Keskin, *J. Mater. Chem. A*, 2019, 7, 9593–9608.
- 24 O. K. Farha, I. Eryazici, N. C. Jeong, B. G. Hauser, C. E. Wilmer, A. A. Sarjeant, R. Q. Snurr, S. T. Nguyen, A. Ö. Yazaydin and J. T. Hupp, *J. Am. Chem. Soc.*, 2012, 134, 15016–15021.
- 25 I. M. Hönicke, I. Senkovska, V. Bon, I. A. Baburin, N. Bönisch, S. Raschke, J. D. Evans and S. Kaskel, *Angew. Chemie - Int. Ed.*, 2018, 57, 13780–13783.
- 26 S. Qiu, M. Xue and G. Zhu, *Chem. Soc. Rev.*, 2014, 43, 6116–6140.
- 27 Y. Basdogan and S. Keskin, *CrystEngComm*, 2015, 17, 261–275.
- 28 C. Zhang, Y. Yan, Q. Pan, L. Sun, H. He, Y. Liu, Z. Liang and J. Li, *Dalt. Trans.*, 2015, 44, 13340–13346.
- 29 Y. M. Ma, T. Liu and W. H. Huang, *J. Solid State Chem.*, 2018, 258, 176–180.
- 30 B. Aguila, D. Banerjee, Z. Nie, Y. Shin, S. Ma and P. K. Thallapally, *Chem. Commun.*, 2016, 52, 5940–5942.
- 31 N. S. Bobbitt, M. L. Mendonca, A. J. Howarth, T. Islamoglu, J. T. Hupp, O. K. Farha and R. Q. Snurr, *Chem. Soc. Rev.*, 2017, 46, 3357–3385.
- 32 Z. Wang, Z. Wang, B. Lin, X. Hu, Y. Wei, C. Zhang, B. An, C. Wang and W. Lin, *ACS Appl. Mater. Interfaces*, 2017, 9, 35253–35259.
- 33 N. Stock and S. Biswas, *Chem. Rev.*, 2012, 112, 933–969.
- 34 M. Rubio-Martinez, C. Avci-Camur, A. W. Thornton, I. Imaz, D. MasPOCH and M. R. Hill, *Chem. Soc. Rev.*, 2017, 46, 3453–3480.
- 35 N. Chaoui, M. Trunk, R. Dawson, J. Schmidt and A. Thomas, *Chem. Soc. Rev.*, 2017,

## Chapter 1. Introduction

- 46, 3302–3321.
- 36 D. Yuan, W. Lu, D. Zhao and H. C. Zhou, *Adv. Mater.*, 2011, **23**, 3723–3725.
- 37 R. T. Woodward, L. A. Stevens, R. Dawson, M. Vijayaraghavan, T. Hasell, I. P. Silverwood, A. V. Ewing, T. Ratvijitvech, J. D. Exley, S. Y. Chong, F. Blanc, D. J. Adams, S. G. Kazarian, C. E. Snape, T. C. Drage and A. I. Cooper, *J. Am. Chem. Soc.*, 2014, **136**, 9028–9035.
- 38 D. S. Ahmed, G. A. El-Hiti, E. Yousif, A. A. Ali and A. S. Hameed, *J. Polym. Res.*, 2018, **25**, 75.
- 39 A. J. M. and O. M. Y. A. P. Cote, A. I. Benin, N. W. Ockwig, M. O’Keeffe, *Science (80-. )*, 2005, **310**, 1166–1170.
- 40 A. P. Côté, H. M. El-Kaderi, H. Furukawa, J. R. Hunt and O. M. Yaghi, *J. Am. Chem. Soc.*, 2007, **129**, 12914–12915.
- 41 H. Furukawa and O. M. Yaghi, *J. Am. Chem. Soc.*, 2009, **131**, 8875–8883.
- 42 A. K. G. & K. S. Novoselov, *Nat. Mater.*, 2007, **6**, 183–191.
- 43 M. Xu, T. Liang, M. Shi and H. Chen, *Chem. Rev.*, 2013, **113**, 3766–3798.
- 44 H. M. El-Kaderi, J. R. Hunt, J. L. Mendoza-Cortes, A. P. Cote, R. E. Taylor, M. O’Keeffe and O. M. Yaghi, *Science (80-. )*, 2007, **316**, 268–272.
- 45 C. Férey, C. Mellot-Draznieks, C. Serre, F. Millange, J. Dutour, S. Surblé and I. Margiolaki, *Science (80-. )*, 2005, **309**, 2040–2042.
- 46 P. Horcajada, C. Serre, M. Vallet-Regí, M. Sebban, F. Taulelle and G. Férey, *Angew. Chemie - Int. Ed.*, 2006, **45**, 5974–5978.
- 47 R. W. Tilford, S. J. Mugavero, P. J. Pellechia and J. J. Lavigne, *Adv. Mater.*, 2008, **20**, 2741–2746.
- 48 F. J. Uribe-Romo, J. R. Hunt, H. Furukawa, C. Klöck, M. O’Keeffe and O. M. Yaghi, *J. Am. Chem. Soc.*, 2009, **131**, 4570–4571.
- 49 S. Dalapati, S. Jin, J. Gao, Y. Xu, A. Nagai and D. Jiang, *J. Am. Chem. Soc.*, 2013, **135**, 17310–17313.
- 50 L. Wang, C. Zeng, H. Xu, P. Yin, D. Chen, J. Deng, M. Li, N. Zheng, C. Gu and Y. Ma,

## Chapter 1. Introduction

- Chem. Sci.*, 2019, **10**, 1023–1028.
- 51 J. Wang and S. Zhuang, *Coord. Chem. Rev.*, 2019, **400**, 213046.
- 52 F. Zamora, P. Albacete, A. E. Platero-Prats, E. M. Pérez, A. López-Moreno and S. Mena-Hernando, *Chem. Commun.*, 2018, **55**, 1382–1385.
- 53 P. Wang, Q. Xu, Z. Li, W. Jiang, Q. Jiang and D. Jiang, *Adv. Mater.*, 2018, **30**, 1801991.
- 54 N. L. Campbell, R. Clowes, L. K. Ritchie and A. I. Cooper, *Chem. Mater.*, 2009, **21**, 204–206.
- 55 B. P. Biswal, S. Chandra, S. Kandambeth, B. Lukose, T. Heine and R. Banerjee, *J. Am. Chem. Soc.*, 2013, **135**, 5328–5331.
- 56 S. Kandambeth, K. Dey and R. Banerjee, *J. Am. Chem. Soc.*, 2019, **141**, 1807–1822.
- 57 K. Dey, M. Pal, K. C. Rout, S. S. Kunjattu, A. Das, R. Mukherjee, U. K. Kharul and R. Banerjee, *J. Am. Chem. Soc.*, 2017, **139**, 13083–13091.
- 58 P. Kuhn, M. Antonietti and A. Thomas, *Angew. Chemie - Int. Ed.*, 2008, **47**, 3450–3453.
- 59 P. Kuhn, A. Thomas and M. Antonietti, *Macromolecules*, 2009, **42**, 319–326.
- 60 P. Katekomol, J. Roeser, M. Bojdys, J. Weber and A. Thomas, *Chem. Mater.*, 2013, **25**, 1542–1548.
- 61 S. Ren, M. J. Bojdys, R. Dawson, A. Laybourn, Y. Z. Khimyak, D. J. Adams and A. I. Cooper, *Adv. Mater.*, 2012, **24**, 2357–2361.
- 62 X. Zhu, C. Tian, S. M. Mahurin, S. H. Chai, C. Wang, S. Brown, G. M. Veith, H. Luo, H. Liu and S. Dai, *J. Am. Chem. Soc.*, 2012, **134**, 10478–10484.
- 63 K. Wang, L. M. Yang, X. Wang, L. Guo, G. Cheng, C. Zhang, S. Jin, B. Tan and A. Cooper, *Angew. Chemie - Int. Ed.*, 2017, **56**, 14149–14153.
- 64 J. X. Jiang, F. Su, A. Trewin, C. D. Wood, N. L. Campbell, H. Niu, C. Dickinson, A. Y. Ganin, M. J. Rosseinsky, Y. Z. Khimyak and A. I. Cooper, *Angew. Chemie - Int. Ed.*, 2007, **46**, 8574–8578.
- 65 J. X. Jiang, F. Su, A. Trewin, C. D. Wood, H. Niu, J. T. A. Jones, Y. Z. Khimyak and A. I. Cooper, *J. Am. Chem. Soc.*, 2008, **130**, 7710–7720.

## Chapter 1. Introduction

- 66 J. X. Jiang, F. Su, H. Niu, C. D. Wood, N. L. Campbell, Y. Z. Khimyak and A. I. Cooper, *Chem. Commun.*, 2008, **8**, 486–488.
- 67 A. Li, R. F. Lu, Y. Wang, X. Wang, K. L. Han and W. Q. Deng, *Angew. Chemie - Int. Ed.*, 2010, **49**, 3330–3333.
- 68 R. Dawson, D. J. Adams and A. I. Cooper, *Chem. Sci.*, 2011, **2**, 1173.
- 69 R. Dawson, A. Laybourn, Y. Z. Khimyak, D. J. Adams and A. I. Cooper, *Macromolecules*, 2010, **43**, 8524–8530.
- 70 J.-X. Jiang, C. Wang, A. Laybourn, T. Hasell, R. Clowes, Y. Z. Khimyak, J. Xiao, S. J. Higgins, D. J. Adams and A. I. Cooper, *Angew. Chemie Int. Ed.*, 2011, **50**, 1072–1075.
- 71 R. Dawson, A. I. Cooper and D. J. Adams, *Prog. Polym. Sci.*, 2012, **37**, 530–563.
- 72 L. Li, W. Y. Lo, Z. Cai, N. Zhang and L. Yu, *Macromolecules*, 2016, **49**, 6903–6909.
- 73 L. Sun, Y. Zou, Z. Liang, J. Yu and R. Xu, *Polym. Chem.*, 2014, **5**, 471–478.
- 74 J. Schmidt, M. Werner and A. Thomas, *Macromolecules*, 2009, **42**, 4426–4429.
- 75 A. Li, H.-X. Sun, D.-Z. Tan, W.-J. Fan, S.-H. Wen, X.-J. Qing, G.-X. Li, S.-Y. Li and W.-Q. Deng, *Energy Environ. Sci.*, 2011, **4**, 2062.
- 76 P. Pandey, A. P. Katsoulidis, I. Eryazici, Y. Wu, M. G. Kanatzidis and S. T. Nguyen, *Chem. Mater.*, 2010, **22**, 4974–4979.
- 77 C. Xu and N. Hedin, *J. Mater. Chem. A*, 2013, **1**, 3406–3414.
- 78 L. Tan, B. Li, X. Yang, W. Wang and B. Tan, *Polymer (Guildf)*, 2015, **70**, 336–342.
- 79 Y. Xu, S. Jin, H. Xu, A. Nagai and D. Jiang, *Chem. Soc. Rev*, 2013, **42**, 7965–8178.
- 80 Y. L. Wong, J. M. Tobin, Z. Xu and F. Vilela, *J. Mater. Chem. A*, 2016, **4**, 18677–18686.
- 81 R. S. Sprick, Y. Bai, A. A. Y. Guilbert, M. Zbiri, C. M. Aitchison, L. Wilbraham, Y. Yan, D. J. Woods, M. A. Zwijnenburg and A. I. Cooper, *Chem. Mater.*, 2019, **31**, 305–313.
- 82 Y. Xu, N. Mao, S. Feng, C. Zhang, F. Wang, Y. Chen, J. Zeng and J. X. Jiang, *Macromol. Chem. Phys.*, 2017, **218**, 1700049.
- 83 S. Bandyopadhyay, P. Pallavi, A. G. Anil and A. Patra, *Polym. Chem.*, 2015, **6**, 3775–3780.

## Chapter 1. Introduction

- 84 Z. Li, H. Li, H. Xia, X. Ding, X. Luo, X. Liu and Y. Mu, *Chem. - A Eur. J.*, 2015, **21**, 17355–17362.
- 85 S. Wang, Y. Liu, Y. Yu, J. Du, Y. Cui, X. Song and Z. Liang, *New J. Chem.*, 2018, **42**, 9482–9487.
- 86 P. Kaur, J. T. Hupp and S. T. Nguyen, *ACS Catal.*, 2011, **1**, 819–835.
- 87 S. Bandyopadhyay, A. G. Anil, A. James and A. Patra, *ACS Appl. Mater. Interfaces*, 2016, **8**, 27669–27678.
- 88 Y. Xu, L. Chen, Z. Guo, A. Nagai and D. Jiang, *J. Am. Chem. Soc.*, 2011, **133**, 17622–17625.
- 89 R. Dawson, A. Laybourn, R. Clowes, Y. Z. Khimyak, D. J. Adams and A. I. Cooper, *Macromolecules*, 2009, **42**, 8809–8816.
- 90 V. A. Davankov, S. V. Rogoshin and M. P. Tsyurupa, *J Polym Sci Part C, Polym Symp*, 1974, **101**, 95–101.
- 91 J. H. Ahn, J. E. Jang, C. G. Oh, S. K. Ihm, J. Cortez and D. C. Sherrington, *Macromolecules*, 2006, **39**, 627–632.
- 92 C. D. Wood, B. Tan, A. Trewin, H. Niu, D. Bradshaw, M. J. Rosseinsky, Y. Z. Khimyak, N. L. Campbell, R. Kirk, E. Stöckel and A. I. Cooper, *Chem. Mater.*, 2007, **19**, 2034–2048.
- 93 M. G. Schwab, A. Lennert, J. Pahnke, G. Jonschker, M. Koch, I. Senkovska, M. Rehahn and S. Kaskel, *J. Mater. Chem.*, 2011, **21**, 2131–2135.
- 94 B. Li, R. Gong, W. Wang, X. Huang, W. Zhang, H. Li, C. Hu and B. Tan, *Macromolecules*, 2011, **44**, 2410–2414.
- 95 R. Dawson, L. A. Stevens, T. C. Drage, C. E. Snape, M. W. Smith, D. J. Adams and A. I. Cooper, *J. Am. Chem. Soc.*, 2012, **134**, 10741–10744.
- 96 X. Yang, M. Yu, Y. Zhao, C. Zhang, X. Wang and J.-X. Jiang, *RSC Adv.*, 2014, **4**, 61051–61055.
- 97 S. Yao, X. Yang, M. Yu, Y. Zhang and J.-X. Jiang, *J. Mater. Chem. A*, 2014, **2**, 8054.
- 98 C. Wilson, M. Main, N. Cooper, M. E. Briggs, A. I. Cooper and D. Adams, *Polym. Chem.*,

## Chapter 1. Introduction

- 2017, **8**, 1914–1922.
- 99 D. Chen, S. Gu, Y. Fu, Y. Zhu, C. Liu, G. Li, G. Yu and C. Pan, *Polym. Chem.*, 2016, **7**, 3416–3422.
- 100 S. Mane, Z.-Y. Gao, Y.-X. Li, D.-M. Xue, X.-Q. Liu and L.-B. Sun, *J. Mater. Chem. A*, 2017, **00**, 1–9.
- 101 Y. Yang, Q. Zhang, S. Zhang and S. Li, *Polymer (Guildf)*., 2013, **54**, 5698–5702.
- 102 A. Z. Peng, S. C. Qi, X. Liu, D. M. Xue, S. S. Peng, G. X. Yu, X. Q. Liu and L. B. Sun, *Chem. Eng. J.*, 2019, **369**, 170–179.
- 103 V. Rozyyev, D. Thirion, R. Ullah, J. Lee, M. Jung, H. Oh, M. Atilhan and C. T. Yavuz, *Nat. Energy*, 2019, **4**, 604–611.
- 104 A. M. James, S. Harding, T. Robshaw, N. Bramall, M. D. Ogden and R. Dawson, *ACS Appl. Mater. Interfaces*, 2019, **11**, 22464–22473.
- 105 M. P. Tsyurupa, Z. K. Blinnikova, Y. A. Borisov, M. M. Ilyin, T. P. Klimova, K. V. Mitsen and V. A. Davankov, *J. Sep. Sci.*, 2014, **37**, 803–810.
- 106 D. Bratkowska, A. Davies, N. Fontanals, P. A. G. Cormack, F. Borrull, D. C. Sherrington and R. M. Marc??, *J. Sep. Sci.*, 2012, **35**, 2621–2628.
- 107 J. Luo, X. Zhang and J. Zhang, *ACS Catal.*, 2015, **5**, 2250–2254.
- 108 R. M. N. Kalla, M.-R. Kim and I. Kim, *Ind. Eng. Chem. Res.*, 2018, **57**, 11583–11591.
- 109 J. Luo, J. Lu and J. Zhang, *J. Mater. Chem. A*, 2018, **6**, 15154–15161.
- 110 R. Li, Z. J. Wang, L. Wang, B. C. Ma, S. Ghasimi, H. Lu, K. Landfester and K. A. I. Zhang, *ACS Catal.*, 2016, **6**, 1113–1121.
- 111 L. Tan and B. Tan, *Chem. Soc. Rev.*, 2017, **46**, 3322–3356.
- 112 C. Zhang, S. Wang, Z. Zhan, A. M. Amin and B. Tan, *ACS Macro Lett.*, 2019, **8**, 403–408.
- 113 Q. Zhang, T. Zhai, Z. Wang, G. Cheng, H. Ma, Q. Zhang, Y. Zhao, B. Tan and C. Zhang, *Adv. Mater. Interfaces*, 2019, 1900249.
- 114 X. Wang, H. Ou and J. Huang, *J. Colloid Interface Sci.*, 2019, **538**, 499–506.

## Chapter 1. Introduction

- 115 K. Schute and M. Rose, *ChemSusChem*, 2015, **8**, 3419–3423.
- 116 H. Gao, L. Ding, W. Li, G. Ma, H. Bai and L. Li, *ACS Macro Lett.*, 2016, **5**, 377–381.
- 117 F. Xie, W. Hu, L. Ding, K. Tian, Z. Wu and L. Li, *Polym. Chem.*, 2017, **8**, 6106–6111.
- 118 T. Zhu, F. Xie, T. Huang, K. Tian, Z. Wu, H. Yang and L. Li, *ACS Macro Lett.*, 2018, **7**, 1283–1288.
- 119 P. M. Budd, B. S. Ghanem, S. Makhseed, N. B. McKeown, K. J. Msayib and C. E. Tattershall, *Chem. Commun.*, 2004, 230.
- 120 N. B. McKeown, S. Makhseed and P. M. Budd, *Chem. Commun.*, 2002, **44**, 2780–1.
- 121 B. S. Ghanem, N. B. McKeown, P. M. Budd, N. M. Al-Harbi, D. Fritsch, K. Heinrich, L. Starannikova, A. Tokarev and Y. Yampolskii, *Macromolecules*, 2009, **42**, 7881–7888.
- 122 Y. Rogan, R. Malpass-Evans, M. Carta, M. Lee, J. C. Jansen, P. Bernardo, G. Clarizia, E. Tocci, K. Friess, M. Lanč and N. B. McKeown, *J. Mater. Chem. A*, 2014, **2**, 4874–4877.
- 123 B. S. Ghanem, N. B. McKeown, P. M. Budd, J. D. Selbie and D. Fritsch, *Adv. Mater.*, 2008, **20**, 2766–2771.
- 124 M. Carta, R. Malpass-Evans, M. Croad, Y. Rogan, J. C. Jansen, P. Bernardo, F. Bazzarelli and N. B. McKeown, *Science (80-. )*, 2013, **339**, 303–307.
- 125 M. Carta, R. Malpass-Evans, M. Croad, Y. Rogan, M. Lee, I. Rose and N. B. McKeown, *Polym. Chem.*, 2014, **5**, 5267–5272.
- 126 H. A. Patel and C. T. Yavuz, *Chem. Commun.*, 2012, **48**, 9989.
- 127 Q. Song, S. Cao, R. H. Pritchard, B. Ghalei, S. A. Al-Muhtaseb, E. M. Terentjev, A. K. Cheetham and E. Sivaniah, *Nat. Commun.*, 2014, **5**, 4813.
- 128 N. B. McKeown, *Sci. China Chem.*, 2017, **60**, 1023–1032.
- 129 P. Pandey and R. S. Chauhan, *Prog. Polym. Sci.*, 2001, **26**, 853–893.
- 130 N. B. McKeown, *ISRN Mater. Sci.*, 2012, **2012**, 1–16.
- 131 K. Nagai, T. Masuda, T. Nakagawa, B. D. Freeman and I. Pinnau, *Prog. Polym. Sci.*, 2001, **26**, 721–798.

## Chapter 1. Introduction

- 132 L. M. Robeson, *J. Memb. Sci.*, 1991, **62**, 165–185.
- 133 L. M. Robeson, *J. Memb. Sci.*, 2008, **320**, 390–400.
- 134 P. M. Budd, K. J. Msayib, C. E. Tattershall, B. S. Ghanem, K. J. Reynolds, N. B. McKeown and D. Fritsch, *J. Memb. Sci.*, 2005, **251**, 263–269.
- 135 P. M. Budd, N. B. McKeown, B. S. Ghanem, K. J. Msayib, D. Fritsch, L. Starannikova, N. Belov, O. Sanfirova, Y. Yampolskii and V. Shantarovich, *J. Memb. Sci.*, 2008, **325**, 851–860.
- 136 D. Ramimoghadam, E. M. A. Gray and C. J. Webb, *Int. J. Hydrogen Energy*, 2016, **41**, 16944–16965.
- 137 N. B. McKeown and P. M. Budd, *Chem. Soc. Rev.*, 2006, **35**, 675–683.
- 138 F. Y. Li, Y. Xiao, T.-S. Chung and S. Kawi, *Macromolecules*, 2012, **45**, 1427–1437.
- 139 M. Khdhayyer, A. F. Bushell, P. M. Budd, M. P. Attfield, D. Jiang, A. D. Burrows, E. Esposito, P. Bernardo, M. Monteleone, A. Fuoco, G. Clarizia, F. Bazzarelli, A. Gordano and J. C. Jansen, *Sep. Purif. Technol.*, 2019, **212**, 545–554.
- 140 R. Lin, B. Villacorta Hernandez, L. Ge and Z. Zhu, *J. Mater. Chem. A*, 2018, **6**, 293–312.
- 141 M. R. Khdhayyer, E. Esposito, A. Fuoco, M. Monteleone, L. Giorno, J. C. Jansen, M. P. Attfield and P. M. Budd, *Sep. Purif. Technol.*, 2017, **173**, 304–313.
- 142 T. Mitra, R. S. Bhavsar, D. J. Adams, P. M. Budd and A. I. Cooper, *Chem. Commun.*, 2016, **52**, 5581–5584.
- 143 C. R. Mason, M. G. Buonomenna, G. Golemme, P. M. Budd, F. Galiano, A. Figoli, K. Friess and V. Hynek, *Polymer (Guildf.)*, 2013, **54**, 2222–2230.
- 144 J. Ahn, W. J. Chung, I. Pinnau, J. Song, N. Du, G. P. Robertson and M. D. Guiver, *J. Memb. Sci.*, 2010, **346**, 280–287.
- 145 M. M. Khan, V. Filiz, G. Bengtson, S. Shishatskiy, M. M. Rahman, J. Lillepaerg and V. Abetz, *J. Memb. Sci.*, 2013, **436**, 109–120.
- 146 L. Hao, K. S. Liao and T. S. Chung, *J. Mater. Chem. A*, 2015, **3**, 17273–17281.
- 147 C. H. Lau, K. Konstas, A. W. Thornton, A. C. Y. Liu, S. Mudie, D. F. Kennedy, S. C.

## Chapter 1. Introduction

- Howard, A. J. Hill and M. R. Hill, *Angew. Chemie - Int. Ed.*, 2015, **54**, 2669–2673.
- 148 G. Cheng, T. Hasell, A. Trewin, D. J. Adams and A. I. Cooper, *Angew. Chemie Int. Ed.*, 2012, **51**, 12727–12731.
- 149 A. Deshmukh, S. Bandyopadhyay, A. James and A. Patra, *J. Mater. Chem. C*, 2016, **4**, 4427–4433.
- 150 P. Pallavi, S. Bandyopadhyay, J. Louis, A. Deshmukh and A. Patra, *Chem. Commun.*, 2017, **53**, 1257–1260.
- 151 J.-Y. Lee, C. D. Wood, D. Bradshaw, M. J. Rosseinsky and A. I. Cooper, *Chem. Commun.*, 2006, 2670.
- 152 Y. Yang, B. Tan and C. D. Wood, *J. Mater. Chem. A*, 2016, **4**, 15072–15080.
- 153 M. P. Tsyurupa, T. A. Mrachkovskaya, L. A. Maslova, G. I. Timofeeva, L. V. Dubrovina, E. F. Titova, V. A. Davankov and V. M. Menshov, *React. Polym.*, 1993, **19**, 55–66.
- 154 W. Mai, B. Sun, L. Chen, F. Xu, H. Liu, Y. Liang, R. Fu, D. Wu and K. Matyjaszewski, *J. Am. Chem. Soc.*, 2015, **137**, 13256–13259.
- 155 S. Y. Ding and W. Wang, *Chem. Soc. Rev.*, 2013, **42**, 548–568.
- 156 D. Cao, J. Lan, W. Wang and B. Smit, *Angew. Chemie - Int. Ed.*, 2009, **48**, 4730–4733.
- 157 R. Dawson, E. Stöckel, J. R. Holst, D. J. Adams and A. I. Cooper, *Energy Environ. Sci.*, 2011, **4**, 4239–4245.
- 158 F. R. and C. P. Claudia F. Martín, Ev Stöckel, Rob Clowes, Dave J. Adams, Andrew I. Cooper, Jose J. Pis, *J. Mater. Chem*, 2011, **21**, 5475–5483.
- 159 W. Wang, M. Zhou and D. Yuan, *J. Mater. Chem. A*, 2017, **5**, 1334–1347.
- 160 Z. Fu, J. Jia, J. Li and C. Liu, *Chem. Eng. J.*, 2017, **323**, 557–564.
- 161 Z. Fu, I. M. A. Mohamed, J. Li and C. Liu, *J. Taiwan Inst. Chem. Eng.*, 2019, **97**, 381–388.
- 162 Y. He, Q. Liu, F. Liu, C. Huang, C. Peng, Q. Yang, H. Wang, J. Hu and H. Liu, *Microporous Mesoporous Mater.*, 2016, **233**, 10–15.
- 163 Y. Fu, W. Yu, W. Zhang, Q. Huang, J. Yan, C. Pan and G. Yu, *Polym. Chem.*, 2018, **9**,

## Chapter 1. Introduction

4125–4131.

164 R. X. Yang, T. T. Wang and W. Q. Deng, *Sci. Rep.*, 2015, **5**, 1–9.



# Chapter 2 - Methods

## Chapter 2. Methods

### 2.1. Experimental techniques

#### 2.1.1. Infra-Red Spectroscopy

Infra-red spectra were collected using a Perkin-Elmer 100 spectrometer. All samples were prepared by grinding with a 20x excess of pure KBr dried overnight in a vacuum oven at 80 °C. The sample was pelletized at high pressure (10 tons) and analysed as a thin transparent disc.

#### 2.1.2. Gas Sorption

Nitrogen gas sorption isotherms were collected at 77 K using approximately 100 mg of sample on an ASAP 2020 micromeritics volumetric adsorption analyser. Prior to analysis all samples were degassed for at least 16 hours at 120 °C under a vacuum of at least  $10^{-5}$  bar. BET surface areas were calculated over a relative pressure range ( $P/P_0$ ) of between 0.01 – 0.15. Pore size distributions and pore volumes were calculated from the adsorption isotherms and modelled using the nonlocal density functional theory model (NL-DFT) for N<sub>2</sub> on carbon slit pores found within the micromeritics ASAP software.

#### 2.1.3. Solid State NMR

Solid-State NMR samples were packed into 4 mm zirconia rotors and transferred to a Bruker Avance III HD spectrometer. 1D <sup>1</sup>H-<sup>13</sup>C cross-polarisation magic angle spinning (CP/MAS) NMR experiments were measured at 125.76 MHz (500.13 MHz <sup>1</sup>H) at a MAS rate of 10.0 kHz. The <sup>1</sup>H  $\pi/2$  pulse was 3.4  $\mu$ s, and two-pulse phase modulation (TPPM) decoupling was used during the acquisition. The Hartmann-Hahn condition was set using hexamethylbenzene. The spectra were measured using a contact time of 2.0 ms. The relaxation delay D1 for each sample was individually determined from the proton T1 measurement ( $D1 = 5 \times T1$ ). Samples were collected until sufficient signal to noise was observed, typically greater than 256 scans. The values of the chemical shifts are referred to that of TMS.

#### 2.1.4. Solution NMR

<sup>1</sup>H-NMR spectra were recorded at 400 MHz using a Bruker Avance III HD spectrometer taking around 16 scans per spectrum. <sup>13</sup>C-NMR spectra were recorded on the same instrument taking 1024 scans on average per spectrum.

#### 2.1.5. Gel Permeation Chromatography (GPC)

Molecular weights ( $M_n$ ) and polydispersity indices (PDI) were measured by gel permeation chromatography (GPC). THF was used as the eluent with a flow rate of 1 mL min<sup>-1</sup> at 25 °C using polystyrene as the calibration standard. Universal calibration was applied employing Erma ERC-7512 refractive index detectors using Cirrus GPC-online software for analysis.

## Chapter 2. Methods

### 2.1.6. Dynamic Light Scattering (DLS)

Dynamic light scattering (DLS) of the polymer solutions were carried out using a Malvern Zetasizer nanoZS instrument via the Stokes-Einstein equation which assumes perfectly monodisperse, non-interacting spheres.

DLS is able to give insight into particle size by relating the speed at which a particle is travelling in solution, due to Brownian motion, referred to as the translational diffusion coefficient. This is measured by shining a laser through the sample and measuring the scattering angle which can be related back to particle size through the Stokes-Einstein equation, shown in the equation below:

$$D = \frac{k_B T}{6\pi\eta R_H}$$

Where  $D$  is the translational diffusion coefficient ( $\text{m}^2/\text{s}$ ),  $k_B$  is the Boltzmann constant ( $\text{m}^2/\text{kg}/\text{Ks}^2$ ),  $T$  is the temperature (K),  $\eta$  is the sample viscosity (Pa/s) and  $R_H$  is the hydrodynamic radius (m).

### 2.1.7. Small Angle X-ray Scattering (SAXS)

Small-angle X-ray scattering (SAXS). SAXS data were collected using a laboratory SAXS instrument (Xeuss 2.0, Xenocs, France) equipped with a liquid gallium MetalJet X-ray source (Excillum, Sweden, wavelength  $\lambda = 0.134$  nm), two sets of motorized scatterless slits for beam collimation and a Dectris Pilatus 1M pixel detector (sample-to-detector distance 6.335 m). SAXS patterns were collected over a  $q$  range of  $0.011 \text{ nm}^{-1} < q < 1.0 \text{ nm}^{-1}$ , where  $q = (4\pi\sin\theta)/\lambda$  is the length of the scattering vector and  $\theta$  is one-half of the scattering angle. Glass capillaries of 2 mm diameter were used as a sample holder and 6 data sets were collected over 10 min for each sample (empty capillary, methanol and 5% w/w polymer sample in methanol). Data were reduced (normalization and integration) using the Foxtrot software package supplied with the instrument and further analysed (background subtraction and data modelling) using Irena SAS macros for Igor Pro.<sup>1</sup>

### 2.1.8. UV-Vis Spectroscopy

UV-Vis absorption spectra were recorded in either quartz or polystyrene cuvettes on a Cary 5000 spectrophotometer using spectroscopic grade solvent.

### 2.1.9. Steady-State Fluorescence Spectroscopy

All steady-state fluorescence spectra were recorded on a Horiba Jobin Yvon Fluoromax-4 spectrofluorometer in a quartz cuvette using spectroscopic grade solvent.

## Chapter 2. Methods

### 2.1.10. Scanning Electron Microscopy (SEM)

Scanning electron microscopy (SEM) images were collected on a Fei Inspect F50 Field Emission Gun SEM, run in secondary electron mode. Specimens were prepared by mounting onto carbon tape, supported on aluminium stubs. All SEM images were collected by either Mr. Thomas Robshaw or Dr. Matt Derry.

### 2.1.11. Transmission Electron Microscopy (TEM)

Transmission electron microscopy (TEM) studies were conducted using a Philips CM 100 instrument operating at 100 kV and equipped with a Gatan 1 k CCD camera. A diluted solution of the polymer material (0.10% w/w) was placed on carbon-coated copper grids, allowed to dry and then exposed to ruthenium(VIII) oxide vapour for 7 min at 20 °C prior to analysis. The ruthenium(VIII) oxide was prepared as follows: Ruthenium(IV) oxide (0.30 g) was added to water (50 g) to form a black slurry; addition of sodium periodate (2.0 g) with stirring produced a yellow solution of ruthenium(VIII) oxide within 1 min.<sup>2</sup> All TEM images were collected by Dr. Matthew Derry.

### 2.1.12 Elemental analysis

Elemental analysis was performed through burning an amount of sample in a stream of pure oxygen. The sample was placed in a tin capsule and introduced into the combustion tube of the Elementar Vario MICRO Cube CHN/S analyser via a stream of helium. Combustion products were analysed through first passing the sample through a copper tube to remove excess oxygen and reduce any NO<sub>x</sub> to N<sub>2</sub>. Gases were separated using a Thermal Programmed Desorption column and detected using a Thermal Conductivity Detector.

## 2.2. Gas sorption theory

Given that porous polymers are both insoluble and amorphous, characterisation of these materials is very difficult. One of the most common characterisation methods applied to not only these materials, but all porous materials is gas sorption. Sorption of gas by a porous materials yields much insight into the pore size, volume and surface area of the material under investigation. It is for these reasons why gas sorption is such a key characterisation technique for both crystalline and amorphous porous materials.

Gases (sorbate) are able to interact with the surface of a solid (sorbent) in a number of different ways. These interactions can be strong and involve chemical bond formation (chemisorption) or they can be weak and merely involve Van der Waals interactions (physisorption). In most instances when we are modelling pore sizes and volumes we are mostly interested in the

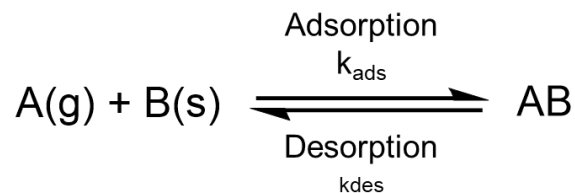
## Chapter 2. Methods

physisorption of an ideal gas onto a porous material at low temperatures. The majority of the time this is nitrogen gas at 77 K.

There are many different models that can be applied to the adsorption of a sorbate onto a sorbent and the first of them to be developed was the Langmuir model.

### 2.2.1 Langmuir Model

In 1916 Irving Langmuir set out his adsorption isotherm which related the adsorption of a gas molecule onto a solid surface as a function of pressure.<sup>3</sup> He proposed that a dynamic equilibrium exists between adsorbed gas molecules and free gas molecules. This can be expressed as:



where A(g) is a free gas molecule, B is an unoccupied surface and AB is an adsorbed gas molecule occupying a surface site.  $k_{ads}$  and  $k_{des}$  represent the respective rates of the adsorption and desorption processes.

We can use kinetic theory to determine the rate of the two processes and at equilibrium, where the two rates are equal the overall rate constant is equivalent to:

$$K = \frac{k_{ads}}{k_{des}} = \frac{[AB]}{[A][B]}$$

At equilibrium what this means is that the rate of desorption from occupied sites is equal to that of adsorption to the occupied sites at a specific pressure. This can be expressed as:

$$k_{des}\theta = k_{ads}P(1 - \theta)$$

where  $\theta$  is the fractional surface coverage

This equation can be rearranged to give  $\theta$  and doing this results in:

$$\theta = \frac{k_{ads}P}{k_{des} + k_{ads}P}$$

Remembering that  $K = k_{ads}/k_{des}$  we get the following:

## Chapter 2. Methods

$$\theta = \frac{KP}{1 + KP}$$

This is well known as the Langmuir adsorption equation. Although acceptable when expressed in this form, given that we are discussing gas sorption theory it seems appropriate to express this in terms of volume of gas adsorbed by a sorbent. This gives the following:

$$\theta = \frac{V_{ads}}{V_{mono}}$$

where  $V_{ads}$  is the volume of gas adsorbed and  $V_{mono}$  is the amount of gas adsorbed corresponding to monolayer coverage.

This equation can then be re-written and arranged to form a linear equation which yields the following:

$$\frac{P}{V} = \frac{P}{V_{mono}} + \frac{1}{KV_{mono}}$$

If we were to then plot a graph of  $P/V$  vs  $V$  we will obtain a straight line where the slope would be equal to  $1/V_{mono}$  and the intercept  $1/KV_{mono}$ .

Although the Langmuir model is a useful model for gas sorption it is limited in that a number of assumptions are made when applying this model. Namely, these are:

1. Dynamic equilibrium exists between adsorbed and free gas molecules
2. The surface of the sorbent is uniform and the enthalpy of adsorption does not vary with coverage
3. Adsorption is limited to only monolayer coverage – after this no further adsorption is witnessed
4. There are no significant interactions between adsorbed molecules

These assumptions limit the validity of the Langmuir model when trying to determine the surface area and pore size of a solid. For example, we know that the surface of most materials is not homogeneous but often heterogeneous (invalidates assumption 2). It is also known that surface coverage is not limited to only a single monolayer (invalidates assumption 3) - this is only really the case at low pressures. Likewise, we know that forces of attraction exist between molecules of the same type (invalidates assumption 4). It is for these reasons that the

## Chapter 2. Methods

Langmuir model for gas adsorption can only truly be valid when working under low pressure conditions, anything more than this, it is necessary to apply a different gas sorption model.

### 2.2.2 BET Theory

Brunauer-Emmett-Teller (BET) theory, named after the scientists who developed it, was formulated on the basis that adsorption is not limited to only monolayer formation and can instead be greater than one layer in thickness.<sup>4</sup> Under the conditions of higher pressures and low temperatures thermal energy decreases and there are more gas molecules present meaning multilayer formation occurs. Much like the Langmuir adsorption model there are assumptions to BET theory, which are:

1. gas molecules adsorb onto a solid infinitely – one monolayer layer need not be complete before another begins
2. only considered interaction is that an adsorbed molecule acts as a single adsorption site for a molecule on the upper layer
3. the molar heat of adsorption for the first layer is higher than that for the succeeding layers – the first layer is equal to the enthalpy of adsorption whereas the other layers are equal to the enthalpy of liquification
4. Langmuir adsorption theory can be applied to each adsorbed layer

The overall equation for BET theory, which takes all of these assumptions into account, is presented as:

$$\theta = \frac{c(P/P_0)}{(1 - P/P_0) (1 + (c - 1)P/P_0)}$$

where P is the equilibrium gas pressure,  $P_0$  is the saturated vapour pressure,  $P/P_0$  is the relative pressure and c is a constant relating to the energy of adsorption:

$$c = e^{(\Delta H_{ads} - \Delta H_{liq})/RT}$$

Once more taking into account volume of gas adsorbed the equation can be expressed in linear form as:

$$\frac{P/P_0}{V(1 - (P/P_0))} = \frac{1}{cV_m} + \frac{c - 1}{cV_m} (P/P_0)$$

where V is the volume of adsorbed gas at pressure P and  $V_m$  is the volume of gas required to form a monolayer

## Chapter 2. Methods

A plot of the left hand side of the equation against  $P/P_0$  gives a linear plot over a relative pressure range of between 0.05 – 0.35 when the BET equation is valid with:

$$\text{slope} = \frac{c-1}{cV_m} \qquad \text{Intercept} = \frac{1}{cV_m}$$

The BET model has been the model most applied to gas adsorption in porous materials as it accounts for multilayer adsorption onto heterogeneous surfaces. For the most part an inert gas, usually nitrogen at its boiling point (77 K) has been the adsorbate of choice. When using  $N_2$  for gas sorption experiments onto a solid sorbent one can calculate the surface area of that material by using the assumed molecular area of a  $N_2$  molecule which is  $1.62 \times 10^{-19} \text{ m}^2$ . The equation shown below can then be used to determine the BET surface area per gram of sample:

$$SA_{BET} = \frac{PV_m}{RT} N_a A$$

where R is the ideal gas constant ( $8.31 \text{ J mol}^{-1} \text{ K}^{-1}$ ), T is the temperature,  $N_a$  is Avogadro's number and A is the area a  $N_2$  molecule occupies ( $1.62 \times 10^{-19} \text{ m}^2$ ).

## Chapter 2. Methods

### 2.2.3 Isotherm Shapes

In 1985 IUPAC divided the shapes of nitrogen gas sorption isotherms into six distinct types<sup>5</sup>. These are shown in Figure 2.1.

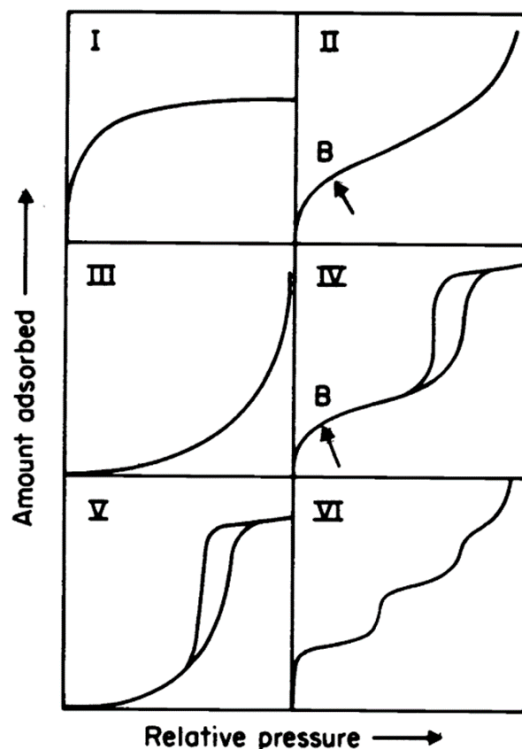


Figure 2.1 IUPAC isotherm classifications from 1985<sup>5</sup>

These 6 types are distinct to a certain type of pore structure and are described as such. Type I isotherms are given by purely microporous materials with little to no external surfaces and show very large uptake at low pressures. The limiting uptake here is governed by the accessible micropore volume not the internal surface area. Type II isotherms are given by non-porous or macroporous sorbents and represents unrestricted monolayer-multilayer adsorption. Point B represents the point at which monolayer coverage is complete. Type III isotherms are convex in shape with respect to the  $P/P_0$  axis and are quite rare. They represent materials in which the adsorbate-adsorbate cohesive forces are stronger than the adsorbate-adsorbent adhesive forces. Type IV isotherms are given by mesoporous materials and are characterised by a hysteresis loop which is associated with capillary condensation taking place in such mesopores. Initially the isotherm is similar to that of a type I and type II as monolayer-multilayer adsorption occurs. Type V isotherms are also quite uncommon and can be thought of as the inverse of a type III - though the cohesive forces between the adsorbate-adsorbent are weak the sorbate is still adsorbed in some pores. Finally a type VI isotherm represents

## Chapter 2. Methods

stepwise multilayer adsorption on a uniform non-porous surface. The step height represents the monolayer capacity for each adsorbed layer.

For many years these six isotherm types were, and still are, the expected shapes one looks for when carrying out gas sorption experiments. However over the past 40+ years, as this field has continuously evolved more groups have been producing more isotherms on many different and diverse materials. This lead to a revised version of the isotherm types and in 2015 IUPAC published an update on the original classifications.<sup>6</sup> The proposed IUPAC classifications of isotherm types are represented in Figure 2.2.

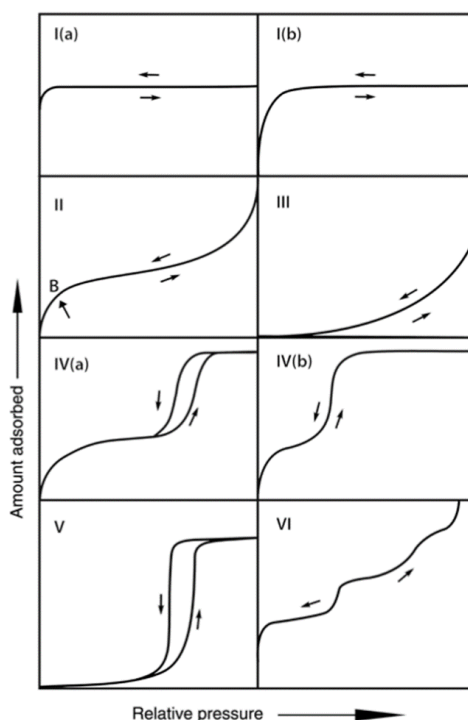


**Figure 2.2** Revised IUPAC isotherm classifications as of 2015<sup>6</sup>

The isotherm types have more or less remained the same as the previous 1985 classification with the two main differences affecting the type I and IV isotherms. The type I isotherm has now been split into two distinct categories a type I(a) which is given by microporous materials having mainly narrow pore sizes (widths < 1 nm) and a type I(b) which are given by microporous materials possessing broader pore size distributions and possibly even some mesopores (between 1 – 2.5 nm). The distinct difference in shape is seen over the low relative pressure region where, for a type I(a) there is much more uptake over a much lower relative pressure region whereas for a type I(b) the uptake is spread out over a slightly larger relative pressure region. Like the type I isotherm, the type IV has also been split into two distinct types named type IV(a) and type IV(b). The differences in these two isotherm types is due to the

## Chapter 2. Methods

size of the mesopores responsible for the capillary condensation which yields the classic hysteresis loop associated with this type. A type IV(a) isotherm has a noticeably large hysteresis loop and is a result of the presence of mesopores greater than 4 nm being present in the sample. Adsorbents which have pore widths smaller than this display a type IV(b) isotherm where the hysteresis is either less prominent or not present at all due to the capillary condensation being much less profound.

### 2.2.3 Adsorption Hysteresis

The presence of hysteresis loops in the multilayer physisorption range of the isotherm are generally associated with capillary condensation.<sup>7</sup> This form of hysteresis mainly occurs in the mesopores of the material and is due to either network effects or adsorption metastability. For example, in an open-ended pore delayed condensation is the result of metastability of the adsorbed layer. This means that the adsorption branch of the isotherm is not in thermodynamic equilibrium. Instead, the equilibrium is established on the desorb should the pores be filled with liquid-like condensate which is why hysteresis is observed.

It has been shown that there is a direct correlation between the observed hysteresis shape and the textural properties of an adsorbent. This has been classified by IUPAC in 1985 and updated in 2015. Figure 2.3 shows the six different hysteresis loops witnessed in gas sorption studies:

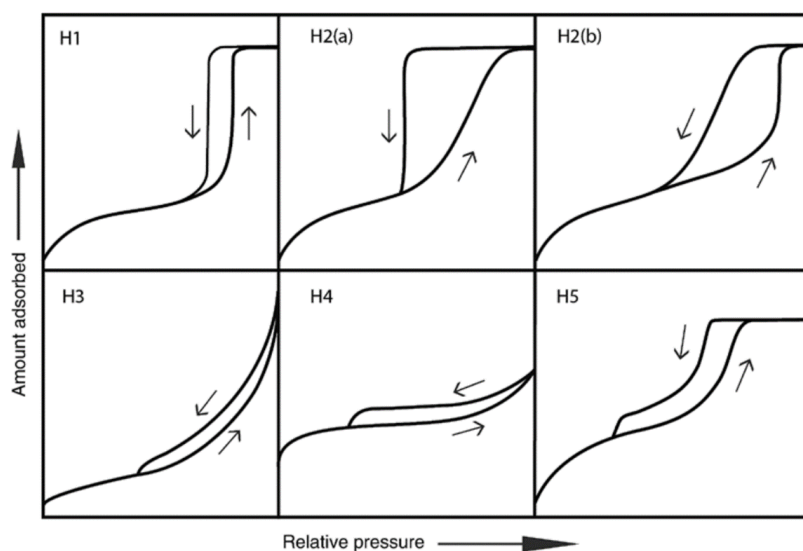


**Figure 2.3** Observed hysteresis loops as classified by IUPAC

The type H1 loop is typical of materials which exhibit a narrow range of uniform pores but has also been reported in networks which possess ink-bottle pores where the widths of the neck is smaller than the cavity. This loop is indicative of delayed condensation on the adsorption

## Chapter 2. Methods

branch. H2 type loops are the result of complex pore structures where network effects dominate and are split into two types. A H2(a) loop has a characteristic steep desorption branch and is the result of pore blocking or cavitation-induced evaporation. The type H2(b) loop is much less steep on the desorption branch and is attributed to pore blocking but this time the neck widths of the pores are much larger. H3 loops have two distinctive features which are; (i) the adsorption branch resembles a type II isotherm and (ii) the lower limit of the desorption branch is located at the cavitation-induced  $P/P_0$  range. A H4 loop is somewhat similar to a H3 but the adsorption branch is much more like a type I isotherm which is due to the filling of more micropores. Finally, a H5 loop has a unique form which is the result of the presence of both open pores and partially blocked mesopores.

## Chapter 2. Methods

### 2.3 References

- 1 J. Ilavsky and P. R. Jemian, *J. Appl. Crystallogr.*, 2009, **42**, 347–353.
- 2 J. S. Trent, *Macromolecules*, 1984, **17**, 2930–2931.
- 3 I. Langmuir, *J. Am. Chem. Soc.*, 1917, **39**, 1848–1906.
- 4 S. Brunauer, L. S. Deming, W. E. Deming and E. Teller, *J. Am. Chem. Soc.*, 1938, **60**, 309–319.
- 5 R. A. W. Sing, K.S.W., Everet, D. H., Haul, *Pure Appl. Chem.*, 1985, **57**, 603–619.
- 6 M. Thommes, K. Kaneko, A. V Neimark, J. P. Olivier, F. Rodriguez-Reinoso, J. Rouquerol and K. S. W. Sing, *Pure Appl. Chem.*, 2015, **87**, 1051–1069.
- 7 K. A. Cychoz and M. Thommes, *Engineering*, 2018, **4**, 559–566.

## *Part A – Towards Applications in Solution*

This part of the thesis describes the work carried out on designing porous polymers towards applications in the solution phase..

# Chapter 3 - Synthesis of PEG-*b*-DVB-*co*-FN Porous Polymeric Dispersions

Dr. Matthew Derry is thanked for carrying out the SAXS work and collecting the SEM and TEM images.

Large portions of this chapter have previously been published in:

A. M. James, M. J. Derry, J. S. Train and R. Dawson, *Polym. Chem.*, 2019, **10**, 3879–3886.

## Chapter3. PPDs from FN and DVB

### 3.1 Introduction

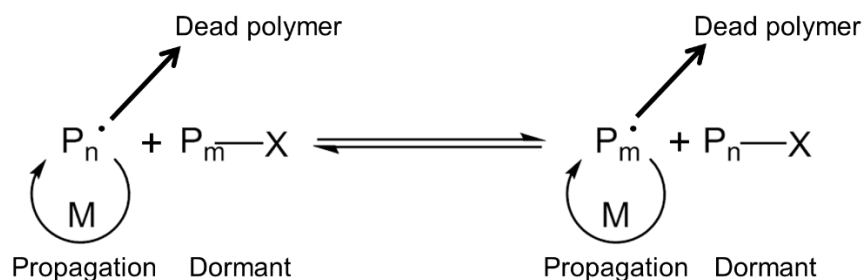
The design and synthesis of solution processable porous materials beyond PIMs has been limited to very few discreet examples often involving numerous synthetic steps, expensive reagents and catalysts and cannot be applied towards other reagents. Therefore, it seems appropriate to design a generic synthetic route, tolerable of many different functionalities which allows for the synthesis of materials offering the advantages of porosity combined with the processability obtained from being solution dispersible.

In 2016 Li and co-workers reported the synthesis of microporous polymers by the radical copolymerisation of divinylbenzene and bismaleimides.<sup>1</sup> This work was followed a year later in 2017 when the same group reported the synthesis of another microporous polymeric network synthesised *via* the same strategy but instead using fumaronitrile as the comonomer.<sup>2</sup> The concept of using radical polymerisation to yield microporous networks offers numerous advantages over the more conventional methods used to yield HCPs, CMPs, COFs etc. Namely, the fact that no metal catalysts are required, the reaction produces no by-products and offers high atom economy, employs less harsh conditions, uses non-toxic/non-corrosive solvents and offers much scope for modification – the sole requisite being a vinyl monomer which can be copolymerised alongside divinylbenzene. However, the same drawback that hinders the processability of all other microporous networks is still very much present in these materials; the complete lack of solubility in common organic solvents.

There have been a recent number of reports detailing the synthesis of porous polymer particles using diblock copolymers based on PEO-*b*-PS synthesised *via* controlled radical polymerisation methods such as ATRP. In these reports the diblock first self-assembles through the judicious choice of solvent. Hypercrosslinking of the resulting material yields hierarchically structured porous polymers whereby the hypercrosslinked PS forms the shell and the PEO self-assembles to form a core.<sup>3,4</sup> The use of diblock copolymers towards hierarchically structured porous materials hold much promise due to the ease of synthesis of the diblocks, the huge scope for variation and the different conceivable structures one could form in solution (e.g. micelles, vesicles, lamellae, worms). However currently all work in this area has seen the hydrophilic chain form the core of the structure with the hypercrosslinking block forming the shell. Thus far, there have been no reports of reversing this structure so as to have a porous core present with long hydrophilic chains on the outside of the material. In theory, this would yield a porous polymeric system which could be solution processable due to the porous insoluble core being suspended in solution by these long free hydrophilic chains.

### Chapter3. PPDs from FN and DVB

Reversible addition-fragmentation chain transfer (RAFT) polymerisation is form of reversible deactivation radical polymerisation (RDRP) which allows for the design of functional polymers with targeted molecular masses, narrow polydispersity and defined molecular architecture. The overlying process of RDRP techniques lies with the partitioning of the propagating radicals between active and dormant states. In other controlled polymerisation techniques such as nitroxide mediated polymerisation (NMP)<sup>5,6</sup> and atom transfer radical polymerisation (ATRP)<sup>7,8</sup>, this is achieved through either nitroxide capping (NMP) or a redox process by which the equilibrium lies heavily with the dormant species (ATRP). The mechanism by which RAFT polymerisation provides control over polymerisation differs fundamentally from these aforementioned techniques. The mechanism of RAFT polymerisation proceeds *via* a degenerative chain transfer process, as outlined in Scheme 3.1, by which the propagating species is in equilibrium with the dormant species.<sup>9-11</sup> The main advantage RAFT polymerisation has over other RDRP processes is that it is compatible with a wide range of functional monomers and reaction conditions which allows for the synthesis of polymers with well-defined molecular architectures. Indeed, the only difference between conventional radical polymerisation and RAFT polymerisation is the inclusion of a suitable RAFT agent meaning rates of reaction and conditions do not require further modification.

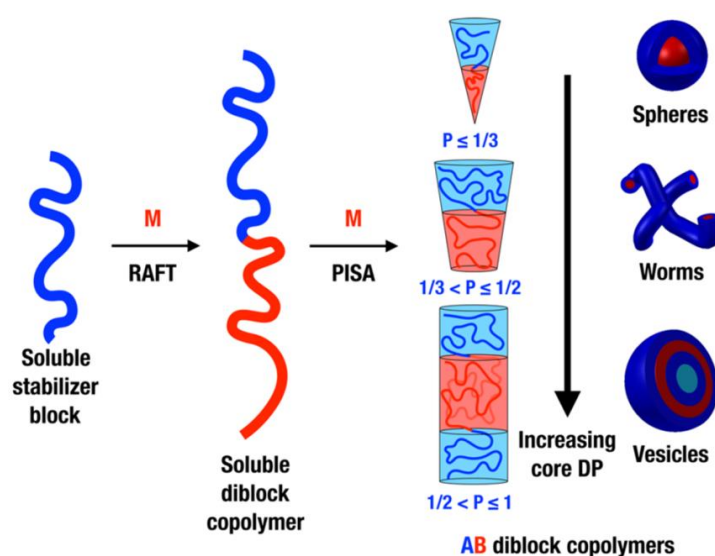


**Scheme 3.1** Reversible-deactivation radical polymerisation by degenerative chain transfer where  $P_n$  and  $P_m$  are the propagating chains,  $M$  is the monomer being polymerised and  $P_m-X$  and  $P_n-X$  are the dormant species<sup>10</sup>

The formation of nano-objects in solution is often achieved by the synthesis of amphiphilic block copolymers followed by microphase separation usually driven by the addition of a non-solvent for one block.<sup>12-14</sup> Though effective, this method involves numerous post-synthetic purification steps and yields very dilute dispersions (often <1 wt. % solids) which are necessary for full control over the self-assembly process. Over the past several years and as a result of the development of different RDRP techniques, considerable attention has driven the development of an alternative route towards block copolymer nano-objects, namely polymerisation-induced self-assembly (PISA). Using a PISA methodology nano-objects are

### Chapter3. PPDs from FN and DVB

formed by chain-extending a soluble homopolymer in a solvent which is a good solvent for the monomer and first block but a poor solvent for the growing second block. Then, as polymerisation proceeds the growing block becomes gradually insoluble which drives *in situ* self-assembly to form block copolymer nano-objects (scheme 3.2).<sup>15,16</sup> This method holds numerous advantages over conventional self-assembly strategies such as the reaction being a one-pot synthesis, the ability to be carried out at high concentrations (up to 50% w/w solids) and allows access to many different morphologies such as micelles<sup>17,18</sup>, vesicles<sup>19</sup>, worms<sup>20</sup> and more<sup>21-23</sup>.



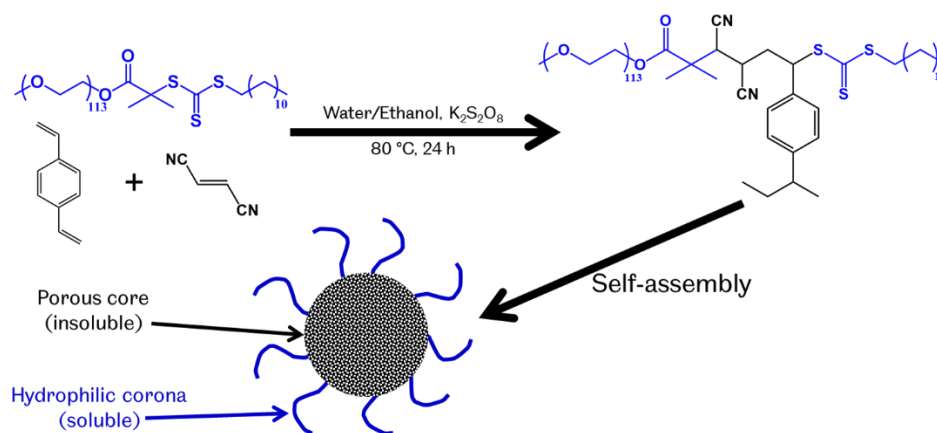
**Scheme 3.2** Synthesis of block copolymer nano-objects through a PISA approach

Though in theory it is possible to apply all controlled polymerisation mechanisms to a PISA process the field has been dominated by the RAFT mechanism. This is predominantly due to the fact that RAFT is compatible with a wide range of monomers and can be carried out in many different solvents ranging from water, alcohols, oils and even ionic liquids. During a RAFT-PISA process a macromolecular chain transfer agent (macro-CTA) is applied as both the modulator of the reaction as well as the soluble stabiliser block. This in turn allows for control of the polymerisation process as well as ensuring self-assembly occurs.

### Chapter3. PPDs from FN and DVB

## 3.2 Chapter Aims

Through the union of RAFT-PISA and polymerising divinylbenzene alongside a suitable co-monomer it should be possible to design porous nanoassemblies which disperse in solution as a result of the free hydrophilic chains yet are porous due to the polymerisation of the two monomers (Scheme 3.3). This chapter reports the design, synthesis and characterisation of such a system through the application of a PEG-based macro-CTA which is used to mediate the polymerisation of divinylbenzene and fumaronitrile in an aqueous alcohol solvent system.



Scheme 3.3 Design principle towards solution stable porous nanoassemblies

A series of microporous polymers are synthesised and characterised which possess a core-shell structure by which the core is comprised of divinylbenzene and fumaronitrile and the shell is comprised of long hydrophilic PEG chains. The bifunctional nature of divinylbenzene ensures the core is porous. However due to the extensive crosslinking in this system the core is also insoluble hence solution stability of the final material is a result of the PEG chains. The extent of solution stability is explored in this chapter by making samples with increasing amounts of monomer which will result in a larger core. This should give rise to materials with larger surface areas yet may also result in a loss of solution stability.

## Chapter3. PPDs from FN and DVB

### 3.3 Optimising Reaction Conditions

#### 3.3.1 Divinylbenzene:Fumaronitrile Ratio

The polymerisation of divinylbenzene and fumaronitrile as reported by Li *et al.*<sup>2</sup> showed a variance in surface area dependant on the starting ratio of divinylbenzene and fumaronitrile. Initially, a fumaronitrile mole ratio of 0.25 is applied which yields a material with a surface area of 589 m<sup>2</sup>/g. The surface area of each material gradually increases as the mole ratio of fumaronitrile increases until a mole ratio of 0.75:1 where a maximum of surface area of 805 m<sup>2</sup>/g is achieved. After this point further increase of the fumaronitrile mole ratio lowers the BET surface area of the material until a final value of 443 m<sup>2</sup>/g is observed for a mole ratio of 2.5:1 (FN:DVB). This work showed that the optimum ratio of FN:DVB which yields the highest specific surface area is 0.75:1 therefore all materials reported in this chapter use this ratio.

HCPN-0.75 was synthesised in toluene which is a good solvent for both monomers, given that both monomers are soluble in this solvent. To be able to induce microphase separation during polymerisation it is vital for the growing chain to chain extend in a solvent in which it is insoluble. Furthermore, both monomers need to be soluble in the solvent system initially to ensure RAFT-dispersion polymerisation occurs. Common solvent systems reported in the literature to induce microphase separation of a hydrophobic polymer chain are typically water, alcohols and mixtures of these two.<sup>15,17</sup> This seems like a suitable choice for this work as given that a hydrophilic polymer (PEG-CTA) is to be chain extended using hydrophobic monomers (DVB and FN) and as such should drive the *in situ* self-assembly process.

#### 3.3.2 Varying Solvent Composition

It has been shown that the RAFT-mediated polymerisation of some monomers when using a pure alcohol system yields nanoassemblies but usually with low conversion (only 60 % after 7 hours). As a result, long reaction times (~24 h) are required to give rise to high monomer conversion (> 90 %). However, work carried out by Jones *et al.* shows that the addition of water to these systems results in a rapid rate increase and yields much higher conversion after less than 8 hours under identical conditions.<sup>27</sup> However, this work also reported that the addition of water also adversely affected sample morphology with formation of higher order morphologies such as worms and vesicles being hindered. Indeed, when more water was added the polymerisation yielded only kinetically trapped spheres.

The polymerisation was carried out in varying solvent mixtures of water and ethanol ranging from 0% up to 100% ethanol in order to try to yield samples that have both high surface areas and remarkable solution stability when dispersed in solution. It was thought that the different

### Chapter3. PPDs from FN and DVB

solvent systems would have a serious effect on the characteristics of the final material owed to a number of reasons such as; the reaction kinetics, miscibility/solubility of the monomer in the chosen solvent system, solubility of initiator and morphology of the final material. Divinylbenzene for example is miscible with ethanol but not with water hence any solvent system that has greater amounts of water than ethanol will result in emulsion droplets of divinylbenzene, stabilised by the PEG macro-CTA, as opposed to the monomer being free in solution. This in turn would have an effect on the rate of polymerisation as this is technically RAFT emulsion polymerisation and not RAFT suspension polymerisation. Likewise, the solubility of the comonomer, fumaronitrile, would also effect the polymerisation process. In ethanol, fumaronitrile has a solubility of ~50 mg/mL yet in water it is <1 mg/mL meaning there will most likely be a much lower degree of polymerisation for this monomer in purely aqueous systems.

As expected, both the yield and surface area of the materials synthesised by varying the water:ethanol ratio varied hugely and with little predictability (Table 3.1). In a purely aqueous solvent system a surface area of 116 m<sup>2</sup>/g was achieved yet the 100% ethanol system was much lower at 11 m<sup>2</sup>/g. The highest surface area was observed for a solvent system comprising of a 60:40 water:ethanol mix that was found to be 274 m<sup>2</sup>/g, though the 50:50 system was very similar at 261 m<sup>2</sup>/g. It is also worth noting that the yields for these two systems were also the highest of all syntheses explored. This suggests that a solvent system of 50:50 or 60:40 water ethanol allows for dissolution of both monomers and macro-CTA as well as giving rise to faster reaction kinetics thereby ensuring high monomer conversion is achieved.

Table 3.1 Obtained % yield and surface areas for each sample synthesised in this section

H <sub>2</sub> O:EtOH Ratio	% Yield	SA <sub>BET</sub> / (m <sup>2</sup> /g)
100:0	56	116
90:10	54	113
80:20	45	133
70:30	50	75
60:40	68	274
50:50	60	261
40:60	56	73
30:70	11	96
20:80	47	251
10:90	25	94
0:100	27	11



### Chapter3. PPDs from FN and DVB

system, giving a higher yield and surface area this solvent system was chosen to take forward and apply towards the synthesis of porous nano-objects.

#### 3.3.3 Varying Reaction Concentration

An important advantage RAFT-PISA has over conventional self-assembly of diblock copolymers is that the reaction can be conducted at relatively high concentrations (often > 25 % w/w). Therefore, it was expected that the synthesis of the porous polymer materials reported here could also be carried out in such a way and have no adverse effect on the outcome of the final material. With this in mind the first synthesis attempt was carried out at 10 % w/w in a solvent mixture comprised of 60:40 water:ethanol. Unfortunately, this reaction resulted in precipitation of the product *in situ* and the final material was completely insoluble. This is most likely due to the polymerisation of divinylbenzene at such high concentrations crosslinking before microphase separation occurs. Therefore, instead of forming crosslinked nanoassemblies, a continuous crosslinked network forms instead, similar to that of the work published by Li and co-workers.

To try and deter the formation of an extended crosslinked network the reaction was carried out at a lower concentration of 1 % w/w. This reaction saw no precipitation of the material in solution and yielded a white solid which, when dispersed in a suitable solvent such as methanol, was found to remain stable in solution. Although the reaction was successful it is problematic to have to carry out the reaction at such low concentrations as this requires large volumes of solvent. Unfortunately when the reaction was attempted at 5 % w/w the system again precipitated out during the reaction and yielded an insoluble material. In order to ensure that the final material was dispersible and porous all further reactions were carried out at 1 % w/w which avoided precipitation of the material during the reaction.

### 3.4 Modifying Core DP

The polymerisation of divinylbenzene and fumaronitrile, in a 1:0.75 mole ratio, *via* a RAFT-mediated PISA route using a macro-CTA in a 60:40 water:ethanol solvent system at 1 % w/w yielded a porous material capable of forming stable solutions after sonication. Thus far, the highest achieved surface area attained for this synthesis was 274 m<sup>2</sup>/g. Although this is respectable, it is still somewhat much lower than the free radical polymerisation of DVB and FN (HCPN-0.75, 805 m<sup>2</sup>/g). Speculatively, the main reason why the surface area is much lower than that of the “parent material” is because the dispersible porous materials all have the macro-CTA present in the final product. Although this is a pivotal part of the sample, it is these chains which induce solution stability, it is nonetheless deadweight and results in the lowering of the surface area of the material.

### Chapter3. PPDs from FN and DVB

Given that it is the polymerisation of divinylbenzene which imparts porosity into the final product it should be possible to increase the surface area of the final material by increasing the ratio of monomer:macro-CTA. This would increase the proportion of the material which imparts porosity into the final sample. Though this could also hinder the dispersibility of the material given that increasing the monomer content would yield a larger insoluble core which may not be able to be dispersed in solution by the PEG chains. The original sample synthesised had a degree of polymerisation (DP) of PEG<sub>113</sub>-*b*-DVB<sub>300</sub>-CO-FN<sub>225</sub> and was found to have a surface area of 274 m<sup>2</sup>/g. By increasing the DP of the core forming block it should be possible to enhance this further. Likewise, a reduction in the core DP should also result in a lowering of the surface area. In order to test this a series of new samples were synthesised which saw the core DP of both monomers modified (Table 3.2).

Table 3.2 Table showing the DPs of each sample synthesised

Sample	Corona DP	Core DP	% Yield	SA <sub>BET</sub> (m <sup>2</sup> /g)
PEG <sub>113</sub> - <i>b</i> -DVB <sub>150</sub> -CO-FN <sub>113</sub>	113	226	65	240
PEG <sub>113</sub> - <i>b</i> -DVB <sub>300</sub> -CO-FN <sub>225</sub>	113	525	68	270
PEG <sub>113</sub> - <i>b</i> -DVB <sub>600</sub> -CO-FN <sub>450</sub>	113	1050	22	409
PEG <sub>113</sub> - <i>b</i> -DVB <sub>1200</sub> -CO-FN <sub>900</sub>	113	2100	53	400
PEG <sub>113</sub> - <i>b</i> -DVB <sub>2400</sub> -CO-FN <sub>1800</sub>	113	4200	55	405
PEG <sub>113</sub> - <i>b</i> -DVB <sub>4800</sub> -CO-FN <sub>3600</sub>	113	8400	62	243
PEG <sub>113</sub> - <i>b</i> -DVB <sub>9600</sub> -CO-FN <sub>7200</sub>	113	16800	31	217

As expected, variance of the core DP resulted in prominent changes to the specific SA<sub>BET</sub> of the synthesised material. When the DP of the core forming block was halved the surface area reduced from 270 m<sup>2</sup>/g to 244 m<sup>2</sup>/g yet when the DP was doubled and then increased fourfold the SA<sub>BET</sub> increased by almost doubled to around 400 m<sup>2</sup>/g (Table 3.2). After reaching a core DP of > 1000 the surface area shows no prominent increase indicating that this may be the highest attainable surface area for this system. Indeed, when even larger samples were targeted the surface area actually began to decrease. This may be a result of poor monomer conversion resulting in incomplete polymerisation which would result in lower surface area samples due to a lower degree of crosslinking in the final product. It may be that targeting larger cores requires longer reaction times than the 24 hours used for these syntheses.

It is also possible that increasing the core forming block could result in a loss of solution stability should the core become too large for the PEG chains to stabilise the core. In order to test this theory each sample was mixed with methanol to make a 1 mg/mL solution and sonicated for 30 minutes to form a homogeneous suspension. After this time, the samples were left undisturbed and observed periodically to see if any sedimentation of the sample

### Chapter3. PPDs from FN and DVB

occurred. Should the sample settle out this would show that the sample is not stable in solution - most likely the result of the core being too big to be dispersed by the PEG chains. This was found to be the case for the samples with core DPs exceeding 4000 (Figure 3.2). The three larger samples with core DPs exceeding 4000 were all found to be incapable of remaining in solution after 24 hours. The first four samples however all showed remarkable solution stability. Given that the aim of this project was to synthesise and apply solution-processable materials the larger samples which showed poor solution stability were deemed unfit for further study. The first four samples in the series however demonstrated good solution stability and all had notable surface areas and as such were taken forward and studied in more detail.

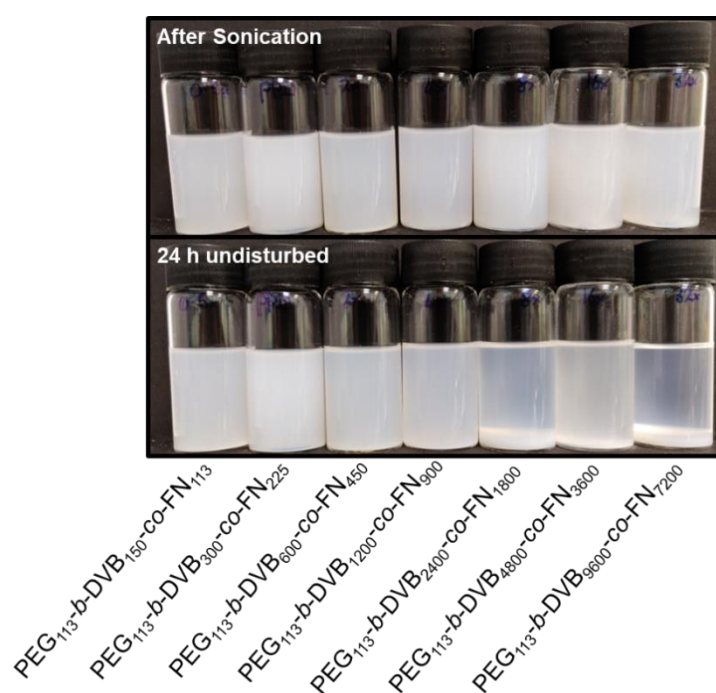


Figure 3.2 Dispersibility of samples after sonication in methanol and after being left for 24 h

### 3.5 Solid State Characterisation

The first four samples in the series as shown in Table 3.2 were characterised in the solid state by the means of Fourier transform infrared spectroscopy, solid state <sup>13</sup>C NMR, elemental analysis and N<sub>2</sub> gas sorption analysis. These techniques allow insight into the chemical composition of the samples and allow for further probing of the porosity of these samples.

## Chapter3. PPDs from FN and DVB

### 3.5.1 Infrared Spectroscopy

The PPD samples are comprised of two different monomers and a PEG based macro-CTA all of which have their own associated FTIR spectrum (Figure 3.3). The PEG macro-CTA has a signal at  $\sim 1100\text{ cm}^{-1}$  associated with the C-O ether stretching frequency of the PEG chains. A signal in the spectrum of fumaronitrile is found at  $\sim 2250\text{ cm}^{-1}$ , present due to the  $\text{C}\equiv\text{N}$  chemical moiety. Finally there is a signal in the IR spectrum of divinylbenzene which relates to the aromatic C=C bending mode.

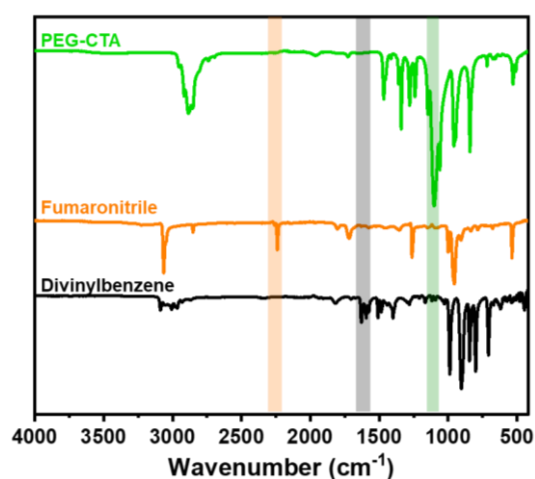
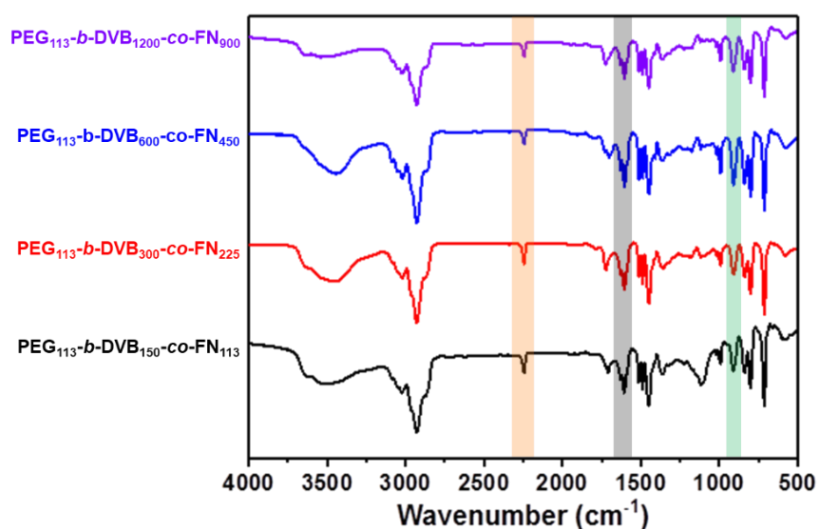


Figure 3.3 FTIR spectra of the PEG-CTA, fumaronitrile and divinylbenzene monomers

The IR frequencies highlighted in Figure 3.3 should all be present in the final material meaning it is possible to use these signal to determine if these three components are present in the final product. Indeed, when examining the FTIR spectra of the synthesised materials (Figure 3.4), we see that these signals are present in the final products thereby indicating that both monomers and CTA have been successfully incorporated. Alongside these signals, there is also a broad signal at  $2850 - 3050\text{ cm}^{-1}$  which looks similar to that present in the initial CTA. Closer inspection of this region shows there are two signals present with the signal centred at  $\sim 2850\text{ cm}^{-1}$  resulting from the alkyl C-H stretches present in the CTA and the newly synthesised polymer backbone. The second signal present at slightly higher wavenumber ( $\sim 3050\text{ cm}^{-1}$ ) is a result of the presence of aromatic C-H stretches present in the aromatic ring of DVB. Each of the samples also have peaks at  $\sim 3500\text{ cm}^{-1}$  present in their IR spectrum which is attributed to the presence of water. This is most likely a result of either the IR collection method, KBr discs were used and KBr is very hygroscopic, but could also be a result of the uptake of moisture by the hygroscopic PEG chains present in all networks.

### Chapter3. PPDs from FN and DVB



**Figure 3.4** FTIR spectra of PEG<sub>113</sub>-*b*-DVB<sub>150</sub>-co-FN<sub>113</sub>, PEG<sub>113</sub>-*b*-DVB<sub>300</sub>-co-FN<sub>225</sub>, PEG<sub>113</sub>-*b*-DVB<sub>600</sub>-co-FN<sub>450</sub> and PEG<sub>113</sub>-*b*-DVB<sub>1200</sub>-co-FN<sub>900</sub>

#### 3.5.2 Solid State NMR Spectroscopy

To further evidence the successful formation and relative incorporation of both monomers and macro-CTA, solid state <sup>13</sup>C NMR spectroscopy was carried out on each sample. Primarily, a solution phase <sup>13</sup>C NMR of each starting material (i.e. the CTA and monomers) was acquired and used to identify key signals present within each sample (Figure 3.5). These signals, along with the expected new peaks, can then be used to quantify the success of the reaction as well as confirm all reagents have been incorporated.

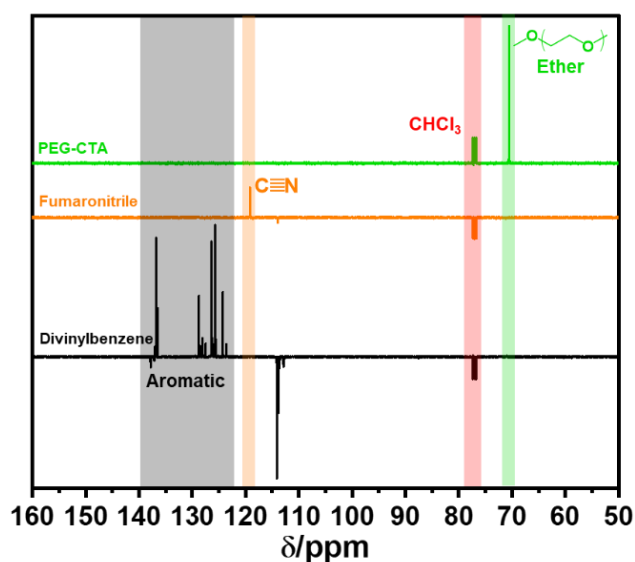


**Figure 3.5** <sup>13</sup>C NMR solution phase spectra of PEG-CTA (green), fumaronitrile (orange) and divinylbenzene (black) monomers in CDCl<sub>3</sub>

### Chapter3. PPDs from FN and DVB

The PEG macro-CTA has a distinct peak at ~70 ppm that corresponds to the CH<sub>2</sub> groups present within the PEG chain. Fumaronitrile exhibits a distinct peak at ~116 ppm due to the presence of the nitrile (C≡N) group. Finally, the divinylbenzene monomer has distinct peaks in the aromatic region, 120 – 140 ppm, corresponding to the aromatic carbons. There are also other peaks within the individual spectra such as the peaks at ~113 ppm seen in the spectrum of divinylbenzene and fumaronitrile which is attributed to the vinyl carbons of the respective monomers.

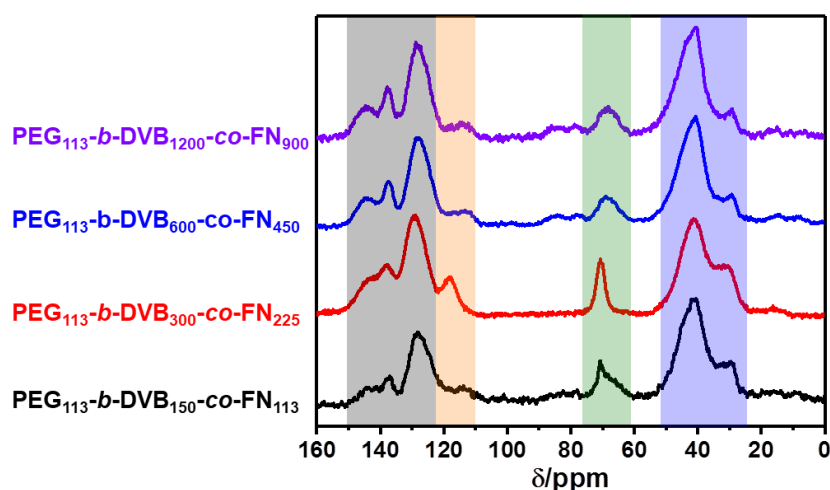


Figure 3.6 <sup>13</sup>C CP/MAS NMR spectra of PEG<sub>113</sub>-*b*-DVB<sub>150</sub>-co-FN<sub>113</sub>, PEG<sub>113</sub>-*b*-DVB<sub>300</sub>-co-FN<sub>225</sub>, PEG<sub>113</sub>-*b*-DVB<sub>600</sub>-co-FN<sub>450</sub> and PEG<sub>113</sub>-*b*-DVB<sub>1200</sub>-co-FN<sub>900</sub>

Solid state <sup>13</sup>C CP/MAS (cross-polarisation magic angle spinning) NMR spectroscopy was carried out (Figure 3.6) on each of the four samples synthesised in this work. The NMR were compared to that of the <sup>13</sup>C solution NMR of the starting materials to evaluate the relative success of the polymerisation. It is immediately clear to see that the PEG groups from the CTA have been incorporated into the final product due to the peak centred at ~70 ppm, present in all four samples. The broad signals present between 120 – 140 ppm are due to the aromatic carbons present from the incorporation of divinylbenzene into the network. To the right of this peak at ~116 ppm is a small peak which is due to the C≡N chemical moieties present due to the polymerisation of fumaronitrile. The new signals (20 – 40 ppm) are indicative of a long alkyl backbone as would be expected from the polymerisation of two vinyl monomer such as fumaronitrile and divinylbenzene. This confirms that the polymerisation of the two monomers was successful given that these signals did not appear in any of the solution phase NMR spectra of the starting material.

A comparison of the ssNMR of the RAFT-mediated route (PEG<sub>113</sub>-*b*-DVB<sub>300</sub>-co-FN<sub>225</sub>) and that of HCPN-0.75 provides further evidence that the reaction has proceeded *via* the

### Chapter3. PPDs from FN and DVB

RAFT-mediated route and not simply free radical polymerisation (Figure 3.7). This figure clearly shows that the HCPN-0.75 sample, which is the result of the free radical polymerisation between divinylbenzene and fumaronitrile has no signal at 70 ppm. This is to be expected due to that signal relating to the PEG chains of the CTA. However there is a clear signal at 70 ppm in the spectrum of PEG<sub>113</sub>-*b*-DVB<sub>300</sub>-*co*-FN<sub>225</sub>, or indeed any of the four samples synthesised using the RAFT-mediated PISA method. If the polymerisation process were to be purely free radical and not controlled then this signal would not be visible, therefore its presence confirms that the CTA had mediated the polymerisation of these two monomers. Notably, all other signals which appear in HCPN-0.75 also appear in the spectrum of PEG<sub>113</sub>-*b*-DVB<sub>300</sub>-*co*-FN<sub>225</sub>.

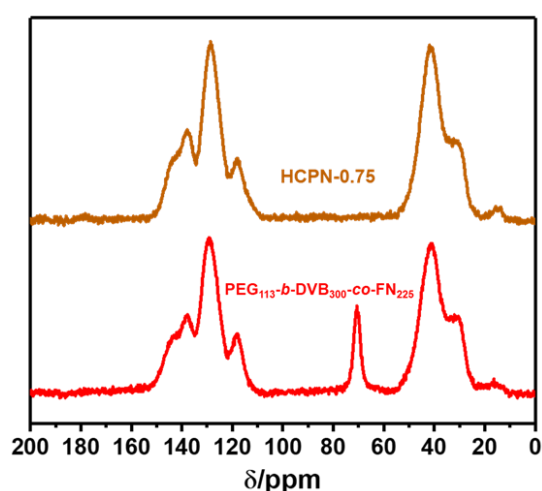


Figure 3.7 <sup>13</sup>C CP/MAS NMR spectra of HCPN-0.75 and PEG<sub>113</sub>-*b*-DVB<sub>300</sub>-*co*-FN<sub>225</sub>

#### 3.5.3 Elemental Analysis

Elemental analysis was carried out to give insight into the relative monomer incorporation of the final product (Table 3.3). All starting materials contain carbon and hydrogen hence this will not yield much insight into the incorporation of either fumaronitrile or CTA. However given that fumaronitrile is the only nitrogen containing monomer and the CTA is the only sulphur containing material these values will give a good indication as to how well these two are incorporated into the final product.

Table 3.3 Elemental analysis data for each sample

Sample	% Carbon		% Hydrogen		% Nitrogen		% Sulfur	
	Theoretical	Found	Theoretical	Found	Theoretical	Found	Theoretical	Found
PEG <sub>113</sub> - <i>b</i> -DVB <sub>150</sub> - <i>co</i> -FN <sub>113</sub>	78.01	80.74	5.66	6.88	14.68	7.31	0.08	0.79
PEG <sub>113</sub> - <i>b</i> -DVB <sub>300</sub> - <i>co</i> -FN <sub>225</sub>	78.55	82.22	5.58	6.75	15.03	7.64	0.04	0.37
PEG <sub>113</sub> - <i>b</i> -DVB <sub>600</sub> - <i>co</i> -FN <sub>450</sub>	78.84	85.18	5.53	7.11	15.20	4.95	0.02	0.26
PEG <sub>113</sub> - <i>b</i> -DVB <sub>1200</sub> - <i>co</i> -FN <sub>900</sub>	78.98	83.82	5.51	6.87	15.29	6.83	0.01	0.45

### Chapter3. PPDs from FN and DVB

All values were found deviate from the theoretical values, which assume full conversion of both monomers. The deviation in expected and found values could be due to a number of different reasons such as an idealised final structure, incomplete polymerisation of the monomers or the presence of water obscuring the results. What is most prominent from these results is that the nitrogen content of all samples is much lower than expected. Furthermore, all samples show a higher than expected carbon content. This may hint at the final material containing more divinylbenzene than fumaronitrile possibly due to the reactivity of divinylbenzene being greater than fumaronitrile – this monomer does after all have two sites from which polymerisation can occur. This point is further echoed by the hydrogen content being higher than expected for all samples synthesised. In particular, if we consider the PEG<sub>113</sub>-*b*-DVB<sub>600</sub>-*co*-FN<sub>450</sub> sample we see that this has by far the lowest nitrogen content but equally also by far the highest carbon and hydrogen content.

The sulphur content found in all the samples is much higher than expected. Given that each sample synthesised has twice the amount of monomer present the sulphur content should half each time assuming 100% conversion is reached. Therefore, we can assume that if the sulphur content is higher than expected than there is less monomer conversion during polymerisation. The yields of each synthesis (Table 3.2) are much less than 100 % so it is known that the reactions have not reached full conversion. Therefore, a higher sulphur content than calculated is to be expected for each sample. The fact that there is sulphur in the final material does however confirm that the polymerisation was mediated by the RAFT-agent and that the CTA has been successfully incorporated into the final material.

### 3.6 Surface Area and Porosity

The porosity of each sample was studied by nitrogen gas sorption isotherms at 77 K (Figure 3.8). All samples display uptake over the low pressure range ( $< 0.1 P/P_0$ ) which is indicative of uptake into the micropores of the sample. Indeed, this is consistent with the nitrogen gas sorption isotherm of HCPN-0.75 as reported by Li *et al.*<sup>2</sup> thereby proving that the polymerisation of divinylbenzene and fumaronitrile has resulted in the generation of a microporous network. All four samples also show very large uptake over a high relative pressure range ( $>0.9 P/P_0$ ), something which was not previously seen in the isotherm of HCPN-0.75. This uptake is usually attributed to gas adsorption into large pores, often macropores, present within a sample. However, it is unlikely that the polymerisation of divinylbenzene and fumaronitrile would result in a macroporous material. It has been previously reported that the hypercrosslinking of block copolymers results in an aggregated network which allows for condensation of nitrogen gas between particles.<sup>3,28</sup> Instead, this large

### Chapter3. PPDs from FN and DVB

uptake of gas is attributed to the condensation of nitrogen gas between the particles formed during the RAFT PISA process. This is further explored in section 3.8 of this chapter.

The surface area of each sample was calculated over the relative pressure range of 0.01 – 0.15  $P/P_0$  (Table 3.4). The surface area of each sample increases as the core DP increases which is to be expected given the core of the material induces porosity. The sample with the lowest monomer content, PEG<sub>113</sub>-*b*-DVB<sub>150</sub>-*co*-FN<sub>113</sub>, has a specific surface area of 244 m<sup>2</sup>/g. Each sample increases in surface area until a maximum of 409 m<sup>2</sup>/g was reached for the PEG<sub>113</sub>-*b*-DVB<sub>600</sub>-*co*-FN<sub>450</sub> sample. After this, further increasing the core DP had no prominent effect on the surface area - PEG<sub>113</sub>-*b*-DVB<sub>1200</sub>-*co*-FN<sub>900</sub> has a surface area of around 400 m<sup>2</sup>/g. This demonstrates that the surface area of the material can be tuned through varying the ratio of core monomer to macro-CTA. Indeed, the phenomenon of increasing the size of the crosslinking or porosity inducing block has been observed before in the work of Matyjaszewski *et al.* who demonstrated that increasing the DP of the PS block, which could be hypercrosslinked, resulted in materials with larger surface areas.<sup>3</sup>

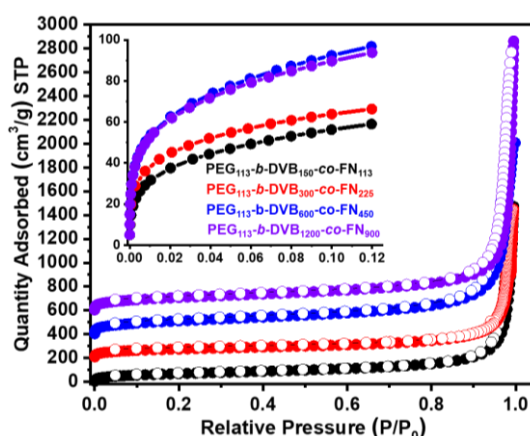


Figure 3.8 Nitrogen adsorption (filled) and desorption (open) isotherms at 77 K of PEG<sub>113</sub>-*b*-DVB<sub>150</sub>-*co*-FN<sub>113</sub>, PEG<sub>113</sub>-*b*-DVB<sub>300</sub>-*co*-FN<sub>225</sub>, PEG<sub>113</sub>-*b*-DVB<sub>600</sub>-*co*-FN<sub>450</sub> and PEG<sub>113</sub>-*b*-DVB<sub>1200</sub>-*co*-FN<sub>900</sub> (each offset by 200 cm<sup>3</sup>/g).

The pore size distribution of each sample was calculated from the adsorption branches of the isotherm using the non-local density functional theory (NLDFT) model (Figure 3.9a). This model confirmed the presence of micropores within all four samples with a pore size distribution centred around 1.8 nm. This analysis also revealed the presence of meso- and macropores within each sample. The plot of cumulative surface area vs pore width (Figure 3.9b) confirms that as the core DP increases the surface area attributed to

### Chapter3. PPDs from FN and DVB

microporosity also increases. Between 30 to 42 % of the total surface area of each sample is attributed to the micropores present in each sample.

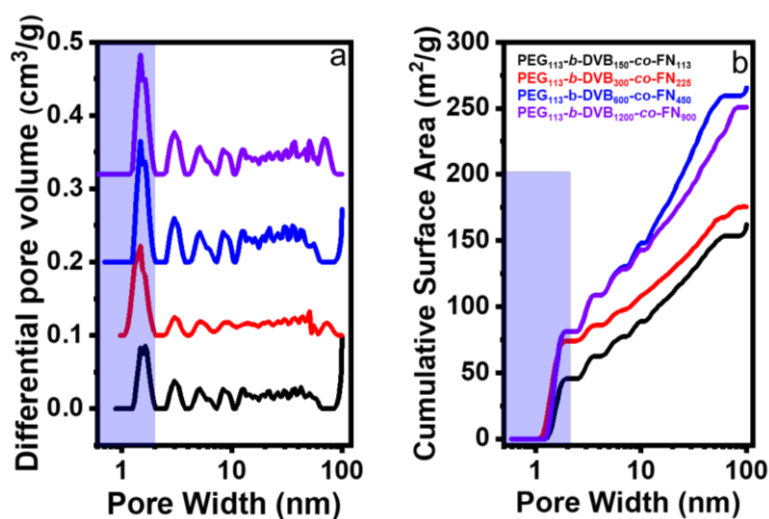


Figure 3.9 (a) NL-DFT differential pore size distribution and (b) cumulative surface area vs pore width of  $\text{PEG}_{113}\text{-}b\text{-DVB}_{150}\text{-CO-FN}_{113}$ ,  $\text{PEG}_{113}\text{-}b\text{-DVB}_{300}\text{-CO-FN}_{225}$ ,  $\text{PEG}_{113}\text{-}b\text{-DVB}_{600}\text{-CO-FN}_{450}$  and  $\text{PEG}_{113}\text{-}b\text{-DVB}_{1200}\text{-CO-FN}_{900}$

Although not plentiful, there are some discreet examples of porous, solution-processable materials reported in the literature (Section 1.4). The materials reported in this thesis and resulting publication<sup>29</sup> compare favourably with those other materials reported in the literature in (Table 3.4). As would be expected, the “soluble” analogues have lower surface areas than the analogous insoluble samples and it is this trade-off that will be vital when designing solution-processable materials.

Table 3.4 Reported BET surface areas of other solution processable porous polymers published

Sample	SA <sub>BET</sub> (m <sup>2</sup> /g)	Ref
$\text{PEG}_{113}\text{-}b\text{-DVB}_{150}\text{-CO-FN}_{113}$	244	This work
$\text{PEG}_{113}\text{-}b\text{-DVB}_{300}\text{-CO-FN}_{225}$	270	This work
$\text{PEG}_{113}\text{-}b\text{-DVB}_{600}\text{-CO-FN}_{450}$	409	This work
$\text{PEG}_{113}\text{-}b\text{-DVB}_{1200}\text{-CO-FN}_{900}$	400	This work
SHCP-3	158	30
SHCP-4	355	30
SHCP-5	530	30
SCMP-1	505	31
TPDC-BZ	610	32
PHCPN	133	33
CzBDP	180	34
Poly(DCDM)-395	646	35
xPCMS-g-PDMAEMA	562	36
xPCMS-g-PNIPAM	596	36

## Chapter3. PPDs from FN and DVB

### 3.7 Dispersibility and Solution Stability

Solid state characterisation confirmed that porous materials have been synthesised which incorporate both monomers and the CTA. Therefore, the next step is to characterise the behaviour of these porous materials in the solution phase.

#### 3.7.1 Solution Stability

Thus far, the only way of identifying the solution stability over time has been very crudely “by-eye” (Figure 3.2). While this provides a crude and initial observation that yields some insight into the solution stability it is purely qualitative. Therefore, it is imperative to develop a more insightful analysis technique to better study the solution stability of the dispersions. Most ideal would be a method that allows for the quantitative determination of the degree of sedimentation that occurs in each sample over a defined period of time.

All the samples synthesised are UV active and show peaks in the UV region due to the presence of divinylbenzene (Figure 3.10). As such, it may be possible to use UV-Vis spectroscopy to determine the stability of the dispersions. If a known quantity of sample is dispersed in a chosen solvent and the UV-Vis spectrum of that sample is recorded immediately the absorbance of that amount of sample is known. Should the sample then be left undisturbed for a period before recording another UV-Vis spectrum any change in the intensity will be a result of the sedimentation within the sample. This change in intensity can then be related to the amount of samples that has fallen out of solution given that the Beer-Lambert law associates absorbance with concentration. This method provides a very simple and convenient way of determining the solutions stability of each dispersion.

All four samples were made up to 0.1 mg/mL solutions and sonicated for 30 minutes to form stable colloidal dispersion. A UV-Vis spectrum of each dispersion was recorded before each sample was left undisturbed for 1 week in a sealed cuvette to ensure the solvent level remained consistent. After this period, another UV-Vis spectrum was recorded and the maxima of the two spectra were used to determine the degree of sedimentation (Figure 3.10).

### Chapter3. PPDs from FN and DVB

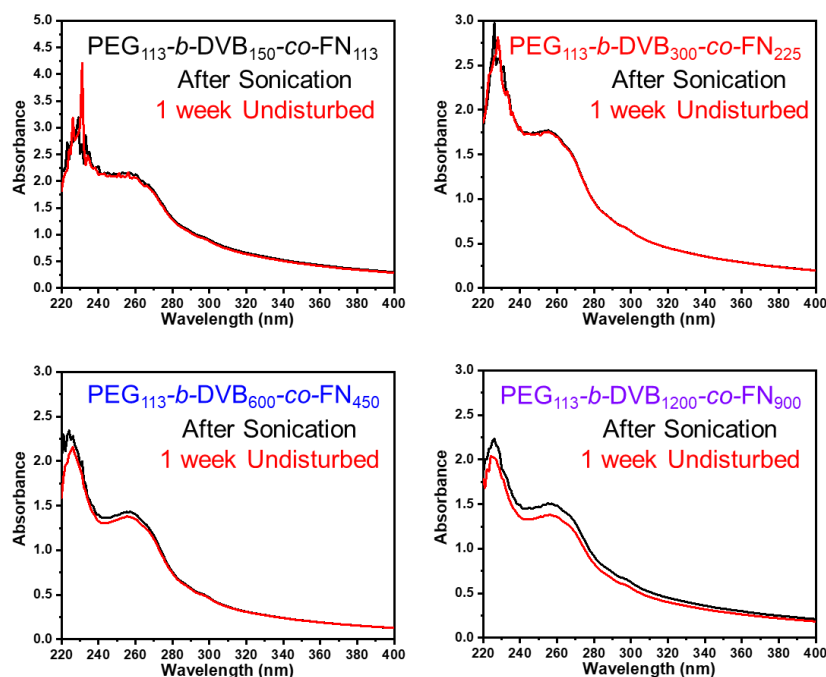


Figure 3.10 UV-Vis spectra of each sample after sonication (black) and after 1 week undisturbed (red). The peak at ~265 nm was used to determine the degree of sedimentation over this time period.

All samples demonstrated good solution stability with very little difference in the UV-Vis spectrum observable after 1 week, which is in agreement with what was visually observed. If the maximum of the one week spectrum is subtracted from the one recorded initially the solution stability of each dispersions can be quantified and the dispersed and sedimented fractions reported. The two samples with the smallest core DP showed the best solution stability with > 99 % of the samples remaining dispersed after one week (Table 3.5). The solution stability seems to be in good agreement with the core DP in that the largest sample shows the worst solution stability, though even this is greater than 90 %. This experiment logically suggests that as the core DP increases the samples becomes less solution stable. This experiment proved simple to carry out, allows for a simple way to determine solution stability and is a great example of the ways in which these samples can be analysed in solution, something much more difficult to do for insoluble porous polymers.

Table 3.5 Solution stability of each sample analysed *via* UV-Vis spectroscopy

Sample	Dispersed fraction	Sedimented fraction
PEG <sub>113</sub> - <i>b</i> -DVB <sub>150</sub> -co-FN <sub>113</sub>	> 99 %	< 1 %
PEG <sub>113</sub> - <i>b</i> -DVB <sub>300</sub> -co-FN <sub>225</sub>	> 99 %	< 1 %
PEG <sub>113</sub> - <i>b</i> -DVB <sub>600</sub> -co-FN <sub>450</sub>	97 %	3 %
PEG <sub>113</sub> - <i>b</i> -DVB <sub>1200</sub> -co-FN <sub>900</sub>	91 %	9 %

### Chapter3. PPDs from FN and DVB

#### 3.7.2 Dynamic Light Scattering

Given that stable colloidal dispersions can be formed after sonication in methanol, it seems appropriate to try and characterise the particles present in these colloidal suspensions. The simplest technique used to characterise polymeric dispersions is dynamic light scattering (DLS). Much like the UV-Vis study, 0.1 mg/mL solutions in methanol were made up and sonicated for 30 minutes, before immediate analysis of the resulting solution. The DLS of the four samples showed particles existed in solution ranging from 229 nm to 942 nm (Table 3.6). These sizes are much larger than compared to more conventional polymer nanoparticles with similar DPs. For example Zhang *et al.* synthesised PEG<sub>113</sub>-b-PS<sub>206</sub> nanoassemblies which were found to be only 31 nm in size.<sup>17</sup> Likewise even ultrahigh molecular weight poly(styrene) particles synthesised by Davis *et al.* were only around 170 nm in diameter and that was with a poly(styrene) M<sub>n</sub> exceeding 1 000 000 g/mol (DP > 9600).<sup>37</sup>

Table 3.6 Hydrodynamic radii of each sample after different sonication times

Sample	Hydrodynamic radii (nm) <sup>a</sup>		
	30 mins sonication	3 h sonication	72 h undisturbed
PEG <sub>113</sub> - <i>b</i> -DVB <sub>150</sub> -CO-FN <sub>113</sub>	241 (0.11)	176 (0.10)	204 (0.10)
PEG <sub>113</sub> - <i>b</i> -DVB <sub>300</sub> -CO-FN <sub>225</sub>	229 (0.08)	216 (0.07)	219 (0.08)
PEG <sub>113</sub> - <i>b</i> -DVB <sub>600</sub> -CO-FN <sub>450</sub>	435 (0.19)	233 (0.11)	230 (0.10)
PEG <sub>113</sub> - <i>b</i> -DVB <sub>1200</sub> -CO-FN <sub>900</sub>	942 (0.24)	205 (0.21)	262 (0.24)

<sup>a</sup>DLS carried out at 25 °C, PDI of each sample in parentheses. <sup>b</sup>DLS carried out after leaving sample undisturbed for 72 hours and then carrying out the measurement.

Given that the sample size in solution was much larger than initially expected it was decided that the samples should be sonicated for a longer period of time. It is possible that the nanoassemblies in solution could be aggregating together and a larger period of sonication should succeed in breaking up these aggregates. Therefore, each sample was sonicated for 3 hours before being immediately analysed. The longer sonication time resulted in a dramatic reduction of the observable hydrodynamic radius (Table 3.6). The resulting sizes are more similar to other bodies of work which report spherical nanoassemblies of amphiphilic diblock copolymers of similar DPs.<sup>19,37,38</sup> After allowing the solutions to stand for 72 hours undisturbed it was found that there was minimal change in the size of the particles in solution. This suggests that the particles are not aggregating back together (Figure 3.11).

### Chapter3. PPDs from FN and DVB

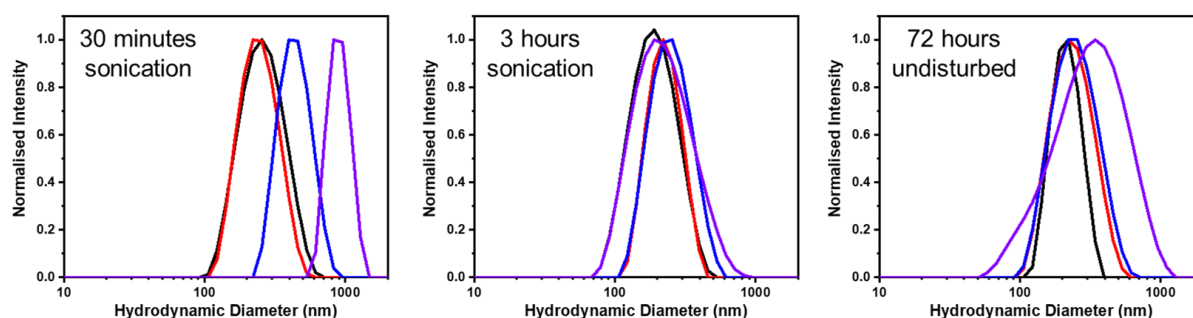


Figure 3.11 DLS curves of PEG<sub>113</sub>-*b*-DVB<sub>150</sub>-*co*-FN<sub>113</sub>, PEG<sub>113</sub>-*b*-DVB<sub>300</sub>-*co*-FN<sub>225</sub>, PEG<sub>113</sub>-*b*-DVB<sub>600</sub>-*co*-FN<sub>450</sub> and PEG<sub>113</sub>-*b*-DVB<sub>1200</sub>-*co*-FN<sub>900</sub> after different sonication times (left & middle) and after being left for 72 hours (right)

Though DLS is a quick and simple technique it is not without its flaws, which most notably is the assumption that all samples being analysed have a spherical morphology. Therefore, any deviations from this would lead to inaccurate results. This is quite obvious to spot through observing the PDI of each sample under investigation. Generally, a PDI of around 0.2 or less is seen as acceptable and confirms that the sample is both stable (i.e. no sedimentation is occurring) and is adopting a spherical morphology. Samples with PDIs of larger than 0.4 are to be treated with some caution given that these samples are either showing a wide size distribution. The samples analysed in this work all gave quite narrow PDIs (below 0.25) which is considered acceptable. However, given that DLS does assume a spherical morphology and thus far the morphology of these samples are still unknown it is imperative to carry out more detailed analysis of the samples so as to probe in more depth the size and morphology.

### 3.8 Small Angle X-Ray Scattering (SAXS) Studies

Small Angle X-Ray Scattering (SAXS) is a powerful and versatile analytical technique for the structural characterisation of nanomaterials in either solution or the solid state. SAXS gives information relating to the morphology and size of the sample under investigation in the range of one to a few hundred nanometres. As such, it seems a suitable technique to further probe the sample morphology and size of the porous polymer dispersions reported in this work.

SAXS, in a similar way to x-ray crystallography, works on the principle of scattering x-rays, measuring the scatter pattern and finally relating this back to the sample under investigation. However, unlike x-ray crystallography, the sample need not be crystalline which allows for the study of amorphous systems such as proteins, emulsions and nanoparticles. The reason much larger structures can be analysed is due to the scattering intensity being measured at angles of  $2\theta$  close to  $0^\circ$  (typically between  $0.1 - 10^\circ$ ).

The setup of a SAXS experiment sees a solution of the sample under investigation placed in a suitable sample holder and illuminated by a beam of monochromatic x-rays (Figure 3.12). As the x-rays pass through the sample they are elastically scattered and this scattering is recorded by a detector. The resulting scattering pattern allows the morphology and size of the sample to be determined. The solvent system is also recorded and subtracted from the SAXS pattern obtained from the sample leaving only the SAXS pattern obtained from the particles under analysis.

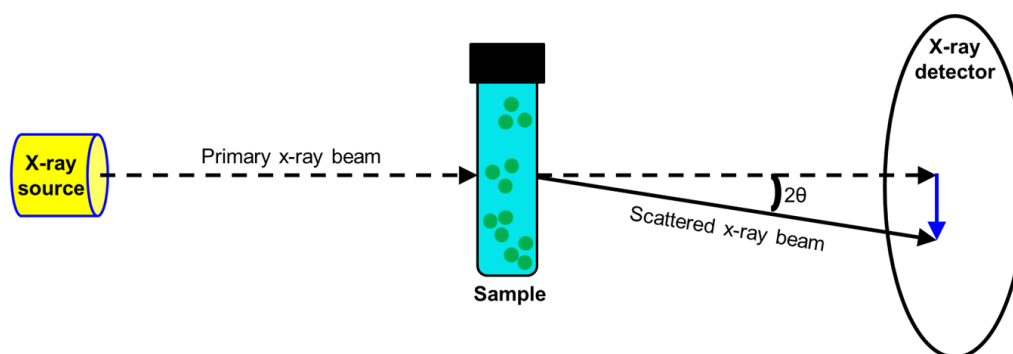


**Figure 3.12** Schematic representation of a SAXS experimental setup

SAXS studies were carried out on the stable dispersions formed for each sample in methanol to probe the morphology adopted by the samples in solution. 5% w/w dispersions in methanol were used to probe the structure of each sample (Figure 3.13a). To simplify the analysis it was necessary to model the data based on the particles being treated as homogeneous solid spheroids. In this instance the scattering intensity of such spheroids can be expressed as:

### Chapter3. PPDs from FN and DVB

$$\frac{d\Sigma}{d\Omega}(q)_n = N_n S_{PY}(q)_n \int_0^\infty g_{Gauss}(R_n) |F(qR_n)|^2 dR_n \quad \text{Equation 3.2}$$

where  $N_n$  is the number of scatterers,  $S_{PY}(q)_n$  is the hard-sphere interaction structure factor based on the Percus-Yevick approximation,<sup>39</sup>  $g_{Gauss}(R_n)$  is their Gaussian size distribution function and  $F(qR_n)$  is the particle form factor. Specifically,  $g_{Gauss}(R_n)$  is expressed as:

$$g_{Gauss}(R_n) = \frac{1}{\sigma_{R_n} \sqrt{2\pi}} e^{-\frac{(R_n - \bar{R}_n)^2}{2\sigma_{R_n}^2}} \quad \text{Equation 3.3}$$

where  $\bar{R}_n$  is the mean radius of the particles and  $\sigma_{R_n}$  is the standard deviation of the size distribution. The particle form factor,  $F(qR_n)$ , is expressed as:

$$I(q) = \frac{d\Sigma}{d\Omega}(q)_1 + \frac{d\Sigma}{d\Omega}(q)_2 \quad \text{Equation 3.4}$$

where  $\Delta\xi$  is the X-ray scattering contrast.

Initial inspection of the background-subtracted SAXS pattern for a 5% w/w dispersion of each sample in methanol indicated that a complex morphology consisting of two populations was present: one of small particles ( $n=1$  in Eq. 3.2 – 3.4) and the other of larger particles ( $n=2$  in Eq. 3.2 – 3.4).

$$I(q) = \frac{d\Sigma}{d\Omega}(q)_1 + \frac{d\Sigma}{d\Omega}(q)_2 \quad \text{Equation 3.5}$$

This two-population approximation provided a satisfactory fit over the entire  $q$ -range and indicated that primary nanoparticles of between 24 nm and 29 nm in diameter (D1) existed within larger aggregates whose diameter ranged from 138 nm to 188 nm (D2) (Figure 3.14b). The Percus-Yevick hard-sphere mean interaction distance between interacting primary particles ( $D_{PY_1}$ ) ranged between 31 nm and 42 nm, and that between larger aggregates ( $D_{PY_2}$ ) was found to be between 239 nm and 279 nm.

Chapter3. PPDs from FN and DVB

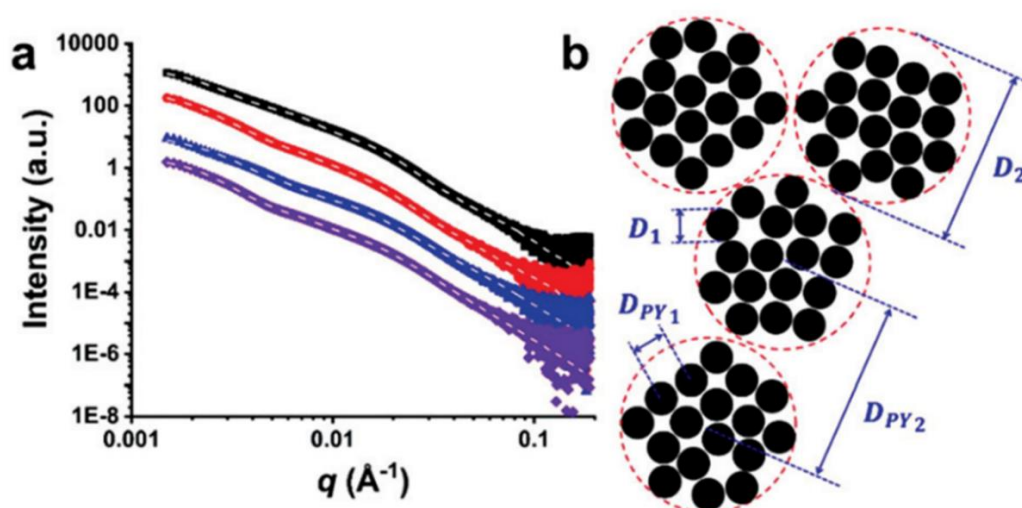


**Figure 3.13** (a) Small angle x-ray scattering of samples  $\text{PEG}_{113}\text{-}b\text{-DVB}_{150}\text{-co-FN}_{113}$ ,  $\text{PEG}_{113}\text{-}b\text{-DVB}_{300}\text{-co-FN}_{225}$ ,  $\text{PEG}_{113}\text{-}b\text{-DVB}_{600}\text{-co-FN}_{450}$  and  $\text{PEG}_{113}\text{-}b\text{-DVB}_{1200}\text{-co-FN}_{900}$ . (b) Representation of particle morphology where  $D_1$  and  $D_2$  are the mean diameter of the primary particles and aggregates and  $D_{PY1}$  and  $D_{PY2}$  are the mean interacting distances between the primary particles and aggregates respectively

SAXS analysis revealed important structural features about the sample morphology DLS studies were not able to. Namely, these are that the samples are not simply individual micelles comprised of a porous core made dispersible by outer hydrophilic PEG corona but instead show a much more complex aggregated morphology. TEM images of each sample were collected to confirm that the SAXS data was correct and the samples did indeed adopt this aggregated morphology. TEM imaging confirms that each sample consists of primary smaller particles which aggregate together to form much larger assemblies as indicated through SAXS analysis (Figure 3.14).

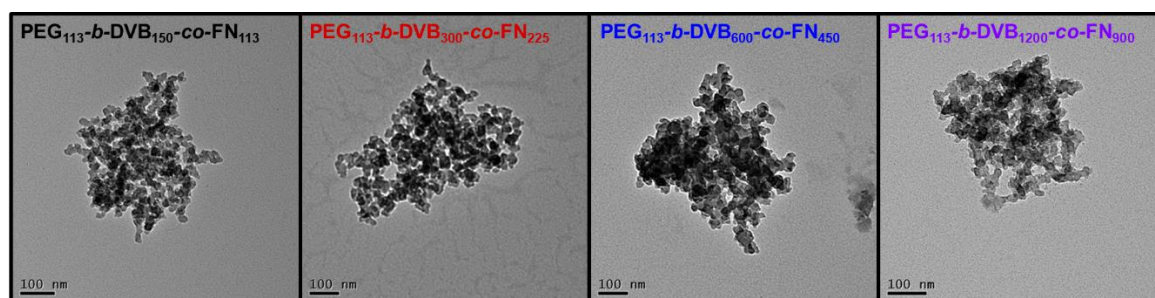


**Figure 3.14** TEM images of  $\text{PEG}_{113}\text{-}b\text{-DVB}_{150}\text{-co-FN}_{113}$ ,  $\text{PEG}_{113}\text{-}b\text{-DVB}_{300}\text{-co-FN}_{225}$ ,  $\text{PEG}_{113}\text{-}b\text{-DVB}_{600}\text{-co-FN}_{450}$  and  $\text{PEG}_{113}\text{-}b\text{-DVB}_{1200}\text{-co-FN}_{900}$  showing the aggregated morphology deduced by SAXS

The presence of this aggregated morphology, as confirmed by SAXS studies and TEM imaging, explains why a dramatic size reduction was observed in the DLS upon further sonication. Furthermore, after 3 hours of sonication the samples do not seem to get any bigger when left undisturbed. This may suggest that the aggregation in these samples is driven by

### Chapter3. PPDs from FN and DVB

two or more different reasons and that one can be overcome through sonication but the other is much harder to overcome. As a result larger mass fractals, which are collections of aggregates, can be broken down into aggregates which are then not able to be further broken down into the individual particles first hypothesised at the advent of this project. The next section of this chapter investigates further this aggregate formation.

## 3.9 Hypothesis of Aggregate Formation

It was proposed in the introduction and chapter aims that the RAFT-mediated PISA of divinylbenzene alongside a co-monomer would yield discrete porous nano-objects. Preliminary DLS studies seemed to support this hypothesis but more comprehensive SAXS and TEM analysis observations revealed that a more complex and aggregated morphology was instead adopted. Though interesting, it is not yet clear why these samples adopt this morphology hence it is imperative to carry out studies to further elucidate the mechanism of formation.

### 3.9.1 Synthesis of Analogous Poly(styrene) Samples

It is thought that the main reason the samples adopt an aggregated morphology is due to the polymerisation of the bifunctional divinylbenzene monomer. It is the bifunctional nature of this monomer to which we accredit the porosity of each sample hence it is imperative that we use this monomer in the synthesis of these materials. However, what could be the case is that the monomer is polymerising before the onset of microphase separation. Therefore, when phase separation occurs and the core of the sample begins to form it could be that some particles become linked together due to this early polymerisation of the DVB monomer. Should this be the case then it is conceivable to imagine that some particles would become linked together resulting in aggregate formation as observed by SAXS and TEM. Analogous samples were prepared by substituting the DVB monomer and replacing it with styrene whilst keeping all other variables constant and the two series were compared.

This synthesis was attempted and the products were analysed *via* DLS and TEM to determine the size and morphology. Ideally the reaction would yield spherical particles which show no aggregation if it were the DVB which was solely responsible for the observed aggregate formation. Figure 3.15 shows the TEM images of the PEG-b-PS-co-FN analogues along with their sizes as determined by DLS. It is clear that the samples synthesised using styrene were not at all aggregated and yielded monodisperse spherical nanoparticles. Given that the only difference in synthesis was the replacement of divinylbenzene for the chemically and structurally similar styrene monomer it is a fair conclusion to draw that the polymerisation of divinylbenzene is responsible for the aggregation present in the DVB samples.

### Chapter3. PPDs from FN and DVB

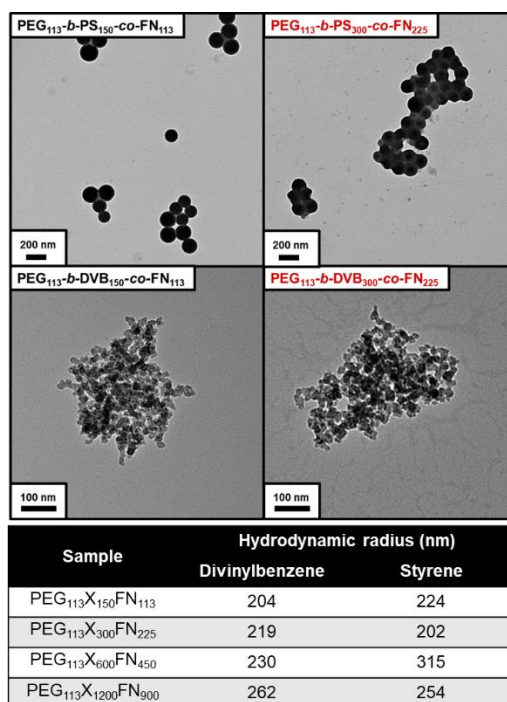


Figure 3.15 (above) TEM images of styrene analogues of the DVB samples and (below) the DLS data for each sample

To gain better insight into how fast this aggregation commences a DLS study was carried out on the synthesis of the PEG<sub>113</sub>-b-DVB<sub>1200</sub>-co-FN<sub>900</sub> sample. At a certain time an aliquot of the reaction mixture was taken and analysed by DLS with the idea being that the onset of aggregation could be determined when there was a significant increase in the observable samples size. This information would be useful because it would give insight into whether aggregation occurs immediately or after a certain amount of time. There was a particular focus on collecting time points early on in the reaction so as not to miss this onset should it occur rapidly.

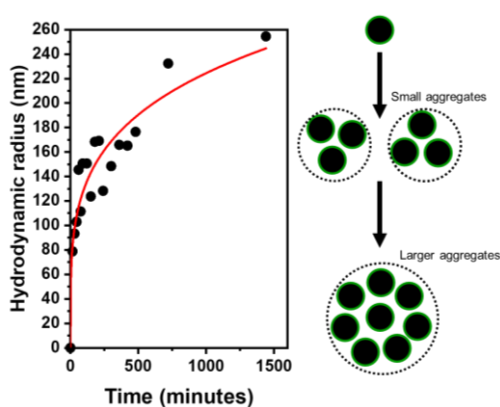


Figure 3.16 (Left) Evolution of particle size over time for the synthesis of PEG<sub>113</sub>-b-DVB<sub>1200</sub>-co-FN<sub>900</sub> and (right) hypothesised mechanism for the generation of porous polymeric aggregates

### Chapter3. PPDs from FN and DVB

After less than one hour a particle size of around 80 nm was recorded suggesting that crosslinking of smaller particles occurs very early on before subsequent aggregation. After this period there was a general trend showing the size increase from around 80 nm up to an eventual size of around 260 nm which was initially observed for this sample after extensive sonication. Interestingly this sample showed the same size as the sample did after sonication for 3 hours. This may prove that these are the largest achievable aggregates relating to the polymerisation process and any other further size increase is a result of these aggregates packing together. This could be significant as it may indicate that once PISA occurs further polymerisation of the DVB only takes place in the cores which gives rise to the porosity within the core of the material and is why the samples are able to form solution-stable dispersions. A hypothesised synthesis mechanism is shown in Figure 3.16 alongside the DLS results obtained by monitoring the synthesis of PEG<sub>113</sub>-*b*-DVB<sub>1200</sub>-CO-FN<sub>900</sub>.

#### 3.10 Swelling of Sample in Various Solvents

Thus far all experiments in solution have been carried out in methanol for consistency and the materials had not been dispersed in any other solvent. The samples are comprised of insoluble porous cores made dispersible by the presence of long hydrophilic PEG chains hence the solution stability is predominantly driven by the solubility of the PEG chains in a chosen solvent. Should the solvent of choice be an anti-solvent for PEG, i.e. hexane or petroleum ether, then the samples would not disperse in solution.

Another factor which may govern the solution stability and indeed size of the nano-objects in solution is the swelling of the porous insoluble core which is made up of divinylbenzene and fumaronitrile. It is a well-known phenomenon that porous polymers, particularly hypercrosslinked polymers and resins based on divinylbenzene, are able to swell when placed in certain solvents.<sup>40-42</sup> In the case of the insoluble material this effect may even be beneficial such as allowing for enhanced uptake of gas and pollutants. Wilson *et al.*<sup>40</sup> even speculated this phenomena could be exploited for medicinal applications and applied to the uptake of wound exudate. However, in the PPD samples, this swelling effect could be detrimental to the solution stability given that another governing factor of solution stability will be the size of the insoluble material which is being dispersed. Should the insoluble core become too big the PEG groups would not be able to stabilise it and the result would be sedimentation of the sample.

To test this theory and explore whether particle size could be tuned through varying the dispersant each solid sample was dispersed in a different solvent and sonicated for 30 minutes. Once again, 0.1 mg/mL solutions were made and analysed *via* DLS to examine the change in

### Chapter3. PPDs from FN and DVB

particle size. Though it has been shown DLS is not ideal to probe the morphology it is reliable to compare data between samples in the same series. Six different solvents were chosen (chloroform, dichloromethane, toluene, tetrahydrofuran, acetone and acetonitrile) all of which are capable of dissolving fumaronitrile but only some could dissolve poly(styrene), the closest soluble linear polymer to a divinylbenzene polymer. It is expected that the divinylbenzene would dominate the swelling characteristics of the core given there is much more of it present and it is the monomer which crosslinks the material. It would be expected that the solvents capable of dissolving poly(styrene) should also be able to swell the core of the material and hence larger particle sizes should be observed for these samples which may lead to solution instability and settling. Likewise samples which do not dissolve poly(styrene) should not be able to significantly swell the samples and no significant size increase would be expected.

Applying this *a priori* approach, the different hydrodynamic radii recorded for each sample as a function of the dispersant was measured *via* DLS (Figure 3.17). The solvents used can be split into two categories, those which form stable dispersions and those which induce sedimentation of the sample. As expected solvents which are able to dissolve poly(styrene) quite readily are found to be the solvents which yield the largest hydrodynamic radii and also result in the most prominent sedimentation. Namely, these solvents are chloroform, dichloromethane and toluene. Indeed when these samples were analysed by DLS the results were so broad that accurate data acquisition proved most difficult. This is in most part down to the fact the samples began to fall out of solution almost immediately after sonication.

The other solvents; tetrahydrofuran, acetone and acetonitrile, all proved to be much better dispersants and allowed for much better data acquisition. Of these solvents, THF and acetone yielded particles with the largest hydrodynamic radius which seems logical given their ability to dissolve poly(styrene). Acetonitrile and methanol, two solvents which cannot dissolve poly(styrene) gave rise to the smallest particle sizes. These results prove that the divinylbenzene component is most responsible for the swelling of the core and as such manipulation of this through judicious choice of dispersant can be used to modify the size of the material in solution.

### Chapter3. PPDs from FN and DVB

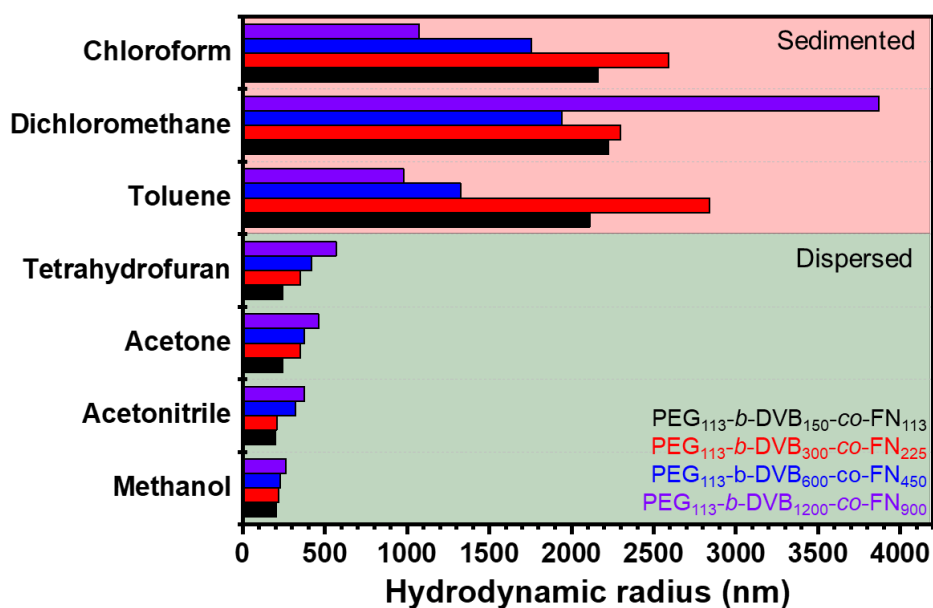


Figure 3.17 Hydrodynamic radii of each sample when dispersed in different solvent

This study also allowed for the determination as to the upper limit of the core size before the sample becomes too large and falls out of solution. The three “bad” solvents all gave rise to sedimentation yet are all solvents which can solubilise PEG. Therefore the main driving force for sample sedimentation in this instance is the core swelling effect. If this is the case then it may also be true to say that the limit of solution stability is the size at which the sample begins to fall out of solution. The largest sample that remained in solution was found to be PEG<sub>113</sub>-*b*-DVB<sub>1200</sub>-CO-FN<sub>900</sub> in THF (568 nm). Conversely, the smallest sample that showed a loss of solution stability was the same sample in toluene which had a size of 978 nm. This suggests that the limit of solution stability is somewhere between 568 – 978 nm though this is assuming the sample behaves in the same way in different solvents and that solution stability is dependant only on core size.

### 3.11 Luminescent Properties

It was found that each sample exhibited luminescent properties when exposed to UV light (Figure 3.18), a surprising observation given the lack of any extended conjugation. As such, this behaviour was investigated to determine both the cause and any potential benefits/applications that could arise from this luminescent behaviour. This section discusses the luminescent properties of the materials. Chapter 5 further discussed this behaviour and how it can be applied to selective chemosensing of different compounds

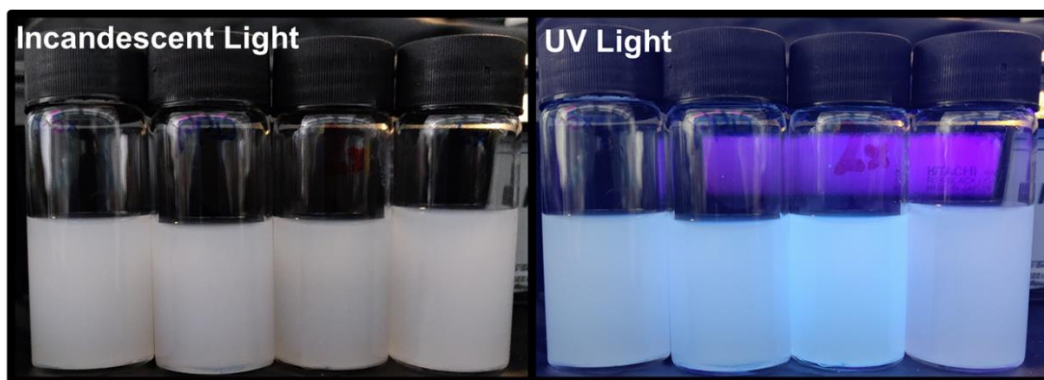
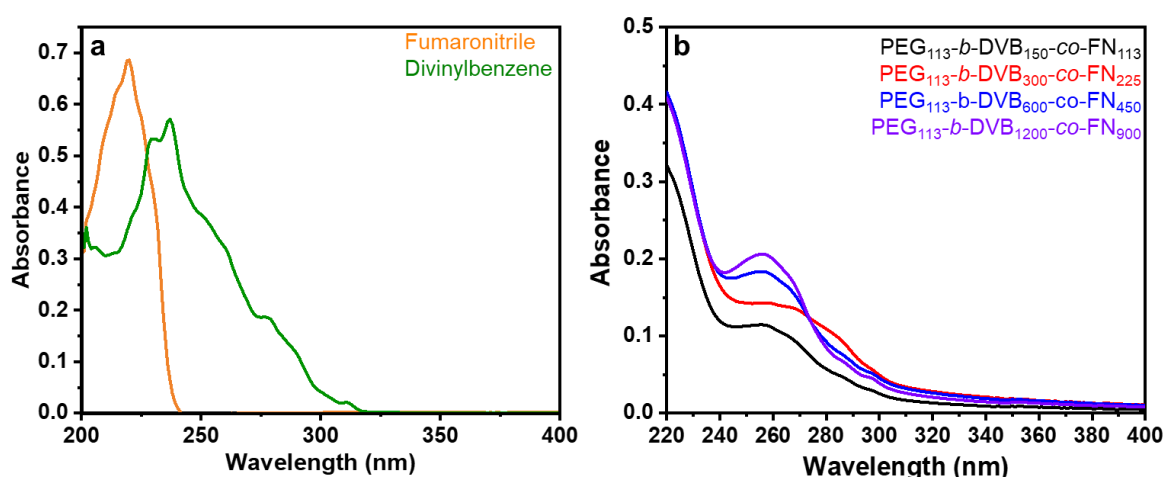


Figure 3.18 Observed luminescence of each sample when irradiated by UV light ( $\lambda_{\max} = 365 \text{ nm}$ )

### 3.11.1 UV-Vis Spectroscopy

A UV-Vis spectrum of each sample was recorded to identify any bands present in the sample that could be causing the luminescent behaviour. All samples exhibit an absorption maxima in the *middle-UV* region (Figure 3.19) centred around 260 nm though it is not clear what the cause of these signals are. Therefore, in order to gain better insight into the luminescence UV-Vis studies on the monomers were carried out. The UV-Vis spectra of the monomers shows that both fumaronitrile and divinylbenzene have an absorption maxima at around 218 and 237 nm respectively. However, in the case of fumaronitrile there is just one sharp peak yet for divinylbenzene there is a broad absorption signal ranging between 213 – 300 nm. Given that this monomer better covers the region of absorption for the polymer samples and that there is more of this monomer present in the sample it is most likely that the luminescent behaviour for these samples is most dominated by the divinylbenzene units present within the core and not the fumaronitrile.



**Figure 3.19** UV-Vis spectra of (a) fumaronitrile and divinylbenzene monomers and (b) PEG<sub>113</sub>-*b*-DVB<sub>150</sub>-co-FN<sub>113</sub>, PEG<sub>113</sub>-*b*-DVB<sub>300</sub>-co-FN<sub>225</sub>, PEG<sub>113</sub>-*b*-DVB<sub>600</sub>-co-FN<sub>450</sub> and PEG<sub>113</sub>-*b*-DVB<sub>1200</sub>-co-FN<sub>900</sub> in methanol

### Chapter3. PPDs from FN and DVB

#### 3.11.2 Fluorescence Spectroscopy

Fluorescence emission spectroscopy allows for the probing of the transition from the excited state back to the ground state after the material has been excited by UV light. The fluorescence emission spectrum of both the monomers and polymers were recorded to better understand the mechanism in play (Figure 3.20).

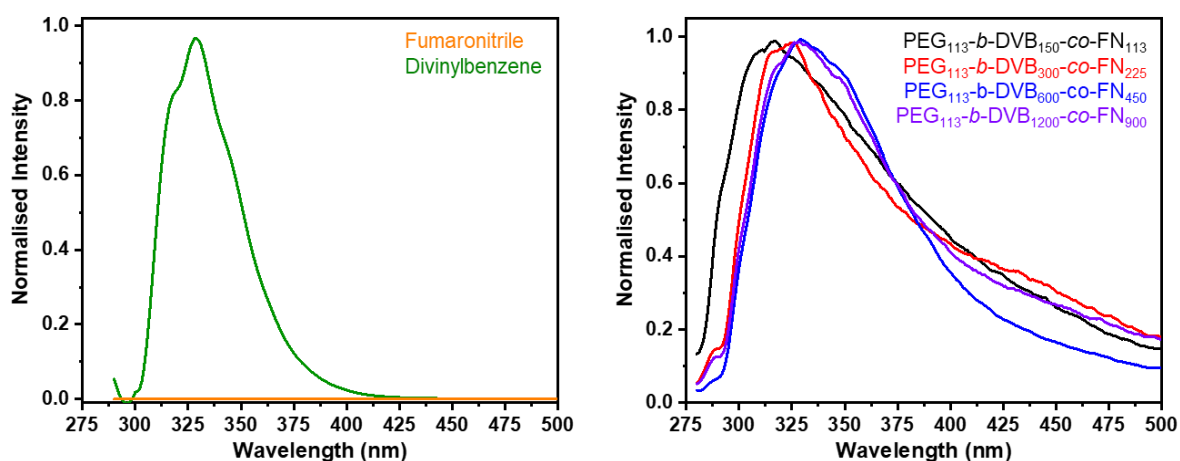


**Figure 3.20** Normalised fluorescence emission spectra obtained for (a) fumaronitrile and divinylbenzene monomers and (b) PEG<sub>113</sub>-*b*-DVB<sub>150</sub>-*co*-FN<sub>113</sub>, PEG<sub>113</sub>-*b*-DVB<sub>300</sub>-*co*-FN<sub>225</sub>, PEG<sub>113</sub>-*b*-DVB<sub>600</sub>-*co*-FN<sub>450</sub> and PEG<sub>113</sub>-*b*-DVB<sub>1200</sub>-*co*-FN<sub>900</sub> in methanol

The most striking observation from the emission profiles of the monomers is the lack of emission from the fumaronitrile monomer. This is in stark contrast to that of divinylbenzene which shows a broad emission peak centred around ~330 nm. The emission spectrum of the divinylbenzene monomer seems to closely resemble that of the polymer materials which further corroborates the UV-Vis spectrum and hints that the divinylbenzene may be the primary cause for the observed luminescence.

It is hypothesised that the cause of the emission is due to the high concentration of aromatic rings present in the core of the polymer sample which are close enough to interact with one another and give rise to fluorescence emission when irradiated. This is very similar to the behaviour of the divinylbenzene monomer in solution because when in solution the monomer units are known to  $\pi$ - $\pi$  stack and form clusters.<sup>43</sup> This is why the monomer gives such an emission spectra when irradiated by UV light. Given that when DVB is polymerised *via* the RAFT-PISA methodology applied in this thesis the result is a core of aromatic rings not too dissimilar from the  $\pi$ - $\pi$  stacking observed in solution of pure monomer.

### Chapter3. PPDs from FN and DVB

#### 3.12 Varying Crosslinking Monomer

Much of this chapter discusses the synthesis of porous polymeric dispersions based on DVB and FN. However, given that the synthesis is purposefully generic it should be possible to replace DVB with another suitable crosslinking monomer to polymerise alongside FN. This section investigates the effect of swapping crosslinking monomer has on the porosity, morphology and characteristics of the final material.

It has been the overarching aim of this work to design a generic, cheap and versatile synthetic approach towards porous polymers in solution. The work described thus far meets these criteria in that all monomers and solvents used are readily available and cheap, the RAFT-agent is cheap to make on multigram scales and the synthesis itself is quick. Hence, when selecting new monomers to replace DVB with it was imperative that the monomers are cheap and commercially available so as to agree to the initial design principle. Chemically, it is vital for the monomers to polymerise alongside FN and more importantly do so in a controlled manner *via* the CTA. As such, three potential crosslinking monomers were found and purchased from Merck for less than £1 per 1 g. The chosen monomers were; 1,3,5-Triacryloylhexahydro-1,3,5-triazine (THT), ethylene glycol dimethacrylate (EGD) and bis-acrylamide (BAM) (Figure 3.21).

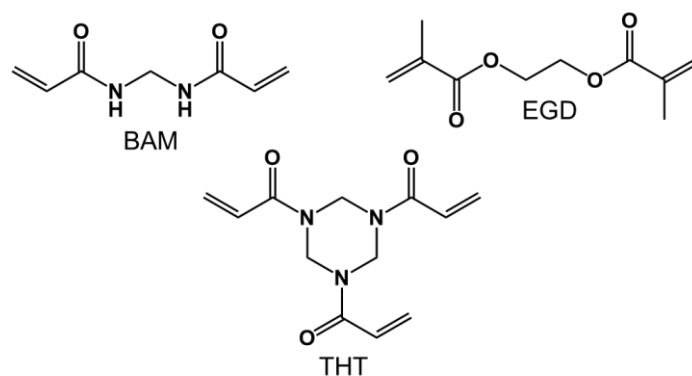


**Figure 3.21** Structures of new crosslinkers

##### 3.12.1 Free Radical Polymerisation

To test if each monomer would polymerise alongside FN insoluble materials were synthesised *via* free radical polymerisation in a method analogous to HCPN-0.75. All samples were synthesised using AIBN as the thermal initiator, carried out in toluene at 80 °C and used the same monomer ratios (0.75:1, FN:Crosslinker). All materials gave white powders in yields ranging between 63 – 93 % after re-precipitation in methanol. The samples were analysed *via* FTIR, elemental analysis, NMR and gas sorption studies to determine monomer incorporation and surface area.

### Chapter3. PPDs from FN and DVB

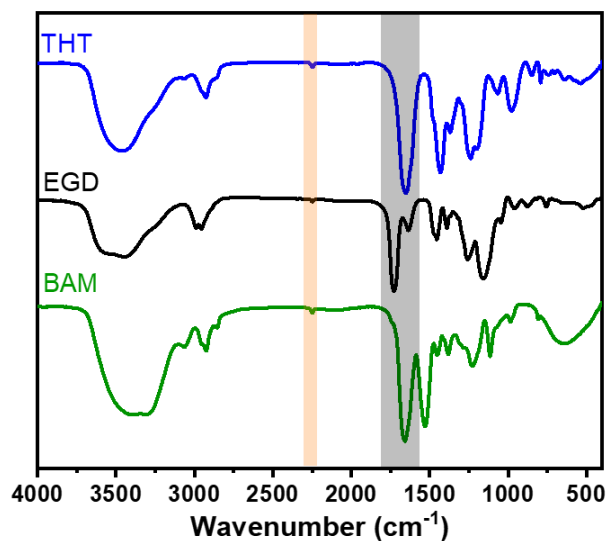


**Figure 3.22** FTIR of insoluble samples

FTIR confirms that both the crosslinking monomer and fumaronitrile has been incorporated into the final product. The signal at  $2250\text{ cm}^{-1}$ , present in all samples, is a result of the inclusion of the nitrile groups from successful polymerisation of fumaronitrile. Signals at between  $1650 - 1730\text{ cm}^{-1}$  are a result of a carbonyl stretching frequency present in all crosslinkers. The THT and BAM monomers are more chemically similar than EGD, the carbonyl is adjacent to a nitrogen atom, and as such, these signals are much closer. The carbonyl signal from the EGD monomer comes at a slightly higher wavenumber, which is due to a slightly different chemical environment. There is also a broad signal between  $2930 - 2950\text{ cm}^{-1}$ , a result of the polymerisation of both monomers forming an alkyl backbone.

**Table 3.7** Elemental analysis for each network synthesised

Sample	% Carbon		% Hydrogen		% Nitrogen	
	Expected	Found	Expected	Found	Expected	Found
FN/BAM	57.55	50.41	4.80	6.34	25.80	15.31
FN/EGD	61.01	56.39	5.13	6.53	15.44	3.78
FN/THT	59.43	53.33	4.54	5.92	25.05	14.96
Pure FN	61.55	-	2.56	-	35.89	-

Elemental analysis of each sample validates the FTIR results and confirms incorporation of both monomers into the final network (Table 3.7). All samples have a % N content which, for the EGD system, shows that FN is present in the final material given that EGD contains no nitrogen. For the other two systems nitrogen is expected in any case given all monomers contain nitrogen. However the values hint that both monomers have been incorporated given that the values are lower for that of a pure FN polymer. In this case, pure FN would be

### Chapter3. PPDs from FN and DVB

expected to have a nitrogen content of around 36 % and none of the samples are close to that value thereby indicating some degree of co-polymerisation has occurred.

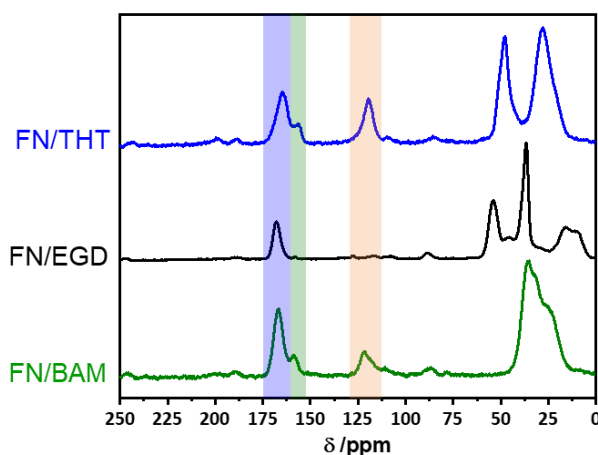


**Figure 3.23**  $^{13}\text{C}$  solid state NMR spectra of (above) FN/THT, (middle) FN/EGD and (below) FN/BAM

Solid-state  $^{13}\text{C}$  CP/MAS NMR was also carried out on the three insoluble samples to determine the success of the reaction (Figure 3.23). The orange highlighted peak at  $\sim 124$  ppm, present in all three samples, is a combination of both the  $\text{C}\equiv\text{N}$  chemical moiety present due to the inclusion of fumaronitrile into the final sample and unreacted vinyl groups present on the crosslinking monomers. The peak at  $\sim 170$  ppm highlighted in blue and present again in all three samples is a result of the carbonyl carbon present in all three crosslinking monomers which shows these monomers have successfully polymerised alongside fumaronitrile. The shoulder at  $\sim 160$  ppm, highlighted in green, is due to the carbonyl carbon adjacent to unreacted vinyl groups. The FN/THT system shows peaks at 25 ppm and 47 ppm which are associated with the  $-\text{CH}-$  and  $-\text{CH}_2-$  carbons of this monomer when polymerised. The two peak at 35 ppm and the shoulder at 25 ppm present in the FN/BAM system are a result of the  $-\text{CH}-$  and  $-\text{CH}_2-$  carbons respectively. Both the FN/THT and FN/BAM materials show small peaks at 85 and 87 ppm respectively are a result of the carbon atoms adjacent to nitrogen atoms. In the FN/EGD system peaks at 12 ppm, 38 ppm and 55 ppm are due to the methyl group,  $-\text{CH}_2-$  alkyl carbons and quaternary carbons present as a result of polymerisation of this monomer respectively. The spectra, alongside the IR and elemental do however highlight that both monomers have been incorporated into the final product to some degree.

### Chapter3. PPDs from FN and DVB

#### 3.12.2 RAFT-PISA of FN and crosslinker

BET surface areas for each sample were determined using the 5 point method over a partial pressure range of between 0.01 – 0.35  $P/P_0$  using nitrogen gas at 77 K. Surface areas were found to range between 54 to 227  $m^2/g$  with the EGD system showing the lowest surface area and THT giving the highest surface area (Appendix, Table A1.1). It is thought that EGD gives rise to the lowest surface area due to the monomer being quite flexible due to the ethylene glycol chain present within the structure. This would also explain why THT, being the most rigid monomer, yields the highest surface area and BAM lies somewhat in-between at 140  $m^2/g$ . All samples are much lower in surface area than HCPN-0.75 (805  $m^2/g$ ), which uses DVB and is the most rigid.

Given that all monomers can be polymerised alongside FN the RAFT-PISA approach, using the macro-CTA was applied to each synthesis in an analogous method to that of FN/DVB. All samples were run at 1 % wt. using KPS as the initiator in a water:ethanol solvent mix and run for 24 hours. The ratio of monomer:CTA used mimicked that which gave the highest surface area for the DVB/FN system (hence CTA:Mon was 1:1050). Both the EGD and THT monomers gave white powders as the product of the reaction in yields of 45 % and 26 % respectively. Unfortunately, the BAM synthesis gave no solid product. This may be due to this monomer being soluble in the solvent system meaning there is no drive towards self-assembly. Another reason could be due to the monomer being incompatible with the CTA meaning only fumaronitrile polymerised and BAM remained in solution unreacted.

A combination of FTIR, solid-state  $^{13}C$  NMR and elemental analysis were used to characterise the synthesised materials. The FTIR of the PISA samples look very similar to that of the insoluble analogues as would be expected (Appendix, Figure A3.4). Unfortunately, it is difficult to use FTIR to elude to the incorporation of the PEG-based macro-CTA due to the signals of the material appearing in the same place to the ether stretch ( $\sim 1050\text{ cm}^{-1}$ ). In the EGD sample, the monomer itself has ether linkages meaning this signal is present in the initial sample. Whereas in the THT sample there is a signal in the same region as the ether stretch so identifying the ether stretch in this sample is very difficult.

### Chapter3. PPDs from FN and DVB

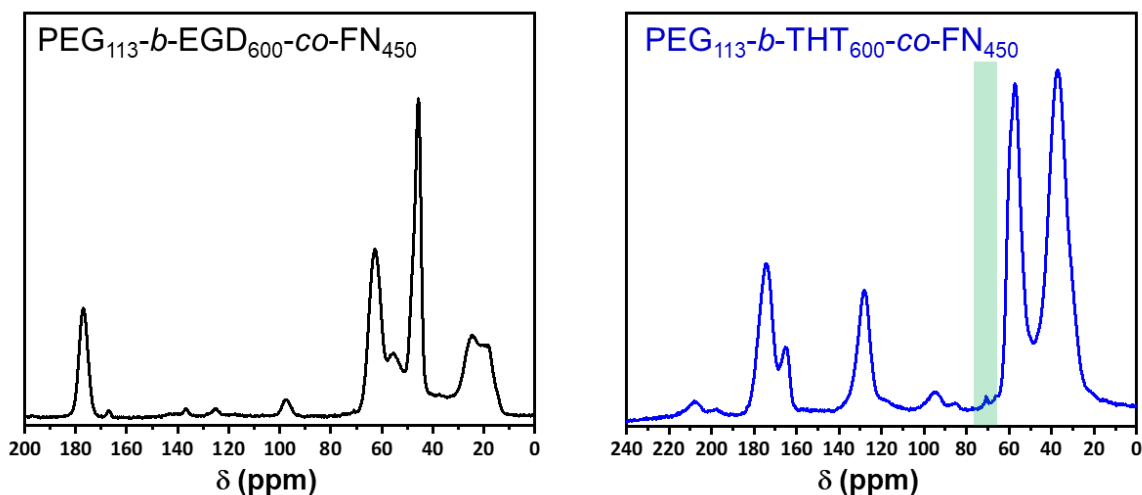


**Figure 3.24**  $^{13}\text{C}$  ssNMR spectra of  $\text{PEG}_{113}\text{-}b\text{-EGD}_{600}\text{-co-FN}_{450}$  and  $\text{PEG}_{113}\text{-}b\text{-THT}_{600}\text{-co-FN}_{450}$

Solid state  $^{13}\text{C}$  NMR gives some qualitative insight into the sample composition (Figure 3.24). The spectra appear to be very similar in appearance to that of the insoluble samples as shown in Figure 3.23 hence the same peak labelling is applied here as is shown in those spectra. The key difference in Figure 3.24 is that the PEG-*b*-THT-co-FN system now has a peak at  $\sim 70$  ppm which is attributed to the presence of the long PEG chains due to the incorporation of the CTA into the final material. This peak was previously not present in the insoluble version of this material. Unfortunately, due to the EGD monomer containing a PEG chain within its structure it is not possible to accurately know if this peak is a result of the CTA being incorporated into the final product or the peak being an artefact of the monomer itself or both.

**Table 3.8** Elemental analysis results of both samples synthesised *via* RAFT-PISA approach

Sample	% Carbon		% Hydrogen		% Nitrogen		% Sulfur	
	Expected	Found	Expected	Found	Expected	Found	Expected	Found
EGD/FN	59.21	58.06	5.69	6.77	8.35	3.32	0.07	0*
THT/FN	61.13	53.53	5.72	6.66	16.89	15.61	0.06	0*

\* LoD for sulfur analysis is 0.3 %

Elemental analysis provides further insight into the success of the polymerisation (Table 3.8). The presence of nitrogen in the EGD sample confirms that the FN has been co-polymerised alongside EGD though the lower than expected value may indicate it has done so to a lesser extent than expected. The THT sample seems to be in much closer agreement meaning that these two monomers may polymerise at similar rates. The higher than expected carbon and hydrogen values would also corroborate a larger proportion of crosslinking monomer being incorporated than the FN. Expected sulphur values are very low due to the large DPs which were targeted and as such no sulphur was detected owed to the LoD being  $< 0.3$  %.

### Chapter3. PPDs from FN and DVB

Both samples were investigated through nitrogen gas sorption isotherms at 77 K to determine the surface area and porosity present within each sample (Figure 3.25). It was found that the EGD sample displayed a type IV(b) isotherm, which is indicative of a mesoporous material. Pore size analysis confirms the presence of mesopores within the sample with pore widths predominantly ranging from 2 – 10 nm. The THT sample quite conversely was found to uptake little to no nitrogen gas and was considered to be essentially non-porous. The BET surface area of both materials, calculated over a relative pressure region of 0.01 – 0.15  $P/P_0$  was found to be 210  $m^2/g$  and 4  $m^2/g$  for the EGD and THT samples respectively.

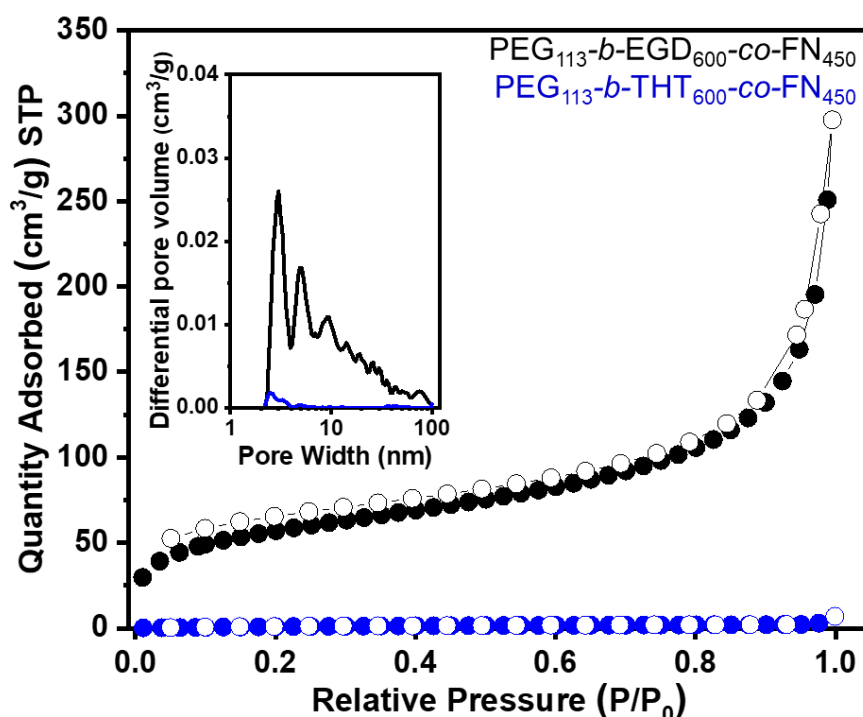


**Figure 3.25** Nitrogen gas sorption isotherms of  $PEG_{113}\text{-}b\text{-EGD}_{600}\text{-}co\text{-FN}_{450}$  and  $PEG_{113}\text{-}b\text{-THT}_{600}\text{-}co\text{-FN}_{450}$ . Inset shows the pore size distribution

#### 3.12.3 Solution-Phase Characterisation

Much like the DVB/FN materials, these samples were found to disperse in different solvents and as such could be characterised using solution-phase techniques. The white powders were mixed with methanol (0.1 mg/mL) and sonicated for 30 minutes to form a stable dispersion, before being analysed *via* DLS, UV-Vis and fluorescence spectroscopy. Both samples form a stable dispersion upon sonication in MeOH which shown no signs of settling out of solution after 24 hours (Figure 3.26). Due to the good solution stability, DLS was recoded for both of these samples in methanol.

### Chapter3. PPDs from FN and DVB

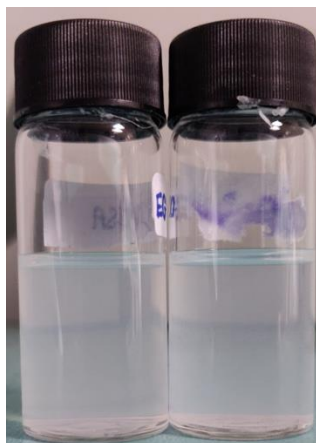


**Figure 3.26** (left) PEG<sub>113</sub>-*b*-EGD<sub>600</sub>-*co*-FN<sub>450</sub> and (right) PEG<sub>113</sub>-*b*-THT<sub>600</sub>-*co*-FN<sub>450</sub> samples after sonication for 30 mins and then being left undisturbed for 24 hours

Dynamic light scattering was carried out on both samples for 30 minutes and 3 hours in methanol solvent using samples at a concentration of 0.1 mg/mL (Figure 3.27). Much like in the FN/DVB systems the hydrodynamic radius of the particles in solution were found to be larger than those measured after 30 minutes. PEG<sub>113</sub>-*b*-EGD<sub>600</sub>-*co*-FN<sub>450</sub> was found to be 425 nm in size with PEG<sub>113</sub>-*b*-THT<sub>600</sub>-*co*-FN<sub>450</sub> being 195 nm. After an extended period of sonication (3 hours) the hydrodynamic radius of both samples were found to reduce in size, being measured as 282 nm and 100 nm for PEG<sub>113</sub>-*b*-EGD<sub>600</sub>-*co*-FN<sub>450</sub> and PEG<sub>113</sub>-*b*-THT<sub>600</sub>-*co*-FN<sub>450</sub> respectively. This lowering in size after extended sonication is indicative of aggregation within the sample and the further sonication is able to break these aggregates up. Indeed, TEM imaging (appendix, Figure A3.5) of the PEG<sub>113</sub>-*b*-EGD<sub>600</sub>-*co*-FN<sub>450</sub> system confirms that the sample has an aggregated morphology similar to that observed when using DVB as the crosslinker. This is perhaps to be expected given that the synthesis remained the same and the DVB was merely exchanged for another crosslinking monomer.

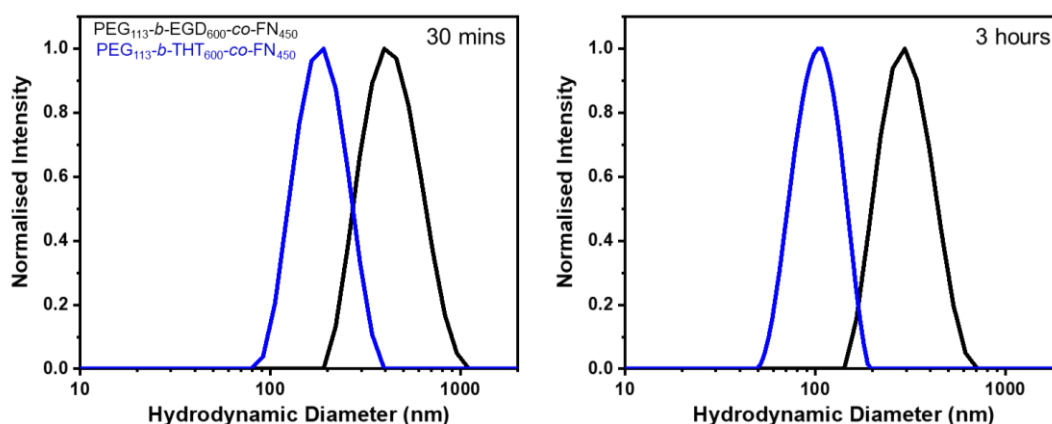


**Figure 3.27** DLS of PEG<sub>113</sub>-*b*-EGD<sub>600</sub>-*co*-FN<sub>450</sub> and PEG<sub>113</sub>-*b*-THT<sub>600</sub>-*co*-FN<sub>450</sub> after sonication for (left) 30 minutes and (right) 3 hours

### Chapter3. PPDs from FN and DVB

The UV-Vis and fluorescence emission spectra of each sample was recorded in methanol and compared against the DVB/FN samples. Previously, the broad peak ranging between 220 – 300 nm in the UV-Vis of the FN/DVB samples was attributed to the presence of the aromatic rings. Therefore, both the EGD and THT samples should not have a peak in this region owing to the fact that there are no aromatic rings present within these samples. A UV-Vis spectrum for each sample was recoded and indeed confirmed that this peak was not present in either of these samples (Figure 3.27). The only peak present in these samples is once centred at around 205 nm. Given that this peak is in the same place as that of the FN monomer (Figure 3.19) and is present in both sample this peak is most likely a result of the incorporation of the FN monomer.

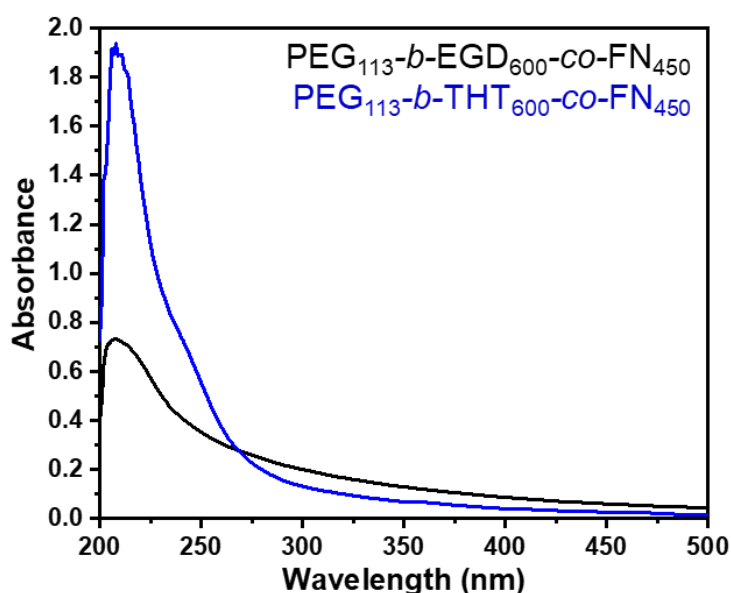


**Figure 3.27** UV-Vis spectra of PEG<sub>113</sub>-*b*-EGD<sub>600</sub>-co-FN<sub>450</sub> and PEG<sub>113</sub>-*b*-THT<sub>600</sub>-co-FN<sub>450</sub>

The FN/DVB samples all displayed fluorescence emission when excited at the wavelength identified using in the UV-Vis spectrum. The luminescence of these samples was attributed to the excitation and relaxation of the aromatic rings present within these samples. Therefore, it is expected that the EGD and THT samples should show no luminescence when excited. Indeed, this is found to be the case and when a dispersion of each material is excited at 205 nm there is no observable fluorescence emanating from the sample (Figure 3.28).

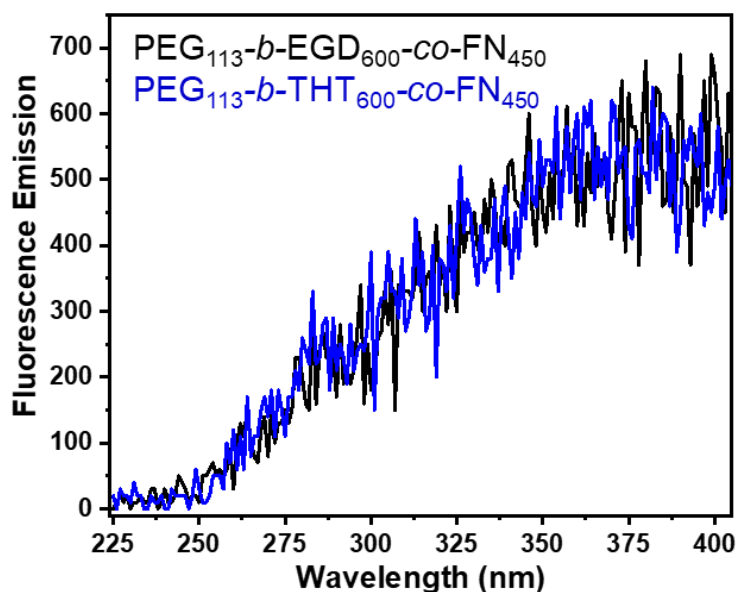


**Figure 3.28** Fluorescence emission spectra of PEG<sub>113</sub>-*b*-EGD<sub>600</sub>-co-FN<sub>450</sub> and PEG<sub>113</sub>-*b*-THT<sub>600</sub>-co-FN<sub>450</sub> (blue) ( $\lambda_{\text{ex}} = 205$  nm)

### 3.13 Conclusion

A novel synthetic approach was applied towards the synthesis of solution-dispersible microporous materials synthesised through polymerising crosslinkable monomers *via* controlled radical polymerisation using a hydrophilic macro-CTA. Fine-tuning of this synthetic approach resulted in a series of microporous materials in which the surface area could be tuned based on the DP of the core-forming block. Upon sonication these materials formed solution stable dispersions which showed little sign of solution instability even after one week. A combination of SAXS and TEM imaging revealed that these samples adopt an aggregated morphology which is most likely the result of the polymerisation of DVB ensuring that a degree of crosslinking between particles occurs before the onset of microphase separation. The versatility of this approach was demonstrated by swapping the DVB monomer out and replacing it with other commercially available and cheap crosslinking monomers. These materials were lower in surface area yet still resulted in porous and solution-processable materials which again adopt an aggregated morphology.

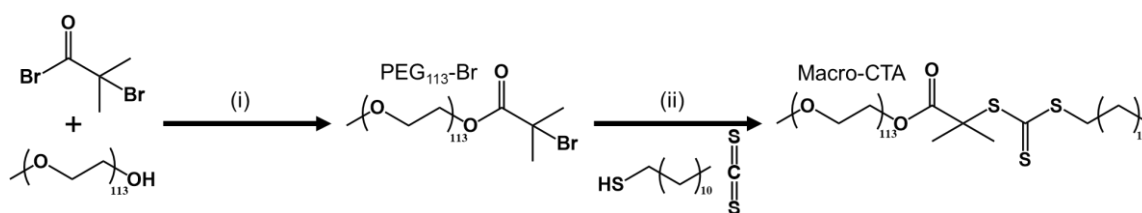
This work reports the first generic and facile approach towards solution-processable microporous materials which is tolerable of many monomers allowing for the design of a range of novel microporous materials. These materials could have interesting solution—phase applications owed to the stability of these samples in solution.

## Chapter3. PPDs from FN and DVB

### 3.14 Experimental

#### 3.14.1 Materials

Poly(ethylene glycol) monomethyl ether (PEG,  $M_n$  5000, PDI 1.09), anhydrous trimethylamine (TEA), 2-bromoisobutyryl bromide, dodecane thiol, potassium phosphate tribasic ( $K_3PO_4$ ), Fumaronitrile (FN, 98 %), 2,2'-Azobis(2- methylpropionitrile) (AIBN, 98 %) and potassium persulfate (> 99.99 %, KPS) were all used as received. Divinylbenzene (DVB, technical grade 80 %) was passed through an alumina column in order to remove the inhibitor before use. N,N'-Methylenebis(acrylamide) (BAM, > 99 %), ethylene glycol dimethacrylate (EGD, 98 %) and 1,3,5-triacrylylhexanhydro-1,3,5-triazine (THT, 98 %) were used as received. All chemicals mentioned were purchased from Sigma-Aldrich. Dry toluene was obtained in a method analogous to the one outlined by Grubbs.<sup>24</sup> Magnesium sulfate and carbon disulphide were purchased from Fisher and used as received. All other chemicals were used without any further purification.



Scheme 3.4 Schematic showing the synthesis of PEG<sub>113</sub>-Br and Macro-CTA. (i) is described in section 3.13.2, (ii) is described in section 3.13.3.

#### 3.14.2 Synthesis of PEG<sub>113</sub>-Br

PEG<sub>113</sub>-Br was prepared in a method similar to that reported by Chen *et al.*<sup>25</sup> Poly(ethylene glycol) monomethyl ether (8 g, 1.6 mmol, 1 eq.) was dissolved in anhydrous toluene (100 mL) in a two-neck round bottom flask. TEA (0.32 mL, 2.3 mmol, 1.4 eq.) was added and the solution was cooled to 0 °C. 2-bromoisobutyryl bromide (0.26 mL, 2.1 mmol, 1.3 eq.) was added dropwise over the course of 1 h before being left to stir overnight at room temperature. The solvent was reduced before being precipitated into an excess of cold diethyl ether (200 mL). The crude product was dried under vacuum, dissolved in water before being extracted with DCM. The organic layers were collected, combined and dried over MgSO<sub>4</sub> before the solvent was removed under reduced pressure to afford the PEG<sub>113</sub>-Br product which was stored in a 5 °C fridge. (Yield = 87%. Found C: 53.78%, H: 9.07%, Expected C: 53.96%, H: 8.97%).

#### 3.14.3 Synthesis of PEG-based macro-chain transfer agent (CTA)

The PEG-based macro-CTA was synthesised using a method adapted from a paper published by O'Reilly and co-workers.<sup>26</sup> Dodecane thiol (0.60 mL, 2.5 mmol, 1 eq.) was added to a stirred

### Chapter3. PPDs from FN and DVB

suspension of  $K_3PO_4$  (0.53 g, 2.5 mmol, 1 eq.) in acetone (50 mL) and stirred for 10 minutes. Carbon disulphide (0.36 mL, 6 mmol, 2.5 eq.) was added to the suspension and left to stir for a further 10 minutes. PEG<sub>113</sub>-Br (10 g, 2 mmol, 0.8 eq.) in acetone (30 mL) was added to the suspension which was left to stir overnight at room temperature. The solvent was removed by rotary evaporation precipitated into an excess of *n*-hexane twice and once into diethyl ether to further purity. The sample was dried in the vacuum oven overnight at 40 °C to afford the RAFT macro-CTA (Yield = 88%. Found C: 54.51%, H: 9.05%, S: 1.84%, Expected C: 54.52%, H: 9.13%, S: 1.80%).

#### 3.14.4 Synthesis of HCPN-0.75

The insoluble porous polymer of FN/DVB was synthesised in an identical method to that reported by Li and co-workers.<sup>2</sup> DVB (0.26 g, 2 mmol, 1 eq.), FN (0.117 g, 1.5 mmol, 0.75 eq.) and toluene (10 mL) were all added to a 2-neck round bottom flask under nitrogen. The flask was heated to 80 °C and polymerisation was initiated through the addition of AIBN (3.8 mg, 0.023 mmol, 0.01 eq.). After 24 h the polymerisation was quenched and the solution poured into methanol to precipitate the polymer. The solid was washed with methanol and Soxhlet extracted with THF for 16 h. The final product was collected and dried under vacuum at 60 °C.

#### 3.14.5 PEG<sub>113</sub>-*b*-DVB<sub>300</sub>-co-FN<sub>225</sub> (RAFT only) *via* RAFT polymerisation

A RAFT-mediated polymerisation route was employed utilising the PEG-based macro. The PEG-based macro CTA (0.13 g, 0.02 mmol, 1 eq.) and FN (0.35 g, 4.5 mmol, 225 eq.) were added to a 2-necked round bottom flask. The flask was evacuated and back-filled with nitrogen 3 times. Toluene (30 mL) and DVB (0.85 mL, 6 mmol, 300 eq.) were added to the flask to create a 5 % wt. solution. The solution was bubbled through with nitrogen gas to ensure the system was devoid of air before heating to 70 °C. Polymerisation was initiated through the addition of AIBN (0.66 mg, 0.004 mmol, 0.2 eq) and held at 70 °C for 24 h. The solid was washed with methanol and tetrahydrofuran (THF) and extracted from THF in Soxhlet apparatus for 16 h. The final product was collected and dried under vacuum at 60 °C.

#### 3.14.5 PEG<sub>113</sub>-*b*-DVB<sub>150</sub>-co-FN<sub>113</sub> *via* RAFT mediated PISA

The PEG-based macro CTA (0.13 g, 0.02 mmol, 1 eq.) and FN (0.175 g, 2.25 mmol, 113 eq.) were added to a 2-necked round bottom flask. The flask was evacuated and back-filled with nitrogen 3 times. Water and ethanol in a 60:40 ratio along with DVB (0.425 ml, 3 mmol, 150 eq.) were added to the flask to create a 1 % wt. solution. The solution was bubbled through with nitrogen gas to ensure the system was devoid of air before heating to 70 °C. Polymerisation was initiated through the addition of potassium persulfate (KPS, 1.08 mg,

### Chapter3. PPDs from FN and DVB

0.004 mmol, 0.2 eq.) and held at 70 °C for 24 h. The product was isolated as a white solid through reprecipitation into diethyl ether before drying *in vacuo* at 40 °C for 16 h.

#### 3.14.6 PEG<sub>113</sub>-*b*-DVB<sub>300</sub>-co-FN<sub>225</sub> via RAFT mediated PISA

The PEG-based macro CTA (0.13 g, 0.02 mmol, 1 eq.) and FN (0.35 g, 4.5 mmol, 225 eq.) were added to a 2-necked round bottom flask. The flask was evacuated and back-filled with nitrogen 3 times. Water and ethanol in a 60:40 ratio along with DVB (0.85 ml, 6 mmol, 300 eq.) were added to the flask to create a 1 % wt. solution. The solution was bubbled through with nitrogen gas to ensure the system was devoid of air before heating to 70 °C. Polymerisation was initiated through the addition of potassium persulfate (KPS, 1.08 mg, 0.004 mmol, 0.2 eq.) and held at 70 °C for 24 h. The product was isolated as a white solid through reprecipitation into diethyl ether before drying *in vacuo* at 40 °C for 16 h.

#### 3.14.7 PEG<sub>113</sub>-*b*-DVB<sub>600</sub>-co-FN<sub>450</sub> via RAFT mediated PISA

The PEG-based macro CTA (0.13 g, 0.02 mmol, 1 eq.) and FN (0.70 g, 9 mmol, 450 eq.) were added to a 2-necked round bottom flask. The flask was evacuated and back-filled with nitrogen 3 times. Water and ethanol in a 60:40 ratio along with DVB (1.70 ml, 12 mmol, 600 eq.) were added to the flask to create a 1 % wt. solution. The solution was bubbled through with nitrogen gas to ensure the system was devoid of air before heating to 70 °C. Polymerisation was initiated through the addition of potassium persulfate (KPS, 1.08 mg, 0.004 mmol, 0.2 eq.) and held at 70 °C for 24 h. The product was isolated as a white solid through reprecipitation into diethyl ether before drying *in vacuo* at 40 °C for 16 h.

#### 3.14.8 PEG<sub>113</sub>-*b*-DVB<sub>1200</sub>-co-FN<sub>900</sub> via RAFT mediated PISA

The PEG-based macro CTA (0.13 g, 0.02 mmol, 1 eq.) and FN (1.40 g, 18 mmol, 900 eq.) were added to a 2-necked round bottom flask. The flask was evacuated and back-filled with nitrogen 3 times. Water and ethanol in a 60:40 ratio along with DVB (3.40 ml, 24 mmol, 1200 eq.) were added to the flask to create a 1 % wt. solution. The solution was bubbled through with nitrogen gas to ensure the system was devoid of air before heating to 70 °C. Polymerisation was initiated through the addition of potassium persulfate (KPS, 1.08 mg, 0.004 mmol, 0.2 eq.) and held at 70 °C for 24 h. The product was isolated as a white solid through reprecipitation into diethyl ether before drying *in vacuo* at 40 °C for 16 h.

#### 3.14.9 Synthesis of insoluble FN/EGD Polymer via Free Radical Polymerisation

In a method analogous to the synthesis of HCPN-0.75; EGD (0.40 g, 2 mmol, 1 eq.), FN (0.117 g, 1.5 mmol, 0.75 eq.) and toluene (10 mL) were all added to a 2-neck round bottom flask under nitrogen. The flask was heated to 80 °C and polymerisation was initiated through the

### Chapter3. PPDs from FN and DVB

addition of AIBN (3.8 mg, 0.023 mmol, 0.01 eq.). After 24 h the polymerisation was quenched and the solution poured into methanol to precipitate the polymer. The solid was washed with methanol and Soxhlet extracted with THF for 16 h. The final product was collected and dried under vacuum at 60 °C.

#### 3.14.10 Synthesis of insoluble FN/THT Polymer *via* Free Radical Polymerisation

In a method analogous to the synthesis of HCPN-0.75; EGD (0.50 g, 2 mmol, 1 eq.), FN (0.117 g, 1.5 mmol, 0.75 eq.) and toluene (10 mL) were all added to a 2-neck round bottom flask under nitrogen. The flask was heated to 80 °C and polymerisation was initiated through the addition of AIBN (3.8 mg, 0.023 mmol, 0.01 eq.). After 24 h the polymerisation was quenched and the solution poured into methanol to precipitate the polymer. The solid was washed with methanol and Soxhlet extracted with THF for 16 h. The final product was collected and dried under vacuum at 60 °C.

#### 3.14.11 Synthesis of PEG<sub>113</sub>-b-EGD<sub>600</sub>-co-FN<sub>450</sub> *via* RAFT mediated PISA

In an identical method to that used to synthesise PEG-*b*-DVB-*co*-FN samples, the PEG-based macro CTA (0.065 g, 0.01 mmol, 1 eq.) and FN (0.35 g, 4.5 mmol, 450 eq.) were added to a 2-necked round bottom flask. The flask was evacuated and back-filled with nitrogen 3 times. Water and ethanol in a 60:40 ratio along with EGD (1.20 g, 6 mmol, 600 eq.) were added to the flask to create a 1 % wt. solution. The solution was bubbled through with nitrogen gas to ensure the system was devoid of air before heating to 70 °C. Polymerisation was initiated through the addition of potassium persulfate (KPS, 1.08 mg, 0.004 mmol, 0.2 eq.) and held at 70 °C for 24 h. The product was isolated as a white solid through reprecipitation into diethyl ether before drying *in vacuo* at 40 °C for 16 h. Yield 45 %

#### 3.14.12 Synthesis of PEG<sub>113</sub>-b-THT<sub>600</sub>-co-FN<sub>450</sub> *via* RAFT mediated PISA

In an identical method to that used to synthesise PEG-*b*-DVB-*co*-FN samples, the PEG-based macro CTA (0.065 g, 0.01 mmol, 1 eq.) and FN (0.35 g, 4.5 mmol, 450 eq.) were added to a 2-necked round bottom flask. The flask was evacuated and back-filled with nitrogen 3 times. Water and ethanol in a 60:40 ratio along with THT (1.50 g, 6 mmol, 600 eq.) were added to the flask to create a 1 % wt. solution. The solution was bubbled through with nitrogen gas to ensure the system was devoid of air before heating to 70 °C. Polymerisation was initiated through the addition of potassium persulfate (KPS, 1.08 mg, 0.004 mmol, 0.2 eq.) and held at 70 °C for 24 h. The product was isolated as a white solid through reprecipitation into diethyl ether before drying *in vacuo* at 40 °C for 16 h. Yield: 26 %

### 3.15 Appendix

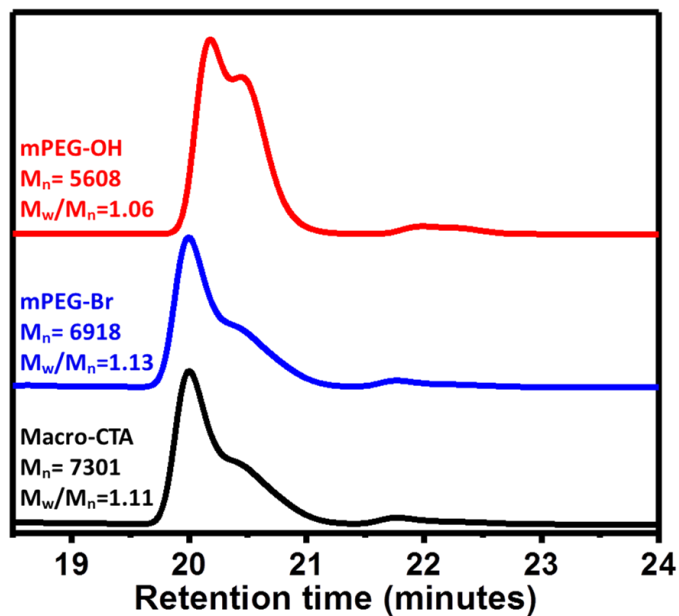


Figure A3.1 GPC chromatograms of **mPEG-OH**, **mPEG-Br** and **PEG-CTA** run against a PS standard detected by refractive index.

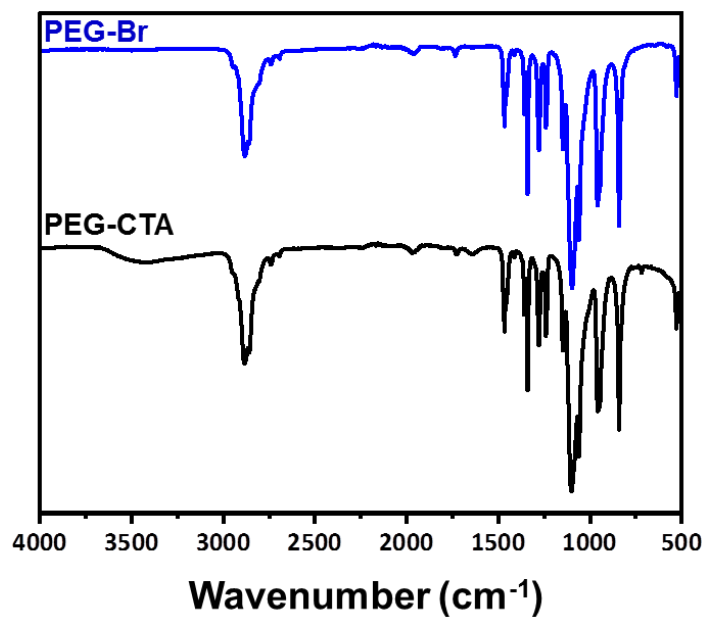


Figure A3.2 FTIR spectra of **PEG-Br** and **PEG-CTA**

Chapter3. PPDs from FN and DVB

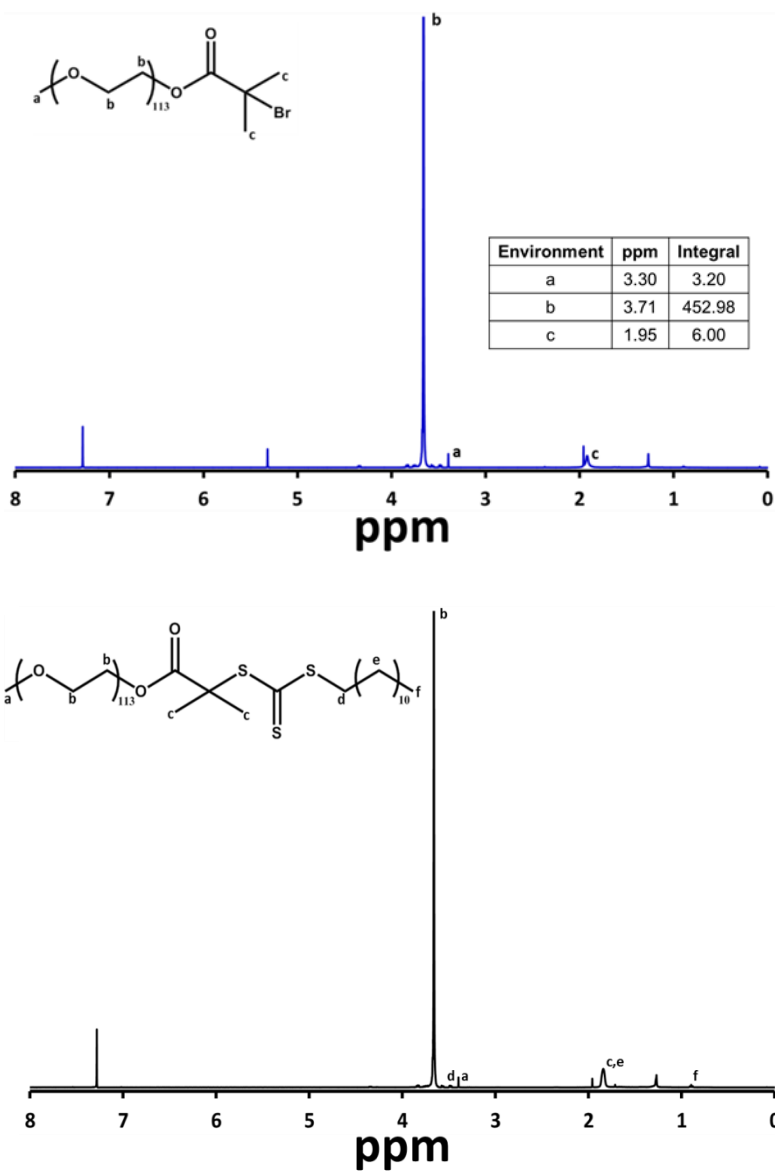


Figure A3.3 <sup>1</sup>H-NMR of PEG-Br (top) and PEG-CTA (bottom) in CDCl<sub>3</sub>

Table A1.1 Yields and surface area of samples synthesised using alternate crosslinkers

Sample	% Yield	S <sub>ABET</sub> (m <sup>2</sup> /g)
FN/BAM	63	140
FN/EGD	93	54
FN/THT	83	227

Chapter3. PPDs from FN and DVB

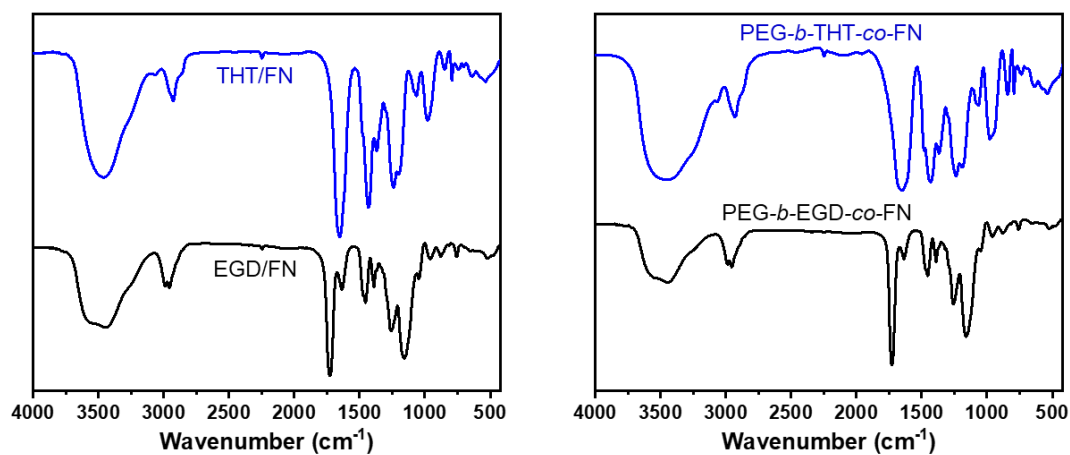


Figure A3.4 FTIR of (left) insoluble analogues and (right) dispersible samples synthesised via the RAFT-PISA route

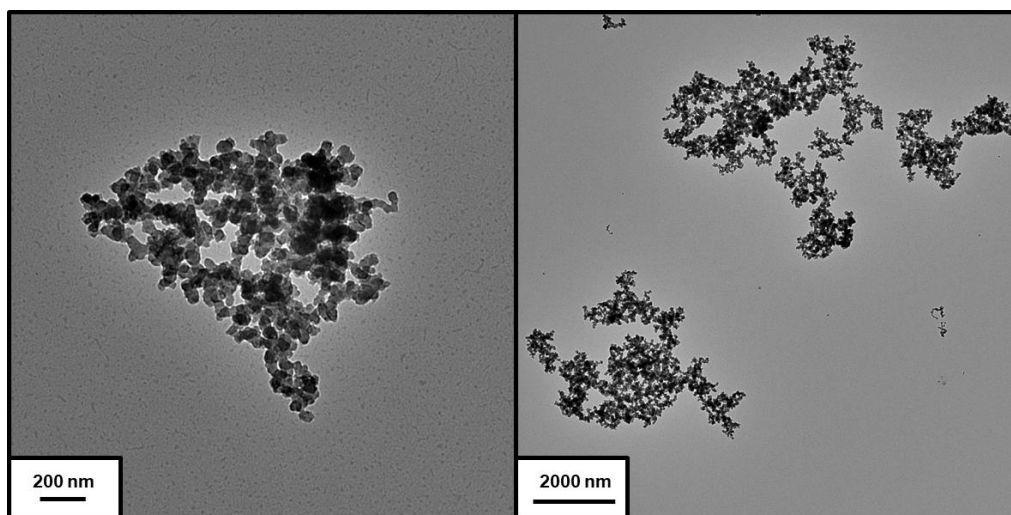


Figure A3.5 TEM images of PEG<sub>113</sub>-*b*-EGD<sub>600</sub>-*co*-FN<sub>450</sub>

### 3.16 References

- 1 H. Gao, L. Ding, W. Li, G. Ma, H. Bai and L. Li, *ACS Macro Lett.*, 2016, **5**, 377–381.
- 2 F. Xie, W. Hu, L. Ding, K. Tian, Z. Wu and L. Li, *Polym. Chem.*, 2017, **8**, 6106–6111.
- 3 H. Xu, J. Wu, B. Zheng, W. Mai, F. Xu, L. Chen, H. Liu, R. Fu, D. Wu and K. Matyjaszewski, *Chem. Commun.*, 2017, **53**, 5294–5297.
- 4 T. N. Gao, T. Wang, W. Wu, Y. Liu, Q. Huo, Z. A. Qiao and S. Dai, *Adv. Mater.*, 2019, **31**, 1806254.
- 5 R. B. Grubbs, *Polym. Rev.*, 2011, **51**, 104–137.
- 6 J. Nicolas, Y. Guillaneuf, D. Bertin, D. Gigmes and B. Charleux, in *Progress in Polymer Science*, 2013, **38**, 63–235.
- 7 C. Boyer, N. A. Corrigan, K. Jung, D. Nguyen, T.-K. Nguyen, N. N. M. Adnan, S. Oliver, S. Shanmugam and J. Yeow, *Chem. Rev.*, 2016, **116**, 1803–1949.
- 8 K. Matyjaszewski, *Macromolecules*, 2012, **45**, 4015–4039.
- 9 J. Chiefari, Y. K. Chong, F. Ercole, J. Krstina, J. Jeffery, T. P. T. Le, R. T. A. Mayadunne, G. F. Meijs, C. L. Moad, G. Moad, E. Rizzardo and S. H. Thang, *Macromolecules*, 1998, **31**, 5559–5562.
- 10 D. J. Keddie, *Chem. Soc. Rev.*, 2014, **43**, 496–505.
- 11 D. J. Keddie, G. Moad, E. Rizzardo and S. H. Thang, *Macromolecules*, 2012, **45**, 5321–5342.
- 12 Y. Mai and A. Eisenberg, *Chem. Soc. Rev.*, 2012, **41**, 5969.
- 13 G. Riess, *Prog. Polym. Sci.*, 2003, **28**, 1107–1170.
- 14 S. B. Darling, *Prog. Polym. Sci.*, 2007, **32**, 1152–1204.
- 15 S. L. Canning, G. N. Smith and S. P. Armes, *Macromolecules*, 2016, **49**, 1985–2001.
- 16 X. Wang and Z. An, *Macromol. Rapid Commun.*, 2019, **40**, 1800325.
- 17 C. Gao, H. Zhou, Y. Qu, W. Wang, H. Khan and W. Zhang, *Macromolecules*, 2016, **49**, 3789–3798.
- 18 Y. Y. Won, H. Ted Davis and F. S. Bates, *Science*, 1999, **283**, 960–963.
- 19 W.-M. Wan, X.-L. Sun and C.-Y. Pan, *Macromolecules*, 2009, **42**, 4950–4952.
- 20 Y. Pei and A. B. Lowe, *Polym. Chem.*, 2014, **5**, 2342–2351.
- 21 B. Charleux, G. Delaittre, J. Rieger and F. D’Agosto, *Macromolecules*, 2012, **45**, 6753–6765.
- 22 G. Wang, M. Schmitt, Z. Wang, B. Lee, X. Pan, L. Fu, J. Yan, S. Li, G. Xie, M. R. Bockstaller and K. Matyjaszewski, *Macromolecules*, 2016, **49**, 8605–8615.
- 23 B. Karagoz, L. Esser, H. T. Duong, J. S. Basuki, C. Boyer and T. P. Davis, *Polym.*

### Chapter3. PPDs from FN and DVB

- Chem.*, 2014, **5**, 350–355.
- 24 A. B. Pangborn, M. A. Giardello, R. H. Grubbs, R. K. Rosen and F. J. Timmers, *Organometallics*, 1996, **15**, 1518–1520.
  - 25 J. Chen, M. Liu, H. Gong, Y. Huang and C. Chen, *J. Phys. Chem. B*, 2011, **115**, 14947–55.
  - 26 J. Skey and R. K. O'Reilly, *Chem. Commun.*, 2008, 4183–4185.
  - 27 E. R. Jones, M. Semsarilar, P. Wyman, M. Boerakker and S. P. Armes, *Polym. Chem.*, 2016, **7**, 851–859.
  - 28 Y. Xu, T. Wang, Z. He, M. Zhou, W. Yu, B. Shi and K. Huang, *Polymer*, 2018, **151**, 92–100.
  - 29 A. M. James, M. J. Derry, J. S. Train and R. Dawson, *Polym. Chem.*, 2019, **10**, 3879–3886.
  - 30 Y. Yang, B. Tan and C. D. Wood, *J. Mater. Chem. A*, 2016, **4**, 15072–15080.
  - 31 G. Cheng, T. Hasell, A. Trewin, D. J. Adams and A. I. Cooper, *Angew. Chemie Int. Ed.*, 2012, **51**, 12727–12731.
  - 32 P. Pallavi, S. Bandyopadhyay, J. Louis, A. Deshmukh and A. Patra, *Chem. Commun.*, 2017, **53**, 1257–1260.
  - 33 X. Wu, H. Li, B. Xu, H. Tong and L. Wang, *Polym. Chem.*, 2014, **5**, 4521–4525.
  - 34 S. Bandyopadhyay, S. Kundu, A. Giri and A. Patra, *Chem. Commun.*, 2018, **54**, 9123–9126.
  - 35 Y. Yang, L. Feng, J. Ren, Y. Liu, S. Jin, L. Su, C. Wood and B. Tan, *Macromol. Rapid Commun.*, 2018, **39**, 1800441.
  - 36 W. Mai, B. Sun, L. Chen, F. Xu, H. Liu, Y. Liang, R. Fu, D. Wu and K. Matyjaszewski, *J. Am. Chem. Soc.*, 2015, **137**, 13256–13259.
  - 37 N. P. Truong, M. V. Dussert, M. R. Whittaker, J. F. Quinn and T. P. Davis, *Polym. Chem.*, 2015, **6**, 3865–3874.
  - 38 N. J. Warren and S. P. Armes, *J. Am. Chem. Soc.*, 2014, 136, 10174–10185.
  - 39 D. J. Kinning and E. L. Thomas, *Macromolecules*, 1984, **17**, 1712–1718.
  - 40 C. Wilson, M. Main, N. Cooper, M. E. Briggs, A. I. Cooper and D. Adams, *Polym. Chem.*, 2017, **8**, 1914–1922.
  - 41 R. T. Woodward, L. A. Stevens, R. Dawson, M. Vijayaraghavan, T. Hasell, I. P. Silverwood, A. V. Ewing, T. Ratvijitvech, J. D. Exley, S. Y. Chong, F. Blanc, D. J. Adams, S. G. Kazarian, C. E. Snape, T. C. Drage and A. I. Cooper, *J. Am. Chem. Soc.*, 2014, **136**, 9028–9035.
  - 42 M. P. Tsyurupa and V. A. Davankov, *React. Funct. Polym.*, 2002, **53**, 193–203.
  - 43 R. Zhao and R. Q. Zhang, *Phys. Chem. Chem. Phys.*, 2016, **18**, 25452–25457.

# Chapter 4 - Applications of PEG-*b*-DVB-*co*-FN Porous Polymeric Dispersions

Sections of this chapter have previously been published in:

A. M. James, M. J. Derry, J. S. Train and R. Dawson, *Polym. Chem.*, 2019, **10**, 3879–3886.

## Chapter 4. Applications of PEG-*b*-DVB-co-FN

### 4.1 Chapter Aims

In this chapter, potential applications for the dispersible porous polymer materials synthesised in Chapter 3 are explored and discussed.

In the first section of this chapter, the dispersible porous polymer materials are applied towards the chemosensing of harmful nitroaromatic compounds in solution. The combination of a porous core alongside solution stability makes these materials ideal candidates for the uptake of organic compounds from solution. Furthermore, the fluorescent properties of the porous polymer particles arising from the electron rich core can be exploited to form a donor-acceptor interaction with the electron-poor nitroaromatic compounds which quenches the fluorescence of the dispersion thereby acting as a solution phase chemosensor.

In the second section, the uptake of gas by the materials is explored for a range of different gases (N<sub>2</sub>, CH<sub>4</sub> and CO<sub>2</sub> in order to determine the selectivity and capacity. Further comparison between samples will reveal if enhancing the size of the core results in increased uptake and whether this uptake is selective towards one gas.

## Chapter 4. Applications of PEG-*b*-DVB-co-FN

### 4.2 Chemosensing of Nitroaromatics

The core of each material is comprised of electron rich aromatic rings which were shown to be able to interact with one another and give rise to fluorescence emission under UV irradiation. Given that the core of the material is porous, hydrophobic and electron rich it is possible to encapsulate small organic molecules which are also hydrophobic. Should these molecules be electron deficient then they may be able to interact with the electron rich core and affect the luminescent properties.

Nitroaromatic compounds such as picric acid (PA) and trinitrotoluene (TNT) are small organic molecules which are well known for their explosive nature as well as being a hazard to the environment.<sup>1</sup> As well as being a threat to national security, owing to their explosive potential, nitroaromatic compounds are also a major health issue due to their toxicity, mutagenesis and carcinogenesis. Their abundance in the environment is mainly due to their excessive use as pesticides but they also find their uses in the chemical industry, often produced during different chemical syntheses.<sup>2</sup> Therefore there is a need to be able to detect these contaminants in the natural environment and then remove them to mitigate damage to natural life.

Nitroaromatic compounds are electron deficient due to the presence of one or more nitro groups (-NO<sub>2</sub>) substituted on the aromatic ring and are therefore electron acceptors. There are a number of reports on the use of porous polymers (mostly COFs<sup>3,4</sup> or CMPs<sup>5,6</sup>) which contain electron rich units to detect nitroaromatic compounds in solution *via* a fluorescence quenching mechanism. The interaction of these porous materials with the nitroaromatic compound is able to quench the fluorescence of the material resulting in an observable change. Given that the materials published in this work are all fluorescent and electron rich it seems conceivable that they may also be able to detect these compounds in solution. Hence, the detection capabilities of the materials towards nitroaromatic compounds were investigated.

## Chapter 4. Applications of PEG-*b*-DVB-*co*-FN

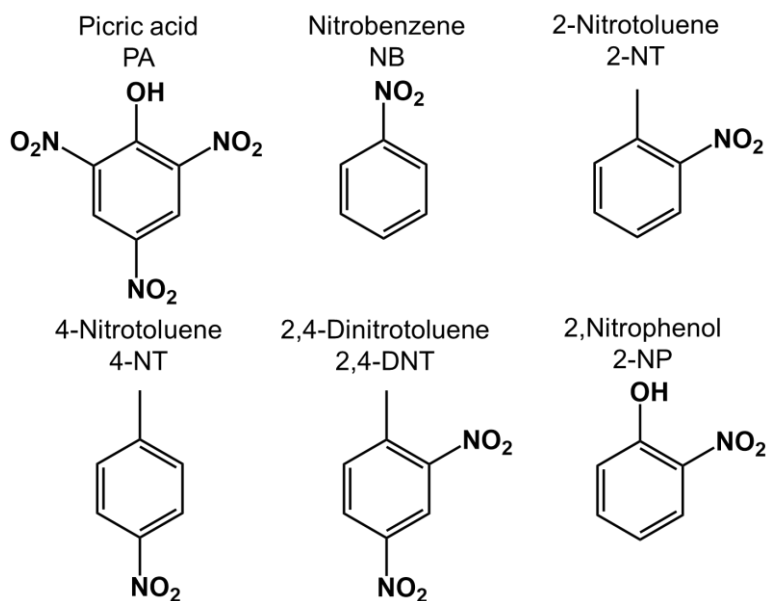


**Figure 4.1** Structures of nitroaromatic compounds investigated

Initially, the nitroaromatic compounds (Figure 4.1), picric acid (PA), nitrobenzene (NB), 2-nitrotoluene (2-NT), 4-nitrotoluene (4-NT), 2,4-dinitrotoluene (2,4-DNT) and 2-nitrophenol (2-NP) were all tested to determine if and how efficiently they are able to quench the fluorescence of each polymer dispersion (see experimental section 4.4 for details). PEG<sub>113</sub>-*b*-DVB<sub>300</sub>-*co*-FN<sub>225</sub> was used as a representative sample given that it has a surface area which sits in the middle of the series and it was shown by UV-Vis to be one of the most solvent stable samples. The quenching efficiency was calculated using the equation:

$$\% \text{ Fluorescence Quenching} = \frac{(I_0 - I)}{I_0} \times 100$$

where  $I_0$  is the emission of the polymer without any quencher present and  $I$  is emission after addition of quencher.



**Figure 4.2** Observed fluorescence quenching of a dispersion of PEG<sub>113</sub>-*b*-DVB<sub>300</sub>-*co*-FN<sub>225</sub> when exposed to 38 ppm of picric acid in MeOH

## Chapter 4. Applications of PEG-*b*-DVB-co-FN

All nitroaromatic compounds tested were able to quench the fluorescence of the sample upon a small addition of each nitroaromatic to the polymer dispersion (Figure 4.2). It was found that NB, PA and 2-NT were the most effective at quenching the emission with < 40 ppm being required to fully quench the emission. The general trend of quenching efficiency follows the order: NB > PA > 2-NT > 4-NT > 2-NP > 2,4-DNT (Figure 4.3). It may be expected that, given the quenching mechanism is a result of the interaction between an electron rich core and an electron deficient compounds, the efficiency should relate to the number of substitutions on the benzene ring. However, given that the polymer samples are dispersed, there are a number of other factors to consider such as the size of the pores and how easy it is for the nitroaromatics to diffuse into the pores. This diffusion could also be affected by the number of nitroaromatic groups substituted onto the ring which may alter the chemical properties of the compound meaning it may be more energetically favourable to remain in solution rather than diffuse into the core of the sample. For example, adding more nitro groups may lead to repulsion when confined in the core of the porous sample which would lead to leaching of the analyte back into solution. What is clear though is that the polymer sample demonstrates a clear quenching effect as a direct result of the interaction between itself and the nitroaromatic compounds.

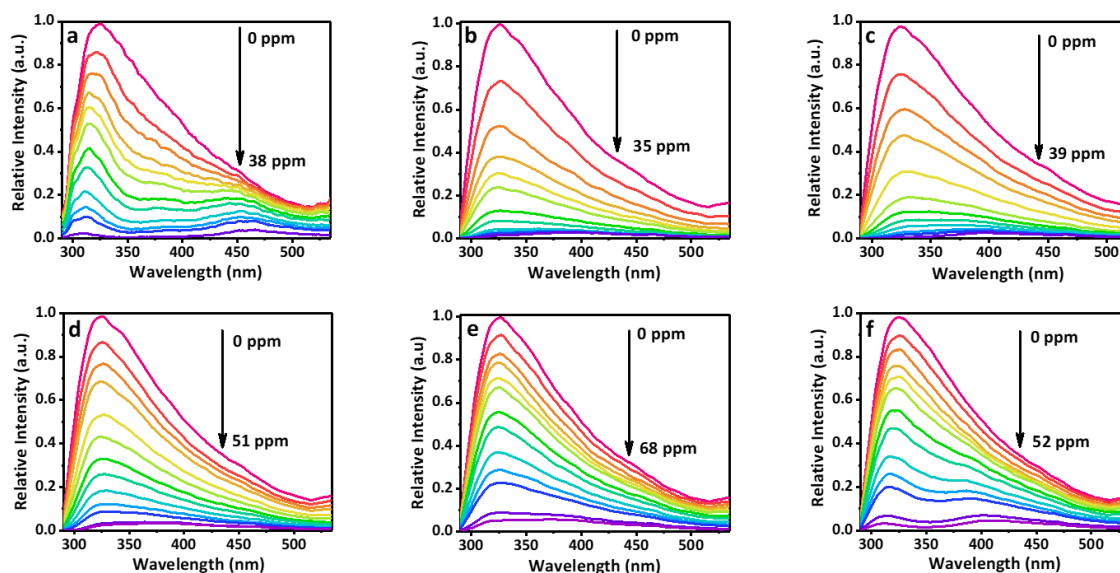


**Figure 4.3** Fluorescence emission spectra obtained for PEG<sub>113</sub>-*b*-DVB<sub>300</sub>-co-FN<sub>225</sub> upon addition of; (a) PA, (b) NB, (c) 2-NT, (d) 4-NT, (e) 2,4-DNT and (f) 2-NP in methanol

As well as being sensitive any good sensor also needs to show preferential selectivity for that which it is detecting over other compounds present in solution. Therefore, to gain insight into the selectivity of the sample five chemically similar species were tested on PEG<sub>113</sub>-*b*-DVB<sub>300</sub>-co-FN<sub>225</sub> to see whether they would elicit the same fluorescent quenching

#### Chapter 4. Applications of PEG-*b*-DVB-co-FN

effect. The compounds used for the test were benzene (Ph), chlorobenzene (CPh), toluene (MePh), nitromethane (NO<sub>2</sub>Me) and dimethylformamide (DMF). It was found that none of the five chemically similar analytes were able to significantly quench the fluorescence of the sample to the same degree as the nitroaromatics. A quenching efficiency of 23 % was the best reported for nitromethane upon addition of 200 ppm of this analyte yet was still far below that of > 99 % reported for all the nitroaromatics studied (Figure 4.4). This proves that there is an element of selectivity in the nature of the quenching given that only the nitroaromatic compounds were able to fully quench the emission.

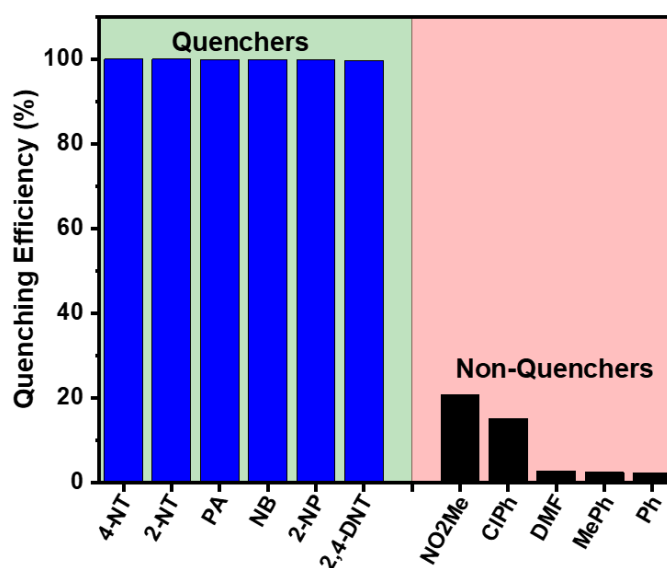


**Figure 4.4** Quenching efficiencies of PEG<sub>113</sub>-*b*-DVB<sub>300</sub>-co-FN<sub>225</sub> when using nitroaromatic compounds and chemically similar compounds upon addition of 200 ppm of analyte to 2.5 mg of polymer sample

Of all the nitroaromatics studied, the most dangerous to human health and of most concern to national security is picric acid. Therefore, all the samples synthesised were exposed to picric acid and their quenching efficiencies were determined (Figure 4.5) The addition of 38 ppm of picric acid to 2.5 mg of polymer dispersion sees the fluorescence emission of each sample quenched by over 99 %, once more highlighting the remarkable sensitivity of these materials towards this contaminant.

## Chapter 4. Applications of PEG-*b*-DVB-*co*-FN

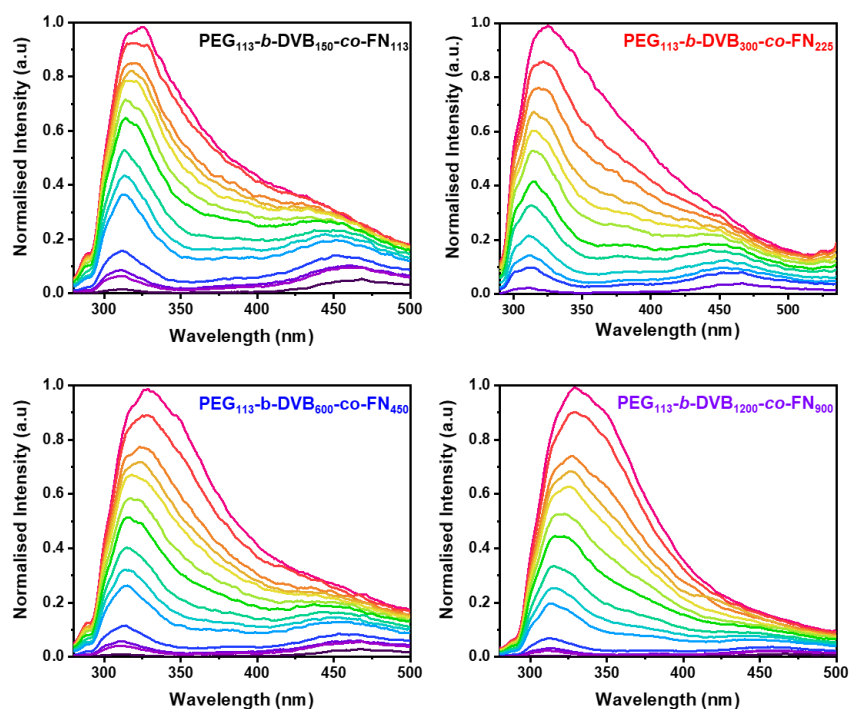


**Figure 4.5** Observed fluorescence quenching of each sample when exposed to 38 ppm of picric acid in methanol

To further probe the sensitivity of each sample to picric acid the limit of detection for each polymer dispersion was calculated by exposing the sample to increasing amounts of a picric acid solution. The normalised emission maxima were plotted against picric acid concentration and the limit of detection (LoD) was calculated using the following equation:

$$LoD = 3 \times \sigma / K$$

where  $\sigma$  is the standard deviation and  $K$  is the slope of the graph.

The linear plots obtained from carrying out the above-described procedure are shown in Figure 4.6 with each sample giving a straight line, as would be expected for this experiment.

## Chapter 4. Applications of PEG-*b*-DVB-*co*-FN

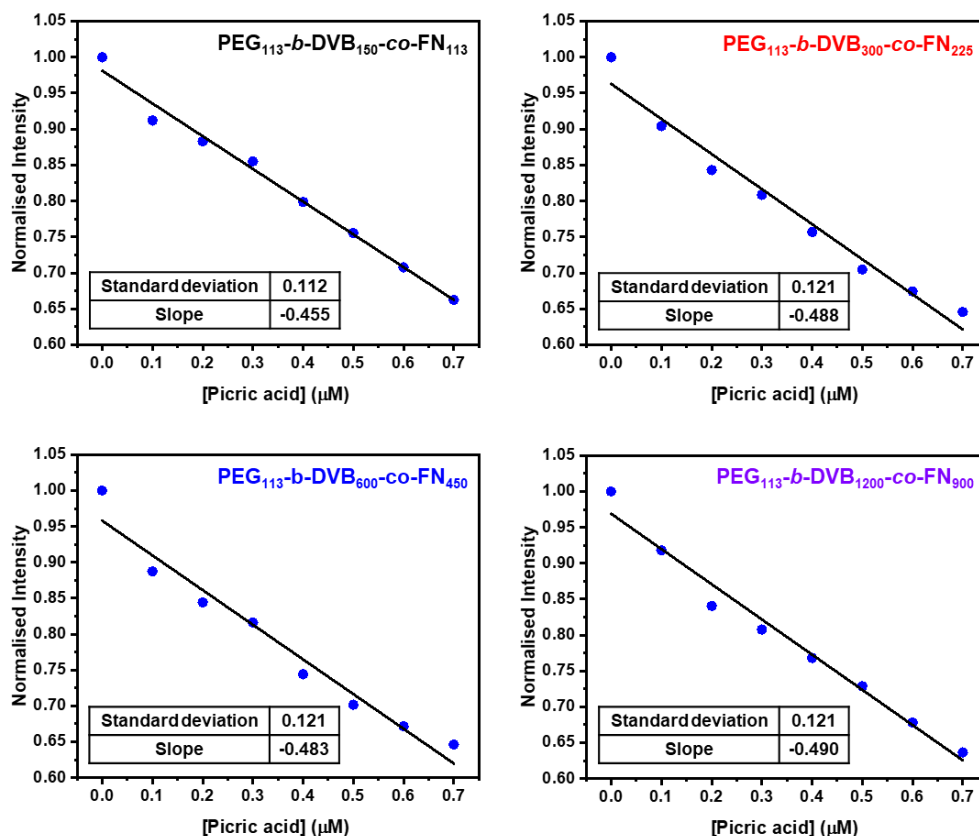


**Figure 4.6** Plots of picric acid concentration vs normalised intensity used to calculate the limit of detection for each polymer sample

**Table 4.1** LoD values for each sample studied in this work

Sample	LoD (ppb)
PEG <sub>113</sub> - <i>b</i> -DVB <sub>150</sub> - <i>co</i> -FN <sub>113</sub>	170
PEG <sub>113</sub> - <i>b</i> -DVB <sub>300</sub> - <i>co</i> -FN <sub>225</sub>	169
PEG <sub>113</sub> - <i>b</i> -DVB <sub>600</sub> - <i>co</i> -FN <sub>450</sub>	172
PEG <sub>113</sub> - <i>b</i> -DVB <sub>1200</sub> - <i>co</i> -FN <sub>900</sub>	170

All samples display very similar LoD values at around 170 ppb and are within error of one another (Table 4.1). It may be expected that, due to the quenching mechanism being the result of the interaction between the picric acid and electron rich core, samples with larger core DPs would give better detection limits. But it may be the case that the limit of detection is more driven by diffusion into the core and due to all samples having similar pore sizes and similar solution stability, it is perhaps unsurprising that we see little variance in these values. The limit of detection values reported here are comparable to other porous polymers reported to detect nitroaromatic compounds in solution.<sup>7,8</sup>

#### Chapter 4. Applications of PEG-*b*-DVB-co-FN

It has been shown that the porous materials reported in Chapter 3 can be applied towards the chemosensing of environmentally harmful and potentially explosive materials in solution through exploiting the porosity and solution stability of the material. The materials were found to be selective towards only nitroaromatic compounds and when other chemically similar compounds were tested they were not able to quench the fluorescence emission of the material. The ability to detect picric acid is particularly useful given its explosive nature and widespread use in agricultural pesticides. Therefore the LoD for each porous polymer was studied using this compounds. It was found that the LoD for each material was around 170 ppb which is comparable to that of other porous materials. Overall this study highlights the potential new applications to which these solution stable porous materials can be applied.

## Chapter 4. Applications of PEG-*b*-DVB-co-FN

### 4.3 Gas Uptake and Selectivity

The ability to uptake gas is a feature that has been extensively explored for many microporous organic polymer materials over the last decade and has been accelerated somewhat due to the current climate crisis the world is facing. The ability to capture CO<sub>2</sub>, specifically from anthropogenic sources is regarded as one of the best medium term solutions to mitigate climate change before ultimately moving away from non-renewable and carbon emitting energy sources. As such, there have been many reports on the use of MOPs for applications in the selective capture of CO<sub>2</sub>.<sup>9-13</sup>

Microporous polymers have numerous advantages over other porous materials such as MOFs and zeolites when being applied towards the uptake of different gases. These include; a low density framework which allows for high uptakes per gram of material to be achieved, ease of functionality which allows for selective uptake towards certain gases and high thermal and chemical stability which allows for applications in real-world systems. Therefore, the FN/DVB materials synthesised in chapter 3 were tested for their uptake potential of CO<sub>2</sub>, CH<sub>4</sub> and N<sub>2</sub> to determine the capacity and selectivity of these gases. Of particular interest in this work is to examine whether the increase of porosity by targeting larger cores gives rise to enhanced uptake capabilities and whether this uptake is selective. The effect of the PEG chains on the total uptake will also be studied given that they contain heteroatoms and, when in the solid state, may pack around the core of the material and give rise to a mixed-porous system similar to work reported by Matyjaszewski *et al.*<sup>14</sup> In this work it is theorised that the “dipole–quadrupole interaction between the CO<sub>2</sub>-philic ethylene oxide (EO) units and the CO<sub>2</sub> molecules” leads to increased CO<sub>2</sub> capture performance and so it will be interesting to see if such an effect is exhibited in these samples and whether this diminished as we increase the monomer:CTA ratio.

#### 4.3.1 Carbon Dioxide Uptake and Selectivity

CO<sub>2</sub> uptake was measured volumetrically for each material at both 298 and 273 K (Figure 4.7). At 298 K uptake varied from between 0.4 – 0.7 mmol/g whereas at 273 K this increased and was found to range between 0.7 – 1.1 mmol/g. Interestingly, there was found to be no trend between porosity and overall uptake capacity. PEG<sub>113</sub>DVB<sub>300</sub>FN<sub>225</sub> displayed the highest CO<sub>2</sub> uptake despite having one of the lowest surface areas of all four samples. However, this sample did contain one of the largest proportions of CTA meaning that the interaction between the ethylene oxide units and the CO<sub>2</sub> may have increased the uptake for this material. The lowest uptake was reported for the highest surface area sample, PEG<sub>113</sub>DVB<sub>600</sub>FN<sub>450</sub>, which should have the lowest one of the lowest proportions of CTA and hence may further back up

## Chapter 4. Applications of PEG-*b*-DVB-co-FN

the hypothesis reported by Matyjaszewski *et al.*<sup>14</sup> Unfortunately, the actual DP and thus monomer inclusion for each sample cannot be quantitatively determined due to the insolubility of the core.

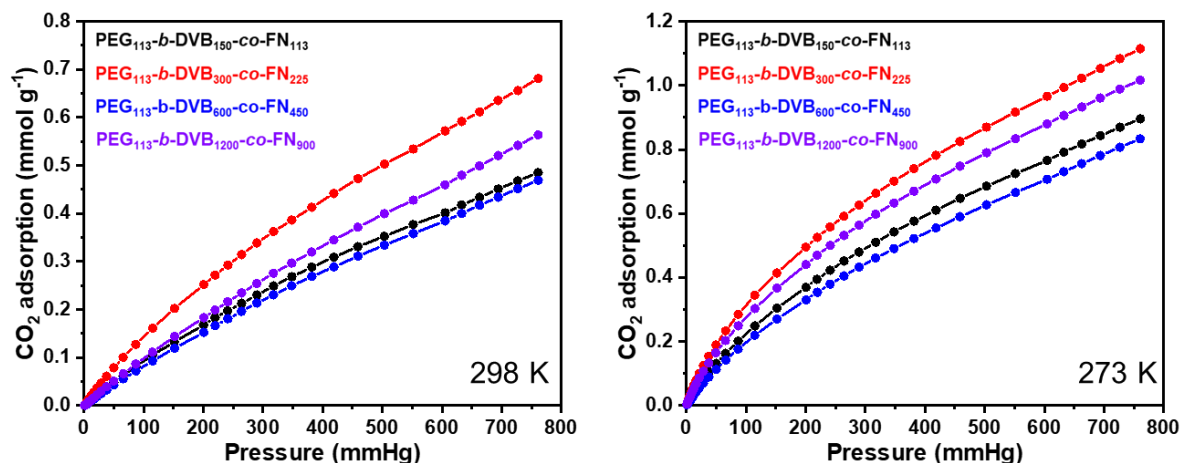


**Figure 4.7** CO<sub>2</sub> uptake for all samples at (left) 298 K and (right) 273 K

The uptake measured by these materials is lower than those reported for other porous polymer materials which range from 2 – 5 mmol/g at 273 K.<sup>13</sup> However, those reported in the literature are all insoluble and specifically designed towards the end application of selective CO<sub>2</sub> uptake. The materials synthesised in this work are designed specifically to be solution processable and as such, less emphasis was placed upon gas uptake performance. A better comparison would be to compare these materials with other soluble porous materials such as PIMs or the SHCPs synthesised by Wood *et al* in 2016 (see introduction section 1.5). In 2011, Guiver *at al* reported the uptake capacity of PIM-1 to be ~2 mmol/g, which is not too dissimilar from the results obtained in this work especially if the higher surface area of PIM-1 compared to these materials is taken into consideration.<sup>15</sup> Likewise, Wood *et al.* reported the CO<sub>2</sub> uptake of SHCP to vary between 1.23 – 1.84 mmol/g with increasing surface area which again is not much higher than the results found for the FN/DVB materials.<sup>16</sup>

The overall CO<sub>2</sub> uptake follows the trend PEG<sub>113</sub>-*b*-DVB<sub>300</sub>-co-FN<sub>225</sub> > PEG<sub>113</sub>-*b*-DVB<sub>1200</sub>-co-FN<sub>900</sub> > PEG<sub>113</sub>-*b*-DVB<sub>150</sub>-co-FN<sub>113</sub> > PEG<sub>113</sub>-*b*-DVB<sub>600</sub>-co-FN<sub>450</sub> which is not consistent with the surface area of the materials. However, on closer inspection the trend does seem to follow that of the ratio between micropore: total pore volume. Samples containing a larger proportion of micropores have higher uptake than those boasting more mesopore volume (Table 4.2). It has been well reported in the literature that gas sorption is preferential into smaller pores at atmospheric pressure.<sup>17</sup> Therefore, it is not too surprising to see the uptake vary as a function of increasing microporosity present within each sample. The reason that PEG<sub>113</sub>DVB<sub>300</sub>FN<sub>225</sub> shows better uptake than PEG<sub>113</sub>DVB<sub>1200</sub>FN<sub>900</sub> may be a synergistic effect between the large

## Chapter 4. Applications of PEG-*b*-DVB-*co*-FN

domains of microporosity combined with the higher ratio of CTA: monomer which is increasing the CO<sub>2</sub> affinity of the material. Indeed, a similar trend is observed when studying the isotheric heats of adsorption of each material (Figure 4.8). It is found that PEG<sub>113</sub>-*b*-DVB<sub>1200</sub>-*co*-FN<sub>900</sub>, which has the largest proportion of micropores has by far the highest isotheric heat of adsorption yet PEG<sub>113</sub>-*b*-DVB<sub>600</sub>-*co*-FN<sub>450</sub>, which contains the lowest proportion of micropores has the lowest isotheric heat of adsorption.

**Table 4.2** Pore volumes and CO<sub>2</sub> uptakes for each sample

Sample	Total pore volume <sup>a</sup> (cm <sup>3</sup> /g)	Micropore volume <sup>b</sup> (cm <sup>3</sup> /g)	Micropore/total pore volume	CO <sub>2</sub> uptake <sup>c</sup> (mmol/g)
PEG <sub>113</sub> - <i>b</i> -DVB <sub>150</sub> - <i>co</i> -FN <sub>113</sub>	0.48	0.09	0.19	0.90 (0.49)
PEG <sub>113</sub> - <i>b</i> -DVB <sub>300</sub> - <i>co</i> -FN <sub>225</sub>	0.45	0.10	0.20	1.11 (0.68)
PEG <sub>113</sub> - <i>b</i> -DVB <sub>600</sub> - <i>co</i> -FN <sub>450</sub>	0.79	0.14	0.18	0.83 (0.47)
PEG <sub>113</sub> - <i>b</i> -DVB <sub>1200</sub> - <i>co</i> -FN <sub>900</sub>	0.67	0.14	0.21	1.02 (0.56)

<sup>a</sup>Calculated at 0.99 P/P<sub>0</sub>, <sup>b</sup>Calculated at 0.1 P/P<sub>0</sub>, <sup>c</sup>CO<sub>2</sub> uptake at 273 K (298 K)

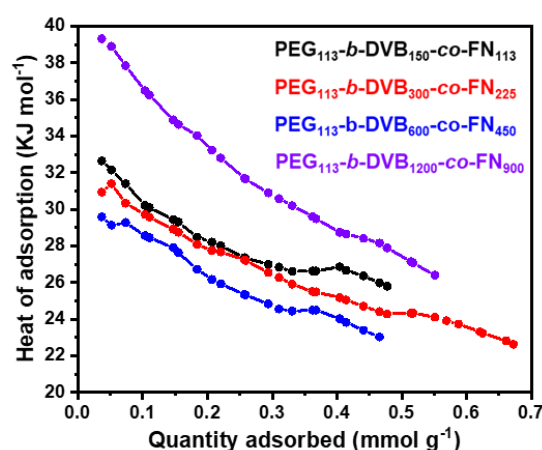


**Figure 4.8** Isotheric heats of adsorption of each material as a function of CO<sub>2</sub> uptake

Uptake capacity is an important characteristic to consider for any potential sorbent. However, what is of equal importance is the selectivity of said uptake. Should a material have outstanding storage capacity but do so in a non-selective manner that uptake is essentially useless, particularly when the uptake of gas in industrial processes is always applied to mixed gas streams and never pure streams of gas. With this in mind, the selective uptake of CO<sub>2</sub> over N<sub>2</sub> was determined through measuring the uptake capacity of N<sub>2</sub> for each sample and comparing this to that of CO<sub>2</sub> at 273 K. CO<sub>2</sub> and N<sub>2</sub> mixes are the most commonly studied given that this is the mixture produced when burning fossil fuels to generate power. Flue gas, the stream of gas produced in fossil fuel power plants, in its most simplistic form, can be thought of as a humid 2:1 mixture of N<sub>2</sub>:CO<sub>2</sub>. In reality, there are many other components such as toxic NO<sub>x</sub>, CO and SO<sub>2</sub> though these vary depending on the type of fuel burnt.<sup>18</sup>

## Chapter 4. Applications of PEG-*b*-DVB-*co*-FN

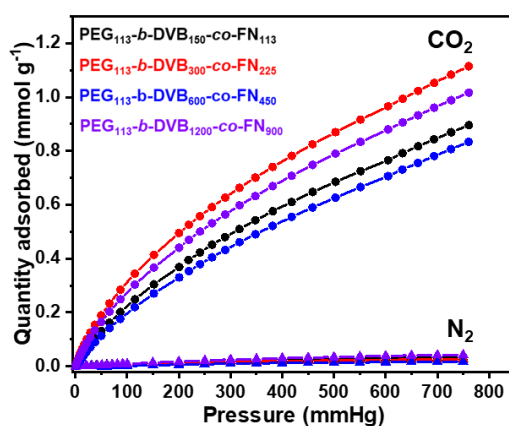


**Figure 4.9** CO<sub>2</sub> (circles) and N<sub>2</sub> (triangles) uptake for each PEG-*b*-FN-*co*-DVB sample at 273 K

Nitrogen uptake at 273 K was recorded (Figure 4.9) and found to be much lower than the CO<sub>2</sub> uptake, ranging between 0.01 – 0.045 mmol/g. Rather interestingly, the samples showing the highest and lowest uptake varies from the CO<sub>2</sub> experiment. In the nitrogen experiments, the largest sample (PEG<sub>113</sub>DVB<sub>1200</sub>FN<sub>900</sub>) shows the highest uptake whereas the second largest sample (PEG<sub>113</sub>DVB<sub>600</sub>FN<sub>450</sub>) shows the lowest uptake. In the CO<sub>2</sub> experiment, the highest uptake was found for PEG<sub>113</sub>DVB<sub>300</sub>FN<sub>225</sub> with PEG<sub>113</sub>DVB<sub>600</sub>FN<sub>450</sub> showing the lowest uptake.

The CO<sub>2</sub>:N<sub>2</sub> selectivity can be determined using two methods, Henry's law selectivity and ideal selectivity. Henry's Law selectivity is calculated at low pressure (<100 mmHg) and relies on the fact that at low pressures the uptake of gas increases linearly with pressure. Therefore, it is possible to plot this data and fit it to a straight line before taking a ratio of each uptake and expressing this as selectivity. Ideal uptake is calculated at 1 bar and is determined by taking a ratio of the uptake of each gas at this pressure. Both ways of expressing selectivity are equally valid and as such were calculated for each sample at 273 K, though realistically ideal selectivity is more representative of real world processes (Table 4.3).

**Table 4.3** CO<sub>2</sub>:N<sub>2</sub> selectivity values calculated for each sample

Sample	Henry's Law Selectivity	Ideal Selectivity
PEG <sub>113</sub> - <i>b</i> -DVB <sub>150</sub> - <i>co</i> -FN <sub>113</sub>	38	28
PEG <sub>113</sub> - <i>b</i> -DVB <sub>300</sub> - <i>co</i> -FN <sub>225</sub>	49	41
PEG <sub>113</sub> - <i>b</i> -DVB <sub>600</sub> - <i>co</i> -FN <sub>450</sub>	63	48
PEG <sub>113</sub> - <i>b</i> -DVB <sub>1200</sub> - <i>co</i> -FN <sub>900</sub>	38	28

Despite displaying the lowest uptake of all materials, PEG<sub>113</sub>DVB<sub>600</sub>FN<sub>450</sub> actually demonstrates the best selectivity at 63:1 and 48:1 at low pressure and atmospheric pressure respectively. Conversely, PEG<sub>113</sub>DVB<sub>1200</sub>FN<sub>900</sub> shows the poorest selectivity at 38:1 and 28:1 again at low and high pressure respectively. The overall trend in selectivity follows the pattern: PEG<sub>113</sub>DVB<sub>600</sub>FN<sub>450</sub> > PEG<sub>113</sub>DVB<sub>300</sub>FN<sub>225</sub> > PEG<sub>113</sub>DVB<sub>150</sub>FN<sub>113</sub> > PEG<sub>113</sub>DVB<sub>1200</sub>FN<sub>900</sub>. The

## Chapter 4. Applications of PEG-*b*-DVB-*co*-FN

calculated selectivity values are much higher than that of SCMP-1 which has a CO<sub>2</sub>:N<sub>2</sub> selectivity of around 8:1 at 273 K.<sup>19</sup>

### 4.3.2 Methane Uptake

In addition to CO<sub>2</sub>, methane is also a very concerning greenhouse gas given that its impact on climate change is around 34 times more severe than that of CO<sub>2</sub> over a hundred year period.<sup>20,21</sup> Most of the methane produced anthropogenically is tied to fossil fuel production such as the processing of natural gas. However, large proportions of methane are also released as a result of the agriculture industry, namely livestock, as well as landfills which emit methane as rubbish decomposes.<sup>22</sup> The problem methane poses to the climate will intensify as the global temperature rises due to the higher temperatures resulting in microorganisms releasing even more methane into the atmosphere.<sup>23,24</sup> Due to the potency of methane as a greenhouse gas, the uptake potential of methane using these materials was investigated.

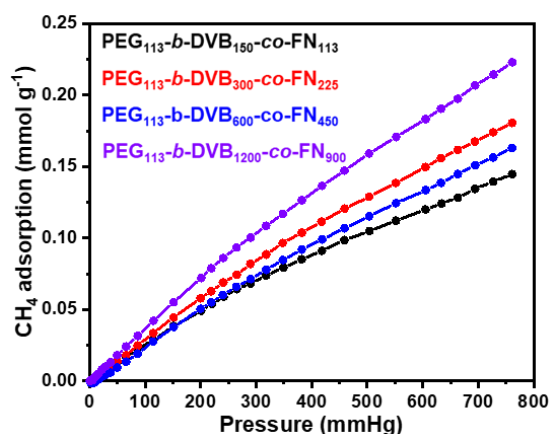


**Figure 4.10** CH<sub>4</sub> uptake for each PEG-*b*-FN-*co*-DVB sample at 273 K

Usually, methane uptake is measured at high pressures (> 50 bar) as this is representative of storage and transportation conditions when applying methane as a fuel. However, during steam reformation processes, when methane is reacted with water to produce hydrogen gas in the presence of a catalyst, the methane is present at much lower pressures. Given that the material discussed here are porous and therefore could act as supports for catalysts methane uptake at atmospheric pressure was recorded as this may give an insight into how penetrable the materials are to the gas and as such, if they would be suitable supports. CH<sub>4</sub> uptake was measured volumetrically for each sample at 273 K (Figure 4.10). CH<sub>4</sub> capacity was found to vary between 0.14 – 0.22 mmol/g with PEG<sub>113</sub>-*b*-DVB<sub>1200</sub>-*co*-FN<sub>900</sub> displaying the highest uptake and PEG<sub>113</sub>-*b*-DVB<sub>150</sub>-*co*-FN<sub>113</sub> showing the lowest uptake. This uptake is higher than that recorded for N<sub>2</sub> under the same conditions though is much lower than the uptake recorded for CO<sub>2</sub>. However the CH<sub>4</sub> uptake is 5 fold higher than that reported for the SHCP materials

#### Chapter 4. Applications of PEG-*b*-DVB-co-FN

reported by Wood *et al* in 2016.<sup>16</sup> This experiment confirmed that the core of the sample is clearly able to interact with the gas and as such it could be expected that any catalyst embedded within the core of the material would also be able to interact with the gas. Given that these samples are both chemically and thermally stable, tolerant to water vapour and their synthesis can be up-scaled there is every possibility that these materials would make a suitable catalytic support for this process.

The steam reformation process converts CH<sub>4</sub> to H<sub>2</sub> and produces CO<sub>2</sub> as a by-product hence it may be interesting to know the relative selectivity these materials have towards these gases. Therefore, the selectivity values were calculated based on the uptakes of these two gases (Table 4.4). It was found that CO<sub>2</sub> is preferentially adsorbed over CH<sub>4</sub> with selectivity values ranging between 5:1 to 6:1, at 1 bar. Selectivity was found to decrease as surface area increased which may be of the lower PEG content in the samples Lowering the PEG content by increasing the core DP would result in less interactions thereby making the uptake less selective. This may also suggest that, unlike CO<sub>2</sub>, CH<sub>4</sub> does not interact with the ether groups of the CTA.

**Table 4.4** CO<sub>2</sub>:CH<sub>4</sub> selectivity values calculated for each sample

Sample	Henry's Law Selectivity	Ideal Selectivity
PEG <sub>113</sub> - <i>b</i> -DVB <sub>150</sub> -co-FN <sub>113</sub>	10	6
PEG <sub>113</sub> - <i>b</i> -DVB <sub>300</sub> -co-FN <sub>225</sub>	15	6
PEG <sub>113</sub> - <i>b</i> -DVB <sub>600</sub> -co-FN <sub>450</sub>	13	5
PEG <sub>113</sub> - <i>b</i> -DVB <sub>1200</sub> -co-FN <sub>900</sub>	10	5

## Chapter 4. Applications of PEG-*b*-DVB-*co*-FN

### 4.4 Conclusion

In the first part of this chapter it was shown how the materials could act as chemosensors towards nitroaromatic compounds in solution through a fluorescence quenching mechanism. The addition of less than 60 ppm of nitroaromatic compound was able to quench the fluorescence emission of a dispersion of PEG<sub>113</sub>-*b*-DVB<sub>300</sub>-*co*-FN<sub>225</sub> with over 99 % efficiency highlighting the potential applications of these materials. This sensing was found to be selective against other chemically similar compounds such as benzene and nitromethane with neither compound capable of eliciting the same response. The limit of detection for each material towards picric acid was tested and it was found to be 170 ppb which is comparable to other porous materials.

The materials synthesised in Chapter 3 were also applied towards the uptake of different gases such as CO<sub>2</sub>, CH<sub>4</sub> and N<sub>2</sub>. The CO<sub>2</sub> uptake of each material varied between 0.8 – 1.1 mmol/g which was found to be comparable to other soluble porous polymers. The CO<sub>2</sub>:N<sub>2</sub> selectivity of each material was also calculated and ranged between 38:1 to 63:1 at low pressure and between 28:1 to 48:1 atmospheric pressure. This was found to be better than other soluble porous polymers such as SCMP-1. The CH<sub>4</sub> uptake was also measured and was found to be lower than the CO<sub>2</sub> uptake though still higher than the N<sub>2</sub> uptake and 5 fold higher than that of SHCP materials.

## Chapter 4. Applications of PEG-*b*-DVB-co-FN

### 4.5 Experimental

#### 4.5.1 Materials

Nitrobenzene (NB, 99 %) was purchased from Alfa Aesar. 2-nitrotoluene (2-NT, > 99 %), 4-nitrotoluene (4-NT, 99 %), 2,4-dinitrotoluene (2,4-DNT, 97 %), 2-nitrophenol (2-NP, 98 %) and picric acid (PA, moistened with water > 98 %) were all purchased from Sigma-Aldrich. All chemicals were used as received without any further purification.

#### 4.5.2 Fluorescence Quenching Studies

10 mmol stock solutions of each nitroaromatic were made up in methanol. A 1 mg/mL stock solution of the polymer dispersion was made up through sonicating the white powder for 30 minutes. A 2.5 cm<sup>3</sup> aliquot of the polymer dispersion was taken and placed into a quartz cuvette. The fluorescence intensity of this solution was measured initially and then after sequential additions of an aliquot of the nitroaromatic stock solution. The fluorescence intensity was normalised against the initial intensity and the quenching ability was determined using equation 4.1.

## 4.6 References

- 1 P. Kovacic and R. Somanathan, *J. Appl. Toxicol.*, 2014, **34**, 810–824.
- 2 A. Deshmukh, S. Bandyopadhyay, A. James and A. Patra, *J. Mater. Chem. C*, 2016, **4**, 4427–4433.
- 3 S. Dalapati, S. Jin, J. Gao, Y. Xu, A. Nagai and D. Jiang, *J. Am. Chem. Soc.*, 2013, **135**, 17310–17313.
- 4 W. Zhang, L. G. Qiu, Y. P. Yuan, A. J. Xie, Y. H. Shen and J. F. Zhu, *J. Hazard. Mater.*, 2012, **221–222**, 147–154.
- 5 S. Wang, Y. Liu, Y. Yu, J. Du, Y. Cui, X. Song and Z. Liang, *New J. Chem.*, 2018, **42**, 9482–9487.
- 6 Z. Xiang and D. Cao, *Macromol. Rapid Commun.*, 2012, **33**, 1184–1190.
- 7 H. Ma, B. Li, L. Zhang, D. Han and G. Zhu, *J. Mater. Chem. A*, 2015, **3**, 19346–19352.
- 8 R. Sun, X. Huo, H. Lu, S. Feng, D. Wang and H. Liu, *Sensors Actuators, B Chem.*, 2018, **265**, 476–487.
- 9 D. M. D'Alessandro, B. Smit and J. R. Long, *Angew. Chemie Int. Ed.*, 2010, **49**, 6058–6082.
- 10 R. Dawson, A. I. Cooper and D. J. Adams, *Polym. Int.*, 2013, **62**, 345–352.
- 11 M. E. Boot-Handford, J. C. Abanades, E. J. Anthony, M. J. Blunt, S. Brandani, N. Mac Dowell, J. R. Fernández, M.-C. Ferrari, R. Gross, J. P. Hallett, R. S. Haszeldine, P. Heptonstall, A. Lyngfelt, Z. Makuch, E. Mangano, R. T. J. Porter, M. Pourkashanian, G. T. Rochelle, N. Shah, J. G. Yao and P. S. Fennell, *Energy Environ. Sci.*, 2014, **7**, 130–189.
- 12 J. Wang, L. Huang, R. Yang, Z. Zhang, J. Wu, Y. Gao, Q. Wang, D. O'Hare and Z. Zhong, *Energy Environ. Sci.*, 2014, **7**, 3478–3518.
- 13 W. Wang, M. Zhou and D. Yuan, *J. Mater. Chem. A*, 2017, **5**, 1334–1347.
- 14 H. Xu, J. Wu, B. Zheng, W. Mai, F. Xu, L. Chen, H. Liu, R. Fu, D. Wu and K. Matyjaszewski, *Chem. Commun.*, 2017, **53**, 5294–5297.

#### Chapter 4. Applications of PEG-*b*-DVB-co-FN

- 15 N. Du, H. B. Park, G. P. Robertson, M. M. Dal-Cin, T. Visser, L. Scoles and M. D. Guiver, *Nat. Mater.*, 2011, **10**, 372–375.
- 16 Y. Yang, B. Tan and C. D. Wood, *J. Mater. Chem. A*, 2016, **4**, 15072–15080.
- 17 F. R. and C. P. Claudia F. Martín, Ev Stöckel, Rob Clowes, Dave J. Adams, Andrew I. Cooper, Jose J. Pis, *J. Mater. Chem*, 2011, **21**, 5475–5483.
- 18 T. C. Drage, C. E. Snape, L. a. Stevens, J. Wood, J. Wang, A. I. Cooper, R. Dawson, X. Guo, C. Satterley and R. Irons, *J. Mater. Chem.*, 2012, **22**, 2815.
- 19 G. Cheng, T. Hasell, A. Trewin, D. J. Adams and A. I. Cooper, *Angew. Chemie Int. Ed.*, 2012, **51**, 12727–12731.
- 20 D. J. Wuebbles and K. Hayhoe, *Earth-Science Rev.*, 2002, **57**, 177–210.
- 21 S. Kirschke, P. Bousquet, P. Ciais, M. Saunois, J. G. Canadell, E. J. Dlugokencky, P. Bergamaschi, D. Bergmann, D. R. Blake, L. Bruhwiler, P. Cameron-Smith, S. Castaldi, F. Chevallier, L. Feng, A. Fraser, M. Heimann, E. L. Hodson, S. Houweling, B. Josse, P. J. Fraser, P. B. Krummel, J. F. Lamarque, R. L. Langenfelds, C. Le Quéré, V. Naik, S. O’doherly, P. I. Palmer, I. Pison, D. Plummer, B. Poulter, R. G. Prinn, M. Rigby, B. Ringeval, M. Santini, M. Schmidt, D. T. Shindell, I. J. Simpson, R. Spahni, L. P. Steele, S. A. Strode, K. Sudo, S. Szopa, G. R. Van Der Werf, A. Voulgarakis, M. Van Weele, R. F. Weiss, J. E. Williams and G. Zeng, *Nat. Geosci.*, 2013, **6**, 813–823.
- 22 M. Sharifzadeh, G. Triulzi and C. L. Magee, *Energy Environ. Sci.*, 2019, **12**, 2789–2805.
- 23 G. Yvon-Durocher, A. P. Allen, D. Bastviken, R. Conrad, C. Gudasz, A. St-Pierre, N. Thanh-Duc and P. A. Del Giorgio, *Nature*, 2014, **507**, 488–491.
- 24 K. M. Walter, S. A. Zimov, J. P. Chanton, D. Verbyla and F. S. Chapin, *Nature*, 2006, **443**, 71–75.

## Chapter 4. Applications of PEG-*b*-DVB-co-FN

# **Chapter 5 - White Light Emission using DVB/AA Porous Polymeric Dispersions**

## Chapter 5. White-Light Emission

### 5.1 Chapter Aims

In Chapter 3 the synthesis of solution-processable porous polymers using DVB and FN was reported. The main advantage of this synthesis technique is the potential for synthetic diversity using a variety of different outer and inner block monomers. In this chapter the same synthesis technique will be applied but acrylic acid will be used in place of fumaronitrile and polymerised alongside divinylbenzene to form the core of the material *via* the same RAFT-PISA methodology using the same PEG-based CTA.

This chapter will also explore the post-synthetic modification of the resulting material. The acrylic acid monomer contains a carboxylic acid chemical motif which has much scope for modification *via* a reduction to form an alcohol, reaction with an alcohol to form an ester or even a reaction with a second carboxylic acid to synthesis an anhydride. The introduction of metal ions into the material is also possible due to the chelating nature of this group as is the reaction with an amine to yield an amide. Given that it is possible to carry out these reactions on the monomer it should, theoretically, be equally as viable to carry out the reaction on the final product.

The porous polymer synthesised in this chapter, post-synthetically modified with 9-anthracenemethanol will embed anthracene moieties into the core of the material. Under UV irradiation, anthracene demonstrates blue fluorescence emission in the visible region of light which can be used to give insight into the success of the post-synthetic modification. Furthermore, this feature can also be exploited to produce a white-light emitting solution when mixed with another organic fluorophore. Here, the final material plays a dual role in both encapsulating the second fluorophore and emitting blue light. Upon tuning of the concentrations of both the polymer dispersion and encapsulated dye the white-light emission of the dispersion was evaluated based on the CIE coordinates, CRI and CCT values.

## Chapter 5. White-Light Emission

### 5.2 Radical Polymerisation of DVB and AA

Much like the DVB/FN system the first reaction carried out was the free radical polymerisation of DVB and AA to see whether these two monomers would co-polymerise to yield an insoluble porous network. A series of samples were targeted by varying the ratio of DVB:AA starting at 50:50 and rising to 90:10. The DVB mol ratio used was at least 50 % given that anything less would most likely result in a non-porous product. Table 5.1 shows the yields and surface areas obtained upon free radical polymerisation of DVB and AA. Samples were labelled as IP-X/Y in which X denotes the mole fraction of DVB and Y the mole fraction of acrylic acid.

**Table 5.1** Obtained yields and surface areas of each DVB/AA network synthesised

Sample	% Yield	SA <sub>BET</sub> (m <sup>2</sup> /g) <sup>a</sup>
IP-50/50	45%	23
IP-60/40	49%	19
IP-70/30	66%	370
IP-80/20	76%	457
IP-90/10	89%	592

<sup>a</sup>BET surface areas were determined over the partial pressure range of 0.05 – 0.35 P/P<sub>0</sub>

As expected there is a clear trend in surface area and ratio of DVB used in the reaction. Increasing quantities of DVB leads to an increase in surface area due to the polymerisation of this monomer creating pores within the network. Samples with less than 70% DVB are essentially non-porous but samples comprised of greater than 70% DVB give notable BET surface areas. The yields of each network were also found to increase as the ratio of DVB was increased suggesting that AA may not be polymerising at the same rate as the DVB monomer.

To prove that both monomers had been successfully incorporated into the final product FTIR spectra were collected for each of the synthesised networks (Figure 5.1). The main indicator which shows successful incorporation of the AA monomer into the network is the sharp peak at ~ 1750 cm<sup>-1</sup> which is the carbonyl stretching frequency of this monomer. This signal is found to become less intense as the mole fraction of this monomer decreases suggesting some control over the final product ratio has been obtained. All samples also show a signal at ~2900 cm<sup>-1</sup>, attributed to the presence of the polymer backbone, which hints at successful polymerisation of both monomers.

## Chapter 5. White-Light Emission

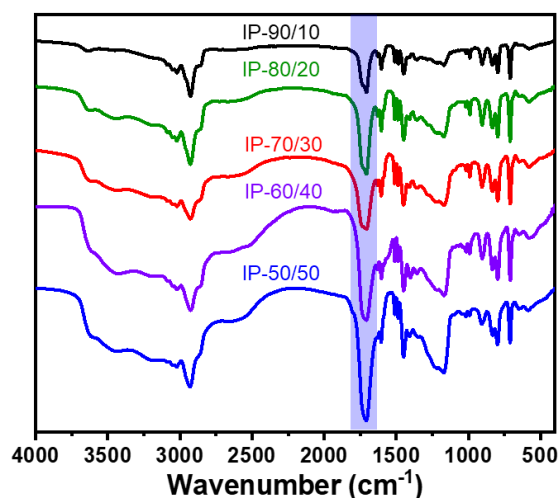


**Figure 5.1** FTIR spectra obtained for each sample synthesised

To further investigate the relative monomer incorporation of each network elemental analysis was conducted on each sample. Table 4.2 shows the expected and obtained values for each network.

**Table 5.2** Elemental analysis values determined for each sample

Sample	% Carbon		% Hydrogen		% Oxygen	
	Expected	Found	Expected	Found	Expected	Found <sup>a</sup>
IP-50/50	71.16	69.85	6.60	7.01	22.25	-
IP-60/40	75.39	73.51	6.81	7.55	17.80	-
IP-70/30	79.62	76.03	7.03	7.17	13.35	-
IP-80/20	83.85	79.84	7.25	7.43	8.90	-
IP-90/10	88.08	83.55	7.47	7.57	5.45	-

<sup>a</sup>Oxygen values could not be determined due to the sample being combusted in a stream of pure oxygen

All samples broadly agree with the expected amounts calculated assuming 100 % incorporation of both monomers into the final network. However the % carbon values found seem to be lower than expected and the % hydrogen seem to be a little higher than expected. This could be a result of incomplete polymerisation during the reaction, a hypothesis that would seem to agree with the reported yields of these syntheses

## Chapter 5. White-Light Emission

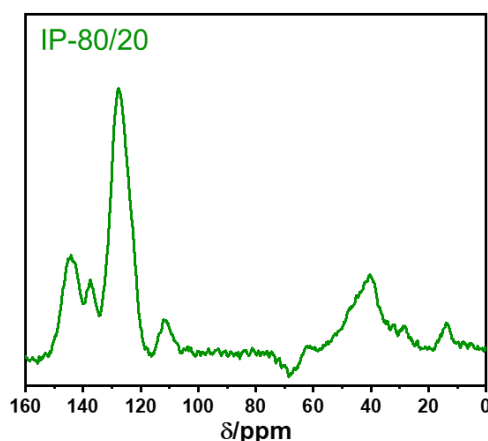


**Figure 5.2** Solid state  $^{13}\text{C}$  NMR of IP-80/20

$^{13}\text{C}$  CP/MAS ssNMR of IP-80/20 was measured in order to elucidate the structure of the final product and thereby determine the success of the polymerisation (Figure 5.2). The peaks centred at 16 and 41 ppm are due to the alkyl carbons present as a result of the polymerisation of the two monomers. Peaks at 128 and 138 ppm are present due to the aromatic carbons present due to the successful polymerisation of DVB. The peak at 145 ppm is attributed to the carboxylic acid carbon present as a result of the incorporation of the AA monomer into the final network. Finally, the peak at around 115 ppm is a result of the vinyl carbons present due to incomplete polymerisation of the divinylbenzene indicating that full conversion has not been reached. The solid state NMR, IR and elemental analysis combined with the gas sorption analysis suggests that the polymerisation resulted in a porous material incorporating both monomers into the final network.

### 5.3 RAFT-PISA of DVB and AA

#### 5.3.1 Synthesis of Dispersible Porous Polymers

The insoluble polymers synthesised and described in section 5.2 show that only those with a DVB mole ratio of at least 70 % result in a porous final material. In Chapter 3 it was shown that the PISA synthesis results in a decrease in the BET surface area of the sample compared to the insoluble networks synthesised using the same monomer ratio. Most likely, this is due to the introduction of the non-porous yet important hydrophilic PEG chains which stabilise the polymeric networks in solution. Due to the relatively low surface areas produced from the polymerisation of DVB:AA in ratios of 50:50 and 60:40 it was decided not to attempt the synthesis of dispersible porous polymers using these ratios. More promising are the three samples with higher DVB ratios which gave surface areas  $> 350 \text{ m}^2/\text{g}$ . Therefore, the synthesis was conducted using the ratios which yielded the most porous insoluble analogues.

## Chapter 5. White-Light Emission

### 5.3.2 Solid State Characterisation

The polymerisation of DVB and AA via the RAFT-mediated polymerisation route using the same PEG-based CTA as the previous chapter resulted in the generation of white powdery solids in yields ranging between 30 – 40 %, similar to the values obtained when synthesising the FN analogues. Solid-state characterisation in the form of FTIR, elemental analysis and solid state NMR was carried out on the synthesised samples to elucidate the final structure and relative incorporation of both monomers and CTA.

The FTIR spectrum of each sample (Figure 5.3) has signals at  $\sim 1117\text{ cm}^{-1}$  and  $\sim 3650\text{ cm}^{-1}$  which are a result of the ether stretch of the PEG-based CTA and the  $-\text{OH}$  group of the acrylic acid respectively. The broad signal ranging between  $2900 - 3000\text{ cm}^{-1}$  is present due to the polymerisation of the two monomers resulting in the formation of a polymer backbone containing  $-\text{CH}-$  and  $-\text{CH}_2-$  alkyl groups. The signal at  $\sim 1750\text{ cm}^{-1}$  is present due to the carbonyl group which arises from the successful polymerisation of acrylic acid.

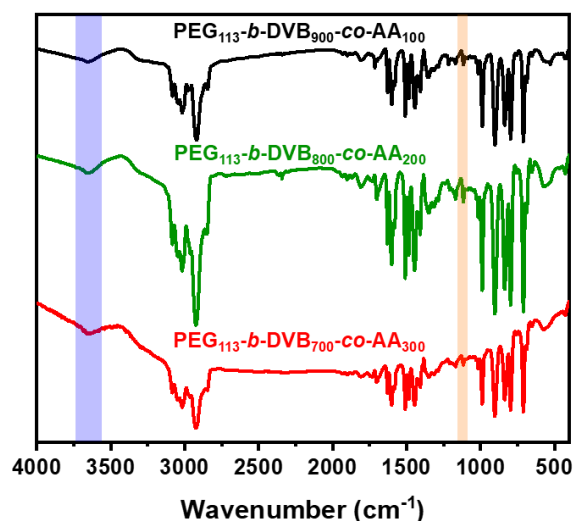


**Figure 5.3** FTIR spectrum of the three PPD samples synthesised in this chapter

The chemical composition of the synthesised materials was calculated using elemental analysis (Table 5.3). Both the carbon and hydrogen vary from what is expected though this has been seen before in other porous polymers and is often due to incomplete combustion of the use of an idealised structure.<sup>1-3</sup> However, another possibility for these deviations could be due to lower conversion of the acrylic acid monomer into the polymer network as shown from the yields of the reaction (appendix, Table S5.2). Less acrylic acid and more divinylbenzene would increase the carbon and hydrogen content from what is expected due to the oxygen content being lowered as a result of this. However, both elemental analysis and FTIR data, does show that some degree of polymerisation has taken place involving both monomers.

## Chapter 5. White-Light Emission

**Table 5.3** Elemental analysis values obtained for all PPD samples synthesised

Sample	% Carbon		% Hydrogen		% Sulfur	
	Expected	Found	Expected	Found	Expected	Found <sup>a</sup>
PEG <sub>113</sub> - <i>b</i> -DVB <sub>700</sub> - <i>co</i> -AA <sub>300</sub>	86.55	90.31	5.78	7.85	0.06	< 0.3
PEG <sub>113</sub> - <i>b</i> -DVB <sub>800</sub> - <i>co</i> -AA <sub>200</sub>	87.88	90.73	6.39	7.77	0.06	< 0.3
PEG <sub>113</sub> - <i>b</i> -DVB <sub>900</sub> - <i>co</i> -AA <sub>100</sub>	89.30	91.77	7.04	7.89	0.06	< 0.3

<sup>a</sup>Limit of detection of sulphur analysis is 0.3 %

Solid-state <sup>13</sup>C NMR was carried out to further elucidate the structure of the final material and validate the FTIR and elemental analysis findings (Figure 5.4), spinning side bands are marked with an asterisk. The peaks at 31 and 40 ppm are present as a result of the –CH<sub>2</sub>– and –CH– alkyl carbons which are the result of the polymerisation between the two monomers. The resonance at 137 ppm is attributed to the aromatic carbon bonded to an alkyl carbon and the peak at 128 ppm to aromatic C-H<sub>Ar</sub> carbons. The peak at 145 ppm is assigned to the carboxylic acid carbon present due to the successful incorporation of the acrylic acid monomer into the final material. There is a small peak at 70 ppm present in both samples, which is a result of the PEG chain present on the CTA and highlights the successful inclusion of the CTA into the final product. The peak at 113 ppm is due to unreacted vinyl groups most likely present as a result of incomplete polymerisation of divinylbenzene.

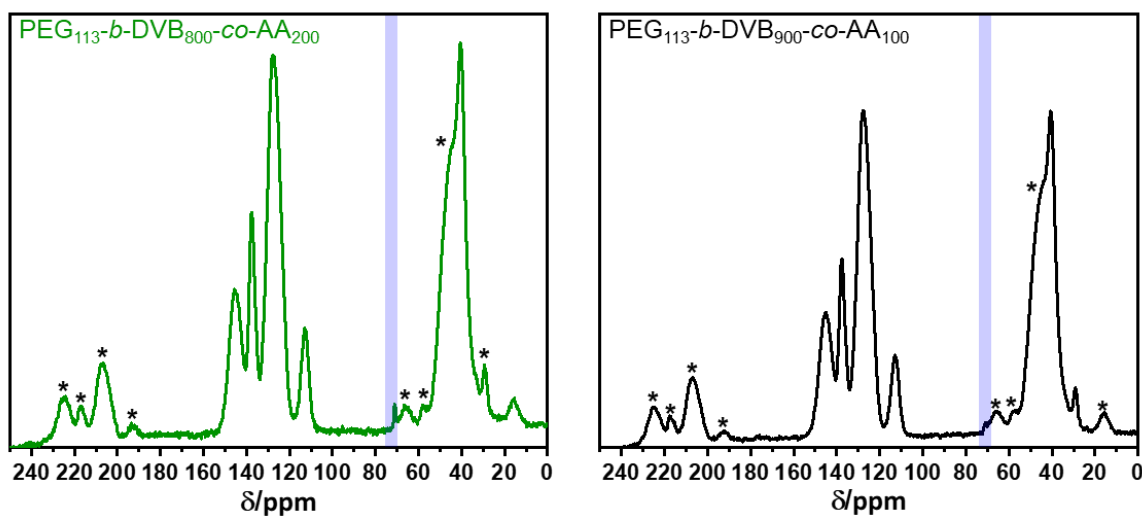


**Figure 5.4** <sup>13</sup>C solid state NMR of (left) PEG<sub>113</sub>-*b*-DVB<sub>800</sub>-*co*-AA<sub>200</sub> and (right) PEG<sub>113</sub>-*b*-DVB<sub>900</sub>-*co*-AA<sub>100</sub>. Asterisk's denote spinning side bands

## Chapter 5. White-Light Emission

### 5.3.3 Nitrogen Gas Sorption isotherms

The porosity and surface area of each sample was evaluated using nitrogen gas sorption isotherms at 77 K (Figure 5.5). Much like the FN/DVB materials described in Chapter 3, all samples show prominent uptake in the high relative pressure region ( $> 0.9 P/P_0$ ) which is attributed to the condensation of nitrogen between particles. In contrast to the FN/DVB system there is however no significant uptake in the microporous region of the isotherm ( $< 0.1 P/P_0$ ) which suggests that the sample contains few to no micropores. The pore size distribution for each sample agrees with this observation with each sample containing predominantly mesopores. The most prominent pore size in all three samples is centred around 3 nm which lies at the smaller end of the mesopore region. There are however other mesopores present ranging from 3 – 10 nm. After this point it seems that the samples with a lower DVB content possess more larger pores which is most likely a result of the higher AA content resulting in less extensive crosslinking of the network. This, in turn, would lead to the presence of larger pores.

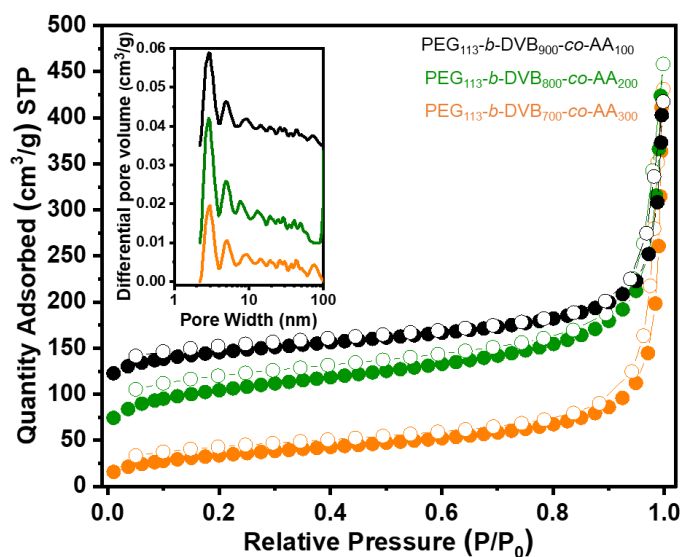


**Figure 5.5** Nitrogen adsorption (filled) and desorption (empty) isotherms at 77 K for the three samples (each offset by 50 cm<sup>3</sup>/g), inset shows the pore size distribution

The surface area of each sample, calculated over the relative pressure range of 0.01 – 0.15  $P/P_0$ , was found to range between 108 – 201 m<sup>2</sup>/g (Table 5.4). PEG<sub>113</sub>-*b*-DVB<sub>700</sub>-*co*-AA<sub>300</sub> gave the lowest surface area while PEG<sub>113</sub>-*b*-DVB<sub>800</sub>-*co*-AA<sub>200</sub> was shown to possess the highest surface area. Conversely, PEG<sub>113</sub>-*b*-DVB<sub>900</sub>-*co*-AA<sub>100</sub> gave the highest micropore:total pore ratio ( $V_{0.1}/V_{tot}$ ) suggesting that the higher DVB content results in more extensive crosslinking and therefore formation of smaller pores. Likewise, PEG<sub>113</sub>-*b*-DVB<sub>700</sub>-*co*-AA<sub>300</sub>

## Chapter 5. White-Light Emission

had the lowest micropore ratio which further evidences the link between pore size and DVB content in each sample.

**Table 5.4** Surface area and pore volume data for each PPD sample

Sample	$S_{\text{ABET}}$ ( $\text{m}^2/\text{g}$ )	$V_{\text{TOT}}^{\text{a}}$	$V_{0.1}^{\text{b}}$	$V_{0.1}/V_{\text{tot}}$
PEG <sub>113</sub> - <i>b</i> -DVB <sub>700</sub> -co-AA <sub>300</sub>	108	0.17	0.04	0.24
PEG <sub>113</sub> - <i>b</i> -DVB <sub>800</sub> -co-AA <sub>200</sub>	201	0.25	0.07	0.28
PEG <sub>113</sub> - <i>b</i> -DVB <sub>900</sub> -co-AA <sub>100</sub>	168	0.19	0.06	0.32

<sup>a</sup>Total pore volume, calculated at 0.99 P/P<sub>0</sub>. <sup>b</sup>Micropore volume, calculated at 0.1 P/P<sub>0</sub>

### 5.3.4 Dynamic Light Scattering

As in Chapter 3, the solid samples were dispersed in a chosen solvent and sonicated to form a stable dispersion of the porous polymer in solution. When dispersed in methanol the samples did not prove to be as stable as the FN system and unfortunately settled out after around 24 hours. This is most likely due to the swelling of the core by the methanol solvent given that acrylic acid is soluble in methanol and thus will result in an increase in the core size to such an extent that the samples are too big to be stabilised by the PEG chains. This is similar to what was observed when the FN/DVB samples were dispersed in solvents such as chloroform and toluene.

Despite this swelling and subsequent instability of the samples it was possible to determine the sizes of the particles by using DLS. The samples were dispersed in two solvents, methanol and THF, as these solvents will cause swelling of the two different monomers. Methanol will solvate the acrylic acid but not the divinylbenzene whereas THF will do the opposite and swell the divinylbenzene but not the acrylic acid. The DLS curves obtained for these experiments are shown in Figure 5.6.

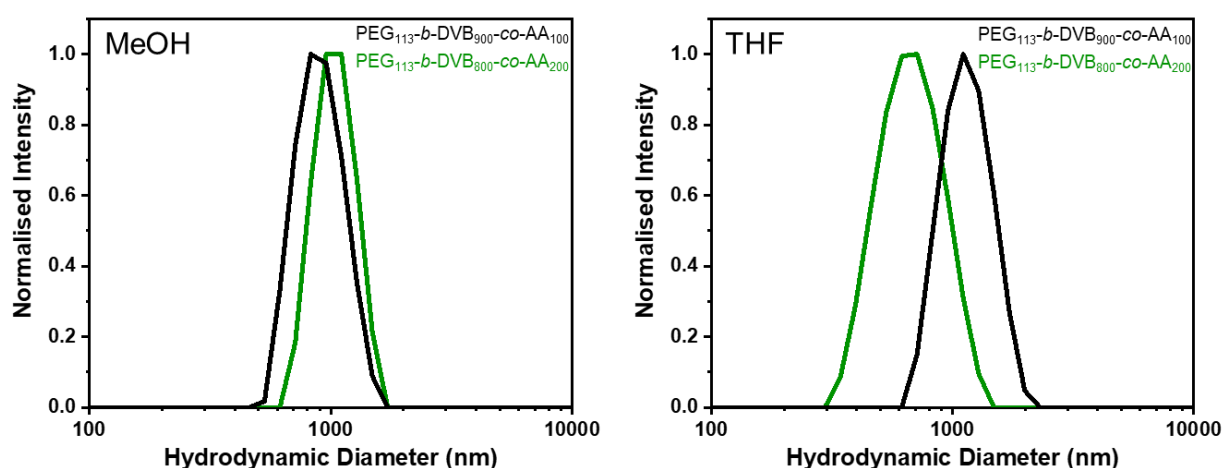


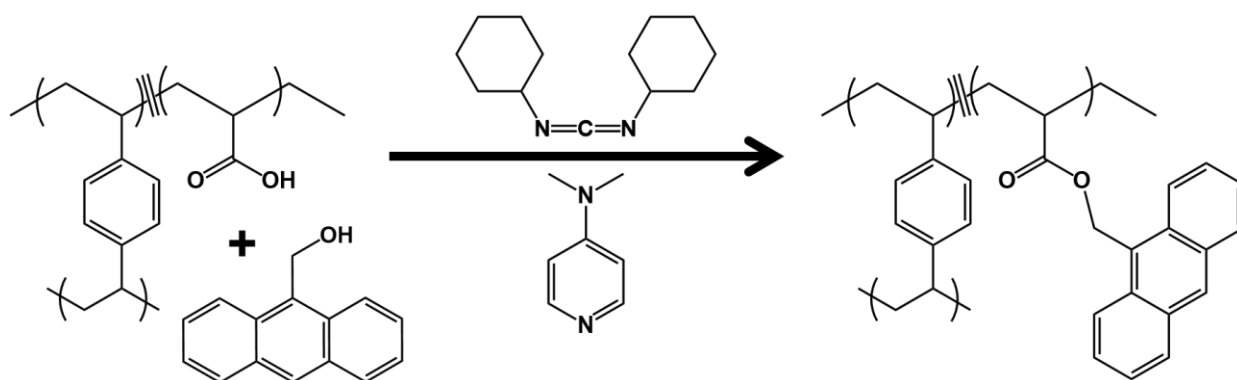
**Figure 5.6** DLS curves obtained for PPD samples in (left) MeOH and (right) THF

## Chapter 5. White-Light Emission

In methanol the PEG<sub>113</sub>-*b*-DVB<sub>900</sub>-*co*-AA<sub>100</sub> sample is the smallest with a hydrodynamic diameter of around 540 nm with the PEG<sub>113</sub>-*b*-DVB<sub>800</sub>-*co*-AA<sub>200</sub> sample being much larger with a diameter of around 910 nm. This order is perhaps expected given that the PEG<sub>113</sub>-*b*-DVB<sub>800</sub>-*co*-AA<sub>200</sub> sample contains more acrylic acid and therefore is expected to swell more than the other samples containing less acrylic acid. When dispersed in THF the samples are a little larger with hydrodynamic diameters of 680 nm and 1312 nm for PEG<sub>113</sub>-*b*-DVB<sub>800</sub>-*co*-AA<sub>200</sub> and PEG<sub>113</sub>-*b*-DVB<sub>900</sub>-*co*-AA<sub>100</sub> respectively. It would be expected that the samples are larger in THF given that the THF will swell the divinylbenzene and not the acrylic acid and there is more of the former than the latter. This is also the reason as to why the PEG<sub>113</sub>-*b*-DVB<sub>900</sub>-*co*-AA<sub>100</sub> sample is much larger than the PEG<sub>113</sub>-*b*-DVB<sub>800</sub>-*co*-AA<sub>200</sub> sample. Much like in methanol the samples also settle out overnight in THF solvent indicating a lack of long term stability which is in contrast to the FN/DVB samples.

### 5.4 Post-Synthetic Modification of DVB/AA PPDs

Post-synthetic modification of the PPDs was carried out in order to incorporate anthracene moieties into the core of the sample. This involved exploiting the carboxylic acid groups, present due to the polymerisation of acrylic acid, and carrying out an esterification reaction using 9-anthracenemethanol, similar to one reported by Pazicni *et al.*<sup>4</sup> This reaction scheme is presented in scheme 5.1 (see section 5.7.5 for full synthetic procedure).



**Scheme 5.1** Overall synthetic procedure towards anthracene functionalised porous materials

Before being attempted on the porous polymer the esterification was first carried out on the acrylic acid monomer to test its efficacy. The esterification reaction of acrylic acid and 9-anthracenemethanol afforded the 9-anthracene methacrylate as the product in a 73 % yield. This proves that the reaction was possible using this monomer and hence should be reproducible when using the acrylic acid containing PPD material. <sup>1</sup>H NMR was used to determine the purity of the target compound and compared well to previously published work<sup>5</sup>

## Chapter 5. White-Light Emission

(Figure S5.1). Unfortunately, it was not possible to use this anthracene containing monomer as the co-monomer in the RAFT-PISA synthesis due to its insolubility in the solvent system.

When synthesising the anthracene acrylate monomer it was possible to determine the purity through solution phase  $^1\text{H-NMR}$ , a standard in most synthetic organic procedures. However, when post-synthetically modifying the PPD samples this is not possible given the fact that the sample, especially the core, is not soluble but instead dispersible. Therefore, it is necessary to find another way to quantify the success of the reaction. Given the fact that the sample is dispersible we can separate out the product from the reagents through centrifugation. After the reaction, each sample was centrifuged and washed to remove any unreacted reagents and by-products. However, this does not tell us if the reaction was successful especially given that the final product did not differ much visually from the original material (white powder to white/faint yellow powder).

Given that anthracene is being incorporated into the material for its luminescent properties it should be possible to exploit both UV-Vis and fluorescence spectroscopy to give insight into the success of the esterification reaction. Indeed, it is known that the PPD materials exhibit both UV-Vis and fluorescence spectra as a result of the DVB within the sample but should anthracene be present there should be new peaks in both of these spectra. Figure 5.7 shows the UV-Vis and fluorescence spectra of the PPD samples before and after the esterification reaction with 9-anthracenemethanol.

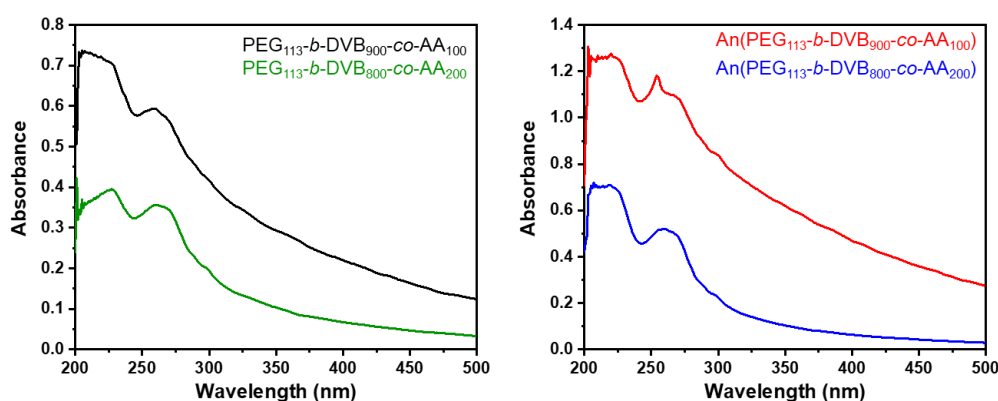


**Figure 5.7** UV-Vis spectra of sample pre- (left) and post- (right) synthetic modification

The UV-Vis spectra (Figure 5.7) of the samples before and after anthracene incorporation show little variance which is most likely due to the very low loading of anthracene into the final sample. Anthracene gives a distinct peak at 350 nm in the UV-Vis spectrum but this is not visible in the samples supposedly containing it, either due to it not being present or to it being present but in very small concentrations. One other issue that hinders these peaks being

## Chapter 5. White-Light Emission

visible is the fact that these samples, being dispersions and not solutions, do not give a flat baseline. Instead, we see this raised baseline, which is a result of scattering of light that hinders the visibility of some peaks. Fluorescence emission spectroscopy of each sample was carried out to further probe the anthracene loading content within each sample (Figure 5.8).

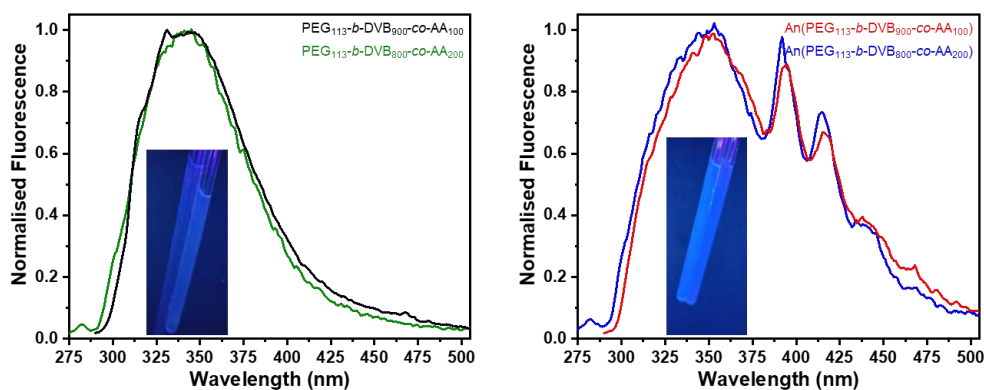


**Figure 5.8** Fluorescence emission spectra of PPDs (left) and An-PPDs (right). Inset shows the samples irradiated under UV light ( $\lambda = 365$  nm)

Somewhat in contrast to the UV-Vis spectra there is now a noticeable difference in the emission spectra of the PPDs and An-PPDs. The introduction of the anthracene groups into the sample yields new emission peaks at between 400 – 430 nm as well as maintaining the peak at  $\sim 350$  nm which is an artefact of the PPD samples. These new peaks are due to the presence of anthracene within the sample given that they appear in the same place as pure anthracene (see appendix Figure S5.2). Further to this, the pictures of the solutions (inset Figure 5.8) also show the slight difference in appearance when irradiated under UV light. The An-PPDs appear to be much brighter and a deeper blue compared to the PPD analogues.

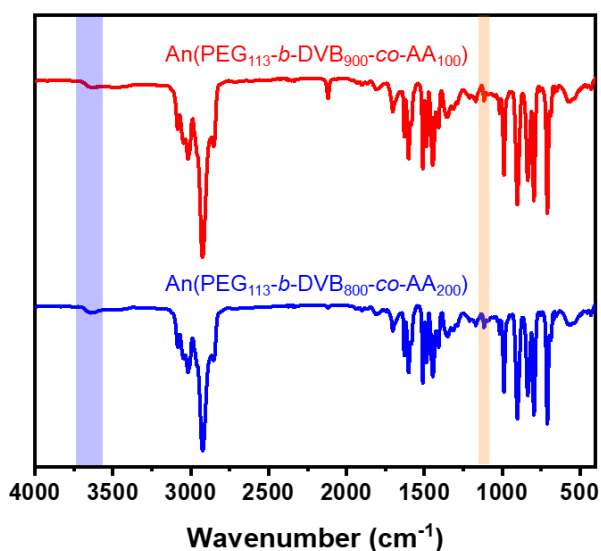


**Figure 5.9** FTIR spectrum of both porous polymer samples after post-synthetic modification

## Chapter 5. White-Light Emission

The FTIR spectra of each An-PPD sample (Figure 5.9) remains largely unchanged as expected, yet there are some key differences which indicate a chemical change has occurred. As expected, the signal at  $1117\text{ cm}^{-1}$ , present as a result of the ether stretch of the PEG-based CTA, remains present as does the broad stretching frequency between  $2900 - 3000\text{ cm}^{-1}$  which is a result of the alkyl backbone. However, the broad peak at  $\sim 3650\text{ cm}^{-1}$ , present due as a result of the  $-\text{OH}$  stretch of the acrylic acid, has now diminished quite significantly. This is a result of the esterification reaction meaning that the carboxylic acid has been converted into an ester group and the anthracene has been successfully incorporated chemically into the final structure and not simply adsorbed into the pores of the material.

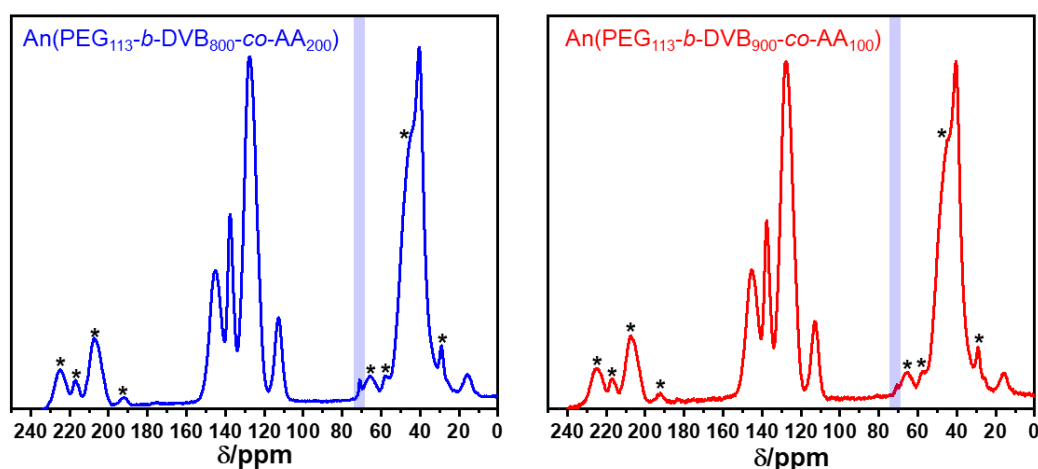


**Figure 5.10**  $^{13}\text{C}$  solid-state NMR of (left)  $\text{An}(\text{PEG}_{113}\text{-}b\text{-DVB}_{800}\text{-co-AA}_{200})$  and (right)  $\text{An}(\text{PEG}_{113}\text{-}b\text{-DVB}_{900}\text{-co-AA}_{100})$  (asterisk's denote spinning side bands).

Much like the FTIR, the solid-state  $^{13}\text{C}$  NMR of the anthracene incorporated samples remain mainly unchanged when compared to the original samples. Hence, peaks at 16 and 40 ppm are caused by the polymer backbone. The peaks at 128 and 137 ppm are present due to the aromatic carbons and these now represent both the divinylbenzene and incorporated anthracene units. The peak at 145 ppm is present due to the carbonyl carbon with the peak at 113 ppm being a result of unreacted vinyl groups.

Nitrogen gas sorption analysis at 77 K (Figure 5.11) gives insight into the effect the post-synthetic modification had on the porosity of each sample. Incorporation of the anthracene moiety lowered the surface area from  $201\text{ m}^2/\text{g}$  to  $188\text{ m}^2/\text{g}$  for  $\text{An}(\text{PEG}_{113}\text{-}b\text{-DVB}_{800}\text{-co-AA}_{200})$  and  $168\text{ m}^2/\text{g}$  to  $152\text{ m}^2/\text{g}$  for  $\text{An}(\text{PEG}_{113}\text{-}b\text{-DVB}_{900}\text{-co-AA}_{100})$ . This is due to the incorporation of bulky aromatic groups filling some of the pores of the sample. The changes to the surface are minimal though this is to be expected given the small amounts of acrylic acid groups present within the sample available to be modified. Likewise, there was also a small reduction

## Chapter 5. White-Light Emission

in the total pore and micropore volume after post-synthetic modification (see appendix, table S5.3) which further hints at incorporation of a bulky chemical moiety filling the pores of the sample.

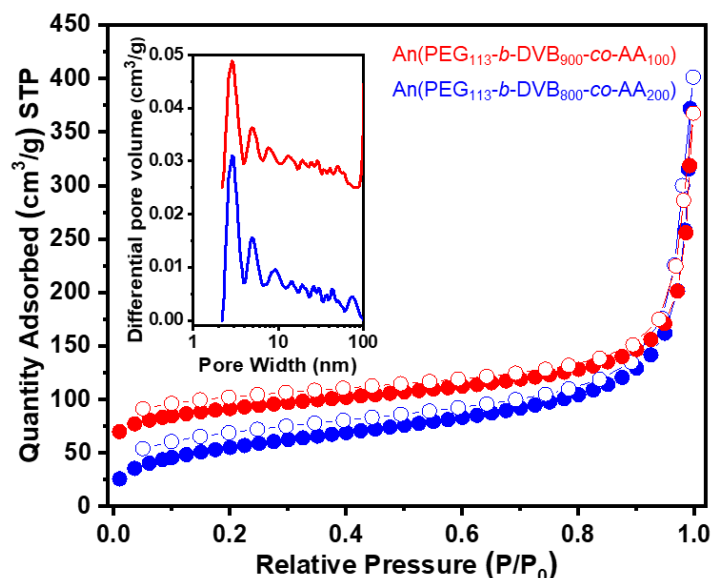


**Figure 5.11** Nitrogen adsorption (filled) and desorption (empty) isotherms at 77 K for both samples after post-synthetic modification (offset by 50 cm<sup>3</sup>/g), inset shows the pore size distribution

TEM images of the samples before and after incorporation of the anthracene units seem to show a slight change in morphology. Initially, each sample was present as the mass aggregates, much like those reported in Chapter 3 for the FN/DVB analogues. However, upon incorporation of the anthracene, the samples seem to show the presence of larger spherical domains, particularly for the An(PEG<sub>113</sub>-*b*-DVB<sub>900</sub>-*co*-AA<sub>100</sub>) sample. It is unknown as to what has caused these larger spheres to form though the aggregated morphology as seen for the PPD samples is still present within all four samples. This shows that the material is able to be post-synthetically modified and still retain its initial aggregated structure which demonstrates the stability of the sample. This may also show how the aggregated morphology is a function of extensive crosslinking which cannot be broken during the reaction.

## Chapter 5. White-Light Emission

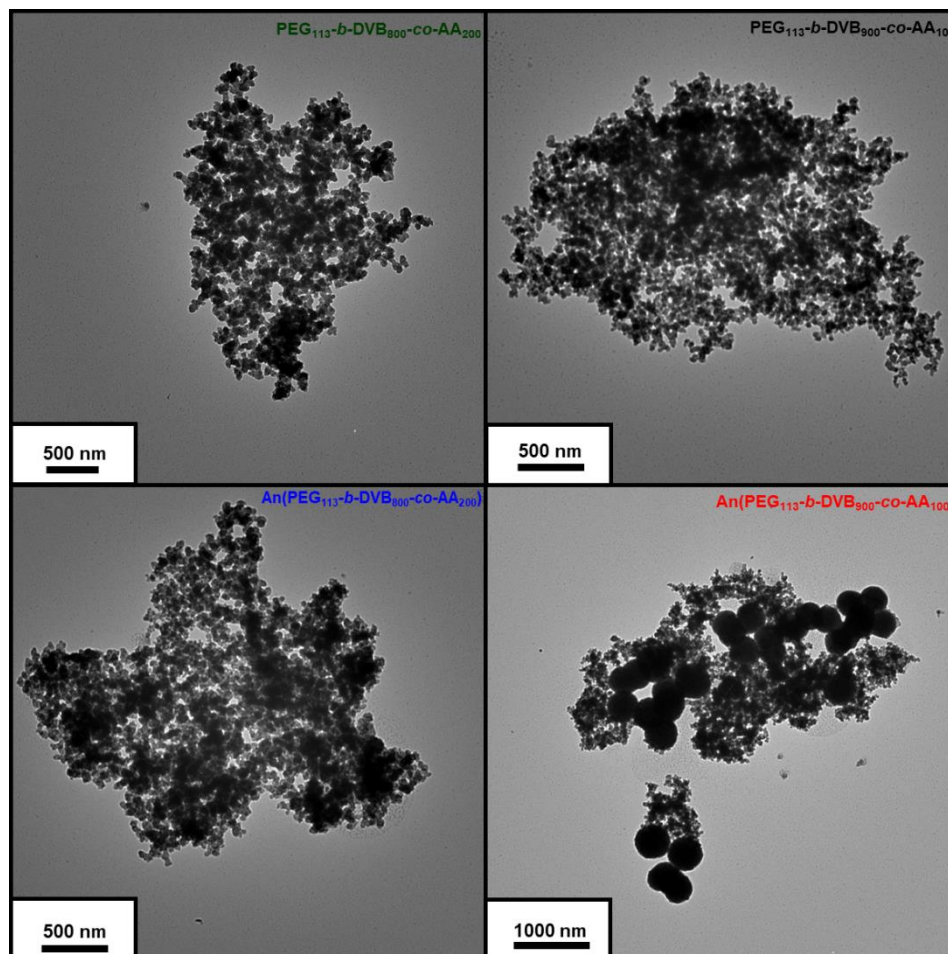


**Figure 5.12** TEM images of  $\text{PEG}_{113}\text{-}b\text{-DVB}_{800}\text{-co-AA}_{200}$ ,  $\text{PEG}_{113}\text{-}b\text{-DVB}_{900}\text{-co-AA}_{100}$ ,  $\text{An}(\text{PEG}_{113}\text{-}b\text{-DVB}_{800}\text{-co-AA}_{200})$  and  $\text{An}(\text{PEG}_{113}\text{-}b\text{-DVB}_{900}\text{-co-AA}_{100})$

### 5.5 White Light Emission

White light can be generated from organic materials by the combination of a blue emitting material and a yellow emitting material. The combined emission of these two fluorophores allows for complete coverage over the visible region of light which result in white light emission. Recently, there have been a few examples reported in the literature using porous polymers to produce white light.<sup>6-8</sup> The result of this white light emission stems from the synthesis of a conjugated porous polymer which emits a specific wavelength of light when irradiated by UV light. The porous material can then either encapsulate another fluorophore or undergo further post-synthetic modification which results in dual emission covering the entire visible spectrum of light thereby emitting white light. For example, Patra *et al.*<sup>6</sup> succeeded in synthesising a soluble CMP which emitted in the yellow region of light and could produce white light when mixed with a blue organic dye. Likewise Wang *et al.*<sup>7</sup> synthesised hyperbranched polymer particles which were post-synthetically modified to give nanoscale-CMPs that, when mixed with a red emitting dye, emit white light.

## Chapter 5. White-Light Emission

The An-PPD samples synthesised in this work are able to emit in the blue region, as a result of the anthracene incorporation. Rhodamine B is an organic material which emits in the yellow region of visible light and as such finds its use as a staining agent in microbiology. Furthermore, due to the An-PPDs being porous they should be able to incorporate and immobilise the rhodamine B into the core of the sample where it can interact with the anthracene units when irradiated with UV light. This dual emission, when tuned properly, would result in the emission of white light and is not too dissimilar from work carried out by Lin *et al.*<sup>9</sup> who synthesised a MOF using anthracene linkers before encapsulating rhodamine B to yield white light emission.

### 5.5.1 White Light Parameters

White light sources are evaluated using three parameters: Commission Internationale L'Eclairage (CIE coordinates), correlated colour temperature (CCT) and the colour rendering index (CRI). A perfect white light source has CIE coordinates of ( $x = 0.33$ ,  $y = 0.33$ ). The CCT is a measure of the colour appearance of a white light source. Light produced from warm-white light sources appear to yellow in colour, much like the older sodium lamps and halogen bulbs, and have CCT values ranging between 2700 – 3500 K. Cool-white light is seen to be blue in appearance and has CCT values ranging between 4500 – 7000 K and is what most LEDs produced emit. Finally a neutral white light source has a CCT value of between 3500 – 4500 K with horizon daylight having a CCT value of 5000 K.<sup>10</sup> Finally, the CRI is a measure of how accurate a given light source is at rendering colour compared to a reference source. It is measured on a scale of 0 – 100 with scores of above 90 being excellent, 60 – 85 being good and below 60 being quite poor. Most LEDs currently have CRI values of between 80 – 90 with daylight being around 75. Therefore, an ideal white light source would have CIE coordinates of ( $x = 0.33$ ,  $y = 0.33$ ), a CCT of close to 5000 K and a CRI as high as possible.

### 5.5.2 CIE Plots of An-PPDs and Rhodamine B

As mentioned above, white light emission is achieved when emission covers the entire visible region of light. This can be achieved by mixing blue and yellow emitting fluorophores together. Therefore the CIE coordinates of both the An(PEG<sub>113</sub>-*b*-DVB<sub>800</sub>-*co*-AA<sub>200</sub>) and rhodamine B were evaluated through their fluorescence emission spectra using the colour plotting software ColourCalculator version 7.59 provided by OSRAM. An(PEG<sub>113</sub>-*b*-DVB<sub>800</sub>-*co*-AA<sub>200</sub>) was used in these experiments due to its higher loading of anthracene. Figure 5.13 shows the CIE plots given by An(PEG<sub>113</sub>-*b*-DVB<sub>800</sub>-*co*-AA<sub>200</sub>) and the pure rhodamine B dye (the fluorescence emission spectrum of rhodamine B is shown in the appendix, Figure S5.3).

## Chapter 5. White-Light Emission

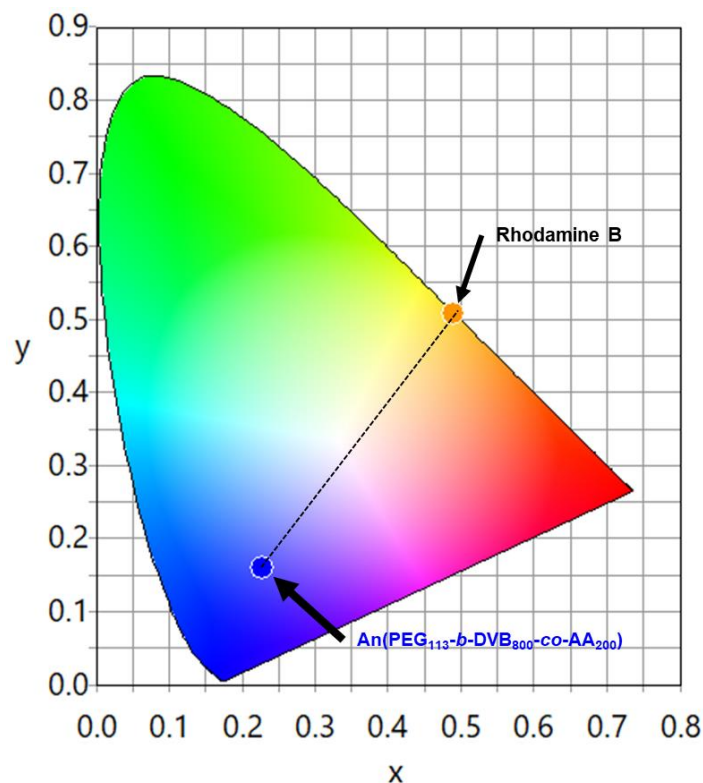


**Figure 5.13** CIE plot showing the position of An(PEG<sub>113</sub>-b-DVB<sub>800</sub>-co-AA<sub>200</sub>) and rhodamine B

As expected, An(PEG<sub>113</sub>-b-DVB<sub>800</sub>-co-AA<sub>200</sub>) lies in the blue region of this graph and the rhodamine B dye lies in the orange/yellow region due to the respective fluorescence emission of each sample. It is to be expected that through the judicious the mixing of the two fluorophores it should be possible to generate white light - an imaginary line joining these two samples would pass through the white light region of the CIE plot.

To try and produce white light varying quantities of a 0.1 mM rhodamine B stock solution was added to a 1 mg/mL dispersion of An(PEG<sub>113</sub>-b-DVB<sub>800</sub>-co-AA<sub>200</sub>). The fluorescence emission of the resulting solutions were recorded and used to generate the CIE coordinates which were then plotted (Figure 5.14).

## Chapter 5. White-Light Emission

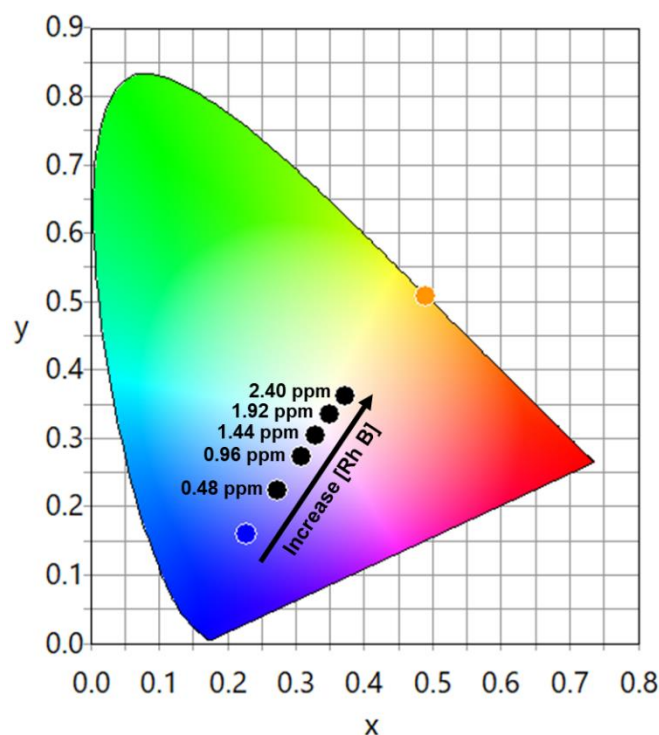


**Figure 5.14** CIE plot showing the CIE coordinates as more rhodamine B is added to a suspension of An(PEG<sub>113</sub>-*b*-DVB<sub>800</sub>-*co*-AA<sub>200</sub>)

The sequential addition of the rhodamine B stock sees the CIE coordinates of the resulting samples move towards that of the pure rhodamine B. In doing so the plot passes through the position of white light, this is best achieved when 3  $\mu$ L (1.44 ppm) and 4  $\mu$ L (1.92 ppm) of stock solution is added. Addition of these amounts gives CIE coordinates of ( $x = 0.329$ ,  $y = 0.303$ ) and ( $x = 0.350$  and  $y = 0.335$ ) respectively. 1 – 2  $\mu$ L of rhodamine B stock seems to be inadequate yet 5  $\mu$ L is too much and is now past the white light region.

To further scope this smaller amounts between 3 and 4  $\mu$ L were added to the An(PEG<sub>113</sub>-*b*-DVB<sub>800</sub>-*co*-AA<sub>200</sub>) dispersion in order to try and achieve CIE coordinates closer to that of white light. The emission spectra of the resulting samples were used to determine the CIE coordinates that were then plotted (Figure 5.15 & appendix table S5.4). It was found that addition of either 3.4  $\mu$ L (1.63 ppm) or 3.6  $\mu$ L (1.73 ppm) of rhodamine B stock was sufficient to generate white light with coordinates close to that of a perfect white light source ( $x = 0.33$ ,  $y = 0.33$ ).

## Chapter 5. White-Light Emission

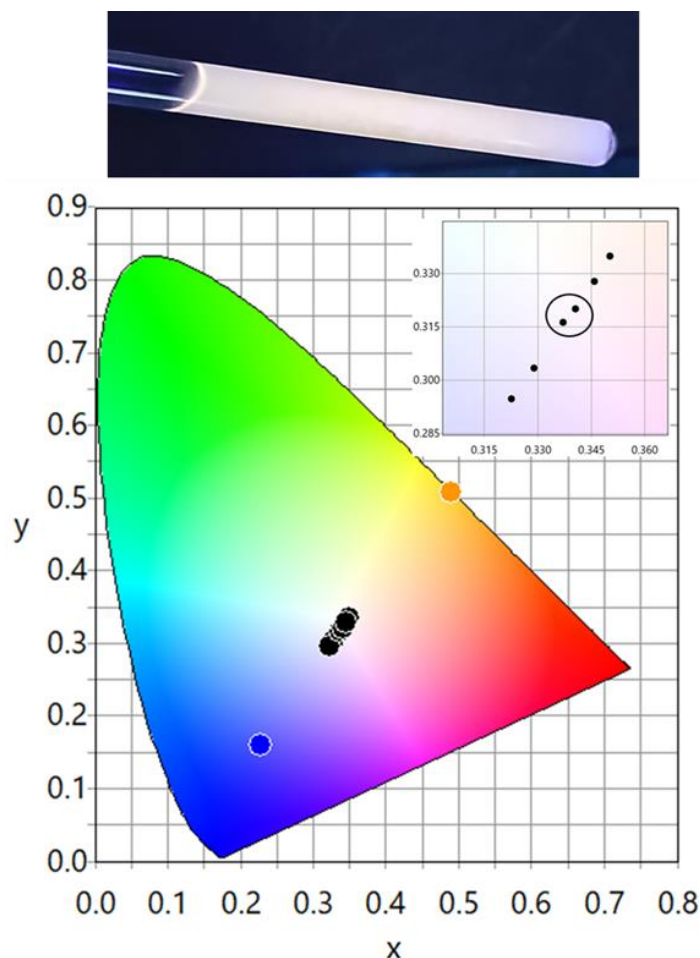


**Figure 5.15** (Above) White light generated by UV irradiation of an An(PEG<sub>113</sub>-*b*-DVB<sub>800</sub>-*co*-AA<sub>200</sub>) dispersion with 3.4  $\mu$ L of rhodamine B. (Below) CIE plot obtained after each addition of rhodamine B stock (inset is an expansion of the white light region).

### 5.5.3 Addition of Fluorescein to An-PPD:Rhodamine B suspension

Currently the best white light sample produced in this work had CIE coordinates of ( $x = 0.3372$ ,  $y = 0.3162$ ). These coordinates show that the  $x$  value seems to be in a suitable position though the  $y$  coordinate is a little lower than pure white light. Further addition of rhodamine B would move these coordinates to the right towards but not necessarily up. This would result in a larger  $x$  value but not much increase in the  $y$  coordinate. Therefore, to increase the  $y$  coordinate it is necessary to add a fluorophore which would increase the  $y$  value without affecting the  $x$  coordinate. Fluorescein is a green emitting material which could be added to the suspension of An-PPD:rhodamine B in order to tweak the CIE coordinates and move them closer to ideal white light. The CIE coordinates of pure fluorescein are ( $x = 0.3025$ ,  $y = 0.6200$ ) as determined from the fluorescence emission spectrum in methanol (see appendix Figure S5.4). These CIE coordinates places fluorescein in the green region of the CIE plot above rhodamine B but also to the left given its smaller  $x$  value. This should mean that addition

## Chapter 5. White-Light Emission

of this solution to RhB@An(PEG<sub>113</sub>-*b*-DVB<sub>800</sub>-co-AA<sub>200</sub>) will result in an increase of the y coordinate without affecting the x coordinate. Much like the previous experiment with rhodamine B it is possible to add small quantities of fluorescein to optimise the resulting emission (Figure 5.16).

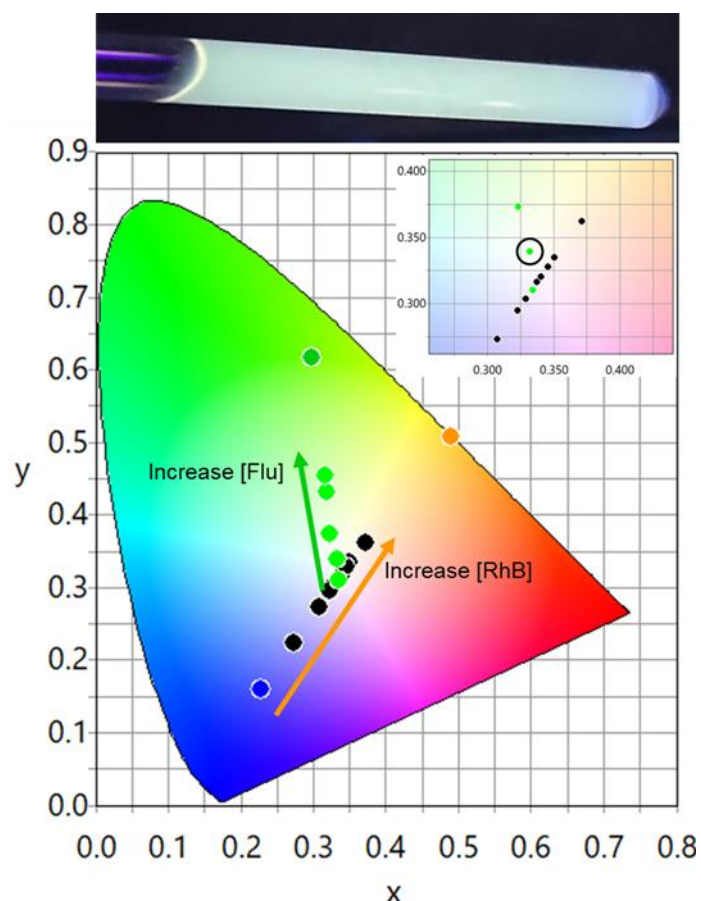


**Figure 5.16** (Above) White light generated by UV irradiation of RhB:Flu@An(PEG<sub>113</sub>-*b*-DVB<sub>800</sub>-co-AA<sub>200</sub>). (Below) The CIE coordinates obtained when adding sequential amounts of fluorescein to an RhB@An(PEG<sub>113</sub>-*b*-DVB<sub>800</sub>-co-AA<sub>200</sub>) suspension. Dark green dot shows the position of pure fluorescein

It was found that only 0.24 ppm of fluorescein was required to generate a solution with CIE coordinates very close to white light ( $x = 0.3322$ ,  $y = 0.3393$ ). As expected the addition of fluorescein elevated the y coordinate but did not greatly affect the x coordinate which allowed for tuning of the overall position of this solution (Figure 5.16).

### 5.5.4 CCT and CRI of White Light Suspensions

Though CIE coordinates are the clearest and most common method to characterise a white light source the CCT and CRI parameters are still important factors to consider for any white light emitting source. Therefore, the CCT and CRI values for the optimum solutions made in

## Chapter 5. White-Light Emission

this work were determined using the same ColourCalculator software used to obtain the CIE coordinates.

The CCT value obtained for the RhB@An(PEG<sub>113</sub>-*b*-DVB<sub>800</sub>-*co*-AA<sub>200</sub>) sample (containing 1.44 ppm of rhodamine B) has a CCT value of 5239 K. This places this white light source in the region of white light often attributed to cool white light emitting materials, which have a slight blue appearance. However, this value is not too far away from the CCT value of horizon daylight which is 5000 K. Upon addition of fluorescein the CCT value increases to 5511 K which is not too significant and is still very much in the region of cool white light (4500 – 7000 K). The CRI value of RhB@An(PEG<sub>113</sub>-*b*-DVB<sub>800</sub>-*co*-AA<sub>200</sub>) was found to be around 50 which is quite low meaning it would not be a suitable source of light to use in a place which requires good visibility, i.e. a warehouse or industrial building where identifying subtle differences is a key part of a job. Addition of fluorescein to this suspension sees the CRI increase slightly to 54 though again this value is still poor in relation to LED sources. These results imply that, although the CIE coordinates are close to that of an ideal white light source these solutions still require further modification to try and increase these values and generate more optimised white light emission.

### 5.5.5 Quantum Yield

The quantum yield of a sample is defined as the ratio of photons absorbed to photons emitted through fluorescence and is essentially a measure of the efficiency of the fluorescence process. It can be calculated experimentally by measuring the absorbance and fluorescence emission of both a standard and the sample under investigation by using the equation<sup>11</sup>:

$$\Phi_X = \Phi_{ST} \left( \frac{Grad_X}{Grad_{ST}} \right) \left( \frac{n_X^2}{n_{ST}^2} \right)$$

where  $\Phi$  is the quantum yield of the analyte (x) and standard (ST), Grad is the gradient of the plotted absorbance and fluorescence data and n is the refractive index of the solvent).

Using this method the quantum yield of the RhB@An(PEG<sub>113</sub>-*b*-DVB<sub>800</sub>-*co*-AA<sub>200</sub>) was estimated. Figure 5.17 shows the data obtained when plotting the maxima of the fluorescence and absorbance for both the standard rhodamine B solution and the RhB@An(PEG<sub>113</sub>-*b*-DVB<sub>800</sub>-*co*-AA<sub>200</sub>) suspension. It is important that the standard used for the quantum yield determination has a similar absorbance and emission spectrum to that of the analyte. Given that rhodamine B does and is commonly used as a standard in these experiments it seemed logical to use this pure solution as the standard.

## Chapter 5. White-Light Emission

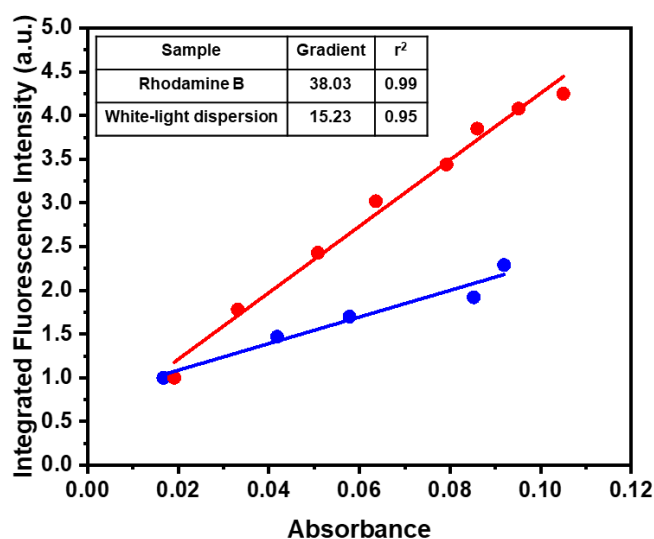


**Figure 5.17** Data used to calculate the quantum yield of RhB@An(PEG<sub>113</sub>-*b*-DVB<sub>800</sub>-*co*-AA<sub>200</sub>)

The quantum yield of the RhB@An(PEG<sub>113</sub>-*b*-DVB<sub>800</sub>-*co*-AA<sub>200</sub>) sample was found to be 38 %. This is superior to other porous polymer materials used to generate white light who range between 10 % – 35 %.<sup>6,9</sup>

### 5.5.6 Literature Comparison

There have been some examples of porous materials being used for applications in white light emission. Most of these examples work in a similar way to this work in that a porous fluorophore encapsulates another fluorophore(s) and the dual emission of these materials gives rise to white light. To gain a better insight as to how the work carried in this chapter fares to similar work in the literature a comparison was carried out with other porous materials (Table 5.4).

**Table 5.5** Comparison of the white light parameters of similar bodies of work

Sample	CIE X	CIE Y	CCT	CRI	QY	Ref.
RhB@An(PEG <sub>113</sub> - <i>b</i> -DVB <sub>800</sub> - <i>co</i> -AA <sub>200</sub> )	0.3372	0.3162	5239	50	38 %	This Work
RhB:Flu@An(PEG <sub>113</sub> - <i>b</i> -DVB <sub>800</sub> - <i>co</i> -AA <sub>200</sub> )	0.3322	0.3393	5511	54	-	This Work
RhB@Al-DBA	0.32	0.30	6058	-	12 %	9
TPDC-BZ (solution)	0.34	0.31	5290	84	14 %	6
TPDC-BZ (NPs)	0.29	0.32	7750	93	35 %	6
TPDC-BZ (gel)	0.31	0.28	6942	79	14 %	6
3% Eu <sup>3+</sup> :Y <sub>2</sub> WO <sub>6</sub>	0.327	0.312	5571	-	11 – 38 %	12

## Chapter 5. White-Light Emission

The CIE coordinates for the samples produced in this work seem to more closely match those of an ideal white light source. However the CRI values are much lower than others reported in the literature. The CCT values of the samples in this work seem to be similar to other literature examples and are similar to that of a cold white light source.

### 5.6 Conclusion

The same synthetic approach used to synthesise PEG-b-DVB-co-FN porous dispersions was applied to yield similar porous materials but this time using acrylic acid in place of the fumaronitrile. The ability to replace one co-monomer with another highlights the versatility of the synthetic approach and demonstrated how easy it is to synthesise new materials through modifying only one feature. The resulting material was found to be porous and isostructural in nature to the FN/DVB systems in that both were found to form aggregated morphologies instead of spherical individual micelles. This feature is still attributed to the presence of DVB.

What was not previously investigated with the FN/DVB system was the ability to post-synthetically modify the resulting material. In this chapter the acrylic acid, polymerised and present in the final material, was reacted with 9-anthracenemethanol *via* an esterification reaction to give a final material containing anthracene units. The success of this reaction was confirmed by both solid state (FTIR, ssNMR) and solution phase (UV-Vis and fluorescence emission spectroscopy) analysis techniques, something which would not be possible with conventional insoluble porous polymers. These techniques confirmed that the reaction had resulted in the presence of anthracene units present in the core of the material.

Finally, given that the sample was now both porous and luminescent it was possible to encapsulate other organic fluorophores and use these materials to produce white-light. This was done through fine-tuning the mixtures of both polymer and organic fluorophore to produce white light. These results were compared to other porous materials used for these applications where it was found that the results compared very favourably.

## Chapter 5. White-Light Emission

### 5.7 Experimental

#### 5.7.1 Materials

Divinylbenzene (DVB, technical grade 80 %) and acrylic acid (AA, extra pure 98 %) were purchased from Sigma-Aldrich and Acros organics respectively and were passed through an alumina column before use to remove inhibitors. Azobis(2- methylpropionitrile) (AIBN, 98 %), potassium persulfate (KPS, > 99.99 % pure), 9-anthracenemethanol (9-AnMeOH, 97 %), N,N'-dicyclohexylcarbodiimide (DCC, > 99.9 % pure, GC grade), 4-dimethylaminopyridine (DMAP, reagent plus > 99 % pure), rhodamine B (> 95 % pure, HPLC grade) and fluorescein (free acid, 95 % dye content) were all purchased from Sigma-Aldrich and used as received. All solvents were purchased from Fisher scientific and used as received. Dry chloroform was obtained in a method analogous to the one outlined by Grubbs.<sup>13</sup>

#### 5.7.2 Free Radical Polymerisation of Divinylbenzene and Acrylic Acid

A series of DVB/AA co-polymers were synthesised by varying the ratio of DVB to AA (see appendix, table S5.1). The general reaction procedure for one sample is outlined as follows. To a sample vial divinylbenzene (0.28 mL, 2 mmol, 1 eq.) and acrylic acid (0.14 mL, 2 mmol, 1 eq.) were added. The vial was sealed with a rubber septum and placed under nitrogen through three freeze-pump-thaw cycles after which toluene (10 mL) was added. The vial was placed in an oil bath and heated to 80 °C after which AIBN (4 mg, 0.02 mmol, 1% wt. wrt monomers) was added to initiate polymerisation. The solution was held at 80 °C for 24 hours before being cooled to room temperature and collected *via* reprecipitation into methanol. The samples was washed with before being washed with THF and methanol under soxhlet apparatus overnight before being collected and dried overnight at 60 °C under vacuum.

#### 5.7.3 RAFT-PISA of DVB and AA using a PEG macro-CTA

A series of samples were made through varying the incorporation of DVB and AA. The synthesis of one sample is outlined here, see appendix table S5.2, for reaction quantities for other samples. The PEG-based macro-CTA (0.13 g, 0.02 mmol 1 eq., see chapter 3 for experimental) was added to a 2-neck round bottom flask which was evacuated and back-filled with nitrogen three times. Water (72 mL) and ethanol (60 mL), in a 60:40 ratio, were added along with DVB (2 mL, 14 mmol, 700 eq.) and AA (0.41 mL, 6 mmol, 300 eq.) to create a 1 wt % solution. Nitrogen gas was bubbled through the solution for approximately 30 mins to thoroughly degas the sample before heating to 70 °C. Polymerisation was initiated through the addition of KPS (1 mg, 0.004 mmol, 0.2 eq.). After 24 hours the solution was centrifuged and the white sediment stirred in diethyl ether before being collected under vacuum. The final white solid was dried under vacuum at 40 °C for 16 hours.

## Chapter 5. White-Light Emission

### 5.7.3 Esterification of PEG<sub>113</sub>-*b*-DVB<sub>800</sub>-*co*-AA<sub>200</sub> Using 9-Anthracenemethanol

An amount of the synthesised PPD (0.50 g) was added to a round bottom flask filled with dry chloroform (30 mL). The solution was sonicated for 30 minutes to form a homogeneous and stable dispersion. To this solution was added 9-anthracenemethanol (0.832 g, 4 mmol), *N,N'*-dicyclohexylcarbodiimide (0.825 g, 4 mmol) and 4-dimethylaminopyridine (0.061 g, 0.5 mmol) in chloroform (10 mL) and was stirred for 24 hours at room temperature. The solution was centrifuged at 4000 rpm for 60 minutes which led to the sample sitting on top of the liquid due to its light density. The sample was collected *via* vacuum filtration before being washed with more chloroform and methanol to remove the *N,N'*-dicyclohexylurea formed during the reaction. Finally the sample was dried under vacuum overnight at 60 °C to give a white/pale-yellow solid as the final product.

### 5.7.4 Esterification of PEG<sub>113</sub>-*b*-DVB<sub>900</sub>-*co*-AA<sub>100</sub> using 9-Anthracenemethanol

An amount of the synthesised PPD (0.50 g) was added to a round bottom flask filled with dry chloroform (30 mL). The solution was sonicated for 30 minutes to form a homogeneous and stable dispersion. To this solution was added 9-anthracenemethanol (0.416 g, 2 mmol), *N,N'*-dicyclohexylcarbodiimide (0.412 g, 2 mmol) and 4-dimethylaminopyridine (0.03 g, 0.25 mmol) in chloroform (10 mL) and was stirred for 24 hours at room temperature. The solution was centrifuged at 4000 rpm for 60 minutes which led to the sample sitting on top of the liquid due to its light density. The sample was collected *via* vacuum filtration before being washed with more chloroform and methanol to remove the *N,N'*-dicyclohexylurea formed during the reaction. Finally, the sample was dried under vacuum overnight at 60 °C to give a white/pale-yellow solid as the final product.

### 5.7.5 Synthesis of 9-Anthracenemethyl Acrylate Monomer

The synthesis of 9-anthracene methacrylate was carried out in an analogous manner to the synthesis outlined by Pazicni *et al.*<sup>4</sup> 9-Anthracenemethanol (2.50 g, 12 mmol), *N,N'*-dicyclohexylcarbodiimide (4.95 g, 12 mmol) and 4-dimethylaminopyridine (0.22 g, 1.8 mmol) were all added to a 2-necked round bottom flask and placed under nitrogen. Dry acetonitrile (30 mL) and acrylic acid (1.65 mL, 24 mmol) before being left to stir at room temperature for 24 h. The mixture was vacuum filtrated to remove the *N,N'*-dicyclohexylurea formed during the reaction and the filtrate concentrated under reduced pressure. The final product was precipitated into methanol and dissolved in chloroform three times to remove any further impurities before being dried *in vacuo* at 40 °C overnight. Yield: 1.143 g (73 %). <sup>1</sup>H-NMR (400 MHz, CDCl<sub>3</sub>): δ 8.55 (s, 1H), 8.39 (d, 2H), 8.07 (d, 2H), 7.65 – 7.56 (m, 2H), 7.54 - 7.49 (m, 2H), 6.45 (dd, 1H), 6.27 (s, 2H), 6.16 (dd, 1H), 5.83 (dd, 1H).

## Chapter 5. White-Light Emission

## 5.8 Appendix

Table S5.1 Reaction quantities used to synthesis the insoluble DVB/AA porous polymers

Sample	DVB	AA	AIBN	% Yield
IP-50/50	0.28 mL, 2 mmol	0.14 mL, 2 mmol	4.0 mg	45
IP-60/40	0.34 mL, 2.4 mmol	0.11 mL, 1.6 mmol	4.3 mg	49
IP-70/30	0.40 mL, 2.8 mmol	0.08 mL, 1.2 mmol	4.5 mg	66
IP-80/20	0.46 mL, 3.2 mmol	0.05 mL, 0.8 mmol	4.8 mg	76
IP-90/10	0.51 mL, 3.6 mmol	0.025 mL, 0.4 mmol	5.0 mg	89

10 mL of toluene solvent was used for each reaction, AIBN was added at 1% wt wrt. monomer mass, yield was calculated based on total amount of monomer added

Table S5.2 Reaction quantities used to synthesis PPD samples

Sample	DVB	AA	CTA	KPS	% Yield
PEG <sub>113</sub> - <i>b</i> -DVB <sub>700</sub> - <i>co</i> -AA <sub>300</sub>	2.00 mL, 14 mmol	0.41 mL, 6 mmol	0.13 g, 0.02 mmol	1 mg	40
PEG <sub>113</sub> - <i>b</i> -DVB <sub>800</sub> - <i>co</i> -AA <sub>200</sub>	2.28 mL, 16 mmol	0.28 mL, 4 mmol	0.13 g, 0.02 mmol	1 mg	35
PEG <sub>113</sub> - <i>b</i> -DVB <sub>900</sub> - <i>co</i> -AA <sub>100</sub>	2.56 mL, 18 mmol	0.14 mL, 2 mmol	0.13 g, 0.02 mmol	1 mg	30

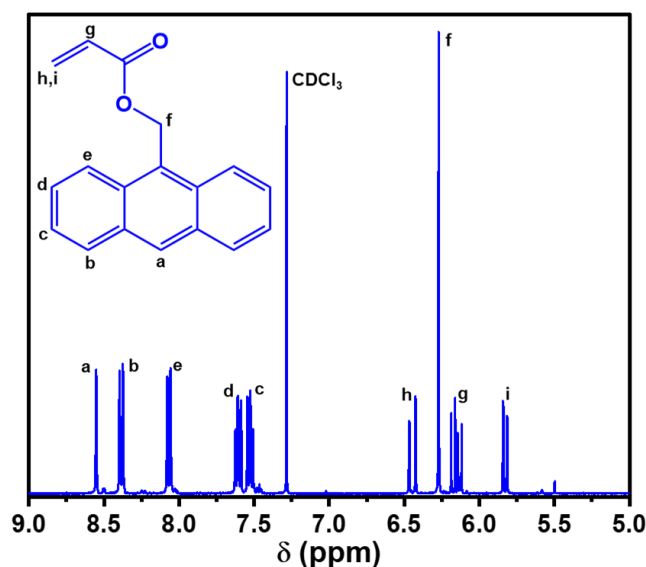

 Figure S5.1 <sup>1</sup>H-NMR of 9-anthracenemethyl acrylate in CDCl<sub>3</sub>

Table S5.3 Surface area and pore volume data for each An-PPD sample

Sample	SA <sub>BET</sub> (m <sup>2</sup> /g)	V <sub>TOT</sub>	V <sub>0.1</sub>	V <sub>0.1</sub> /V <sub>TOT</sub>
An-PPD(80/20)	188	0.24	0.06	0.25
An-PPD(90/10)	152	0.19	0.05	0.26

Chapter 5. White-Light Emission

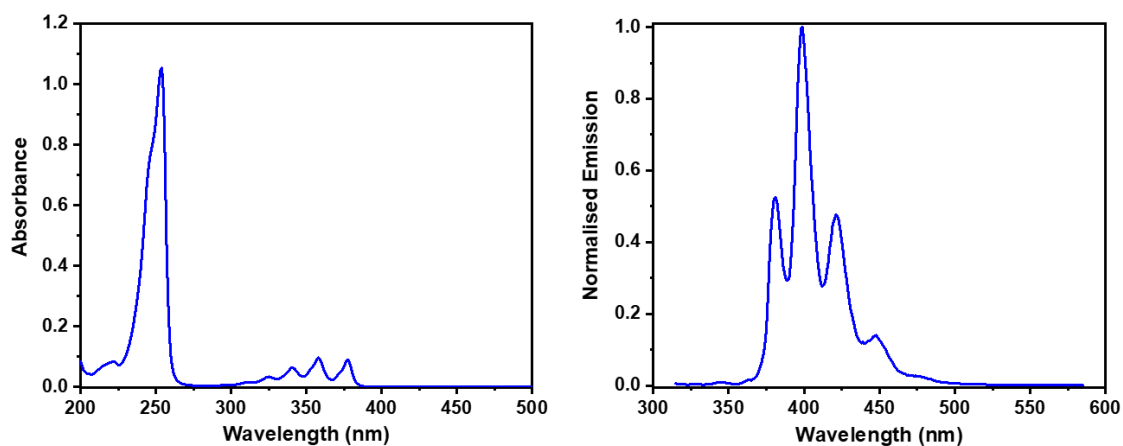


Figure S5.2 UV-Vis (left) and fluorescence emission (right) spectra of anthracene

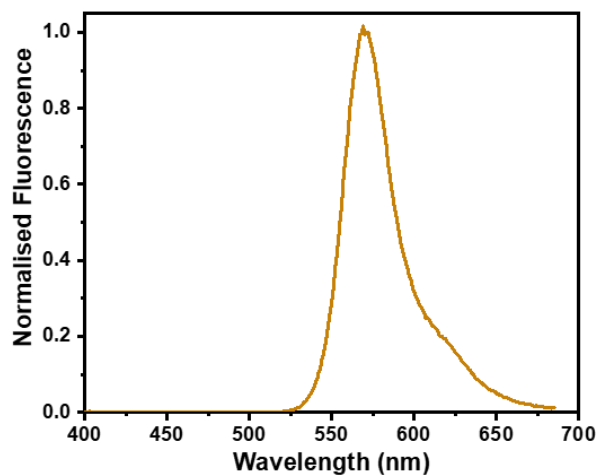
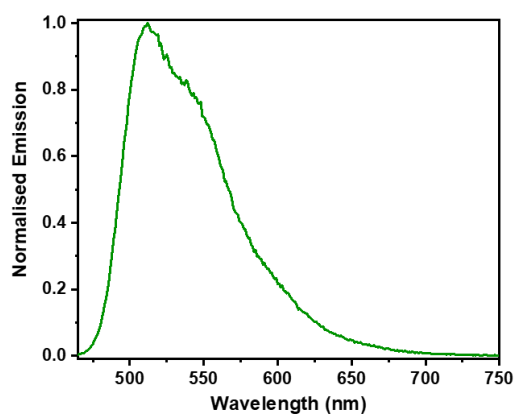


Figure S5.3 Fluorescence emission spectrum of rhodamine B

Table S5.3 CIE coordinates of each sample after addition of rhodamine B

Rhodamine B (uL)	CIE x	CIE y
3.0	0.3290	0.3034
3.2	0.3227	0.2947
3.4	0.3372	0.3162
3.6	0.3407	0.3201
3.8	0.3459	0.3277
5.0	0.3504	0.3349

## Chapter 5. White-Light Emission



**Figure S5.4** Fluorescence emission spectrum of fluorescein

## Chapter 5. White-Light Emission

### 5.9 References

- 1 R. Dawson, L. A. Stevens, T. C. Drage, C. E. Snape, M. W. Smith, D. J. Adams and A. I. Cooper, *J. Am. Chem. Soc.*, 2012, **134**, 10741–10744.
- 2 S. Yao, X. Yang, M. Yu, Y. Zhang and J.-X. Jiang, *J. Mater. Chem. A*, 2014, **2**, 8054.
- 3 N. Fontanals, J. Cortés, M. Galià, R. M. Marcé, P. A. G. Cormack, F. Borrull and D. C. Sherrington, *J. Polym. Sci. Part A Polym. Chem.*, 2005, **43**, 1718–1728.
- 4 K. J. Rodriguez, A. M. Hanlon, C. K. Lyon, J. P. Cole, B. T. Tuten, C. A. Tooley, E. B. Berda and S. Pazicni, *Inorg. Chem.*, 2016, **55**, 9493–9496.
- 5 D. Han, H. Lu, W. Li, Y. Li and S. Feng, *RSC Adv.*, 2017, **7**, 56489–56495.
- 6 P. Pallavi, S. Bandyopadhyay, J. Louis, A. Deshmukh and A. Patra, *Chem. Commun.*, 2017, **53**, 1257–1260.
- 7 P. Zhang, K. Wu, J. Guo and C. Wang, *ACS Macro Lett.*, 2014, **3**, 1139–1144.
- 8 J. Liu, K.-K. Yee, K. K.-W. Lo, K. Y. Zhang, W.-P. To, C.-M. Che and Z. Xu, *J. Am. Chem. Soc.*, 2014, **136**, 2818–2824.
- 9 Z. Wang, Z. Wang, B. Lin, X. Hu, Y. Wei, C. Zhang, B. An, C. Wang and W. Lin, *ACS Appl. Mater. Interfaces*, 2017, **9**, 35253–35259.
- 10 A. K. R. Choudhury and A. K. R. Choudhury, *Princ. Colour Appear. Meas.*, 2014, 1–52.
- 11 C. Würth, M. Grabolle, J. Pauli, M. Spieles and U. Resch-Genger, *Nat. Protoc.*, 2013, **8**, 1535–1550.
- 12 R. Van Deun, D. Ndagsi, J. Liu, I. Van Driessche, K. Van Hecke and A. M. Kaczmarek, *Dalt. Trans.*, 2015, **44**, 15022–15030.
- 13 A. B. Pangborn, M. A. Giardello, R. H. Grubbs, R. K. Rosen and F. J. Timmers, *Organometallics*, 1996, **15**, 1518–1520.

## *Part B – Applications in Sustainability*

This part of the thesis describes the work carried out on designing HCPs towards sustainable applications. Chapter 6 presents work on the design and application of sulfonated HCPs for use in the environmental sequestration of Sr and Cs. Chapter 7 investigates functionalised HCPs towards capturing CO<sub>2</sub> from industrial point sources *via* a pressure-swing approach.

# Chapter 6 - Remediation of Sr and Cs using Sulfonated Hypercrosslinked Polymers

This work has been published in *ACS Applied Materials & Interfaces* and can be found on their journal website using the DOI (<https://doi.org/10.1021/acsami.9b06295>).

James, A. M. *et al.* Selective Environmental Remediation of Strontium and Cesium Using Sulfonated Hyper-Cross-Linked Polymers (SHCPs). *ACS Appl. Mater. Interfaces* **11**, 22464–22473 (2019).

## Chapter 6. Sr and Cs Sequestration Using Sulfonated HCPs

### 6.1 Chapter Foreword

#### Selective Environmental Remediation of Strontium and Cesium Using Sulfonated Hyper-Cross-Linked Polymers (SHCPs)

Alex M. James, Samuel Harding, Thomas Robshaw, Neil Bramall, Mark D. Ogden, and Robert Dawson

Microporous polymer are very good candidates for the removal of metal ions from aqueous solution due to a number of different reasons. These materials possess high surface areas, demonstrate high stability, can incorporate functionality into the final material both pre- and post-synthesis and can be synthesised very readily. As such, there have been a number of reports using MOPs to uptake a variety of different metal ions from aqueous solutions of varying pH and temperature. However, MOPs have some significant disadvantages such as the need for metal catalysts in their synthesis, which is both environmentally harmful and increases the cost of the synthesis, two issues which need to be overcome in order to allow the synthesis to be scaled-up.

In this chapter, which is presented as a research paper, the metal-free synthesis of a sulfonated HCP is reported based on the polymerisation of BCMBP using sulphuric acid as the catalyst. Upon synthesis, the material is post-synthetically modified using chlorosulfonic acid which decorates the material with sulfonate groups. The final material, SHCP-1, has a BET surface area exceeding 800 m<sup>2</sup>/g and is able to selectively remove both Sr and Cs from aqueous solution in the presence of other competing ions.

Below is a breakdown of the main tasks of each author named on this manuscript:

**Alex M James** – Came up with the research concept for the project and attained research funding to hire SH to carry out the work. Supervised SH for duration of project, oversaw and carried out synthesis of materials reported in work, conducted all gas sorption experiments and interpreted the data collected from other characterisation methods reported in the paper and wrote the manuscript. Supervised by RD.

**Samuel Harding** – Supervised by AMJ for entire duration of project. Involved in the synthesis of the materials reported in work and collected some characterisation data.

**Thomas Robshaw** – Supervised by RD and MDO. Collected the kinetic uptake data and isotherm studies

**Neil Brammal** – Carried out all ICP-MS data experiments and data analysis reported in this work

**Mark. D. Ogden** – Supervisor of TR, was involved in writing the introduction section of the manuscript.

## Chapter 6. Sr and Cs Sequestration Using Sulfonated HCPs

**Robert Dawson** – Supervisor of AMJ and TR was involved in writing of manuscript and aided in interpreting the data collected by SH, AMJ and TR.

Funding for SH was obtained by AMJ through application to the SURE (Sheffield Undergraduate Research Experience) scheme. This scheme allows for postgraduates students to write a research proposal, which undergoes internal peer review before being awarded. Finally, the postgraduate interviews and hires an undergraduate student to undertake an eight-week research placement fully under their supervision. As such, SH and AMJ would like to thank the SURE scheme for both the student stipend and consumables budget the scheme awarded to them.

# Selective Environmental Remediation of Strontium and Cesium Using Sulfonated Hypercrosslinked Polymers (SHCPs)

Alex M. James,<sup>a</sup> Samuel Harding,<sup>a</sup> Thomas Robshaw<sup>ab</sup> Neil Bramall,<sup>a</sup> Mark D. Ogden<sup>b</sup> and Robert Dawson<sup>a\*</sup>

<sup>a</sup>Department of Chemistry, Dainton Building, University of Sheffield, UK, S3 7HF

<sup>b</sup>Department of Chemical and Biological Engineering, Sir Robert Hadfield Building, University of Sheffield, UK, S1 3JD

**ABSTRACT:** Sulfonated hypercrosslinked polymers based on 4,4'-bis(chloromethyl)-1,1'-biphenyl (BCMBP) were synthesized via metal-free (SHCP-1) and conventional Lewis acid-catalyzed (SHCP-2) Friedel-Crafts alkylation routes. The sulfonated polymers possessed BET surface areas in excess of 500 m<sup>2</sup> g<sup>-1</sup>. SHCP-1 was investigated for its ability to extract Sr and Cs ions from aqueous solutions via the ion-exchange reaction of the sulfonic acid moiety. Equilibrium uptake data could be accurately modelled by the Dubinin-Radushkevich isotherm, with maximum calculated loading values of 95.6 ± 2.8 mg g<sup>-1</sup> (Sr) and 273 ± 37 mg g<sup>-1</sup> (Cs). Uptake of both target ions was rapid, with pseudo 2nd-order rate constants calculated as 7.71 ± 1.1 (× 10<sup>-2</sup>) for Sr and 0.113 ± 0.014 for Cs. Furthermore, the polymer was found to be selective towards the target ions over large excesses of naturally occurring competing metal ions such as Na and K. We conclude that hypercrosslinked polymers may offer intrinsic advantages over other adsorbents for the remediation of aqueous Sr and Cs contamination.

**Keywords:** porous materials, microporous polymers, metal-free synthesis, ion-exchange, separations,

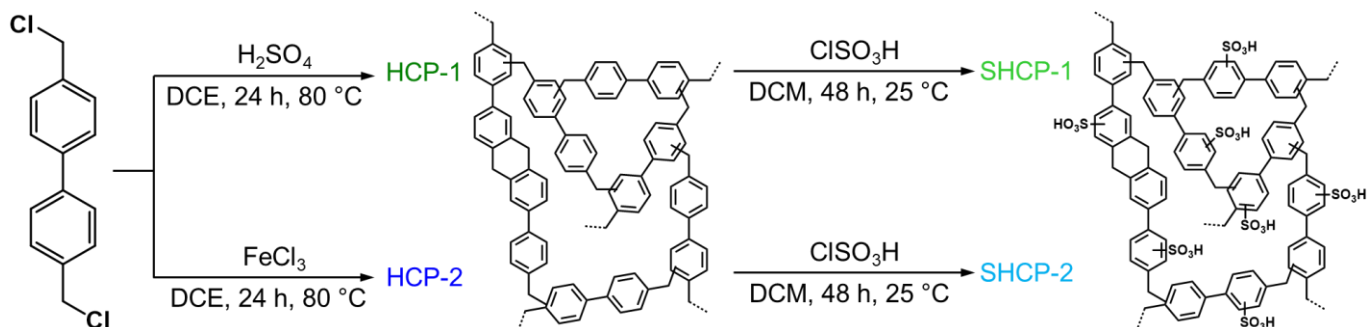
## Introduction

Prior to 1986, the release of fission products to the environment was predominantly as a result of nuclear weapons testing and direct discharges from nuclear reprocessing facilities.<sup>1</sup> Since then, the world has seen two category 7 nuclear accidents at Chernobyl in the Ukraine (1986) and Fukushima Daiichi (2011) in Japan which resulted in the uncontrolled release of fission products into the environment. Fission products <sup>137</sup>Cs and <sup>90</sup>Sr are of a particular concern due to both their radiotoxicity and their ability to bioaccumulate.<sup>2</sup> <sup>137</sup>Cs (t<sub>1/2</sub> = 30.17 years) is a strong beta-gamma emitter and <sup>90</sup>Sr (t<sub>1/2</sub> = 28.8 years) is a beta emitter and a large source of radiation, having a specific activity of 5.21 TBq·g<sup>-1</sup>.<sup>3</sup> Cesium metabolically and chemically behaves similarly to potassium and sodium in terrestrial ecosystems, whereas strontium behaves analogously to calcium.<sup>4</sup> It is estimated that 1.5 × 10<sup>16</sup> Bq of <sup>137</sup>Cs was released from the Fukushima Daiichi accident and 3.8 × 10<sup>16</sup> Bq from Chernobyl.<sup>2</sup> <sup>90</sup>Sr releases were estimated much lower with activities of 4 × 10<sup>15</sup> and 3.5 × 10<sup>13</sup> Bq<sup>6</sup> for the Chernobyl and Fukushima Daiichi accidents respectively.

A variety of techniques have been applied to the removal of these problematic radionuclides from ground water and aqueous solutions. Previous tests, using conventional water treatment technologies of coagulation, flocculation and settling proved only effective enough to remove 56% of <sup>137</sup>Cs<sup>7</sup> and 5.9-12% of <sup>90</sup>Sr<sup>8</sup> depending on the coagulant. Solvent extraction systems have also been widely studied.

These generally use a crown ether functionality, with selectivity related to cavity size. Such materials have demonstrated good recoveries, but require carefully-chosen, poorly-hydrated counteranions to maximise efficiency<sup>9-11</sup> and their potential for use in direct environmental remediation is obviously limited.

In terms of solid-phase extractants, adsorbents based on ion-exchange have demonstrated good efficacy in the removal of these radionuclides from a variety of aqueous solutions. Examples of these are polymeric resins,<sup>4,12</sup> natural and synthetic zeolites,<sup>13,14</sup> titanates,<sup>15</sup> silica,<sup>16</sup> and titanosilicates.<sup>17</sup> Inorganic ion-exchangers are more mechanically and thermally stable than their polymer counterparts, offer good resistance to radiolysis and have high capacity in many cases (>3 meq·g<sup>-1</sup>).<sup>18</sup> However, the exchange processes are often reversible and Na and K ions at high concentrations can be significant interferences,<sup>14,19</sup> which is especially problematic for remediation of brine. Polymeric ion-exchangers are generally more chemically stable<sup>20</sup> and a wide variety of functionalities can be imparted on to the solid matrix for targeted and non-reversible ion removal.<sup>21,22</sup> There is therefore potential for the development of a novel, solid-phase adsorbent for capture of Sr and Cs ions, combining both selectivity and applied practicality. Key parameters for an effective ion-exchanger are the maximum loading capacity, which correlates directly to the number of exchanging moieties on the surface, and the rate of extraction. Porosity of the adsorbent can be increased to effectively improve the surface area but the diffusion of analytes into the porous network can slow the kinetics of the extraction.<sup>20</sup>



**Scheme 1.** Synthesis and sulfonation of hypercrosslinked polymer networks.

Hypercrosslinked polymers (HCPs) are a sub class of microporous organic polymers (MOPs) with high surface areas (typically  $500\text{--}2000\text{ m}^2\cdot\text{g}^{-1}$ ).<sup>23–25</sup> They are both chemically and thermally stable, can be synthesised using cheap and facile methods from readily available precursors and can be easily functionalised.<sup>26</sup> Rigid aromatic monomers possessing “internal crosslinkers”, such as chloromethyl groups, can be reacted via a Friedel-Crafts alkylation route in the presence of a Lewis-acid such as  $\text{FeCl}_3$ ,  $\text{AlCl}_3$  and  $\text{SnCl}_4$ .<sup>27–29</sup> Rigid aromatic monomers not possessing such internal crosslinkers can also be reacted via an “external crosslinker” such as formaldehyde dimethyl acetal. This strategy, referred to as the “knitting” method, was developed in 2011 by Tan and co-workers<sup>30</sup> and is a convenient way to introduce functionalization into the final material.<sup>31,32</sup> Although the metal catalysts used are effective and yield materials with high surface areas, they require stoichiometric quantities, produce large amounts of acidic waste, and have to be rigorously washed out of the network post-synthesis, yet in most cases cannot be completely removed from the final product. This is particularly relevant for water-treatment applications, as iron-fouling can be a significant issue in industrial ion exchange columns. Recently Schute *et al.* used  $\text{H}_2\text{SO}_4$  as the Lewis-acid catalyst for the hypercrosslinking of a range of monomers via both internal and external crosslinking routes.<sup>33</sup> This method took less time to reach full conversion, did not require inert reaction conditions and was more economic and environmentally-friendly than metal-catalysed synthesis. Although the materials produced had slightly lower surface areas ( $921\text{ m}^2\cdot\text{g}^{-1}$  vs  $1182\text{ m}^2\cdot\text{g}^{-1}$  with  $\alpha,\alpha'$ -*p*-dichloroethylene monomer), the technique was a convenient and facile route towards microporous networks.

HCPs have previously been explored for various applications including gas separation,<sup>34</sup> catalysis<sup>23</sup> and wastewater treatment.<sup>35, 36</sup> The ability to tailor the final microstructure<sup>37</sup> and functionality<sup>38</sup> of the polymer towards the application is a key property which makes HCPs inherently suitable materials to treat wastewater streams and remove pollutants. They have not yet however, been investigated for Cs and Sr removal. The sulfonic acid group is a well-known functionality in the field of ion-exchange and is commonly used with macroporous or gel-type polymer matrices to create the well-known strong acid cation (SAC) ion-exchange resin.

There is a well-known order of selectivity of cations for this functionality, influenced by both charge and ionic radius.<sup>39</sup> With this in mind, it can be hypothesised that both Sr and Cs ions will be selectively extracted from aqueous solution by adsorbents incorporating sulfonic acid groups, even with high concentrations of naturally occurring ions such as Na and K, which are markedly lower in the selectivity series.

Therefore, we report the synthesis of BCMBP hypercrosslinked networks synthesised using both  $\text{H}_2\text{SO}_4$  (HCP-1) and  $\text{FeCl}_3$  (HCP-2) as the acid catalyst, followed by sulfonation using chlorosulfonic acid as the sulfonating agent (Scheme 1). This is the first report of a functionalised Friedel-Crafts HCP synthesised without metal catalysts and the first ever characterised sulfonic acid-bearing hypercrosslinked polymer networks. The polymers are thoroughly assessed for use as selective adsorbents for Cs and Sr and are shown to possess excellent selectivity in solutions of high ionic strength, with high Na and K concentrations, pointing towards potential for environmental remediation of brackish water.

## Materials and Methods

### Chemical reagents

4,4'-Bis(chloromethyl)-1,1'-biphenyl, (BCMBP, 95%), iron (III) chloride ( $\text{FeCl}_3$ , 97%), anhydrous 1,2-dichloroethane (DCE, 99%), chlorosulfonic acid (99%), strontium chloride ( $\text{SrCl}_2$ , anhydrous powder, >99%) and caesium nitrate (>99.99%) were purchased from Sigma-Aldrich. Sulfuric acid (95%) was purchased from Fischer scientific. Sodium chloride ( $\text{NaCl}$ , 99.9%) was purchased from VWR chemicals and potassium nitrate ( $\text{KNO}_3$ , >99%) was purchased from Acros organics. All chemicals were used as received unless otherwise stated.

### Synthesis of HCP-1 using $\text{H}_2\text{SO}_4$ as the Lewis-acid catalyst

BCMBP (3.00 g, 13.44 mmol, 1 eq.), was dissolved in DCE ( $30\text{ cm}^3$ ) and heated to  $80\text{ }^\circ\text{C}$ .  $\text{H}_2\text{SO}_4$  ( $7.2\text{ cm}^3$ , 13.44 mmol, 1 eq.) was added and the temperature was held for 1 h. The reaction was cooled to  $25\text{ }^\circ\text{C}$  and the solution was left to stir for 72 h. The resulting black solid was collected via vacuum filtration and washed with water and methanol until the solution was neutral. The solid was dried overnight in vacuo at  $60\text{ }^\circ\text{C}$  to yield the final black product (2.23 g, 73%), Elemental analysis calculated for  $\text{C}_{14}\text{H}_{10}$ , Expected: C 94.38%, H 5.62%. Found, C 81.17%, H 5.35%.

### Synthesis of HCP-2 using FeCl<sub>3</sub> as the Lewis-acid catalyst

BCMBP (2.04 g, 8 mmol, 1 eq.) was added to a round bottom flask under nitrogen before DCE (30 cm<sup>3</sup>) was added to dissolve the monomer. To the solution iron chloride (2.80 g, 16 mmol, 2 eq.) was added as a slurry in DCE (20 cm<sup>3</sup>) and the mixture was heated to 80 °C for 16 h. The mixture was cooled to room temperature and vacuum filtration afforded a black solid. The solid was extracted with methanol using soxhlet apparatus for 12 h before being dried *in vacuo* at 60 °C to yield the final black product (1.54 g, 108%). Elemental analysis calculated for C<sub>14</sub>H<sub>10</sub>, Expected: C 94.38%, H 5.62%. Found, C 87.76%, H 5.45%.

### Sulfonation of hypercrosslinked polymers (SHCP-1 and SHCP-2 synthesis)

Hypercrosslinked BCMBP (1.50 g) was added to DCE (50 cm<sup>3</sup>) and left for 1 h to stir to allow the polymer network to swell in the solvent. Chlorosulfonic acid (10 cm<sup>3</sup>) was added to the solution and left to stir at 25 °C for 72 h. The product was collected *via* vacuum filtration and washed with water and methanol ensuring the run off was a neutral pH. The resulting solid was dried under vacuum at 60 °C overnight to yield the final black product. Yields, 1.96 and 1.70 g. Elemental analysis calculated for C<sub>14</sub>H<sub>10</sub>SO<sub>3</sub>, Expected: C 65.12%, H 3.88% S 12.40%. Found, C 60.14%, H 4.20%, S 10.81%; SHCP-2, C 57.75%, H 5.55%, S 7.15%

### Characterisation

Fourier transform infrared (FTIR) spectroscopy was performed using a Perkin-Elmer Spectrum 100. Samples were mixed with KBr and pressed into a disk before being measured in transmission mode. Solid-State NMR samples were packed into 4 mm zirconia rotors and transferred to a Bruker Avance III HD spectrometer. 1D <sup>1</sup>H-<sup>13</sup>C cross-polarisation magic angle spinning (CP/MAS) NMR experiments were measured at 125.76 MHz (500.13 MHz <sup>1</sup>H) at a MAS rate of 10.0 kHz. The <sup>1</sup>H π/2 pulse was 3.4 μs, and two-pulse phase modulation (TPPM) decoupling was used during the acquisition. The Hartmann-Hahn condition was set using hexamethylbenzene. The spectra were measured using a contact time of 2.0 ms. The relaxation delay D<sub>i</sub> for each sample was individually determined from the proton T<sub>1</sub> measurement (D<sub>i</sub> = 5 × T<sub>1</sub>). Samples were collected until sufficient signal to noise was observed, typically greater than 256 scans. The values of the chemical shifts are referred to that of TMS.

Elemental analysis was performed through burning an amount of sample in a stream of pure oxygen. The sample was placed in a tin capsule and introduced into the combustion tube of the Elementar Vario MICRO Cube CHN/S analyser via a stream of helium. Combustion products were analysed through first passing the sample through a copper tube to remove excess oxygen and reduce any NO<sub>x</sub> to N<sub>2</sub>. Gases were separated using a Thermal

Programmed Desorption column and detected using a Thermal Conductivity Detector.

Scanning electron microscopy (SEM) images were recorded using a Jeol JSM-6010LA instrument. Samples were mounted on carbon tape on aluminium stubs, without any coating treatment.

Gas sorption measurements were performed using a micromeritics ASAP 2020Plus analyser employing high purity gases. Nitrogen gas sorption measurements were analysed at 77 K using ~100 mg of sample. BET surface areas were calculated over a relative pressure range of 0.01-0.15 P/P<sub>0</sub>. Differential pore sizes were calculated using the NL-DFT method using the model for Carbon Slit Pores by NLDFIT. All samples were degassed at 120 °C under dynamic vacuum immediately prior to analysis.

### Metal uptake studies

Solutions of various Sr, Cs, Na and K concentrations were made up in accordance with the information presented in Table S1 by dissolving the relevant metal salts in 100 cm<sup>3</sup> of deionized water. 20 mg of SHCP-1 was added to a sample vial along with 5 cm<sup>3</sup> of the chosen solution. Samples were left to stir for a defined time period, before the solid was filtered out using a 0.25 μm filter. Samples for equilibrium studies were left for 24 h. Samples for kinetic studies were left for 1 - 60 min. The resulting solutions were analysed by inductively coupled plasma mass spectrometry (ICP-MS), using an Agilent 7500CE Mass Spectrometer, to determine accurate metal concentrations of solutions. The metal solution concentrations were also determined prior to contact with the polymers. The equilibrium pH of solutions, both before and after polymer-contact, was also determined, using a standard combination electrode.

### Results and Discussion

#### Synthesis and sulfonation of hypercrosslinked polymers SHCP-1 and SHCP-2

Hypercrosslinked BCMBP was synthesised *via* a hypercrosslinking reaction using either H<sub>2</sub>SO<sub>4</sub> (HCP-1) or FeCl<sub>3</sub> (HCP-2) as the catalyst, resulting in black solids collected in good yields of 73% and 96% respectively. Post-synthetic sulfonation of HCP-1 and HCP-2 was carried out *via* a similar procedure to that reported by Lu *et al.* to sulfonate a porous polymer network (PPN-6),<sup>40</sup> using chlorosulfonic acid as the sulfonating agent, to yield SHCP-1 and SHCP-2. Although PPN-6-SO<sub>3</sub>H is superficially similar to our own networks, the high cost of the homo-coupling monomer (> £200 g<sup>-1</sup>) would limit the use of this material as an environmental remediation tool. There are many previous reports of functionalised HCPs,<sup>31, 32, 41</sup> but they have all used metal catalysts such as FeCl<sub>3</sub> to synthesise the porous network. Hence to date, there have been no reports of functionalised HCPs synthesised *via* metal-free routes, which is more environmentally benign and avoids the possibility of contamination from residual catalyst still present in the network. As expected, an increase in mass upon the addition of the sulfonic acid group was observed after the reaction with chlorosulfonic

**Table 1.** Elemental analysis data for polymer networks. All values refer to mass %

	HCP Expected <sup>a</sup>	HCP-1	HCP-2	SHCP Expected <sup>b</sup>	SHCP-1	SHCP-2
C	94.38	81.17	87.76	65.12	60.14	57.75
H	5.62	5.35	5.45	3.88	4.20	5.55
S	0.00	1.95	0.00	12.40	10.81	7.15

<sup>a</sup>Assuming no sulfonation. <sup>b</sup>Assuming 1 site is sulfonated per monomer.

acid. A mass increase of 30% was observed upon sulfonation of HCP-1 while for HCP-2 the mass increase was 13%, suggesting a lesser degree of sulfonation.

### Solid-state analysis of materials

A combination of SEM, FTIR spectroscopy, solid-state NMR, elemental analysis and gas sorption studies were employed to characterize the products. Scanning electron micrographs of HCP-1 and SHCP-1 (Figure S1) demonstrated a very inconsistent morphology, with occasional microspheres of different diameters being visible within the overall fused network. The sulfonation functionalisation did not change the visible morphology, as would be expected from previous literature.<sup>42</sup>

The FTIR spectra (Figure S2) of HCP-1 and SHCP-1 both contain similar stretches at 1600, 1500 and 1200  $\text{cm}^{-1}$  relating to the C=C stretches from the aromatic rings in the final network.<sup>43</sup> Signals at 600 and 1050  $\text{cm}^{-1}$ , present in the spectrum of the sulfonated SHCP-1, are assigned to the C-S stretch and the S=O symmetric stretch respectively. The presence of these additional signals demonstrates the successful incorporation of the sulfonate groups into the polymer network. However, these signals, along with a broad stretch at 3500  $\text{cm}^{-1}$  indicating the presence of an -OH group, are also present in the HCP-1 spectrum, albeit much less intense than those in the sulfonated product. This suggests that the hypercrosslinking reaction, which uses  $\text{H}_2\text{SO}_4$  as the acid catalyst, was also able to partially sulfonate the material.<sup>33</sup>

Elemental analysis further evidences the successful incorporation of the sulfonate groups (Table 1). 1.95% S was observed for HCP-1, again suggesting that some sulfonation of the network had taken place during hypercrosslinking. After the reaction with chlorosulfonic acid, this increased to 10.81% for SHCP-1. An expected calculation based on one sulfonation per monomer would yield 12.4 % S content. From the elemental analysis we can therefore assume a substitution of slightly less than one sulfonic acid group per monomer within the network. As expected, the hypercrosslinking reaction using  $\text{FeCl}_3$  (HCP-2) shows S content of 0.00%.

The solid-state NMR spectrum of sample HCP-1 (Figure S3) shows resonances at ~138 ppm, attributed to quaternary aromatic carbon environments; ~130 ppm, attributed to

aromatic carbons adjacent to hydrogen and ~37 ppm, attributed to the -CH<sub>2</sub>- bridges. After sulfonation, there is a change in the intensity of the aromatic resonances, with a reduction in the intensity of the Ar-H signal compared to that of the quaternary carbons, due to sulfonation. Nitrogen adsorption/desorption isotherms were carried out at 77 K in order to determine both the surface area and pore size of all materials synthesised in this work (Figure 1). All isotherms exhibit a steep uptake at low relative pressure ( $P/P_0 < 0.1$ ), indicative of the presence of micropores within the sample. The BET surface areas of all networks were calculated over a pressure range of 0.01-0.15  $P/P_0$  (Table 2). Initially HCP-1 and -2 exhibit high surface areas of 1239 and 1918  $\text{m}^2\text{g}^{-1}$  respectively, similar to the reported surface areas for these two materials.<sup>33, 44</sup> The  $\text{FeCl}_3$ -catalysed route results in a material with some larger mesopores as evidenced by the hysteresis loop around 0.8  $P/P_0$ . This is confirmed by NLDFT pore size distributions (Figures S4 – S6) which shows the main pore sizes of HCP-2 to be centred around 0.5 and 1.5 nm with some further mesoporosity. Upon sulfonation there is a notable drop in surface area of both HCPs, as would be expected from the addition of mass from the sulfonic acid group. The  $\text{FeCl}_3$ -catalysed HCP-2 shows a significant drop in surface area to 580  $\text{m}^2\text{g}^{-1}$  while the metal-free HCP-1 shows a less prominent decrease in surface area to 850  $\text{m}^2\text{g}^{-1}$ . The large decrease in surface area from HCP-2 to SHCP-2 is most likely due the loss of the larger mesopores (Fig. S5) with the pore size distribution shifting towards the smaller 0.5 nm pore. The pore volume of HCP-2, calculated at 0.1  $P/P_0$  ( $V_{0.1}$ ), remains unchanged after sulfonation whilst the total pore volume ( $V_{\text{tot}}$ ,  $P/P_0 = 0.99$ ) significantly drops from 2.4 to 0.35  $\text{cm}^3/\text{g}$  with  $V_{0.1}/V_{\text{tot}}$  increasing from 0.03 to 0.22. For the metal free route (HCP-1),  $V_{0.1}$  also remains unchanged after sulfonation, while the total pore volumes drop from 0.86 to 0.51  $\text{cm}^3\text{g}^{-1}$  and  $V_{0.1}/V_{\text{tot}}$  increases from 0.20 to 0.33. It is therefore likely that the sulfonation occurs mainly in the mesopores of the HCPs rather than the micropores. This is further demonstrated by the fraction of pore volumes at 0.1  $P/P_0$  via both routes increasing after sulfonation. Mesopores have previously been postulated to play an important role in the mass transfer of ions to active sites in porous adsorbents.<sup>36</sup>

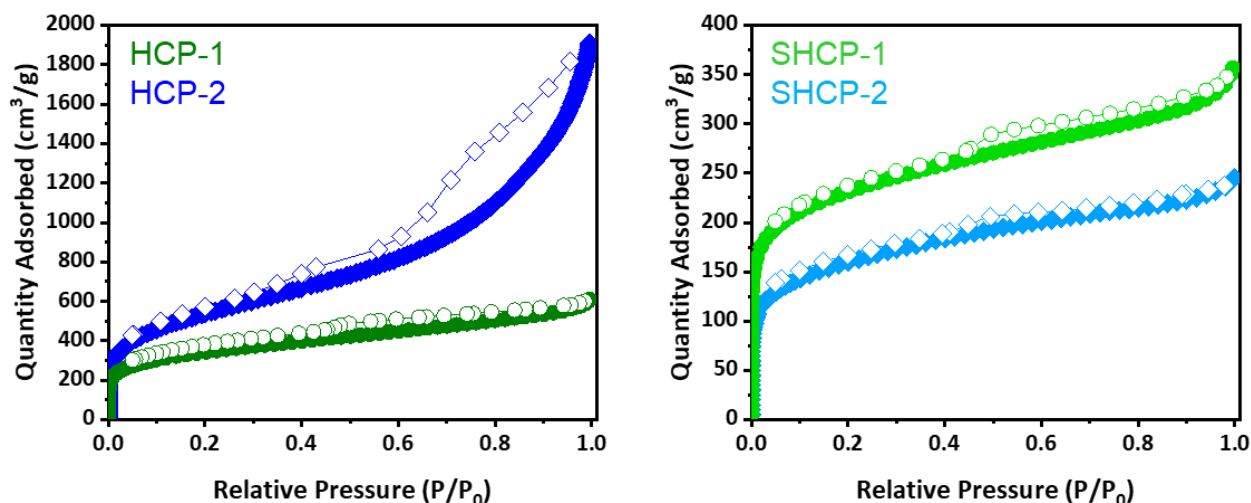


**Figure 1.** Gas sorption isotherms of HCP-1 and HCP-2 (left) and the sulfonated SHCP-1 and SHCP-2 (right).  $\text{H}_2\text{SO}_4$  synthetic route (circles) and  $\text{FeCl}_3$  route (diamonds). Filled symbols show adsorption and empty symbols desorption.

**Table 2.** Gas sorption properties of the synthesised polymers, determined by  $\text{N}_2$  adsorption.

Catalyst	Sample	Surface area ( $\text{m}^2 \text{g}^{-1}$ ) <sup>a</sup>	$V_{\text{tot}}$ ( $\text{cm}^3/\text{g}$ ) <sup>b</sup>	$V_{\text{o.1}}$ ( $\text{cm}^3/\text{g}$ ) <sup>c</sup>	$V_{\text{o.1/tot}}$
$\text{H}_2\text{SO}_4$	HCP-1	1239	0.86	0.17	0.20
	SHCP-1	850	0.51	0.17	0.33
$\text{FeCl}_3$	HCP-2	1918	2.4	0.08	0.03
	SHCP-2	580	0.35	0.08	0.22

<sup>a</sup>Apparent BET surface area calculated over the relative pressure range 0.01-0.15.  $P/P_0$  <sup>b</sup>Total pore volume calculated at 0.99  $P/P_0$ . <sup>c</sup> Micropore volume calculated at 0.1  $P/P_0$ .

### Uptake of Sr and Cs ions from aqueous solution

Metal-organic frameworks (MOFs) such as the sulfonate-functionalised MIL-101- $\text{SO}_3\text{H}$  have been previously shown to selectively uptake both Sr and Cs ions (Table S7 provides a summary of Cs and Sr uptakes in other porous materials). Our metal-free catalysed SHCP-1 however, is synthesised from readily-available and economic starting materials and contains no metal ions which may leach into solution. In general, porous polymers also have increased thermal and chemical stability compared to MOFs and are therefore ideal candidates for metal uptake in harsh environments.<sup>25,36,38</sup> To date there have been no reports of the uptake of Sr and Cs ions by microporous polymers, therefore we investigated the use of SHCP-1 for the selective capture of these ions from solution. A simple immersion of HCP-1 and SCHP-1 in deionised water (Figure S7) demonstrated the greatly improved wettability of the polymer upon addition of the hydrophilic sulfonic acid groups, as has previously been observed,<sup>42</sup> and suggested rapid uptake might be possible due to the enhanced hydrophilicity of the material.

### Isotherm studies

Single metal-loading isotherm data were fitted to the Langmuir and Dubinin-Radushkevich (D-R) adsorption models (Equations 1 and 2) *via* non-linear least-squares regression, using the Microsoft Excel SOLVER programme. Errors were calculated using Billo's Solver Statistics add-in. The Langmuir model has been frequently used to describe the uptake of Sr and Cs ions by various adsorbents and for uptake behaviour of the sulfonic acid functionality,<sup>45,46</sup> whereas the D-R model is less commonly applied.<sup>47</sup>

$$q_e = \frac{q_{\text{max}}K_L C_e}{1 + K_L C_e} \quad (1)$$

$$q_e = (q_{\text{max}}) \exp\left(-B_D \left[RT \ln\left(1 + \frac{1}{C_e}\right)\right]^2\right) \quad (2)$$

For these isotherm models,  $q_e$  is the equilibrium uptake capacity of the polymer ( $\text{mg}\cdot\text{g}^{-1}$ ),  $q_{\text{max}}$  is the theoretical saturation uptake capacity ( $\text{mg}\cdot\text{g}^{-1}$ ),  $K_L$  is a Langmuir equilibrium constant ( $\text{L}\cdot\text{mg}^{-1}$ ),  $C_e$  is the concentration of

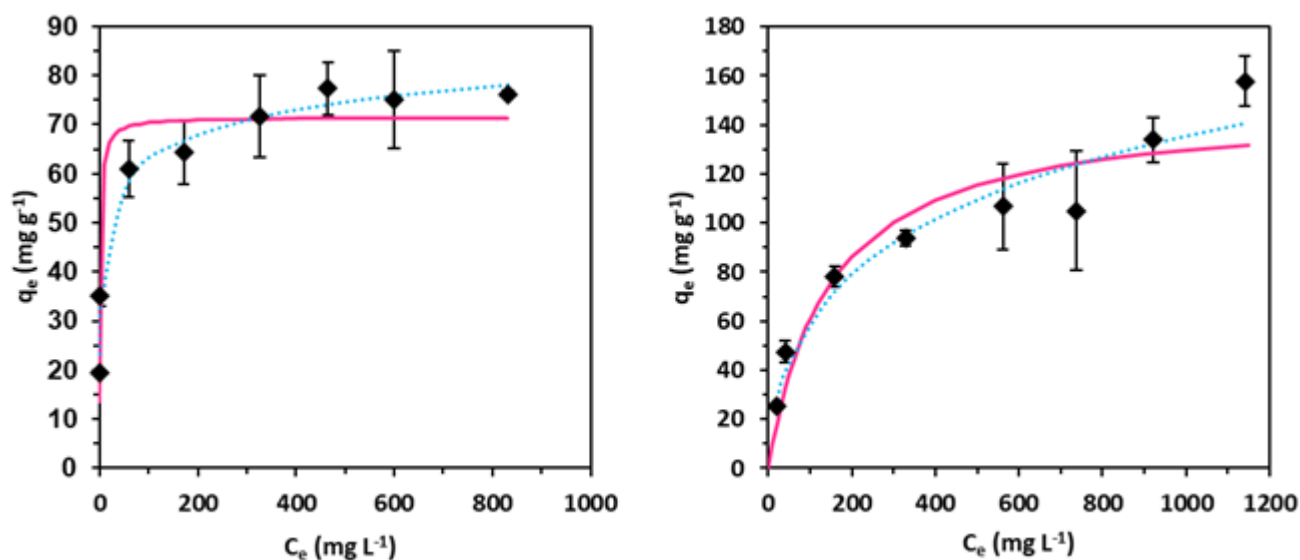


**Figure 2.** Metal adsorption isotherms for uptake of Sr (left) and Cs (right) by SHCP-1. Polymer mass = 20 mg. Solution volume = 5 mL. Initial metal concentration = 1-15 mM. Contact time = 24 h.  $T = 20^{\circ}\text{C}$ . Solid line = Langmuir isotherm model. Dashed line = D-R isotherm model.

metal ion at equilibrium ( $\text{mg}\cdot\text{L}^{-1}$ ),  $B_D$  is a D-R constant ( $\text{J}^2\text{mol}^2$ ),  $R$  is the gas constant ( $8.314\text{ J}\cdot\text{K}^{-1}\cdot\text{mol}^{-1}$ ) and  $T$  is the experimental temperature (K). The D-R model can be used to estimate the desorption energy of the system, according to Equation 3:

$$E_{\text{des}} = \frac{1}{\sqrt{2B_D}} \quad (3)$$

where  $E_{\text{des}}$  is the mean desorption energy ( $\text{kJ}\cdot\text{mol}^{-1}$ ). The isotherms produced for Sr and Cs uptake are shown in Figure 2, while the extracted parameters for both models are shown in Table 3.

The uptake of both metals was more closely described by the D-R model than Langmuir, which suggests that the energies of binding follow a Gaussian distribution, rather than being strictly degenerate.<sup>48</sup> There was also a clear relationship observed, in both cases, between the number of metal ions adsorbed and the number of protons liberated into solution (Figure S8). Overall, it can be inferred that the extraction of Sr and Cs was due to the expected sulfonic acid group ion-exchange mechanism. It is unusual, though not unheard of, for the D-R model to demonstrate superior description to the Langmuir model for metal uptake by ion-exchange on to a functionalised polymer.<sup>20,22,49</sup> It is possible in this instance that the hydrophobic pore interiors of varying volumes create a number of different microenvironments where binding could occur. The  $E_{\text{des}}$  values returned, being  $>8\text{ kJ}\cdot\text{mol}^{-1}$ , strongly suggested a chemisorption mechanism was prevalent, rather than physisorption.<sup>48</sup> The binding energies for Sr are unusually high for an ion-exchange process, which typically results in values in the range of 8-16  $\text{kJ}\cdot\text{mol}^{-1}$ .<sup>22,49,50</sup> This suggests the Sr ions in particular are

strongly held and would be unlikely to leach back into the environment. Although Cs uptake appears to be a weaker interaction, the  $q_{\text{max}}$  values from both models were higher. A comparison of  $q_{\text{max}}$  values from the D-R model with the found S mass % of SHCP-1 results in a theoretical maximum loading efficiency of  $\sim 61\%$  for Cs and  $\sim 32\%$  for Sr. This indicates that some sulfonation took place within the micropores, creating sites unavailable to the metal ions. It also suggests that some Sr cations may bridge across 2 sulfonic acid groups, which would explain the high mean  $E_{\text{des}}$  value observed. This can be seen in Figure S8, which shows that the number of protons released into the aqueous phase is greater for Sr solutions, even though the molar uptake of metal is lesser.

The calculated  $q_{\text{max}}$  values from the D-R model compare favourably to those attained by adsorption of Sr *via* crown ether-functionalised ion-exchange resins ( $7.7\text{ mg Sr}\cdot\text{g}^{-1}$ )<sup>51</sup> and adsorption of Cs and Sr on mineral-based extractants ( $91.7\text{ mg Cs}\cdot\text{g}^{-1}$ ;  $44.7\text{ mg Sr}\cdot\text{g}^{-1}$ ).<sup>52</sup> Indeed, the polymer exhibits a capacity of the same order of magnitude as a commercial ion-exchange resin with a far larger and more elaborate phosphonic acid-based functional group ( $315\text{ mg Cs}\cdot\text{g}^{-1}$ ).<sup>53</sup> Further comparison with literature values is seen in Table S7.

**Table 3.** Extracted parameters for uptake of Sr and Cs by SHCP-1 by fitting to Langmuir and Dubinin-Radushkevich isotherm models.

Model	Parameter	Sr	Cs
Langmuir	$K_L$ (L·mg <sup>-1</sup> )	0.65 ± 0.20	7.0 ± 3.1 (x 10 <sup>-3</sup> )
	$q_{max}$ (mg·g <sup>-1</sup> )	71.5 ± 2.6	148 ± 16
	$R^2$	0.993	0.981
Dubinin-Radushkevich	$B_D$ (J <sup>2</sup> ·mol <sup>2</sup> )	1.50 ± 0.11 (x 10 <sup>-9</sup> )	4.77 ± 0.38 (x 10 <sup>-9</sup> )
	$q_{max}$ (mmol·g <sup>-1</sup> )	1.09 ± 0.03	2.06 ± 0.28
	$q_{max}$ (mg·g <sup>-1</sup> )	95.6 ± 2.8	273 ± 37
	$E_{des}$ (kJ·mol <sup>-1</sup> )	18.2 ± 1.3	10.2 ± 0.8
	$R^2$	0.998	0.990

### Kinetic studies

Results from the single metal-loading kinetic study demonstrated a rapid uptake of Sr and Cs by SHCP-1 (Tables S1 and S2) with >80% of the apparent equilibrium uptake capacity achieved within 60 seconds. In order to confirm the uptake mechanism of metal adsorption, data were fitted to the well-known pseudo 1<sup>st</sup>-order (PFO) and pseudo 2<sup>nd</sup>-order (PSO) kinetic models (Equations 4 and 5), using linear regression.

$$q_t = q_e(1 - e^{-k_1 t}) \quad (4)$$

$$q_t = \frac{k_2 q_e^2 t}{1 + k_2 q_e t} \quad (5)$$

For these kinetic models,  $q_t$  is the uptake of metals at time  $t$  (mg g<sup>-1</sup>),  $k_1$  is the pseudo 1<sup>st</sup>-order rate constant (min<sup>-1</sup>) and  $k_2$  is the pseudo 2<sup>nd</sup>-order rate constant (g mg<sup>-1</sup> min<sup>-1</sup>). Additional parameters, derived from PFO and PSO equations, were calculated using Equations 6 and 7:

$$t_{1/2} = \frac{1}{k_n q_e} \quad (6)$$

$$h_0 = k_2 q_e^2 \quad (7)$$

where  $n = 1$  or  $2$ , corresponding to PFO or PSO equations,  $t_{1/2}$  is the sorption half-time (min) and  $h_0$  is the initial sorption rate (mg g<sup>-1</sup> min<sup>-1</sup>). Agreement with film diffusion and intra-particle diffusion models was also checked (Supporting Information, pages S6-8). The PSO model was found to give an accurate description of the uptake behaviour, as seen in the associated plots of  $t/q_t$  vs  $t$  (Figure 3). Calculated parameters for kinetic data are presented in Table 4.

**Table 4.** Extracted parameters from data-fitting to kinetic models.

Kinetic model	Parameter	Sr	Cs
Pseudo 1 <sup>st</sup> -order	$q_e$ (mg g <sup>-1</sup> )	60.3 ± 6.9	99.9 ± 0.2
	$k_1$ (min <sup>-1</sup> )	1.27 ± 0.48	2.73 ± 7.23
	$R^2$	0.724	0.244
Pseudo 2 <sup>nd</sup> -order	$q_e$ (mg g <sup>-1</sup> )	62.1 ± 0.1	101 ± 1
	$k_2$ g (mg <sup>-1</sup> min <sup>-1</sup> )	7.71 ± 1.1 (x 10 <sup>-2</sup> )	0.113 ± 0.018
	$t_{1/2}$ (min <sup>-1</sup> )	0.209 ± 0.031	8.80 ± 1.4 (x 10 <sup>-2</sup> )
	$h_0$ (mg g <sup>-1</sup> min <sup>-1</sup> )	297 ± 44	1150 ± 180
	$R^2$	0.999	0.998
Film layer diffusion	$R^2$	0.175	0.095
Intra-particle diffusion	$R^2$	0.609	0.042

The uptake of both metals was well-described by the PSO model, which has often been observed to give an accurate description of chemisorption-dominated systems.<sup>54,55</sup> This appears to confirm that the ion-exchange process of the functional groups was responsible for the uptake of metals. The fit of the data to the PFO model and to both diffusion-based models (Figures S8-S11) was poor and the parameters returned were not considered valid. The data overall suggest that the rate-limiting kinetic processes for the removal of metals from solution were the diffusion of ions across the hydration layer of the adsorbent particles and/or the ion-exchange reaction at the polymer surface, rather than diffusion through the pores.<sup>56,57</sup> This is common for adsorbents with a high accessible surface area.<sup>55, 58</sup> The calculated  $k_2$ ,  $t_{1/2}$  and  $h_0$  values all indicated that Cs uptake was more rapid than Sr. Assuming the divalent Sr ions do indeed bridge across two sulfonic acid groups, the Sr uptake can be considered a pseudo-chelating interaction, which is generally a slower process than monovalent ion-exchange.<sup>59</sup> Nonetheless, the derived  $k_2$  values for both metals are relatively high in comparison to the literature,<sup>51,60,61</sup> which again can be attributed to the microporous nature of the adsorbent.

### Competition with other cations

In order to be considered viable for removing problematic metal ions for environmental remediation, a material must not only possess a high loading capacity but also demonstrate selectivity against competing ions in solution. Radioactive Cs and Sr contamination is of particular importance in estuarine environments. For example, following the Fukushima Dai-ichi disaster, the highest <sup>137</sup>Cs

activity recorded outside the actual plant boundaries was in brackish ground water >10 Km from the site.<sup>62</sup> We therefore studied removal of the target ions with a large excess of Na (as NaCl). Potassium is obviously present in saline water in much lesser concentrations. However, experiments were also carried out with equivalent [K<sup>+</sup>] in order to unambiguously determine the selectivity of SHCP-1.

Table 5 shows the results of the selectivity studies. Experiment 1 involved Sr and Cs only. Experiment 2 involved Sr and Cs in the presence of 10 molar equivalents of Na. Experiment 3 involved Sr and Cs in the presence of a 10 molar equivalents of K. Finally experiment 4 involved Sr and Cs with 10 molar equivalents of both Na and K. In all cases, the distribution coefficient (K<sub>d</sub>) for each metal ion was calculated (Supporting Information, p S10).

It was found that SHCP-1 possessed very high selectivity towards Sr and Cs ions. In experiments where large excesses of Na and K were added, the polymer was still able to selectively extract Sr and Cs, showing little to no affinity towards either of the two other ions despite their much higher concentrations. Separation factors (S.F.) for Sr and Cs vs competing ions were calculated as measures of the selectivity of SHCP-1 for target ions, relative to cocontaminant ions (Supporting Information, p S10) and are presented in Table 6. It is clear from Tables 5 and 6 that the selectivity of SHCP-1 follows the order: Sr > Cs > K >> Na, with Sr uptake showing the largest K<sub>d</sub> values and S.F.s across all experiments. The preference for Sr<sup>2+</sup> is due to the higher charge density, compared to the monovalent ions and the selectivity agrees exactly with well-established cation-exchange affinities for SAC resins.<sup>63</sup>

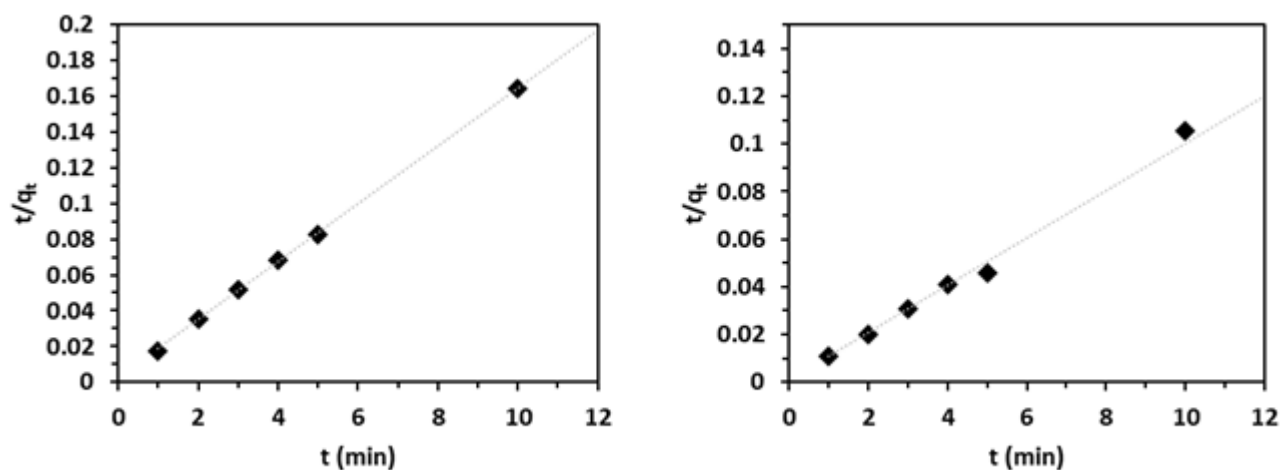


**Figure 3.** Linear fitting of uptake of Sr (left) and Cs (right) by SHCP-1 over time to PSO kinetic model. Polymer mass = 20 mg. Solution volume = 5 mL. Initial metal concentration = 10 mM. Initial pH ≈ 6.0. T = 20°C.

**Table 5.** Sr and Cs uptake performance of SHCP-1 in solutions of competing ions. Polymer mass = 20 mg. Solution volume = 5 mL. Contact time = 24 h. T = 20°C.

Experiment	Ionic strength (mmol·L <sup>-1</sup> )	Metal	C <sub>0</sub> (mg·L <sup>-1</sup> )	q <sub>e</sub> (mg·g <sup>-1</sup> )	K <sub>d</sub>
1	46.5	Sr	817	63.3	112
		Cs	1230	42.0	39.6
2	249	Sr	840	51.3	80.7
		Cs	1250	51.3	49.1
		Na	2320	10.0	4.39
3	246	Sr	848	45.8	68.8
		Cs	1160	38.0	37.7
		K	3920	20	5.21
4	452	Sr	837	35.8	51.5
		Cs	1220	32.5	29.8
		Na	2400	0	<0.1
		K	3840	27.5	7.37

However, the preference of the polymer for Sr over Cs becomes less pronounced in solutions of higher ionic strength. It is known that high ionic strength can modify SAC selectivity, due to the decrease in water activity in the aqueous phase, thus changing the degree of solvation required for the different ions.<sup>67</sup> Chelating uptake processes can also be strongly suppressed by the ionic strength of the solution, specifically for alkali earth metal uptake,<sup>64,65</sup> which further evidences the proposed Sr bridging interaction.

From a selectivity point of view, upon comparison to other materials used to remove Sr and/or Cs from solution, SHCP-1 compares favourably (Table S7). The MOF MIL-101-SO<sub>3</sub>H was previously investigated for Sr and Cs removal and possesses the same chemical moieties to SHCP-1.<sup>66</sup> The S.F. values for MIL-101-SO<sub>3</sub>H were found to be much lower than those of SHCP-1 for the same ions, despite the identical sulfonic acid functionalities. Porous uranyl networks recently reported by Sun *et al.*<sup>67</sup> and Wang *et al.*<sup>68</sup> also showed lesser selectivity than SHCP-1. It is known from classical ion-exchange literature that increasing the degree of cross-linking (and therefore the hydrophobicity) of the resin matrix imparts better selectivity to SAC resins.<sup>63,69</sup> It is thus suggested that HCPs are a more appropriate scaffold for the performance of the sulfonic acid functionality than MOFs. Indeed, SAC selectivity is proportional to matrix swelling pressure, which in turn is dictated by the degree of resin crosslinking. Therefore, HCPs may even offer advantages over conventional ion-exchange resins in this regard.

**Table 6.** Separation factors for both Sr and Cs in the presence of Na and K. Experimental parameters are as per Table 4.

Experiment	Ion(x)	S.F. (x/Cs)	S.F. (x/Sr)	S.F. (x/Na)	S.F. (x/K)
1	Sr	2.83			
	Cs		0.353		
2	Sr	1.64		18.4	
	Cs		0.609	11.2	
3	Sr	1.82			13.2
	Cs		0.549		7.25
4	Sr	1.73		>100	6.99
	Cs		0.579	>100	4.05

SHCP-2 was also investigated for its metal uptake capabilities, it was found that after 24 h, 134 mg of Cs was removed from solution, much less than the 466 mg removed by SHCP-1 (Table S4). Considering the S mass %

for each polymer (Table 1), it seems this is not the only relevant parameter for the uptake of aqueous metal ions and that accessible surface area of the materials is also important. The loss of a large fraction of mesopores in HCP-2 upon sulfonation (Figure S4) may result in some of the sulfonic acid groups being inaccessible for the target ions. HCP-1 loses much less surface area upon sulfonation (Table 2), hence contributing to the superior uptake observed. Correlations between BET surface area and capacity for contaminants have previously been observed for microporous materials.<sup>42,70</sup> Additionally, it was found that residual Fe, present from the FeCl<sub>3</sub> catalytic route, leached into solution during polymer contact (Table S5). This had survived Soxhlet extraction with methanol, post-synthetic modification with chlorosulfonic acid and further washing with water, thus highlighting the issue of obtaining a pure product from hypercrosslinking reactions when using metal catalysts. Residual Fe associated with the polymer is a particular worry when applying these materials to adsorption of metal ions given that uptake performance may suffer, essentially due to competition from leached Fe<sup>3+</sup> ions. These would be more strongly bound to the sulfonate moiety, owing to higher charge density.<sup>39</sup> The H<sub>2</sub>SO<sub>4</sub> catalysed route therefore seems to provide the optimum route towards a material which has a high surface area, contains no residual impurities, is readily post-synthetically modified and capable of extracting both Sr and Cs ions in a selective and efficient manner.

## Conclusions

4,4'-bis(chloromethyl)-1,1'-biphenyl (BCMBP) was hypercrosslinked, using H<sub>2</sub>SO<sub>4</sub> as the catalyst, and post-synthetically sulfonated by reacting with chlorosulfonic acid. The resulting polymers possessed high BET surface areas, with the as-synthesised polymer (HCP-1) measuring 1239 m<sup>2</sup>·g<sup>-1</sup> and the sulfonated version (SHCP-1) measuring 850 m<sup>2</sup>·g<sup>-1</sup>. SHCP-1 was successfully applied to remove both Cs and Sr from solution with q<sub>e</sub> values of 273 and 95.6 mg·g<sup>-1</sup> respectively, calculated via fitting to the Dubinin-Radushkevich isotherm model. Furthermore, SHCP-1 was found to be extremely selective towards these ions, even in the presence of competing ions (Na and K). Separation factors of 18.4 (Sr/Na) and 11.2 (Cs/Na) are superior to many other published adsorbents used for uptake of these ions, which we attribute to the hydrophobic, densely cross-linked nature of the material positively influencing the order of cation selectivity. It is hoped that this work will stimulate further studies into the use of hypercrosslinked polymers for environmental remediation, a purpose for which they are intrinsically suitable. Future work will investigate their use under a range of different conditions.

## AUTHOR INFORMATION

### Corresponding Author

\* Dr Robert Dawson [r.dawson@sheffield.ac.uk](mailto:r.dawson@sheffield.ac.uk)

## Author Contributions

The manuscript was written through contributions of all authors.

## Funding Sources

We would like to thank the following funding sources: A.M.J EPSRC doctoral training grant (EP/K503149/1), S.H. the Sheffield Undergraduate Research Experience (SURE) scheme at the University of Sheffield, T.J.R. EPSRC (Grant no. EP/L016281/1) and Bawtry Carbon International Ltd.

## References

- (1) Casacuberta N., Masqué P., Garcia-Orellana J., Garcia-Tenorio R., Buessler K.O.,  $^{90}\text{Sr}$  and  $^{89}\text{Sr}$  in Seawater off Japan as a Consequence of the Fukushima Dai-ichi Nuclear Accident, *Biogeosciences*, **2013**, *10*, 3649-3659.
- (2) Liu X., Chen G.R., Lee D.J., Kawamoto T., Tanaka H., Chen M.L., Luo Y.K., Adsorption Removal of Cesium from Drinking Waters: A Mini Review on Use of Biosorbents and Other Adsorbents, *Bioresour. Technol.*, **2014**, *160*, 142-149.
- (3) Paasikallio A., Rantavaara A., Sippola J., The Transfer of Cesium-137 and Strontium-90 from Soil to Food Crops After the Chernobyl Accident, *Sci. Total Environ.*, **1994**, *155*, 109-124.
- (4) Oancea A.M.S., Popescu A.R., Radulescu M., Weber V., Pincovski E., Cox M., Kinetics of Cesium and Strontium Ions Removal from Wastewater on Gel and Macroporous Resins, *Solv. Extr. Ion Exc.*, **2008**, *26*, 217-239.
- (5) Garger E.K., Kashpur V.A., Li W.B., Tschiersch J., Radioactive Aerosols Released from the Chernobyl Shelter into the Immediate Environment, *Radiat. Environ. Biophys.*, **2006**, *45*, 105-114.
- (6) Tanaka S., Kado S., Analysis of Radioactive Release from the Fukushima Daiichi Nuclear Power Station, in: J. Ahn, C. Carson, Jensen M., Juraku K., Nagasaki S., Tanaka S. (Eds.) Reflections on the Fukushima Daiichi Nuclear Accident, Springer, Cham, **2015**.
- (7) Goossens R., Delville A., Genot J., Halleux R., Masschelein W.J., Removal of the Typical Isotopes of the Chernobyl Fall-out by Conventional Water Treatment, *Water Res.*, **1989**, *23*, 693-697.
- (8) O'Donnell A.J., Lytle D.A., Harmon S., Vu K., Chait H., Dionysiou D.D., Removal of Strontium from Drinking Water by Conventional Treatment and Lime Softening in Bench-scale Studies, *Water Res.*, **2016**, *103*, 319-333.
- (9) Wang C.Y., Chang D.A., Shen Y.Z., Sun Y.C., Wu C.H., Vortex-assisted Liquid-Liquid Microextraction of Strontium from Water Samples using 4',4''(5'')-di-(tert-butylcyclohexano)-18-crown-6 and Tetraphenylborate, *J. Sep. Sci.*, **2017**, *40*, 3866-3872.
- (10) Gruner B., Plesek J., Baca J., Dozol J.F., Lamare V., Cisarova I., Belohradsky M., Caslavsky J., Crown Ether Substituted Cobalto bis(dicarbollide) Ion as Selective Extraction Agents for Removal of  $\text{Cs}^+$  and  $\text{Sr}^{2+}$  from Nuclear Waste, *New J. Chem.*, **2002**, *26*, 867-875.
- (11) Sistkova N., Kolarova M., Lucanikova M., Belohradsky M., Rais J., Liquid-Liquid Extractions of Microamounts of Cs-137 and Sr-85 with Chlorinated Dicarbolide and Crown Ethers into Mixed Dodecanenitrile/n-dodecane Nonpolar Diluent, *Sep. Sci. Technol.*, **2011**, *46*, 2174-2182.
- (12) Prelot B., Ayed I., Marchandeu F., Zajac J., On the Real Performance of Cation Exchange Resins in Wastewater Treatment Under Conditions of Cation Competition: The Case of Heavy Metal Pollution, *Environ. Sci. Pollut. Res.*, **2014**, *21*, 9334-9343.
- (13) Sylvester P., Clearfield A., The Removal of Strontium and Cesium from Simulated Hanford Groundwater Using Inorganic Ion Exchange Materials, *Solvent Extr. Ion Exc.*, **1998**, *16*, 1527-1539.
- (14) Bortun A.I., Bortun L.N., Clearfield A., Evaluation of Synthetic Inorganic Ion Exchangers for Cesium and Strontium Removal from Contaminated Groundwater and Wastewater, *Solvent Extr. Ion Exc.*, **1997**, *15*, 909-929.
- (15) Oji L.N., Martin K.B., Hobbs D.T., Development of Prototype Titanate Ion-Exchange Loaded-Membranes for Strontium, Cesium and Actinide Decontamination from Aqueous Media, *J. Radioanal. Nucl. Chem.*, **2009**, *279*, 847-854.
- (16) Ramaswamy M., Synthesis, Sorption and Kinetic Characteristics of Silica-hexacyanoferrate Composites, *Solvent Extr. Ion Exc.*, **1999**, *17*, 1603-1618.
- (17) Dyer A., Pillinger M., Amin S., Ion Exchange of Caesium and Strontium on a Titanosilicate Analogue of the Mineral Pharmacosiderite, *J. Mater. Chem.*, **1999**, *9*, 2481-2487.
- (18) Kakutani Y., Weerachawanak P., Hirata Y., Sano M., Suzuki T., Miyake T., Highly Effective K-Merlinoite Adsorbent for Removal of  $\text{Cs}^+$  and  $\text{Sr}^{2+}$  in Aqueous Solution, *RSC Adv.*, **2017**, *7*, 30919-30928.
- (19) Nenoff T.M., Krumhansl J.L.,  $\text{Cs}^+$  Removal from Seawater by Commercially Available Molecular Sieves, *Solvent Extr. Ion Exc.*, **2012**, *30*, 33-40.
- (20) Pepper S.E., Whittle K.R., Harwood L.M., Cowell J., Lee T.S., Ogden M.D., Cobalt and Nickel Uptake by Silica-Based Extractants, *Sep. Sci. Technol.*, **2018**, *53*, 1552-1562.
- (21) Robshaw T., Tukra S., Hammond D.B., Leggett G.J., Ogden M.D., Highly Efficient Fluoride Extraction from Simulant Leachate of Spent Potlining via La-Loaded Chelating Resin. An Equilibrium Study, *J. Haz. Mater.*, **2019**, *361*, 200-209.
- (22) Ogden M.D., Moon E.M., Wilson A., Pepper S.E., Application of Chelating Weak Base Resin Dowex M4195 to the Recovery of Uranium from Mixed Sulfate/Chloride Media, *Chem. Ind. Eng. J.*, **2017**, *317*, 80-89.
- (23) Tan L.X., Tan B., Hypercrosslinked Porous Polymer Materials: Design, Synthesis, and Applications, *48*, **2017**, *46*, 3322-3356.
- (24) Chaoui N., Trunk M., Dawson R., Schmidt J., Thomas A., Trends and Challenges for Microporous Polymers, *Chem. Soc. Rev.*, **2017**, *46*, 3302-3321.
- (25) Dawson R., Cooper A.I., Adams D.J., Nanoporous Organic Polymer Networks, *Prog. Polym. Sci.*, **2012**, *37*, 530-563.
- (26) Dawson R., Ratvijitvech T., Corker M., Laybourn A., Khimyak Y.Z., Cooper A.I., Adams D.J., Microporous Copolymers for Increased Gas Selectivity, *Polym. Chem.*, **2012**, *3*, 2034-2038.
- (27) Li B.Y., Gong R.N., Luo Y.L., Tan B.E., Tailoring the Pore Size of Hypercrosslinked Polymers, *Soft Matter*, **2011**, *7*, 10910-10916.
- (28) Martin C.F., Stockel E., Clowes R., Adams D.J., Cooper A.I., Pis J.J., Rubiera F., Pevida C., Hypercrosslinked Organic Polymer Networks as Potential Adsorbents for Pre-Combustion  $\text{CO}_2$  Capture, *J. Mater. Chem.*, **2011**, *21*, 5475-5483.
- (29) He Z.D., Zhou M.H., Wang T.Q., Xu Y., Yu W., Shi B.Y., Huang K., Hyper-Cross-Linking Mediated Self-Assembly Strategy To Synthesize Hollow Microporous Organic Nanospheres, *ACS Appl. Mater. Interfaces*, **2017**, *9*, 35209-35217.
- (30) Li B.Y., Gong R.N., Wang W., Huang X., Zhang W., Li H.M., Hu C.X., Tan B.E., A New Strategy to Microporous Polymers: Knitting Rigid Aromatic Building Blocks by External Cross-Linker, *Macromolecules*, **2011**, *44*, 2410-2414.
- (31) Dawson R., Stevens L.A., Drage T.C., Snape C.E., Smith M.W., Adams D.J., Cooper A.I., Impact of Water Coadsorption for Carbon Dioxide Capture in Microporous Polymer Sorbents, *J. Am. Chem. Soc.*, **2012**, *134*, 10741-10744.
- (32) Yang X., Yu M., Zhao Y., Zhang C., Wang X.Y., Jiang J.X., Hypercrosslinked Microporous Polymers Based on Carbazole for Gas Storage and Separation, *RSC Adv.*, **2014**, *4*, 61051-61055.

- (33) Schute K., Rose M., Metal-Free and Scalable Synthesis of Porous Hyper-cross-linked Polymers: Towards Applications in Liquid-Phase Adsorption, *ChemSusChem*, **2015**, *8*, 3419-3423.
- (34) Wang W., Zhou M., Yuan D., Carbon Dioxide Capture in Amorphous Porous Organic Polymers, *J. Mater. Chem. A*, **2017**, *5*, 1334-1347.
- (35) Yang Y., Zhang Q., Zhang S., Li S., Triphenylamine-Containing Microporous Organic Copolymers for Hydrocarbons/Water Separation, *RSC Adv.*, **2014**, *4*, 5568-5574.
- (36) Fu Y., Yu W.G., Zhang W.J., Huang Q., Yan J., Pan C.Y., Yu G.P., Sulfur-Rich Covalent Triazine Polymer Nanospheres for Environmental Mercury Removal and Detection, *Polym. Chem.*, **2018**, *9*, 4125-4131.
- (37) Tsyurupa M.P., Blinnikova Z.K., Borisov Y.A., Ilyin M.M., Klimova T.P., Mitsen K.V., Davankov V.A., Physicochemical and Adsorption Properties of Hypercross-linked Polystyrene with Ultimate Cross-linking Density, *J. Sep. Sci.*, **2014**, *37*, 803-810.
- (38) Han X.L., Xu M.Y., Yang S., Qian J., Hua D.B., Acetylcysteine-Functionalized Microporous Conjugated Polymers for Potential Separation of Uranium from Radioactive Effluents, *J. Mater. Chem. A*, **2017**, *5*, 5123-5128.
- (39) Helfferich F.G., Ion Exchange, McGraw-Hill, New York, **1962**.
- (40) Lu W.G., Yuan D.Q., Sculley J.L., Zhao D., Krishna R., Zhou H.C., Sulfonate-Grafted Porous Polymer Networks for Preferential CO<sub>2</sub> Adsorption at Low Pressure, *J. Am. Chem. Soc.*, **2011**, *133*, 18126-18129.
- (41) Mane S., Ponrathnam S., Chavan N., Synthesis and Characterization of Hypercrosslinked Hydroxyl Functionalized Co-polymer Beads, *Eur. Polym. J.*, **2014**, *59*, 46-58.
- (42) B.Y. Li, F.B. Su, H.K. Luo, L.Y. Liang, B.E. Tan, Hypercrosslinked Microporous Polymer Networks for Effective Removal of Toxic Metal Ions from Water, *Micro. Meso. Mater.*, **2011**, *138*, 207-214.
- (43) Wilson C., Main M.J., Cooper N.J., Briggs M.E., Cooper A.I., Adams D.J., Swellable Functional Hypercrosslinked Polymer Networks for the Uptake of Chemical Warfare Agents, *Polym. Chem.*, **2017**, *8*, 1914-1922.
- (44) Lee J.Y., Wood C.D., Bradshaw D., Rosseinsky M.J., Cooper A.I., Hydrogen Adsorption in Microporous Hypercrosslinked Polymers, *Chem. Commun.*, **2006**, 2670-2672.
- (45) Pavel C.C., Popa K., Investigations on the Ion Exchange Process of Cs<sup>+</sup> and Sr<sup>2+</sup> Cations by ETS Materials, *Chem. Eng. J.*, **2014**, *245*, 288-294.
- (46) Kondo K., Nakagawa S., Matsumoto M., Yamashita T., Furukawa I., Selective Adsorption of Metal Ions on Novel Chitosan-Supported Sulfonic Acid Resin, *J. Chem. Eng. JPN*, **1997**, *30*, 846-851.
- (47) Kasap S., Tel H., Piskin S., Preparation of TiO<sub>2</sub> Nanoparticles by Sonochemical Method, Isotherm, Thermodynamic and Kinetic Studies on the Sorption of Strontium, *J. Radioanal. Nuc. Chem.*, **2011**, *289*, 489-495.
- (48) Ho Y.S., Porter J.F., McKay G., Equilibrium Isotherm Studies for the Sorption of Divalent Metal Ions onto Peat: Copper, Nickel and Lead Single Component Systems, *Water Air Soil Pollut.*, **2002**, *141*, 1-33.
- (49) Amphlett J.T.M., Ogden M.D., Foster R.I., Syna N., Soldenhoff K., Sharrad C.A., Polyamine Functionalised Ion Exchange Resins: Synthesis, Characterisation and Uranyl Uptake, *Chem. Eng. J.*, **2018**, *334*, 1361-1370.
- (50) Gilca E., Maicaneanu A., Ilea P., Removal of Zinc Ions as Zinc Chloride Complexes from Strongly Acidic Aqueous Solutions by Ionic Exchange, *Cent. Eur. J. Chem.*, **2014**, *12*, 821-828.
- (51) Surman J.J., Pates J.M., Zhang H., Happel S., Development and Characterisation of a New Sr Selective Resin for the Rapid Determination of Sr-90 in Environmental Water Samples, *Talanta*, **2014**, *129*, 623-628.
- (52) Tamura K., Kogure T., Watanabe Y., Nagai C., Yamada H., Uptake of Cesium and Strontium Ions by Artificially Altered Phlogopite, *Environ. Sci. Technol.*, **2014**, *48*, 5808-5815.
- (53) Chiarizia R., Horwitz E.P., Beauvais R.A., Alexandratos S.D., Diphonix-CS: A Novel Combined Cesium and Strontium Selective Ion Exchange Resin, *Solvent Extr. Ion Exc.*, **1998**, *16*, 875-898.
- (54) Tran H.N., You S.J., Hosseini-Bandegharai A., Chao H.P., Mistakes and Inconsistencies Regarding Adsorption of Contaminants from Aqueous Solutions: A Critical Review, *Water Res.*, **2017**, *120*, 88-116.
- (55) Li Z.P., Li H., Xia H., Ding X.S., Luo X.L., Liu X.M., Mu Y., Triarylboron-Linked Conjugated Microporous Polymers: Sensing and Removal of Fluoride Ions, *Chem. Eur. J.*, **2015**, *21*, 17355-17362.
- (56) Tu N.T.T., Thien T.V., Du P.D., Chau V.T.T., Mau T.X., Khieu D.Q., Adsorptive Removal of Congo Red from Aqueous Solution Using Zeolitic Imidazolate Framework-67, *J. Environ. Chem. Eng.*, **2018**, *6*, 2269-2280.
- (57) Robshaw T.J., Dawson R., Bonser K., Ogden M.D., Towards the Implementation of an Ion-Exchange System for Recovery of Fluoride Commodity Chemicals. Kinetic and Dynamic Studies *Chem. Eng. J.*, **2019**, *367*, 149-159.
- (58) Kołodzyńska D., Krukowska-Bąk J., Kazmierczak-Razna J., Pietrzak R., Uptake of Heavy Metal Ions from Aqueous Solutions by Sorbents Obtained from the Spent Ion Exchange Resins, *Micro. Meso. Mater.*, **2017**, *244*, 127-136.
- (59) Turse R., Rieman W., Kinetics of Ion Exchange in a Chelating, *J. Phys. Chem.*, **1961**, *65*, 1821-1824.
- (60) Kapnisti M., Hatzidimitriou A.G., Noli F., Pavlidou E., Investigation of Cesium Uptake from Aqueous Solutions Using New Titanium Phosphates Ion-Exchangers, *J. Radioanal. Nucl. Chem.*, **2014**, *302*, 679-688.
- (61) Garg G., Chauhan G.S., Ahn J.H., Strontium(II) Ion Uptake on Poly(N-vinyl imidazole)-Based Hydrogels, *J. Appl. Polym. Sci.*, **2012**, *124*, 3721-3727.
- (62) Sanial V., Buesseler K.O., Charette M.A., Nagao S., Unexpected Source of Fukushima-Derived Radiocesium to the Coastal Ocean of Japan, *Proc. Natl. Acad. Sci. U.S.A.*, **2017**, *114*, 11092-11096.
- (63) Harland C.E., Ion Exchange: Theory and Practice, 2nd ed., Royal Society of Chemistry, Cambridge, **1994**.
- (64) Sides J.L., Kenner C.T., Effect of pH and Ionic Strength on the Distribution Coefficients of Alkaline Earth Metals and Nickel with Chelating Ion-Exchange Resins, *Anal. Chem.*, **1966**, *38*, 707-711.
- (65) Luttrell G.H., More C., Kenner C.T., Effect of pH and Ionic Strength on Ion Exchange and Chelating Properties of an Iminodiacetate Ion Exchange Resin with Alkaline Earth Ions, *Anal. Chem.*, **1971**, *43*, 1370-1375.
- (66) Aguila B., Banerjee D., Nie Z.M., Shin Y., Ma S.Q., Thallapally P.K., Selective Removal of Cesium and Strontium Using Porous Frameworks from High Level Nuclear Waste, *Chem. Commun.*, **2016**, *52*, 5940-5942.
- (67) Ai J., Chen F.Y., Gao C.Y., Tian H.R., Pan Q.J., Sun Z.M., Porous Anionic Uranyl-Organic Networks for Highly Efficient Cs<sup>+</sup> Adsorption and Investigation of the Mechanism, *Inorg. Chem.*, **2018**, *57*, 4419-4426.
- (68) Wang Y.L., Liu Z.Y., Li Y.X., Bai Z.L., Liu W., Wang Y.X., Xu X.M., Xiao C.L., Sheng D.P., Juan D.W., Su J., Chai Z.F., Albrecht-Schmitt T.E., Wang S., Umbellate Distortions of the Uranyl Coordination Environment Result in a Stable and Porous Polycatenated Framework That Can Effectively Remove Cesium from Aqueous Solutions, *J. Am. Chem. Soc.*, **2015**, *137*, 6144-6147.

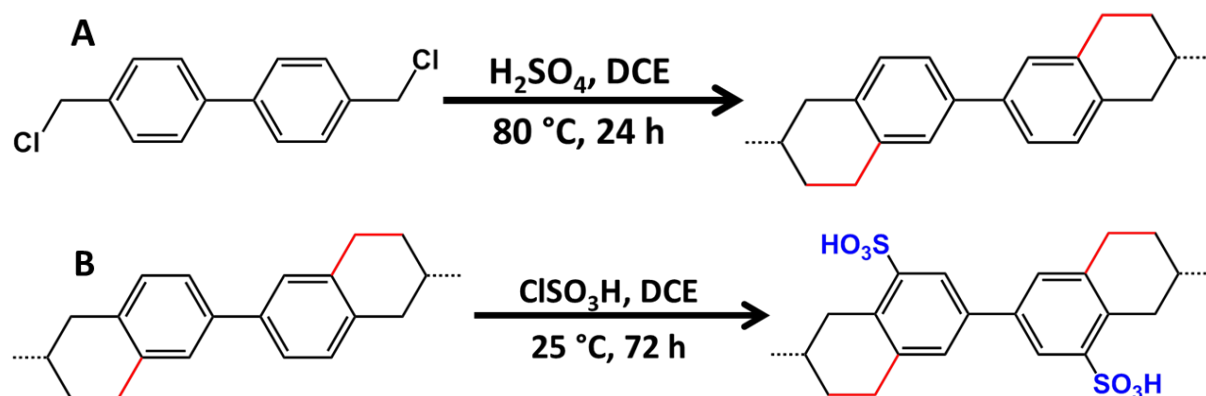
(69) Reichenberg D., Ion-exchange selectivity, in: J.A. Marinsky (Ed.) Ion Exchange (A Series of Advances), Edward Arnold, London, **1966**, pp. 227.

(70) Chen Y.F., Sun H.X., Yang R.X., Wang T.T., Pei C.J., Xiang Z.T., Zhu Z.Q., Liang W.D., Li A., Deng W.Q., Synthesis of Conjugated Microporous Polymer Nanotubes with Large Surface Areas as Absorbents for Iodine and CO<sub>2</sub> Uptake, *J. Mater. Chem. A*, **2015**, 3, 87-91.

## Supporting Information

### Selective Environmental Remediation of Strontium and Cesium Using Sulfonated Hypercrosslinked Polymers (SHCPs)

Alex M. James, Samuel Harding, Neil Bramall, Thomas Robshaw, Mark D. Ogden and Robert Dawson



**Scheme S1.** (A) The general reaction scheme towards the synthesis of HCP-1 using sulfuric acid (1 equiv.) as the catalyst. For the iron chloride catalysis route (HCP-2), the procedure was identical but iron chloride (2 equiv.) was used instead. (B) The sulfonation procedure to synthesis SHCP-1 and SHCP-2.

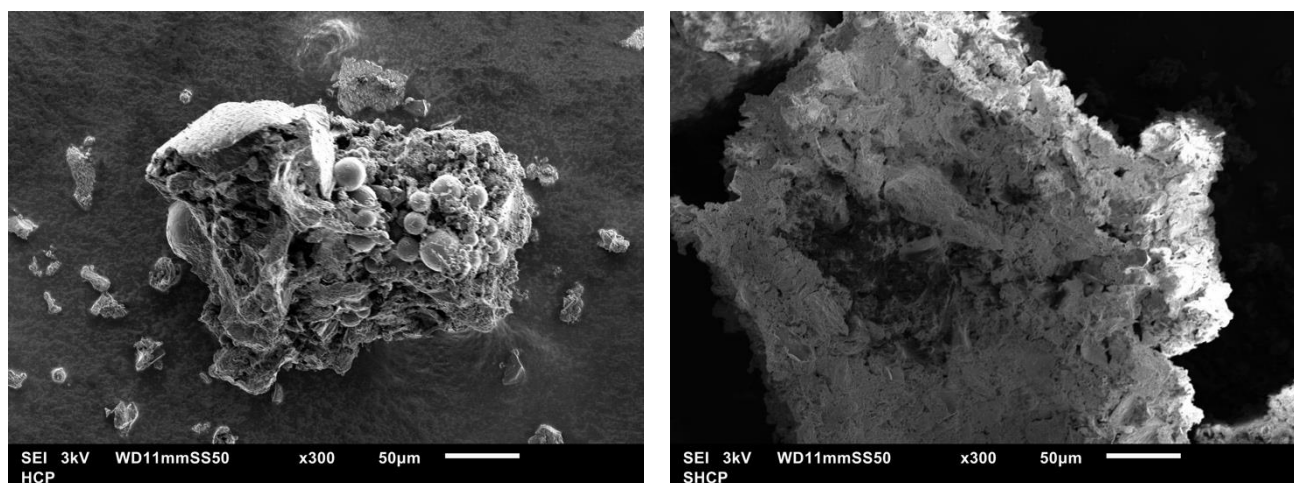


**Figure S1.** Scanning electron micrographs of HCP-1 (left) and SHCP-1 (right).

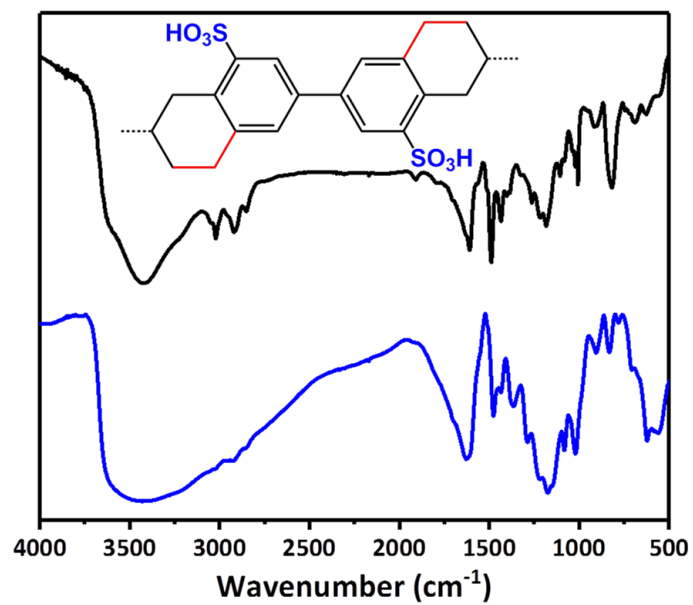


**Figure S2.** FTIR spectra of HCP-1 (black) and SHP-1 (blue).

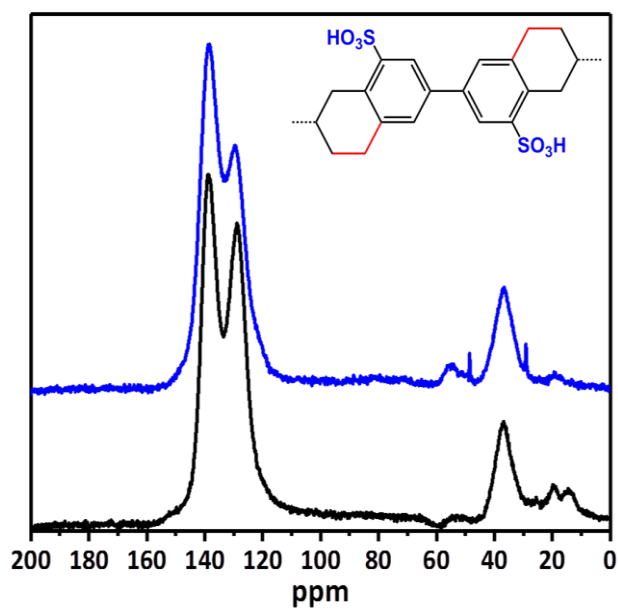


**Figure S3.** Solid state <sup>13</sup>C-NMR spectra of HCP-1 (black) and SHCP-1 (blue).

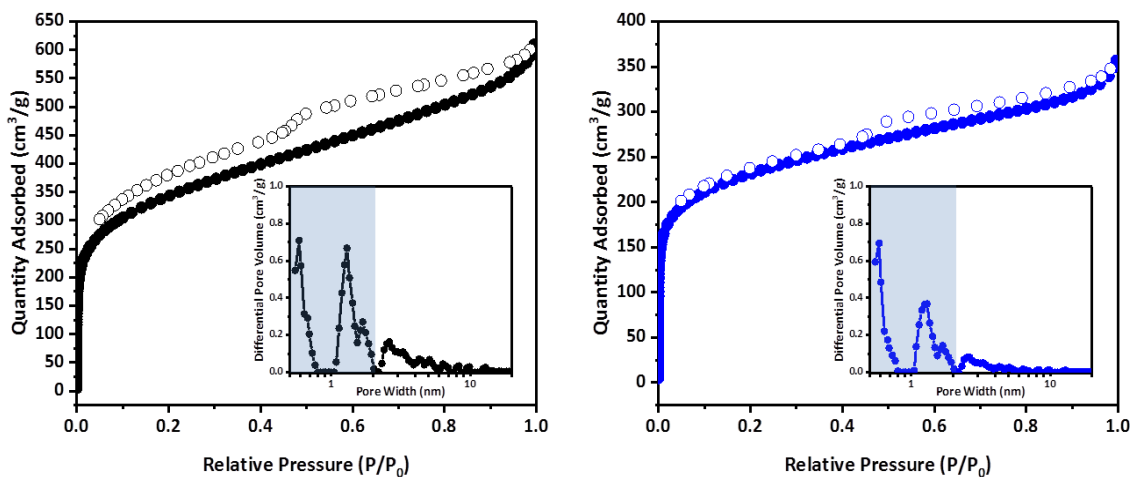


**Figure S4.** Full nitrogen isotherms for HCP-1 (left) and SHCP-1 (right) synthesised via the sulfuric acid route. Inset are pore size distributions for each sample.

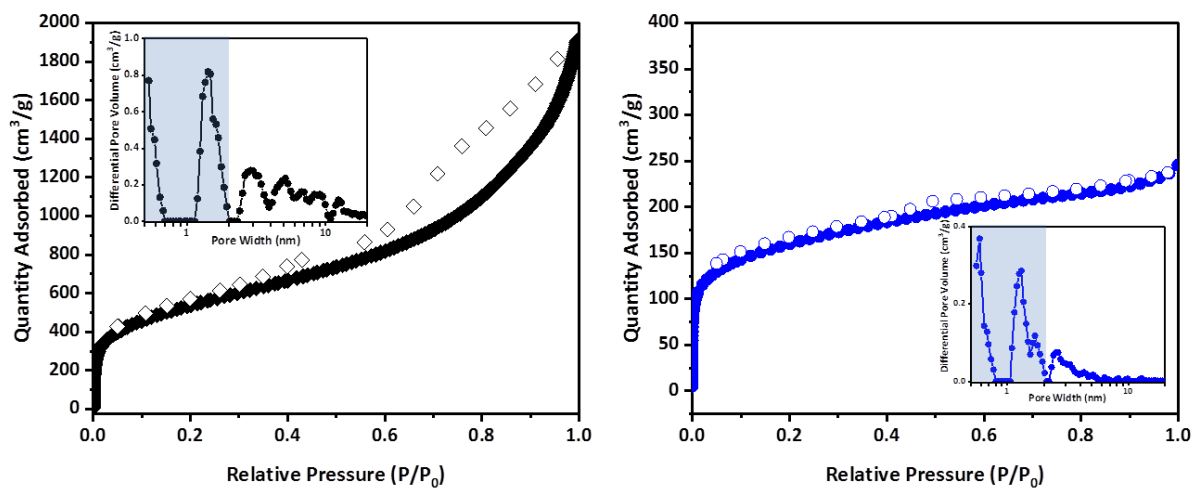


**Figure S5.** Full nitrogen isotherms for HCP-2 (left) and SHCP-2 (right) synthesised via the iron chloride route. Inset are pore size distributions for each sample.

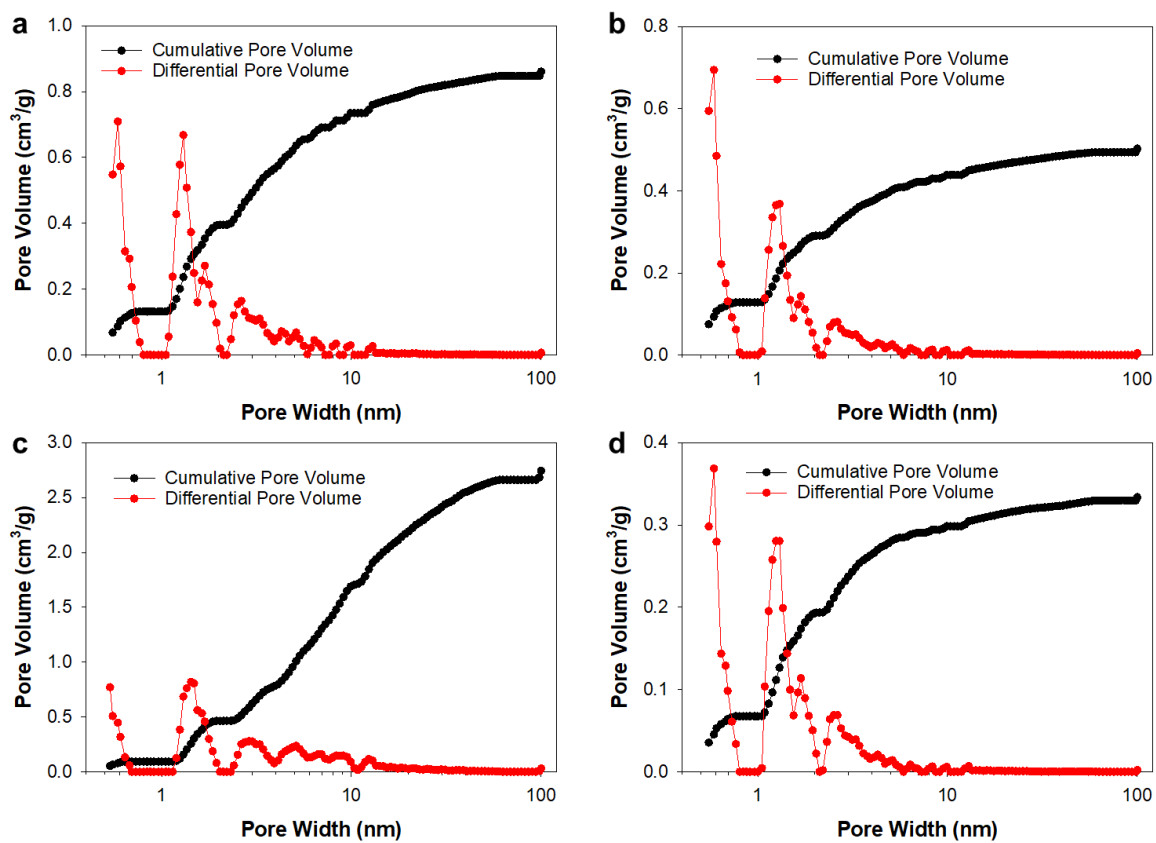


**Figure S6.** Cumulative and Differential Pore Volumes for a) HCP-1, b) SHCP-1, c) HCP-2 and d) SHCP-2.



**Figure S7.** Dispersions of HCP-1 and SHCP-1 in water, briefly agitated and left to stand for ~5 min, demonstrating increase in the hydrophilicity of the network.

## Metal ions uptake studies

For all metal uptake experiments, solutions were made up by dissolving metal salts ( $\text{CsNO}_3$ ,  $\text{SrCl}_2$ ,  $\text{NaCl}$  and  $\text{KNO}_3$ ) in deionised water ( $100 \text{ cm}^3$ ) to the desired concentrations for each metal. For single-metal loading isotherms, concentrations of 1 – 15 mM Cs or Sr were used, for static kinetic experiments, concentrations of 10 mM Cs or Sr were used. For experiments investigating the effects of competing ions, 10 mM Cs/Sr and 100 mM Na/K were used.

## Equilibrium studies

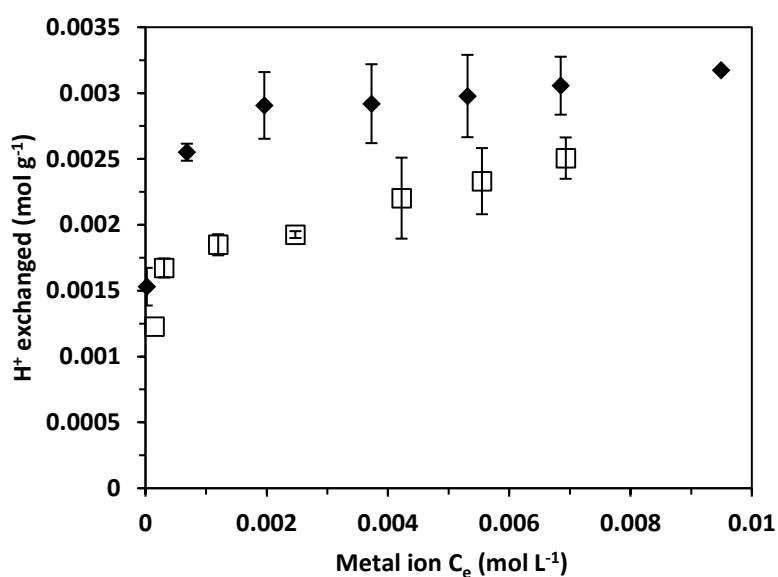


**Figure S8.** Changes in proton concentration of solutions of Sr (◆) and Cs (□) at equilibrium, following contact with SHCP-1. Polymer mass = 20 mg. Solution volume = 5 mL. Initial metal concentration = 1-15 mM. Contact time = 24 h. T = 20°C.

## Kinetic studies

**Table S1.** Sr ion concentration upon contact with SHCP-1 over time. Polymer mass = 20 mg. Solution volume = 5 mL. T = 20°C.

Time (min)	Sr concentration (mg L <sup>-1</sup> )
0 (C <sub>0</sub> )	800
1	567
2	575
3	564
4	554
5	554
10	547
60	552
1440	535

**Table S2.** Cs ion concentration upon contact with SHCP-1 over time. Polymer mass = 20 mg. Solution volume = 5 mL. T = 20°C.

Time (min)	Cs concentration (mg L <sup>-1</sup> )
0 (C <sub>0</sub> )	1190
1	816
2	776
3	784
4	786
5	756
10	793
60	771
1440	724

## Correlation of data to kinetic models

The film-diffusion model is shown in Equation S1:

$$\ln(1 - F) = k_{fd}t \quad (S1)$$

where  $F$  is the fractional attainment of equilibrium at time  $t$  and  $k_{fd}$  is the film-diffusion rate constant ( $\text{min}^{-1}$ ). Therefore, in a plot of  $-\ln(1 - C_t/C_0)$  vs  $t$ , where  $C_t$  is the concentration of metal ion at time  $t$  and  $C_0$  is the initial concentration, a linear gradient would indicate that the uptake rate is controlled by the movement of adsorbate ions within the pores of the resin beads (intraparticle-diffusion). A non-linear gradient would suggest the rate is controlled by the movement of the adsorbate through the hydrous film layer surrounding the adsorbent particles (film-diffusion), or the chemical reaction at the surface [1, 2].

The intra-particle diffusion model is shown in Equation S2:

$$q_t = k_{id}t^{1/2} + C \quad (S2)$$

where  $k_{id}$  is the intraparticle-diffusion rate constant ( $\text{mg g}^{-1} \text{min}^{-1/2}$ ) and  $C$  is a constant relating to the thickness of the adsorbent film layer. For data plots of  $q_t$  vs  $t^{1/2}$ , where  $q_t$  is the uptake capacity of the adsorbent at time  $t$ , it is accepted that, if the plot has a linear gradient and passes through the origin, the adsorption is entirely controlled by intraparticle-diffusion [3, 4].

The models were applied to the data shown in Tables S1 and S2 and plots are shown below. In all cases,  $R^2$  values were determined by linear regression.

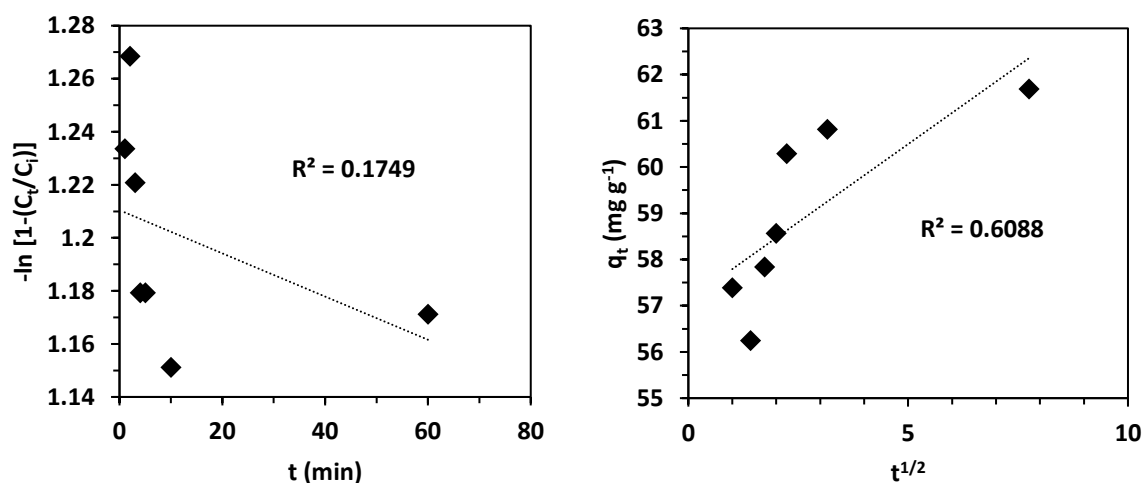
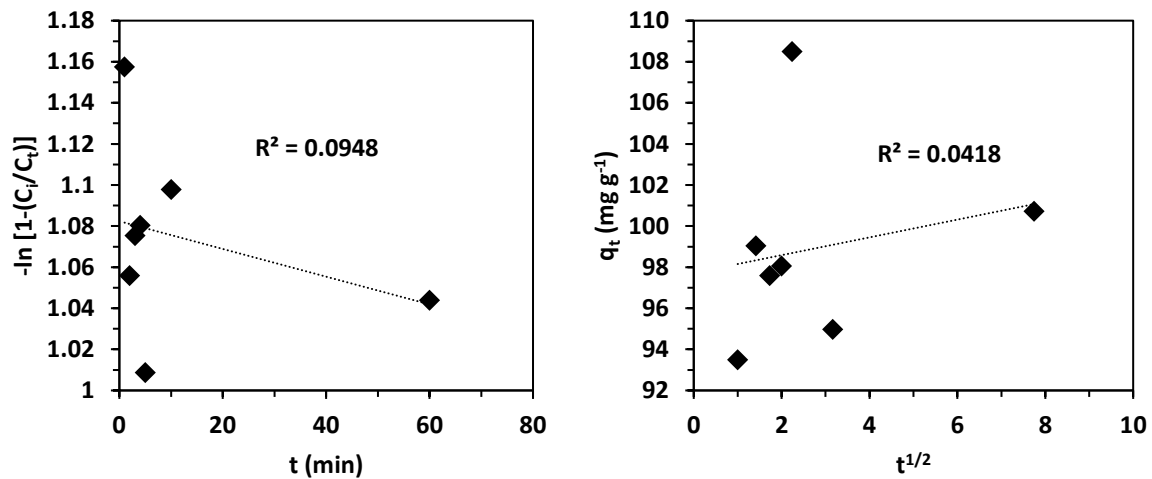


**Figure S8.** Correlation of Sr uptake data with film diffusion (left) and intra-particle diffusion (right) models.



**Figures S9.** Correlation of Cs uptake data with film diffusion (left) and intra-particle diffusion (right) models.

The linear plots of  $\log (q_e/q_t)$  vs  $t$ , to determine the agreement of uptake kinetic data to the pseudo 1<sup>st</sup>-order (PFO) model, described in the main article, are shown below.

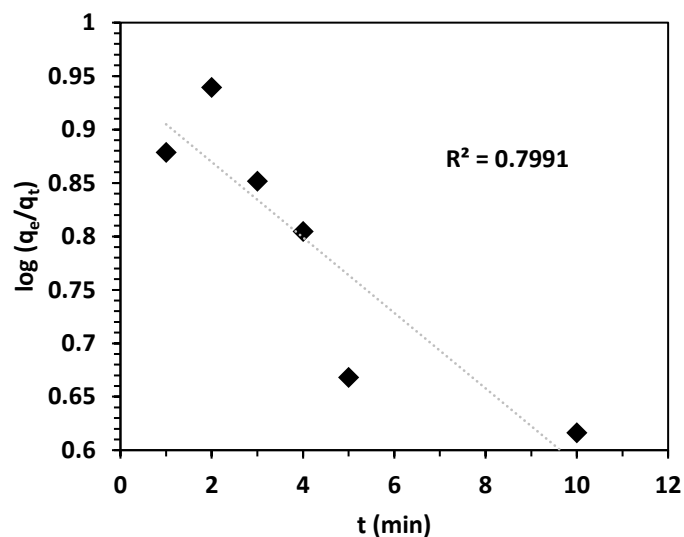


**Figure S10.** Linear PFO model fitting to Sr uptake data.

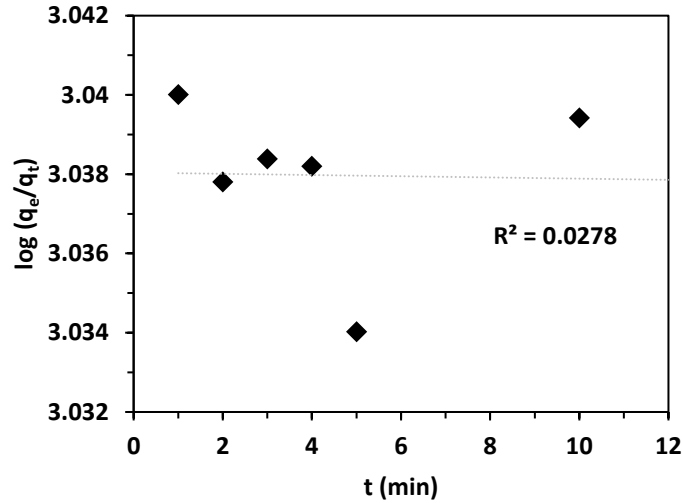


**Figure S11.** Linear PFO model fitting to Cs uptake data.

### Selectivity studies

The differences in metal ion concentrations of various solutions, before and after contact with SCHP-1 and SHCP-2 are shown in the following tables. For all experiments, mass of polymer = 20 mg. Solution volume = 5 mL. T = 20°C. Contact time = 24 h.

**Table S3.1.** Change in Cs and Sr ion concentration upon exposure to SCHP-1. [Sr] = 10 mM. [Cs] = 10 mM.

Time (min)	Metal concentration (ppm)	
	Cs	Sr
C <sub>0</sub>	1229	817
1440	1061	564

**Table S3.2.** Change in Cs, Sr and Na ion concentration upon exposure to SHCP-1. [Sr] = 10 mM. [Cs] = 10 mM. [Na] = 100 mM.

Time (min)	Metal concentration (ppm)		
	Cs	Sr	Na
C <sub>0</sub>	1248	840	2320
1440	1043	635	2280

**Table S3.3.** Change in Cs, Sr and K ion concentration upon exposure to SHCP-1. [Sr] = 10 mM. [Cs] = 10 mM. [K] = 100 mM.

Time (min)	Metal concentration (ppm)		
	Cs	Sr	K
C <sub>0</sub>	1159	848	3920
1440	1007	665	3840

**Table S3.4.** Change in Cs, Sr, Na and K ion concentration upon exposure to SHCP-1. [Sr] = 10 mM. [Cs] = 10 mM. [Na] = 100 mM. [K] = 100 mM.

Time (min)	Metal concentration (ppm)			
	Cs	Sr	Na	K
C <sub>0</sub>	1219	837	2400	3840
1440	1089	694	2400	3730

**Table S4.** Change in Cs and Sr ion concentration upon exposure to SCHP-2. [Sr] = 10 mM. [Cs] = 10 mM.

Time (minutes)	Metal concentration (ppm)	
	Sr	Cs
C <sub>0</sub>	800	1190
1440	718	1056

**Table S5.** Fe leaching from SHCP-2 into solution during the uptake experiment shown in Table S5.

Element	Concentration (ppm)
Fe	0.243

## Calculation of distribution coefficients and separation factors

For the experimental data detailed in Tables S4-S6, the distribution coefficient ( $K_d$ ) for each metal ion in each sample solution was calculated according to Equation S3:

$$K_d = \frac{[\bar{X}]}{[X]} \quad (\text{S3})$$

where  $[\bar{X}]$  = the concentration of the ion of interest adsorbed on to the solid phase at equilibrium ( $\text{mg kg}^{-1}$ ) and  $[X]$  = the concentration of the ion in the aqueous phase at equilibrium ( $\text{mg L}^{-1}$ ).

The S.F. is then calculated from Equation S4:

$$S.F._{(X/Y)} = \frac{K_{d(X)}}{K_{d(Y)}} \quad (\text{S4})$$

Where X is the ion of interest and Y is a competing ion.

Separation factors (S.F.) were furthermore calculated for the sulfonated metal organic framework MIL-101-SO<sub>3</sub>H from data published by Aguila *et al.* [5], in order to compare the performance of SHCP-1 against a porous material with equivalent functional groups.

**Table S6.** Distribution coefficient and separation factor values, calculated from reported uptake data for MIL-101-SO<sub>3</sub>H [5].  $C_0$  and  $C_e$  = initial and equilibrium ion concentrations respectively.  $V$  = volume of solution and  $M$  = mass of adsorbent used.

Adsorbent	Metal	$C_0$ ( $\text{mg L}^{-1}$ )	$C_e$ ( $\text{mg L}^{-1}$ )	$V$ (mL)	$M$ (g)	$K_d$
MIL-101-SO <sub>3</sub> H	Sr	134.6	104.4	5	0.02	72.32
	Cs	73.34	70.00	5	0.02	11.93
	Na	2244	2165	5	0.02	9.12
	K	3722	3468	5	0.02	18.31

$$S.F._{(Cs/Na)} = 1.31, S.F._{(Cs/K)} = 0.65, S.F._{(Sr/Na)} = 7.93, S.F._{(Sr/K)} = 3.94.$$

Likewise, other materials were compared to SHCP-1 in order to contextualise its performance, compared to relevant literature. Table S8 shows the comparison of SHCP-1 against other reported materials which have been shown to uptake Cs and/or Sr.

**Table S7.** Comparison of published materials used to uptake Cs and/or Sr from solution.

Adsorbent	q <sub>e</sub> (mg g <sup>-1</sup> )		K <sub>d</sub>		S.F.				Ref.
	Cs	Sr	Cs	Sr	Cs/Na	Cs/K	Sr/Na	Sr/K	
This work	273	95.6	156.98	121.4	10.25	6.6	15.25	10.25	-
MIL-101-SO <sub>3</sub> H	0.835	7.55	11.93	72.32	1.31	0.65	7.93	3.94	[5]
Indium organic framework	199	43.83	7.5 x 10 <sup>4</sup>	9.49 x 10 <sup>5</sup>	183*	27.5	322	7.21	[6]
Uranyl organic network (1)	108	-	217	-	3.89	4.95	-	-	[7]
Uranyl organic network (2)	29.04	-	432	-	1.58	1.2	-	-	[8]
AMP-PAN <sup>#</sup>	81	15	>100	>100	-	-	-	-	[9]

\*A value of 514 is quoted when the Na counter-ion is NO<sub>3</sub><sup>-</sup>. This value is from the experiment where the counter-ion is Cl<sup>-</sup>, which is a more accurate comparison to our work.

<sup>#</sup>“AMP-PAN” = Ammonium molybdophosphate-polyacrylonitrile.

## References

- [1] G.E. Boyd, A.W. Adamson, L.S. Myers Jr., *Journal of The American Chemical Society*, 69 (1947) 2836-2848.
- [2] N.T.T. Tu, T.V. Thien, P.D. Du, V.T.T. Chau, T.X. Mau, D.Q. Khieu, *Journal of Environmental Chemical Engineering*, 6 (2018) 2269-2280.
- [3] S.E. Pepper, K.R. Whittle, L.M. Harwood, J. Cowell, T.S. Lee, M.D. Ogden, *Separation Science and Technology*, 53 (2018) 1552-1562.
- [4] H.N. Tran, S.J. You, A. Hosseini-Bandegharai, H.P. Chao, *Water Research*, 120 (2017) 88-116.
- [5] B. Aguila, D. Banerjee, Z.M. Nie, Y. Shin, S.Q. Ma, P.K. Thallapally, *Chemical Communications*, 52 (2016) 5940-5942.
- [6] Y.J. Gao, M.L. Feng, B. Zhang, Z.F. Wu, Y. Song, X.Y. Huang, *Journal of Materials Chemistry A*, 6 (2018) 3967-3976.
- [7] J. Ai, F.Y. Chen, C.Y. Gao, H.R. Tian, Q.J. Pan, Z.M. Sun, *Inorganic Chemistry*, 57 (2018) 4419-4426.
- [8] Y.L. Wang, Z.Y. Liu, Y.X. Li, Z.L. Bai, W. Liu, Y.X. Wang, X.M. Xu, C.L. Xiao, D.P. Sheng, D.W. Juan, J. Su, Z.F. Chai, T.E. Albrecht-Schmitt, S. Wang, *Journal of the American Chemical Society*, 137 (2015) 6144-6147.
- [9] Y. Park, Y.C. Lee, W.S. Shin, S.J. Choi, *Chemical Engineering Journal*, 162 (2010) 685-695.



# **Chapter 7 – Pressure Swing CO<sub>2</sub> Adsorption Using Functional Hypercrosslinked Polymers**

## Chapter 7. High Pressure CO<sub>2</sub> Sequestration via PSA

### 7.1 Chapter Foreword

#### A Pressure Swing Approach Toward Selective CO<sub>2</sub> Sequestration Using Functionalized Hypercrosslinked Polymers

Alex M. James, Jake Reynolds, Daniel G. Reed, Peter Styring and Robert Dawson

The low density framework, high chemical and thermal stability, ease of synthesis and inclusion of functionality combined with the high surface areas of microporous polymers has led to numerous publications using these material as sorbents for CO<sub>2</sub> capture and sequestration applications. However, many of these reports sees the uptake carried out at low temperatures and atmospheric pressure and using pure streams of CO<sub>2</sub>, which is not at all representative of actual anthropogenic CO<sub>2</sub> conditions.

In this work a pressure swing methodology (*i.e.* adsorption at high pressure and desorption at low pressure) is applied towards the uptake and separation of dilute stream of CO<sub>2</sub> which is more representative of industrially significant anthropogenic CO<sub>2</sub> point sources. Functionalised hypercrosslinked polymers are synthesised using different monomers and these material are explored to determine the effect different chemical moieties has on uptake capacity and selectivity.

At the time of writing this paper has been submitted and is pending review. A breakdown of author contributions is listed below:

**Alex M James** – Supervised JR in the synthesis and characterisation of the polymer materials synthesised and used in this work. Carried out the high pressure uptake experiments (both CO<sub>2</sub> and N<sub>2</sub>) using the PSA setup. Conducted all gas sorption experiments at 1 bar to determine surface area and pore volume. Wrote the manuscript. Supervised by RD

**Jake Reynolds** – Supervised by AMJ and was involved in the synthesis of the materials used for the gas uptake at elevated pressure.

**Daniel G. Reed** – Designed the PSA setup used to collect the high pressure data for this work. Trained AMJ in how to collect data from the machine. Supervised by PS

**Peter Styring** – Supervisor of DGR, was involved in writing the manuscript.

**Robert Dawson** – Supervisor of AMJ was involved in writing of manuscript.

# A Pressure Swing Approach Toward Selective CO<sub>2</sub> Sequestration Using Functionalized Hypercrosslinked Polymers

Alex M. James,<sup>[a]</sup> Jake Reynolds,<sup>[a]</sup> Dan G. Reed,<sup>[b]</sup> Peter Styring<sup>[b]</sup> and Robert Dawson<sup>\*[a]</sup>

**Abstract:** Functionalized hypercrosslinked polymers (HCPs) with surface areas between 213 – 1124 m<sup>2</sup>/g based on a range of monomers containing different chemical moieties are evaluated for CO<sub>2</sub> capture using a pressure swing adsorption (PSA) methodology under humid conditions and elevated temperatures. The networks demonstrated rapid CO<sub>2</sub> uptake reaching maximum uptakes in under 60 seconds. The most promising networks demonstrating the best selectivity and highest uptakes were applied to a pressure swing setup using simulated flue gas streams. The carbazole, triphenylmethanol and triphenylamine networks were found to be capable of converting a dilute CO<sub>2</sub> stream (> 20 %) into a concentrated stream (> 85 %) after only two pressure swing cycles from 20 bar (adsorption) to 1 bar (desorption). This work demonstrates the ease by which readily synthesised functional porous materials can be successfully applied to a pressure swing methodology and used to separate CO<sub>2</sub> from N<sub>2</sub> from industrially applicable simulated gas streams under more realistic conditions.

## Introduction

The 2015 Paris Agreement aims to limit the average global temperature increase to 2°C. One of the key causes of climate change is anthropogenic carbon dioxide, and recently the UK government has committed to a net zero emissions target by 2050. In the long term the most effective method to lower carbon dioxide (CO<sub>2</sub>) emissions is to switch to renewable energy sources. However, the transition to renewable energy such as solar and wind is likely to take decades hence the continued reliance on non-sustainable energy sources.<sup>[1,2]</sup> In order to meet the short to medium term emissions targets, the capture, storage and utilisation of CO<sub>2</sub> from large anthropogenic point sources such as fossil fuel power plants and the steel industry, is key to mitigating the ever increasing levels of CO<sub>2</sub> in the atmosphere thereby preventing irreversible climate change.<sup>[3]</sup>

One of the key challenges facing materials for carbon capture from anthropogenic point sources is the low concentration of CO<sub>2</sub> in flue gas streams is often around or lower than 20%. The remaining volume is comprised largely of N<sub>2</sub> with smaller amounts of water vapour, oxygen, SO<sub>2</sub> and NO<sub>x</sub> (amongst others).<sup>[4]</sup> In order to capture CO<sub>2</sub> efficiently, any capture process therefore needs to show high selectivity towards CO<sub>2</sub>.

The current state-of-the-art industrial method of capturing CO<sub>2</sub>, dubbed amine scrubbing, has remained unchanged for decades and involves the use of aqueous solutions of amines such as

monoethanolamine (MEA).<sup>[5]</sup> This process relies on chemisorption, by which the MEA selectively reacts with CO<sub>2</sub> to form a carbamate salt.

Over the past few years there has been a move away from the amine scrubbing process due to significant and numerous drawbacks. These include the chemisorption process requiring very high temperatures (ca. 130 °C) to liberate the CO<sub>2</sub> and regenerate the free amine. Attaining these high temperatures is a challenge for industry and comes at a high price both fiscally and environmentally. Nonsensically in order to power this process one has to produce CO<sub>2</sub> to capture CO<sub>2</sub>.<sup>[6]</sup> Other issues include the corrosive nature of the amine solution along with the sensitivity of such solvents to other gaseous impurities present in the flue gas such as SO<sub>x</sub> and NO<sub>x</sub>.<sup>[7-9]</sup> This results in continuous degradation as well as evaporation meaning the amine solution needs to be changed on a regular basis thereby raising the operating cost of the process.<sup>[10]</sup> Due to the difference in the temperature at which the reaction of amines and CO<sub>2</sub> react compared to the temperature required to regenerate the amine, this process is known as a temperature swing approach. Due to the high energy penalty required by the regeneration temperature, this method is not ideal for the capture of CO<sub>2</sub>. In contrast, a physisorption process, whereby the interaction between adsorbent and adsorbate is weaker yet still significant enough for the binding of CO<sub>2</sub> to the substrate surface, requires much less energy to regenerate the free material and liberate the pure gas.<sup>[3,8]</sup>

Most reports of new materials for carbon capture use a temperature swing approach. There is much less literature relating to adsorbents using the alternative pressure swing approach. Pressure swing adsorption (PSA) technology is a growing body of research which is compatible with solid sorbents and has the potential to optimise and replace the current temperature swing technologies applied in industry.<sup>[11,12]</sup> In a pressure swing approach CO<sub>2</sub> is adsorbed at high pressures by a solid sorbent before being desorbed at low pressures or under slight vacuum (VPSA). Different sorbents require different pressure profiles but are typically around 10-30 bar in the adsorption cycle. In comparison to temperature swing, PSA is an inherently low energy technique for which high temperatures are not required during adsorption or desorption. PSA is also a much faster technique compared to temperature swing as there is no thermal lag meaning that the adsorb/desorb cycle can be performed rapidly. There is much scope for variation with PSA such as optimisation of the sorbent, the working pressures and temperatures of the process, all of which can be varied to yield the most efficient and effective system.

In order for a material to be considered a viable choice as a solid sorbent for pressure swing adsorption, certain criteria have to be met. These include; the material being stable and selective towards CO<sub>2</sub> at both low and high pressures. The material must demonstrate good recyclability over many pressure cycles. Furthermore, it is desirable to be both cheap and relatively simple to make with good yields due to the scale of the process and to keep the cost low.

Over the last two decades, as interest in carbon dioxide capture/utilisation, CCS/CCU, has accelerated numerous sorbents demonstrating CO<sub>2</sub> capturing capabilities have been

---

[a] Dr. R. Dawson  
Department of Chemistry  
University of Sheffield  
13 Brook Hill, Sheffield, S3 7HF  
E-mail: r.dawson@sheffield.ac.uk

[b] Prof. Peter Styring  
Department of Chemical and Biological Engineering  
University of Sheffield  
Mappin Street, Sheffield, S1 3DJ

reported mainly using the temperature swing approach.<sup>[3,7,8,13]</sup> These include zeolites,<sup>[14]</sup> hybrid materials such as metal organic frameworks (MOFs),<sup>[15]</sup> activated carbons, ionic liquids,<sup>[16,17]</sup> and microporous organic polymers (MOPs).<sup>[18–24]</sup>

MOPs are a family of porous materials comprised solely of the lighter elements of the periodic table. There are a large number of different sub-classes of MOP such as; conjugated microporous polymers (CMPs)<sup>[25–27]</sup>, covalent organic frameworks (COFs)<sup>[28–31]</sup>, covalent triazine frameworks (CTFs)<sup>[32,33]</sup>, polymers of intrinsic microporosity (PIMs)<sup>[34–37]</sup> which have been applied to various applications ranging from chemosensing,<sup>[32,38–40]</sup> catalysis<sup>[41–44]</sup> and waste water treatment.<sup>[45–48]</sup> CO<sub>2</sub> uptakes of MOPs are typically measured at conditions of around 1 bar and at temperatures ranging from 273–298 K. Some of the best performing MOPs include functionalised networks containing amine groups with uptakes of around 15–20 wt. % at 1 bar and 273 K.<sup>[49,50]</sup> At higher pressures materials such as PAF-1 and PPN-4 have a reported uptake of 130 wt. % (40 bar, 298 K)<sup>[51]</sup> and 212 wt. % (50 bar, 295 K)<sup>[52]</sup> respectively. However, one class of MOP stands out for the application of carbon dioxide capture due to their low skeletal density, chemical and thermal stability and synthesis using cheap, readily available starting materials on a large scale – hypercrosslinked polymers (HCPs).<sup>[20–22,53]</sup> At high pressures there are however relatively few studies. HCPs based on 4,4'-bis(chloromethyl)-1,1'-biphenyl (BCMBP) were shown to have uptakes of up to 58.7 wt. % at 30 bar.<sup>[21]</sup> While this falls short of the PAF/PPN materials, HCP synthesis is considerably less complex and cheaper.

Hypercrosslinked polymers are rigid porous networks with typical surface areas in the range of 500–2000 m<sup>2</sup>/g.<sup>[54–56]</sup> Their synthesis is often based on Friedel-Crafts chemistry using a Lewis-acid catalyst such as iron (iii) chloride to yield a highly crosslinked and permanently microporous insoluble solid product. HCP synthesis requires the use of crosslinking groups, such as methyl chlorides often dubbed “internal crosslinkers”,<sup>[57,58]</sup> or external crosslinkers such as formaldehyde dimethyl acetal (FDA).<sup>[59]</sup> This external “knitting method” allows potentially any rigid aromatic monomer to be hypercrosslinked.

Crucially the “knitting method” provides a route to the incorporation of a range of chemical functionalities into the networks by polymerisation of pre-functionalised monomers. This has led to the investigation of HCPs for a variety of different applications.<sup>[20,60–62]</sup> For CO<sub>2</sub> capture it is well known that different chemical moieties can impart increased selectivity towards CO<sub>2</sub> over other gases due to more favourable interactions with the chemical moiety and the dipole of the CO<sub>2</sub>.<sup>[24,63–65]</sup> These interactions are crucial to maximising their selectivity towards CO<sub>2</sub>. In this work we report the synthesis, characterisation and implementation of functional HCP networks for use as solid sorbents using a PSA approach. The CO<sub>2</sub> uptake capacity and uptake kinetics are measured at high pressure followed by measurements using simulated flue gas compositions. The CO<sub>2</sub>:N<sub>2</sub> selectivity of the materials is calculated and the recyclability potential of the HCPs is evaluated. Further to this, in order to keep the study industrially applicable all samples were exposed to simulated gas streams and the materials themselves were exposed to the humid laboratory conditions and not used straight out of the oven.

## Results and Discussion

Seven hypercrosslinked polymers were synthesised from functionalised monomers all possessing different chemical moieties purposefully to see how these groups affected the CO<sub>2</sub> uptake and selectivity at high pressure. Monomers including alcohol functionalities (triphenylmethanol and BINOL), amine functionality (2° amine carbazole and 3° amine triphenylamine), halogens (fluorobenzene) and a newly synthesised network based on dibenzyl ether which contains ether linkages were all hypercrosslinked (Figure 1). Further to this, a non-functionalised network was synthesised from polystyrene which provides a good comparison between the functionalised and non-functionalised networks. Whilst hypercrosslinked polymers made from poly(styrene),<sup>[66]</sup> carbazole,<sup>[67]</sup> BINOL,<sup>[20]</sup> triphenylamine<sup>[68]</sup> and fluorobenzene<sup>[60]</sup> have previously been reported, this is to our knowledge the first reported synthesis of networks synthesised from dibenzyl ether and triphenylmethanol.

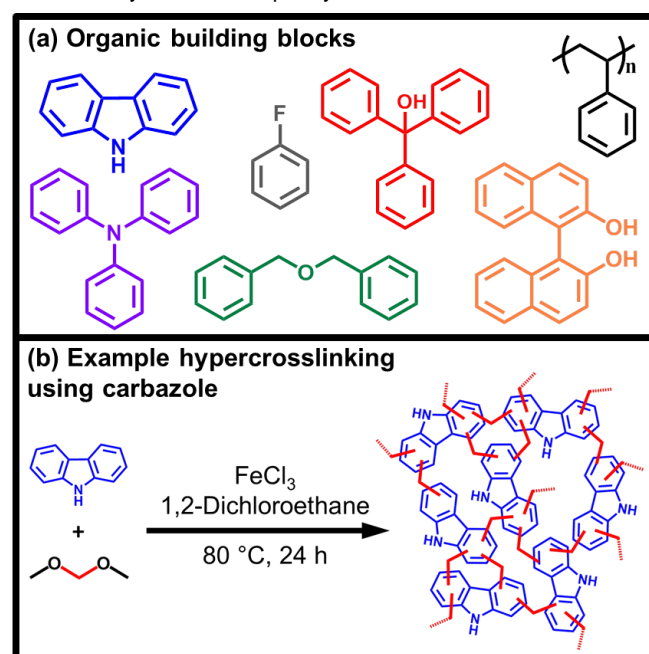


**Figure 1.** Schematic representation of HCP synthesis using the so-called external crosslinking or “knitting” method. (a) Example monomers used in this work, Poly(styrene), triphenylmethanol, BINOL, carbazole, triphenylamine, dibenzyl ether and fluorobenzene and (b) an example of the hypercrosslinking synthesis.

All networks were obtained in good yields (Table S1) similar to that found for other HCPs.<sup>[20,59]</sup> Structural characterisation of the HCPs was performed by elemental analysis (Table S2), infrared spectroscopy (FT-IR) (Figure S1) and <sup>13</sup>C solid state CP/MAS NMR spectroscopy (ssNMR) (Figures 3 & S2). Calculated %C, H and N of the networks were found to be typical for HCPs synthesised via Friedel-Crafts alkylation. There is some variation from the expected values as these are calculated assuming an idealised structure in which all protons have been exchanged for a methylene bridge. The presence of end groups and adsorbed molecules such as CO<sub>2</sub> and water vapour may also contribute to the deviation from theoretical values. Nitrogen values of 5.17 % and 4.35 % were observed for the carbazole and triphenylamine networks respectively, indicating successful incorporation of amines into the structure.

Analysis by FTIR (Figure S1) suggests that the incorporation of the monomers into the networks with characteristic signals at ca. 2800 cm<sup>-1</sup> and 1600 cm<sup>-1</sup> corresponding to the, C-H and C=C stretches respectively while an additional signal at ca. 3500 cm<sup>-1</sup> is assigned to the -OH stretch in the triphenylmethanol network. An ether stretch at ca. 1000 cm<sup>-1</sup> is observed for the dibenzyl ether network.

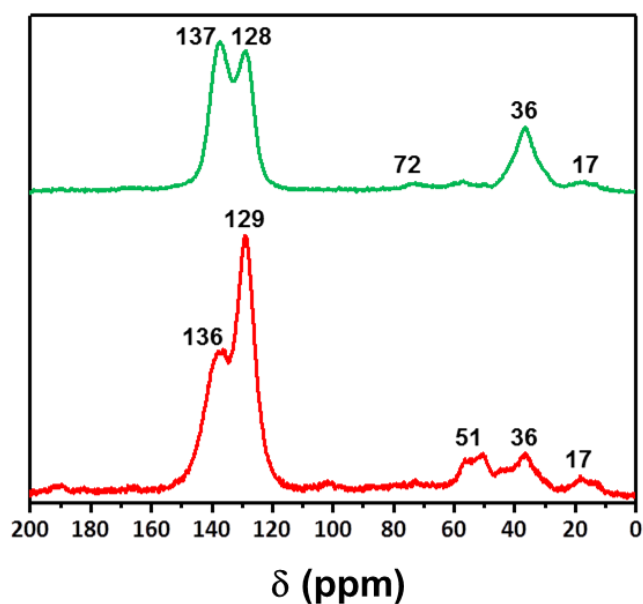


**Figure 2.** CP/MAS solid state <sup>13</sup>C NMR spectra of the dibenzyl ether (above) and triphenylmethanol (below) networks

<sup>13</sup>C ssNMR spectra were collected for all samples and can be seen in Figure S2 whilst the spectra for the two newly synthesised materials are presented in Figure 2. All networks showed two prominent signals at ca. 140 and 130 ppm corresponding to quaternary aromatic carbons (C<sub>Ar</sub>) and aromatic C<sub>Ar-H</sub>. Signals at 36 ppm are assigned to methylene bridges in the networks. The resonance at 51 ppm for the triphenylmethanol network is assigned to the C-OH. For the dibenzyl ether network a resonance at 72 ppm is assigned to the CH<sub>2</sub>-O-CH<sub>2</sub> carbons adjacent to the ether linkage. A further resonance is observed at ca. 17 ppm and is attributed to unreacted end groups arising from the FDA crosslinker.

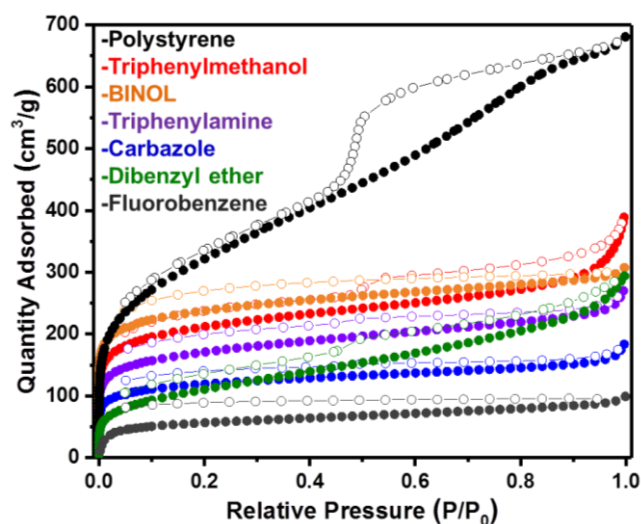


**Figure 3.** Full gas sorption isotherms for all polymer networks synthesised. Poly(styrene), triphenylmethanol, BINOL, carbazole, triphenylamine, dibenzyl ether and fluorobenzene.

The porosity of the networks was measured using nitrogen adsorption/desorption isotherms at 77 K (Figure 3). BET surface areas were calculated over a relative pressure range ( $P/P_0$ ) of 0.01–0.15 with the total pore and micropore volumes calculated at 0.95 and 0.1  $P/P_0$  respectively (Table 1). All networks adsorbed large volumes of nitrogen at low relative pressure (<0.1  $P/P_0$ ), indicating the presence of micropores. All networks demonstrated further uptake at higher partial pressures. This was particularly noticeable for the poly(styrene) network which demonstrates a Type II hysteresis loop on the desorb indicative of further larger (meso)pores as previously reported.<sup>[66]</sup>

All samples were found to be porous with surface areas ranging from 213 m<sup>2</sup>/g to 1124 m<sup>2</sup>/g. The highest surface area was found to be derived from the polystyrene network and is similar to that reported previously in the literature.<sup>[66]</sup> Overall the inclusion of functionality into the networks results in a lower surface area than non-functionalised HCPs. Functional 3D monomers however such as BINOL are still able to produce relatively high surface area networks. Despite their lower surface areas, the effects of the functionality are still interesting for CO<sub>2</sub> capture and the potential for increased selectivity over nitrogen.

The total pore volumes of the materials ranged from 0.14 cm<sup>3</sup>/g to 1.01 cm<sup>3</sup>/g with the fluorobenzene and polystyrene derived HCPs showing the lowest and highest pore volumes respectively as might be expected from the highest and lowest surface area networks. As a proportion of pore volume ( $V_{0.1}/V_{tot}$ ) both carbazole and fluorobenzene showed the largest contribution of micropores while dibenzyl ether was found to have a larger proportion of meso- and macropores. It has been previously reported that smaller pores are preferential over larger pores for CO<sub>2</sub> capture particularly at lower pressures where the uptake has not reached a maximum. It was hypothesised that the networks with a larger % of micropores may therefore be better suited towards CO<sub>2</sub> capture than those possessing larger pores at 25 bar.<sup>[69]</sup>

**Table 1.** Gas sorption properties of HCP networks

Network	SA <sub>BET</sub> (m <sup>2</sup> /g) <sup>[a]</sup>	V <sub>tot</sub> (cm <sup>3</sup> /g) <sup>[b]</sup>	V <sub>0.1</sub> (cm <sup>3</sup> /g) <sup>[c]</sup>	V <sub>0.1</sub> /V <sub>tot</sub>
Poly(styrene)	1124	1.01	0.42	0.42
Triphenylmethanol	781	0.48	0.30	0.63
BINOL	888	0.45	0.35	0.70
Dibenzylether	397	0.39	0.14	0.36
Carbazole	445	0.24	0.17	0.71
Triphenylamine	630	0.37	0.24	0.65
Fluorobenzene	213	0.14	0.10	0.71

[a] Apparent BET surface areas calculated at  $P/P_0 = 0.01 - 0.15$ . [b] Total pore volume at 0.99  $P/P_0$ . [c] Micropore volume at 0.1  $P/P_0$

### Kinetic uptake of CO<sub>2</sub>

High pressure CO<sub>2</sub> adsorption experiments were conducted using the setup as previously reported by Reed and co-workers.<sup>[16,70]</sup> Briefly, an adsorbent was packed into a sealed unit which was exposed to high pressures of gas before being weighed to gravimetrically determine CO<sub>2</sub> uptake. All samples were measured three times and an average of the data was taken and used. All measurements on the functionalised HCPs were recorded at 40 °C to more closely match cooled flue gas temperatures from industrial sources. The stack temperature can vary depending on the process but can be 120 °C for post-combustion processes, 250-350 °C from steel plants and over 1000 °C for smelting works. As such, the flue gas temperatures need to be reduced to values where absorption or adsorption are feasible. Moisture vapour is also an important consideration when for post-combustion capture,<sup>[4,19]</sup> therefore all samples were tested under “wet” conditions. More specifically, after synthesis the samples were dried under vacuum at 60 °C before being allowed to adsorb moisture from the air at 40-50% humidity for at least 24 h before all adsorption measurements. These conditions allow for results more comparable to those used in industry where gas mixtures are hydrated.

Pressures of 10 and 20 bar are typical pressures for PSA which are easily attainable without a significant increase in plant operating costs. The rate at which each network reached saturation at 10 and 20 bar was therefore measured (Figure 4). At 20 bar all HCP networks become fully saturated rapidly with  $t_{90}$  values (the time at which 90% of the total uptake is completed), of 85 seconds or less (Table S5), while at the lower pressure of 10 bar the time to reach saturation was up to 3 mins with the hydrophilic networks triphenylmethanol and BINOL taking longest and the hydrophobic networks poly(styrene) and fluorobenzene the shortest (Figure 4). The rapid sorption period is advantageous should these materials be applied to an industrial PSA approach given that the less time the material has to spend at elevated pressures to greater the economic and energy benefit.

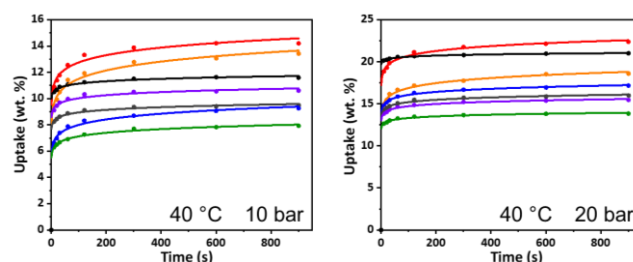


**Figure 4.** Kinetic studies of CO<sub>2</sub> uptake, for poly(styrene), triphenylmethanol, BINOL, carbazole, triphenylamine, dibenzyl ether and fluorobenzene networks at 40 °C and 10 bar (left) and 20 bar (right).

At 10 bar the two –OH containing networks (triphenylmethanol and BINOL) perform the best reporting final uptakes of around 13 and 14 % wt. respectively. Alcohol containing porous polymers have previously been shown to demonstrate good CO<sub>2</sub> capture capabilities, these measurements further demonstrate the advantage of such functionalities at higher pressures.<sup>[20,71]</sup> The highest surface area material – the non-functional poly(styrene) shows uptake at 10 bar at around 11 % wt. This material has a much higher surface area than the two alcohol materials yet still underperforms in comparison to the alcohol networks. At the same time this non-functionalised network outperforms other functionalities, demonstrating that both surface area and functionality is important when designing materials for CCS. The amine containing networks, (triphenylamine and carbazole) and the two other networks, (fluorobenzene and the newly synthesised dibenzyl ether), all perform less well with uptakes ranging from 6 % wt. to 10 % wt.

At 20 bar all samples show increased uptake of CO<sub>2</sub> compared to 10 bar. The triphenylmethanol network continues to show the highest final uptake of around 22 % wt., yet at this elevated pressure the poly(styrene) network is the second best performing material with an uptake of just over 20 % wt. The BINOL network shows a final uptake of just under 17 % wt. The reversal of these two materials may demonstrate that at higher pressures, higher surface area may be more advantageous than chemical functionality. Though, should this be true then, one may expect the fluorobenzene network to show the lowest uptake given its low surface area. In fact, the fluorobenzene network and the triphenylamine network show similar uptakes despite having a surface area being almost 3x lower for fluorobenzene. In this case we attribute the effect to the presence of water which is co-adsorbed in each network. It is known that the presence of water can be detrimental to CO<sub>2</sub> adsorption and the presence of the hydrophobic fluoride functionality may aid the adsorption of CO<sub>2</sub> by the network compared to the higher surface area hydrophilic amine functionalised triphenylamine network. The newly synthesised dibenzyl ether network shows the poorest uptake at ~12 % wt. This poor performance, despite a reasonable surface area, could be somewhat due to the presence of larger pore sizes dominating the material. In comparison, the triphenylmethanol, carbazole and fluorobenzene networks have a greater proportion of smaller micropores aiding their uptake under these conditions.

### Selectivity measurements

In order to investigate how selective the networks were for CO<sub>2</sub> over that of the major component of flue gas (N<sub>2</sub>), the uptake of both CO<sub>2</sub> and N<sub>2</sub> was measured for each HCP network at pressures between 5 and 25 bar at a temperature of 40 °C (Figures S4 & S5). HCP networks were exposed to a pressurised stream of either pure CO<sub>2</sub> or N<sub>2</sub> for a 5-minute adsorption period, the time at which the previous kinetic runs showed to be sufficient for equilibration, after which the gravimetric uptake was recorded and the average uptake calculated over three runs. Using these experiments it is possible to estimate the CO<sub>2</sub>:N<sub>2</sub> selectivity of the networks at high pressures typical for PSA.

**Table 2.** Average CO<sub>2</sub> and N<sub>2</sub> uptake of HCP networks at 40 °C

Network	CO <sub>2</sub> uptake (wt. %)		N <sub>2</sub> uptake (wt. %)	
	10 bar	20 bar	10 bar	20 bar
Poly(styrene)	10.68	20.42	4.30	8.09
Triphenylmethanol	12.02	23.38	3.09	5.94
BINOL	11.29	20.09	3.45	6.28
Dibenzyl ether	7.84	14.73	1.96	3.68
Carbazole	8.76	16.30	2.61	5.12
Triphenylamine	9.13	17.19	2.33	4.02
Fluorobenzene	7.89	14.91	2.77	4.52

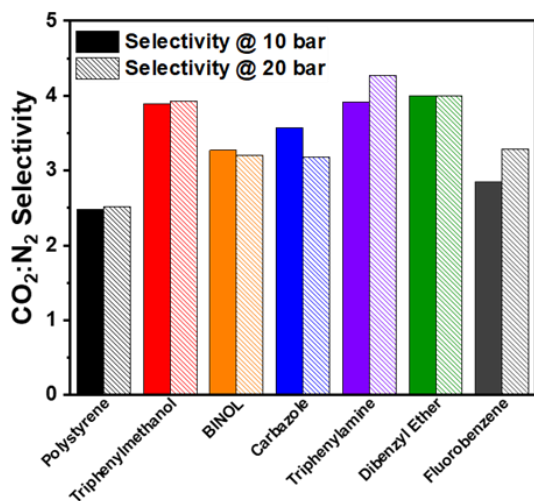


**Figure 5.** CO<sub>2</sub>:N<sub>2</sub> selectivity of networks at 40 °C and 5 bar (solid bars) and 25 bar (dashed bars).

All polymer networks demonstrated some selectivity towards CO<sub>2</sub> over N<sub>2</sub> (Table 2 & Figure 5). The non-functionalised polystyrene network demonstrated uptakes of CO<sub>2</sub> and N<sub>2</sub> of 20.42 wt. % and 8.09 wt. % respectively at 20 bar and 40 °C with a CO<sub>2</sub>:N<sub>2</sub> selectivity of 2.5:1. The functionalised triphenylmethanol network showed the highest uptake for CO<sub>2</sub> of 23.38 wt. % with a N<sub>2</sub> uptake of 5.94 wt. %. Thus the CO<sub>2</sub>:N<sub>2</sub> selectivity at 20 bar and 40 °C is almost 4:1—higher than that of the poly(styrene) network.

All networks demonstrated increased selectivity over the non-functional poly(styrene) network suggesting that chemical functionality is just as important a consideration as surface area when designing porous sorbents for gas uptake. Although these values give some insight into the selective nature of the polymer networks they are nonetheless idealised given that pure gas streams were used throughout the experiment

Whilst some insight into the selectivity of the materials can be derived using pure gas streams, the use of mixed gas streams is more representative of actual industrial flue gas. To investigate how the materials performed at enriching a CO<sub>2</sub> stream the most promising materials were exposed to a gas mix comprised of an 80:20 N<sub>2</sub>:CO<sub>2</sub> at 40 °C and 20 bar for 5 minutes. The concentration of CO<sub>2</sub> in the output gas was measured at 20 bar, after which the pressure was then released from the adsorber. When the pressure reaches 1 bar the concentration of CO<sub>2</sub> was calculated by IR. Finally, the same experiment was repeated using a stream comprised of 50:50 N<sub>2</sub>:CO<sub>2</sub> mix at 40 °C (Figure 6). This test would replicate two cycles whereby the output from the first cycle is fed back in to the PSA setup and the method is repeated once again.

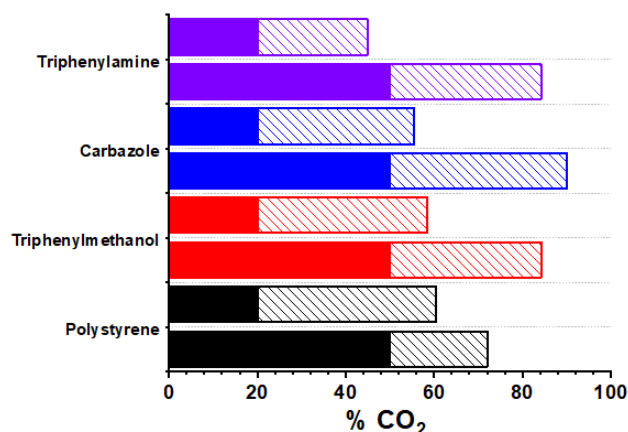


**Figure 6.** CO<sub>2</sub> concentration of the input gas (solid bar) and the output exhaust gas stream at 1 bar (dashed bars) at 40 °C.

Initially, when the chosen samples were exposed to an 80:20 N<sub>2</sub>:CO<sub>2</sub> stream all materials were able to selectively adsorb the CO<sub>2</sub> at 20 bar and then desorb it at 1 bar. This resulted in the successful separation of CO<sub>2</sub> from N<sub>2</sub> and the generation of a gas stream enriched to over 50% CO<sub>2</sub> in the case of triphenylmethanol, poly(styrene) and carbazole after one cycle. We therefore exposed the materials to a 50:50 N<sub>2</sub>:CO<sub>2</sub> stream, the equivalent of feeding the stream from the first test back into the materials and repeated the experiment again. The triphenylmethanol and triphenylamine samples were able to enrich the stream of gas to over 80% CO<sub>2</sub>. This experiment demonstrates that these materials are able to take a dilute stream of flue gas and, after two pressure swing cycles, convert this dilute stream into a concentrated CO<sub>2</sub> stream by preferential adsorption of CO<sub>2</sub> over N<sub>2</sub>.

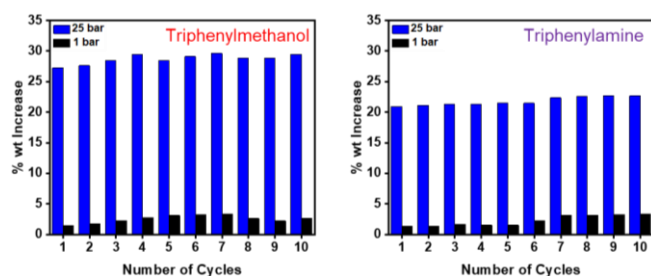


**Figure 7.** Recyclability studies for triphenylmethanol (left) and triphenylamine (right) networks during 10 adsorb/desorb cycles of CO<sub>2</sub> at 25 bar and 40 °C.

Finally, the ability of the sorbents to be used over repeat adsorption-desorption cycles was tested using the best performing triphenylmethanol and triphenylamine networks (Figure 8). These networks were exposed to a 25 bar stream of CO<sub>2</sub> before having the pressure reduced to 1 bar with the uptakes at each pressure recorded and was repeated for 10 cycles. Importantly, as in a typical PSA process the materials were not exposed to a vacuum between runs to remove any CO<sub>2</sub> as not to further increase the energy demands of the process. Both materials reached a maximum uptake at 25 bar and this was found to be reproducible over the 10 cycle run demonstrating no loss in performance over time. Both samples retained some gas at 1 bar though this quantity was minimal (<3% wt.) and had no significant effect on the uptake at higher pressures.

## Conclusions

To conclude, a series of functional porous materials synthesised via conventional hypercrosslinking chemistry were applied as sorbents to selectively separate out CO<sub>2</sub> from simulated flue gas mixes. The uptake capacity, uptake rate and CO<sub>2</sub>:N<sub>2</sub> selectivity at high pressure were all thoroughly examined in order to test the materials at high pressure and using a pressure swing approach. The best performing materials were then taken forward and applied towards actual pressure swing separation experiments using simulated gas mixtures representative of those in industry. Finally, the recyclability of the optimum materials was tested to investigate if their performance was hindered after multiple adsorb/desorb cycles. All materials were found to uptake CO<sub>2</sub> rapidly with most of the uptake being complete within 2 minutes with the –OH functionalised and non-functional poly(styrene) network showing the highest CO<sub>2</sub> capacity. Due to their high and selective uptakes both the triphenylmethanol and triphenylamine networks were taken forward and applied to an actual pressure swing approach where it was found that after only two cycles they were able to convert a 20% CO<sub>2</sub> stream into one exceeding 85% CO<sub>2</sub>. This was an excellent example of how cheaply synthesised porous materials can be easily synthesised and applied to a pressure swing methodology demonstrating excellent CO<sub>2</sub>:N<sub>2</sub> capabilities. It is hoped that this work inspires more research into PSA techniques so as to improve on the current energy intensive and fiscally demanding temperature swing techniques rife throughout industry.

## Experimental Section

### Materials

Anhydrous 1,2-dichloroethane (DCE, > 99%), iron (III) chloride (FeCl<sub>3</sub>, 97%) and formaldehyde dimethyl acetal (FDA, >99%), BINOL (>99%), dibenzyl ether (>99%) and poly(styrene) (Mn=280 000 g/mol) were all purchased from Sigma-Aldrich. Triphenylmethanol (Lancaster synthesis, >99%), carbazole (Alfa Aesar, 95%) and triphenylamine (Fluorochem >99%) were used as received. All chemicals were used as received unless stated otherwise.

### Synthesis of HCPs

Hypercrosslinked porous polymers were synthesised via the “knitting route” using functional aromatic monomers. All reactions were performed under a nitrogen atmosphere (see Table S1 for details). Using triphenylmethanol as an example; triphenylmethanol (3.00 g, 11.54 mmol, 1 eq.) was added to a 2-necked round bottom flask which was degassed by three freeze-pump-thaw cycles. To this vessel DCE (60 mL) and FDA (7.65 mL, 86.57 mmol, 7.5 eq.) were added along with a slurry of FeCl<sub>3</sub> (14.02 g, 86.57 mmol, 7.5 eq.) in DCE. The reaction was heated to 80 °C and left for 16 h to afford a solid black product. The crude black product was washed and filtered with methanol before being solvent extracted with methanol using Soxhlet apparatus overnight. The black solid was washed and filtered with chloroform and methanol before being left to dry overnight under vacuum at 60 °C.

### Characterisation

Fourier transform infrared (FTIR) spectroscopy was performed using a Perkin-Elmer Spectrum 100 fitted with an attenuated total reflectance tip (ATR). Solid-State NMR samples were packed into 4 mm zirconia rotors and transferred to a Bruker Avance III HD spectrometer. 1D <sup>1</sup>H-<sup>13</sup>C cross-polarisation magic angle spinning (CP/MAS) NMR experiments were measured at 125.76 MHz (500.13 MHz <sup>1</sup>H) at a MAS rate of 10.0 kHz. The 1H  $\pi/2$  pulse was 3.4  $\mu$ s, and two-pulse phase modulation (TPPM) decoupling was used during the acquisition. The Hartmann-Hahn condition was set using hexamethylbenzene. The spectra were measured using a contact time of 2.0 ms. The relaxation delay D1 for each sample was individually determined from the proton T1 measurement (D1 = 5  $\times$  T1). Samples were collected until sufficient signal to noise was observed, typically greater than 256 scans. The values of the chemical shifts are referred to that of TMS.

Gas sorption measurements were performed using a Micromeritics ASAP 2020 Plus analyser employing high purity gases. Approximately 100 mg of sample was degassed at 120 °C for 16 h under dynamic vacuum immediately prior to analysis. BET surface areas were calculated using nitrogen gas at 77 K over a pressure range of 0.01-0.15 P/P<sub>0</sub>.

High pressure adsorption experiments were carried out in an identical way to that previously reported by Reed et al.<sup>[70]</sup> using a bespoke packed-bed adsorption column constructed from Swagelok™ (Fig. 8) piping and fitting using a Jasco BP-1580-81 back pressure regulator, an Omega PX409USB High Accuracy Pressure Transducer, a 42AAV48 Midwest Pressure Systems Gas Pressure Booster, and an AND GF-1000 High Capacity 3 decimal place balance. The reactor was isolated from the system using valves and the assembly weighed on the balance. Desorption was measured by slowly opening the valves while still on the balance. Supported sorbent packed densities were measured using a Micromeritics

AccuPyc 1340 Pycnometer. These results obtained from this method have been previously verified through running identical experiments using a Hidden Isochema IGA-0002 adsorption apparatus between 0 – 10 bar. <sup>[70]</sup>

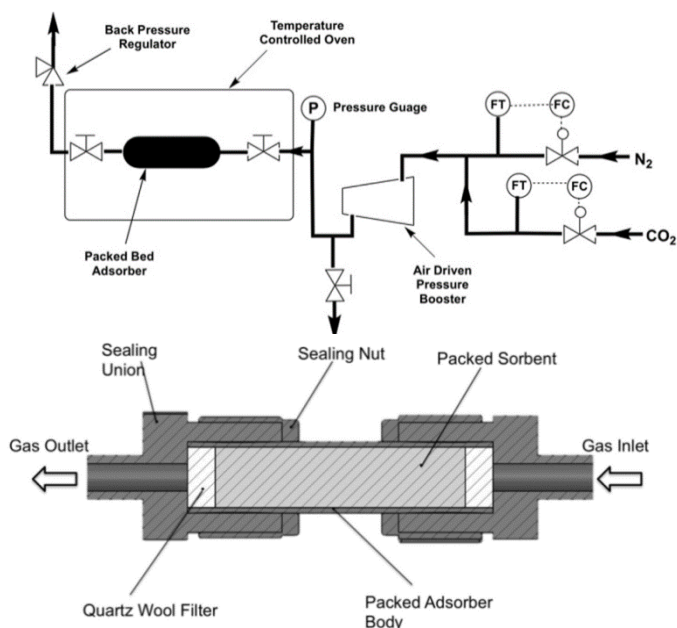


**Figure 8.** (Top) Simplified flow diagram of the experimental apparatus setup used during the high pressure testing. (Bottom) Cross-sectional view of the packed-bed adsorber used for CO<sub>2</sub> separation at high pressures. Figures reproduced with permission from ref. <sup>[70]</sup>. Copyright 2017, Reed, Dowson and Styring.

Given that uptake was determined gravimetrically it was important to calculate the weight of gas present which was not interacting with the sorbent. This is known as the void space. The void space was calculated before each run took place. The accurate internal volume of the adsorber (empty) was found by water displacement ( $V_A$ ). The adsorber rig was then weighed (empty) and under vacuum. Quartz wool was used to ensure that packed polymers were not ejected from the adsorber, and this was also weighed. A portion of quartz wool was packed into one end of the adsorber and the polymer to be tested was then packed on top. The second portion of quartz wool was then added at the other end to seal the polymer in place and the adsorber was closed and sealed. The adsorber was then re-weighed under vacuum to give the packed sorbent weight. The volumes of the sorbent ( $V_S$ ) and quartz wool ( $V_Q$ ) were found using the density data obtained from the pycnometer measurements. These volumes were subtracted from the total internal volume to give the void space as shown in Eq. 1.

$$\text{Void Space} = V_A - (V_S + V_Q) \quad \text{Eq. 1}$$

The CO<sub>2</sub> capacity of the sorbent was calculated using a static gas pressure and was carried out using pure CO<sub>2</sub> gas. The starting weight of the packed adsorber was taken before the gas was introduced. Pure CO<sub>2</sub> then enters the adsorber and the total weight increase of the system was determined (MT). This was achieved by closing the valves to the reactor, removing it from the system and placing it on the balance, the mass of the empty assembly having previously been measured. The mass increase was attributed to the CO<sub>2</sub> that had been adsorbed onto the sorbent ( $M_{ads}$ ) and CO<sub>2</sub> in the void space ( $M_{void}$ ). In order to find the mass of CO<sub>2</sub> in the void space, the density of the gas at that specific pressure and temperature was determined. This void space mass ( $M_{void}$ ) was removed from the total

mass increase (MT). The remaining mass ( $M_{ads}$ ) was then attributed to the gas that had adsorbed onto the sorbent (Eq. 2)

$$M_{ads} = M_T - M_{void} \quad \text{Eq.2}$$

Live IR tracking was carried out via non-dispersive infrared absorption using a CM-40401 SprintIR6S high speed CO<sub>2</sub> sensor, capable of taking 20 readings per second accurate to 70 ppm, purchased from CO<sub>2</sub>Meter. The detector was calibrated using a pure stream of N<sub>2</sub> gas. Data was analysed using GasLab® version 2.0.8.14 which allowed for CO<sub>2</sub> output to be presented as a % concentration.

## Acknowledgements

PS would like to thank the ESPRC for funding of the CO<sub>2</sub>Chem Grand Challenge Network (EP/K007947/1 and EP/P026435/1). Dr. Sandra van Meurs is thanked for running solid state NMR samples.

- [1] International Energy Agency, *World Energy Outlook 2008*; 2008; Vol. 23.
- [2] M. E. Boot-Handford, J. C. Abanades, E. J. Anthony, M. J. Blunt, S. Brandani, N. Mac Dowell, J. R. Fernandez, M.-C. Ferrari, R. Gross, J. P. Hallett, R. S. Haszeldine, P. Heptonstall, A. Lyngfelt, Z. Makuch, E. Mangano, R. T. J. Porter, M. Pourkashanian, G. T. Rochelle, N. Shah, J. G. Yao, P. S. Fennell, *Energy Environ. Sci.* **2014**, *7*, 130.
- [3] A. Samanta, A. Zhao, G. K. H. Shimizu, P. Sarkar, R. Gupta, *Ind. Eng. Chem. Res.* **2012**, *51*, 1438.
- [4] T. C. Drage, C. E. Snape, L. A. Stevens, J. Wood, J. Wang, A. I. Cooper, R. Dawson, X. Guo, C. Satterley, R. Irons, *J. Mater. Chem.* **2012**, *22*, 2815.
- [5] A. J. Reynolds, T. V. Verheyen, S. B. Adeloju, E. Meuleman, P. Feron, *Environ. Sci. Technol.* **2012**, *46*, 3643.
- [6] M. Oschatz, M. Antonietti, *Energy Environ. Sci.* **2017**, *11*, 57.
- [7] D. M. D'Alessandro, B. Smit, J. R. Long, *Angew. Chemie Int. Ed.* **2010**, *49*, 6058.
- [8] J. Wang, L. Huang, R. Yang, Z. Zhang, J. Wu, Y. Gao, Q. Wang, D. O'Hare, Z. Zhong, *Energy Environ. Sci.* **2014**, *7*, 3478.
- [9] P. Luis, *Desalination* **2016**, *380*, 93.
- [10] O. Aschenbrenner, P. Styring, *Energy Environ. Sci.* **2010**, *3*, 1106.
- [11] J. Schell, N. Casas, D. Marx, M. Mazzotti, *Ind. Eng. Chem. Res.* **2013**, *52*, 8311.
- [12] L. Riboldi, O. Bolland, *Energy Procedia* **2017**, *114*, 2390.
- [13] P. Markewitz, W. Kuckshinrichs, W. Leitner, J. Linssen, P. Zapp, R. Bongartz, A. Schreiber, T. E. Müller, *Energy Environ. Sci.* **2012**, *5*, 7281.
- [14] M. Abu Ghali, Y. Dahman, *Energy Technol.* **2017**, *5*, 356.
- [15] M. Ding, R. W. Flaig, H.-L. Jiang, O. M. Yaghi, *Chem. Soc. Rev.* **2019**, *48*, 2783.
- [16] G. R. M. Dowson, D. G. Reed, J.-M. Bellas, C. Charalambous, P.

- Styring, *Faraday Discuss.* **2016**, *192*, 511.
- [17] S. Supasitmongkol, P. Styring, *Energy Environ. Sci.* **2010**, *3*, 1961.
- [18] L. Tan, B. Tan, *Chem. Soc. Rev.* **2017**, *46*, 3322.
- [19] R. T. Woodward, L. A. Stevens, R. Dawson, M. Vijayaraghavan, T. Hasell, I. P. Silverwood, A. V Ewing, T. Ratvijitvech, J. D. Exley, S. Y. Chong, F. Blanc, D. J. Adams, S. G. Kazarian, C. E. Snape, T. C. Drage, A. I. Cooper, *J. Am. Chem. Soc.* **2014**, *136*, 9028.
- [20] R. Dawson, L. A. Stevens, T. C. Drage, C. E. Snape, M. W. Smith, D. J. Adams, A. I. Cooper, *J. Am. Chem. Soc.* **2012**, *134*, 10741.
- [21] C. F. Martin, E. Stöckel, R. Clowes, D. J. Adams, A. I. Cooper, J. J. Pis, F. Rubiera, C. Pevida, *J. Mater. Chem.* **2011**, *21*, 5475.
- [22] R. Dawson, A. I. Cooper, D. J. Adams, *Polym. Int.* **2013**, *62*, 345.
- [23] R. Dawson, E. Stöckel, J. R. Holst, D. J. Adams, A. I. Cooper, *Energy Environ. Sci.* **2011**, *4*, 4239.
- [24] R. Dawson, D. J. Adams, A. I. Cooper, *Chem. Sci.* **2011**, *2*, 1173.
- [25] J. X. Jiang, F. Su, A. Trewin, C. D. Wood, N. L. Campbell, H. Niu, C. Dickinson, A. Y. Ganin, M. J. Rosseinsky, Y. Z. Khimyak, A. I. Cooper, *Angew. Chemie - Int. Ed.* **2007**, *46*, 8574.
- [26] J. Schmidt, M. Werner, A. Thomas, *Macromolecules* **2009**, *42*, 4426.
- [27] D. J. Woods, R. S. Sprick, C. L. Smith, A. J. Cowan, A. I. Cooper, *Adv. Energy Mater.* **2017**, *1700479*, 1700479.
- [28] J. L. Segura, M. J. Mancheño, F. Zamora, *Chem. Soc. Rev.* **2016**, *45*, 5635.
- [29] A. P. Cote, A. I. Benin, N. W. Ockwig, M. O'Keeffe, A. J. Matzger, O. M. Yaghi, *Science (80-. )* **2005**, *310*, 1166.
- [30] S. Dalapati, S. Jin, J. Gao, Y. Xu, A. Nagai, D. Jiang, *J. Am. Chem. Soc.* **2013**.
- [31] P. Kuhn, M. Antonietti, A. Thomas, *Angew. Chemie Int. Ed.* **2008**, *47*, 3450.
- [32] A. Bhunia, D. Esquivel, S. Dey, R. Fernández-Terán, Y. Goto, S. Inagaki, P. Van Der Voort, C. Janiak, *J. Mater. Chem. A* **2016**, *4*, 13450.
- [33] Y. Fu, W. Yu, W. Zhang, Q. Huang, J. Yan, C. Pan, G. Yu, *Polym. Chem.* **2018**, *9*, 4125.
- [34] P. M. Budd, B. S. Ghanem, S. Makhseed, N. B. McKeown, K. J. Msayib, C. E. Tattershall, *Chem. Commun.* **2004**, 230.
- [35] N. B. McKeown, *ISRN Mater. Sci.* **2012**, *2012*, 1.
- [36] P. M. Budd, K. J. Msayib, C. E. Tattershall, B. S. Ghanem, K. J. Reynolds, N. B. McKeown, D. Fritsch, *J. Memb. Sci.* **2005**, *251*, 263.
- [37] D. Ramimoghadam, E. M. Gray, C. J. Webb, *Int. J. Hydrogen Energy* **2016**, *41*, 16944.
- [38] H. Ma, B. Li, L. Zhang, D. Han, G. Zhu, *J. Mater. Chem. A* **2015**, *3*, 19346.
- [39] A. Deshmukh, S. Bandyopadhyay, A. James, A. Patra, *J. Mater. Chem. C* **2016**, *4*, 4427.
- [40] X. Wu, H. Li, B. Xu, H. Tong, L. Wang, *Polym. Chem.* **2014**, *5*, 4521.
- [41] J. Luo, J. Lu, J. Zhang, *J. Mater. Chem. A* **2018**, *6*, 15154.
- [42] R. M. N. Kalla, M.-R. Kim, I. Kim, *Ind. Eng. Chem. Res.* **2018**, *57*, 11583.
- [43] R. Li, Z. J. Wang, L. Wang, B. C. Ma, S. Ghasimi, H. Lu, K. Landfester, K. A. I. Zhang, *ACS Catal.* **2016**, *6*, 1113.
- [44] J. X. Jiang, C. Wang, A. Laybourn, T. Hasell, R. Clowes, Y. Z. Khimyak, J. Xiao, S. J. Higgins, D. J. Adams, A. I. Cooper, *Angew. Chemie - Int. Ed.* **2011**, *50*, 1072.
- [45] B. Li, F. Su, H.-K. Luo, L. Liang, B. Tan, *Microporous Mesoporous Mater.* **2011**, *138*, 207.
- [46] Z. Li, H. Li, H. Xia, X. Ding, X. Luo, X. Liu, Y. Mu, *Chem. - A Eur. J.* **2015**, *21*, 17355.
- [47] R. X. Yang, T. T. Wang, W. Q. Deng, *Sci. Rep.* **2015**, *5*, 1.
- [48] A. M. James, S. Harding, T. Robshaw, N. Bramall, M. D. Ogden, R. Dawson, *ACS Appl. Mater. Interfaces* **2019**, *11*, 22464.
- [49] W. Lu, J. P. Sculley, D. Yuan, R. Krishna, Z. Wei, H.-C. Zhou, *Angew. Chemie Int. Ed.* **2012**, *51*, 7480.
- [50] R. M. Gulam, T. E. Reich, R. Kassab, K. T. Jackson, H. M. El-Kaderi, *Chem. Commun.* **2012**, *48*, 1141.
- [51] T. Ben, H. Ren, S. Ma, D. Cao, J. Lan, X. Jing, W. Wang, J. Xu, F. Deng, J. M. Simmons, S. Qiu, G. Zhu, *Angew. Chemie* **2009**, *121*, 9621.
- [52] D. Yuan, W. Lu, D. Zhao, H.-C. Zhou, *Adv. Mater.* **2011**, *23*, 3723.
- [53] Y. Liu, S. Wu, G. Wang, G. Yu, J. Guan, C. Pan, Z. Wang, *J. Mater. Chem. A* **2014**, *2*, 7795.
- [54] R. Dawson, A. I. Cooper, D. J. Adams, *Prog. Polym. Sci.* **2012**, *37*, 530.
- [55] S. Xu, Y. Luo, B. Tan, *Macromol. Rapid Commun.* **2013**, *34*, 471.
- [56] J. Huang, S. R. Turner, *Polym. Rev.* **2018**, *58*, 1.
- [57] N. Fontanals, J. Cortés, M. Galià, R. Maria Marcé, P. A. G. Cormack, F. Borrull, D. C. Sherrington, *J. Polym. Sci. Part A Polym. Chem.* **2005**, *43*, 1718.
- [58] J.-Y. Lee, C. D. Wood, D. Bradshaw, M. J. Rosseinsky, A. I. Cooper, *Chem. Commun.* **2006**, 2670.
- [59] B. Li, R. Gong, W. Wang, X. Huang, W. Zhang, H. Li, C. Hu, B. Tan, *Macromolecules* **2011**, *44*, 2410.
- [60] C. Wilson, M. J. Main, N. J. Cooper, M. E. Briggs, A. I. Cooper, D. J. Adams, *Polym. Chem.* **2017**, *8*, 1914.
- [61] X. Yang, M. Yu, Y. Zhao, C. Zhang, X. Wang, J. X. Jiang, *RSC Adv.* **2014**, *4*, 61051.
- [62] L. Tan, B. Li, X. Yang, W. Wang, B. Tan, *Polymer (Guildf)*. **2015**, *70*, 336.
- [63] R. Dawson, T. Ratvijitvech, M. Corker, A. Laybourn, Y. Z. Khimyak, A. I. Cooper, D. J. Adams, *Polym. Chem.* **2012**, *3*, 2034.

- [64] W. Wang, M. Zhou, D. Yuan, *J. Mater. Chem. A* **2017**, *5*, 1334.
- [65] D. S. Ahmed, G. A. El-Hiti, E. Yousif, A. A. Ali, A. S. Hameed, *J. Polym. Res.* **2018**, *25*.
- [66] T. Ratvijitvech, M. Barrow, A. I. Cooper, D. J. Adams, *Polym. Chem.* **2015**, *6*, 7280.
- [67] X. Zhu, S. M. Mahurin, S.-H. An, C.-L. Do-Thanh, C. Tian, Y. Li, L. W. Gill, E. W. Hagaman, Z. Bian, J.-H. Zhou, J. Hu, H. Liu, S. Dai, *Chem. Commun.* **2014**, *50*, 7933.
- [68] D. Zhang, L. Tao, Q. Wang, T. Wang, *Polymer (Guildf)* **2016**, *82*, 114.
- [69] F. R. and C. P. Claudia F. Martín, Ev Stöckel, Rob Clowes, Dave J. Adams, Andrew I. Cooper, Jose J. Pis, *J. Mater. Chem* **2011**, *21*, 5475.
- [70] D. G. Reed, G. R. M. Dowson, P. Styring, *Front. Energy Res.* **2017**, *5*, 1.
- [71] S. Yao, X. Yang, M. Yu, Y. Zhang, J.-X. Jiang, *J. Mater. Chem. A* **2014**, *2*, 8054.
-

## Supporting Information

### **A Pressure Swing Approach Toward Selective CO<sub>2</sub> Sequestration Using Functionalised Hypercrosslinked Polymers (FHCPs)**

Alex M. James<sup>a</sup>, Jake Reynolds<sup>a</sup>, Dan G. Reed<sup>b</sup>, Peter Styring<sup>b</sup> and Robert Dawson†<sup>a</sup>

Email: [r.dawson@sheffield.ac.uk](mailto:r.dawson@sheffield.ac.uk)

**Table S1** Preparation of FHCP networks

Network	Monomer		FDA		FeCl <sub>3</sub> quantity		DCE	% Yield
	quantity		quantity		g	mmol	mL	
	g	mmol	mL	mmol				
Triphenylmethanol	3.00	11.54	7.65	86.57	14.02	86.57	60	62
BINOL	2.89	10.00	5.31	60.00	9.72	60.00	50	92
Carbazole	3.34	20.00	7.08	80.00	12.96	80.00	50	107
Triphenylamine	3.68	15.00	7.96	90.00	14.58	90.00	60	55
Dibenzyl ether	3.00	15.00	6.63	75.00	12.15	75.00	50	68
Fluorobenzene	3.00	31.25	6.91	78.20	12.67	78.20	50	69
Poly(styrene)	3.46	33.27	7.35	83.17	13.47	83.17	50	110

**Table S2** Elemental analysis of FHCP networks

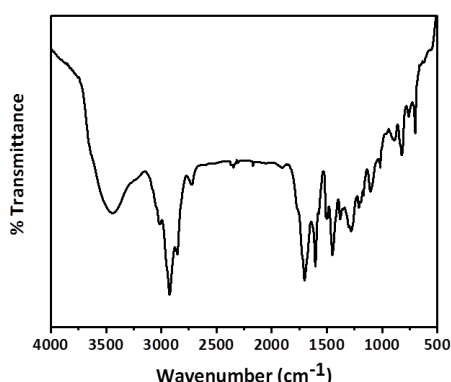
Network	% C		%H		%N	
	Theoretical	Found	Theoretical	Found	Theoretical	Found
	Triphenylmethanol	87.69	82.45	6.15	5.87	-
BINOL	83.92	80.74	4.90	4.58	-	-
Carbazole	88.56	74.51	6.27	5.34	5.17	5.27
Triphenylamine	90.00	77.47	6.82	5.18	3.18	4.35
Dibenzyl ether	84.00	77.64	7.00	6.59	-	-
Fluorobenzene	75.00	66.94	5.21	3.89	-	-
Poly(styrene)	92.31	88.65	7.69	5.48	-	-

## FTIR Data

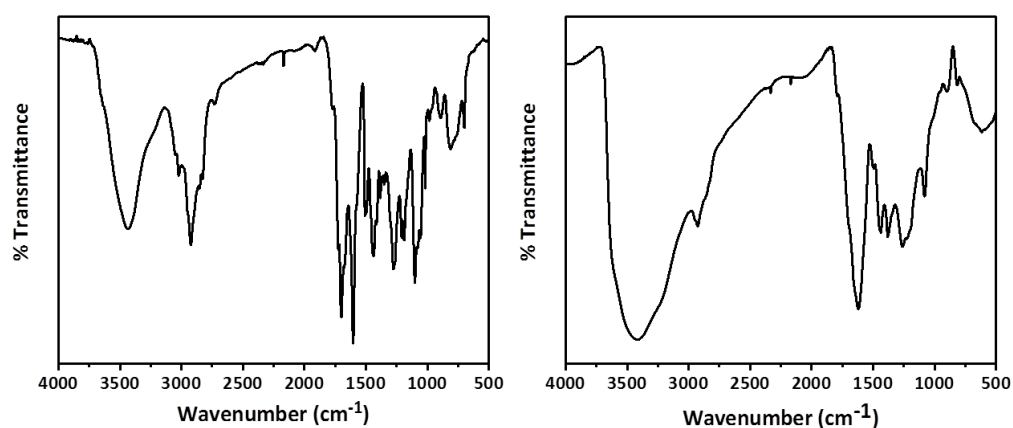
Presented in this section is all the FTIR data recorded for each of the polymer networks synthesised. All polymers display stretches at 1500 - 1700  $\text{cm}^{-1}$  which can be assigned to the C=C aromatic stretches of the polymer networks.<sup>1</sup> Likewise, peaks at ca. 2800  $\text{cm}^{-1}$ , attributed to C-H alkyl stretches, and at 1480 - 1400  $\text{cm}^{-1}$ , attributed to CH<sub>2</sub> bending vibrations, are present as a consequence of the newly introduced methylene bridges from the hypercrosslinking reaction. Peaks which are functional group dependant and therefore unique to networks are presented in table S2 along with the IR spectra for each network (Fig. S1).

**Table S3** Network dependant IR peaks found in each polymer network synthesised

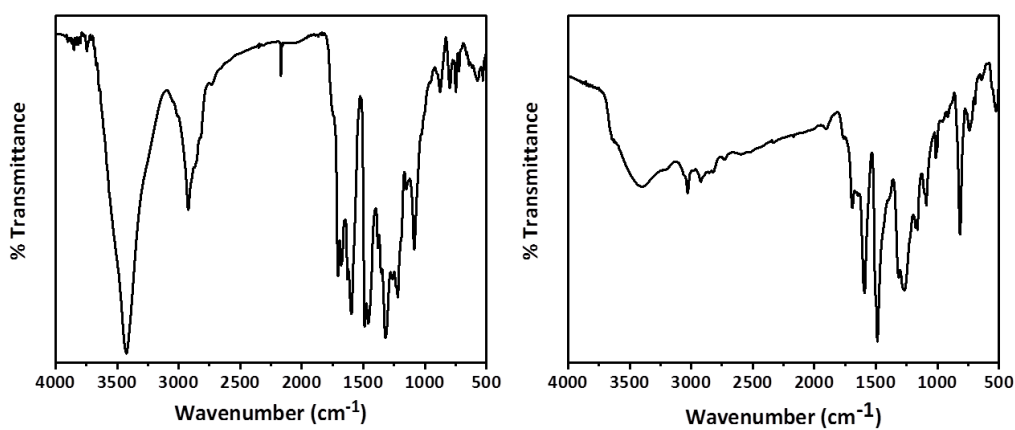
Functionality	Network	Wavenumber ( $\text{cm}^{-1}$ )	Peak Label
-OH	Triphenylmethanol	3450	Alcohol OH stretch
	Triphenylmethanol	1200	Alcohol C-OH stretch
	BINOL	3450	Alcohol OH stretch
	BINOL	1200	Alcohol C-OH stretch
-NR <sub>x</sub>	Carbazole	3350	N-H 2° amine stretch
	Carbazole	1340	C <sub>Ar</sub> -N stretch
	Triphenylamine	3400	N-H 1° amine stretch
	Triphenylamine	1250	C <sub>Ar</sub> -N stretch
R-O-R	Dibenzyl ether	1200	Alkyl aryl ether stretch
	Dibenzyl ether	1050	Alkyl aryl ether stretch
Ph-X	Fluorobenzene	1250	C <sub>Ar</sub> -F stretch



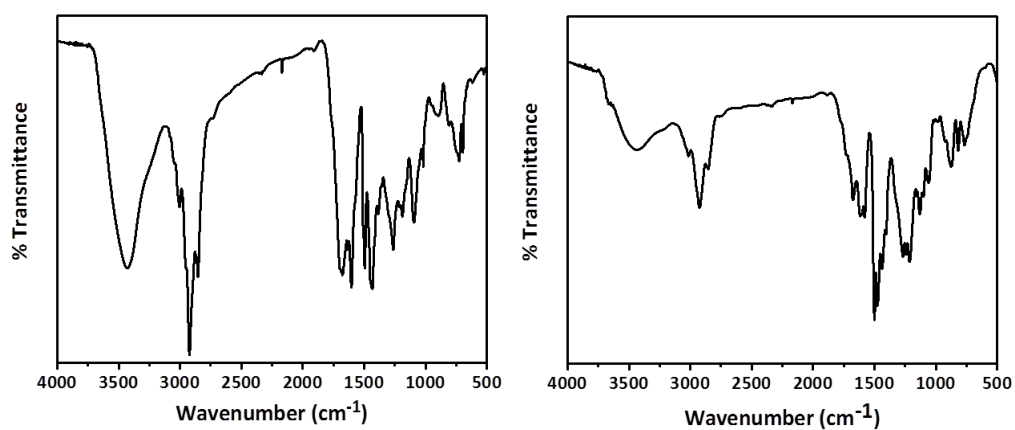
**Figure S1.1** IR spectra of poly(styrene) network.



**Figure S1.2** IR spectra of triphenylmethanol (left) and BINOL (right) networks.



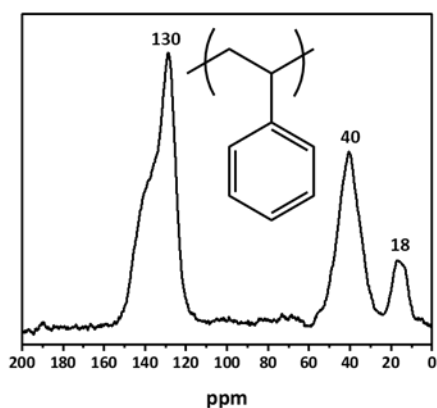
**Figure S1.3** IR spectra of carbazole (left) and triphenylamine (right) networks.



**Figure S1.4** IR spectra of dibenzyl ether (left) and fluorobenzene (right) networks.

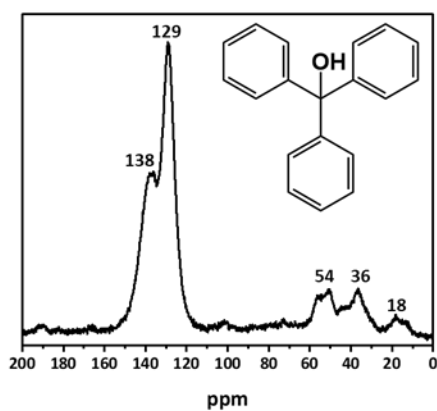
## Solid-state NMR data

All polymer networks were analysed via  $^{13}\text{C}$ -CP/MAS solid state NMR in order to further elucidate their structure and show monomer incorporation into the final networks. Peaks at low ppm (ca. 0 – 60) are present due to the  $-\text{CH}_2-$  groups from the external crosslinker. All other peaks are present due to the monomer and can be seen below:



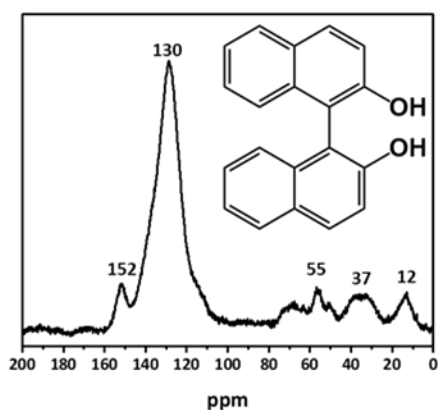
Signal	Assignment
Shoulder at ca. 140 ppm	Quaternary $\text{C}_{\text{Ar}}$
130 ppm	$\text{C}_{\text{Ar}}\text{-H}$
40 ppm	$-\text{CH}_2-$ bridges and $-\text{CH}-$
18 ppm	$-\text{CH}_2-$ backbone

Figure S2.1 Solid-state NMR spectrum of poly(styrene) network



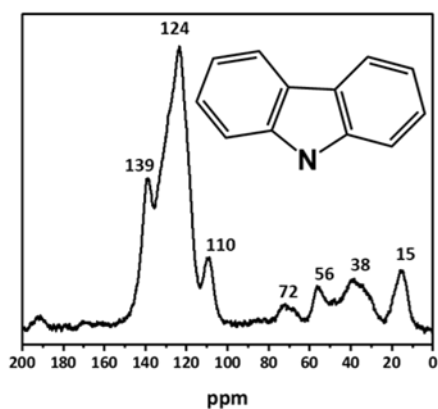
Signal	Assignment
138 ppm	Quaternary $\text{C}_{\text{Ar}}$
129 ppm	$\text{C}_{\text{Ar}}\text{-H}$
54 ppm	$\text{C-OH}$
36 ppm	$-\text{CH}_2-$ bridges
18 ppm	Unreacted end groups

Figure S2.2 Solid-state NMR spectrum of triphenylmethanol network



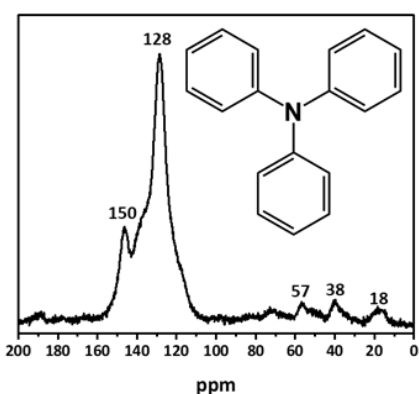
Signal	Assignment
152 ppm	Quaternary carbon adjacent to OH
130 ppm	Quaternary C <sub>Ar</sub> (shoulder) and C <sub>Ar</sub> -H
54 ppm	Unreacted end group
36 ppm	-CH <sub>2</sub> - bridges
18 ppm	Unreacted end groups

Figure S2.3 Solid-state NMR spectrum of BINOL network



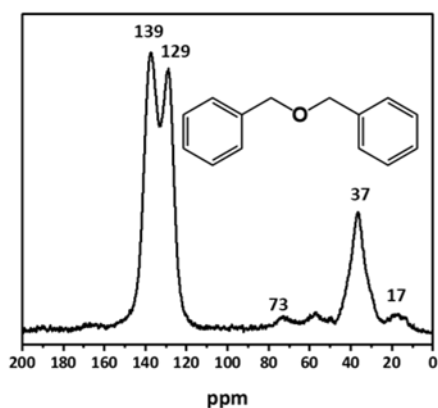
Signal	Assignment
139 ppm	Quaternary C <sub>Ar</sub>
124 ppm	C <sub>Ar</sub> -H
110 ppm	C <sub>Ar</sub> -H (in positions 1 and 8)
54 & 72 ppm	Unreacted end group
38 ppm	-CH <sub>2</sub> - bridges
18 ppm	Unreacted end group

Figure S2.4 Solid-state NMR spectrum of carbazole network



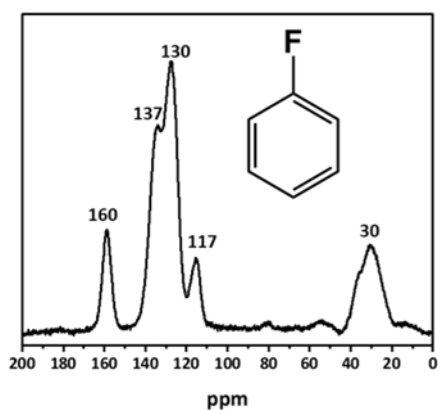
Signal	Assignment
150 ppm	Quaternary C <sub>Ar</sub> adjacent to N
Shoulder ca. 140 ppm	Quaternary C <sub>Ar</sub>
128 ppm	C <sub>Ar</sub> -H
57 ppm	Unreacted end group
38 ppm	-CH <sub>2</sub> - bridges
18 ppm	Unreacted end group

Figure S2.5 Solid-state NMR spectrum of triphenylamine network



Signal	Assignment
139 ppm	Quaternary C <sub>Ar</sub>
129 ppm	C <sub>Ar</sub> -H
73 ppm	CH <sub>2</sub> OCH <sub>2</sub>
37 ppm	-CH <sub>2</sub> - bridges
18 ppm	Unreacted end groups

**Figure S2.6** Solid-state NMR data spectra of dibenzyl ether network



Signal	Assignment
160 ppm	C adjacent to F
139 ppm	Quaternary C <sub>Ar</sub>
130 ppm	C <sub>Ar</sub> -H
117 ppm	C-H ortho to F
30 ppm	-CH <sub>2</sub> - bridges

**Figure S2.7** Solid-state NMR data spectra of fluorobenzene network

### Nitrogen gas sorption isotherms

The surface area of all polymer networks were determined through sorption of N<sub>2</sub> at 77 K and calculated over the pressure range of 0.01 – 0.15 P/P<sub>0</sub>. Pore size distributions were also calculated for each network using NLDFIT by applying the N<sub>2</sub> on carbon slit pores model. This data can be seen below for each synthesised network.

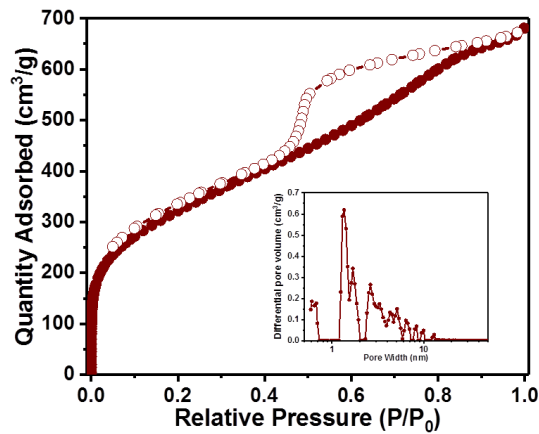


Figure 3.1 Full nitrogen isotherms of poly(styrene) network. Inset is the pore size distribution.

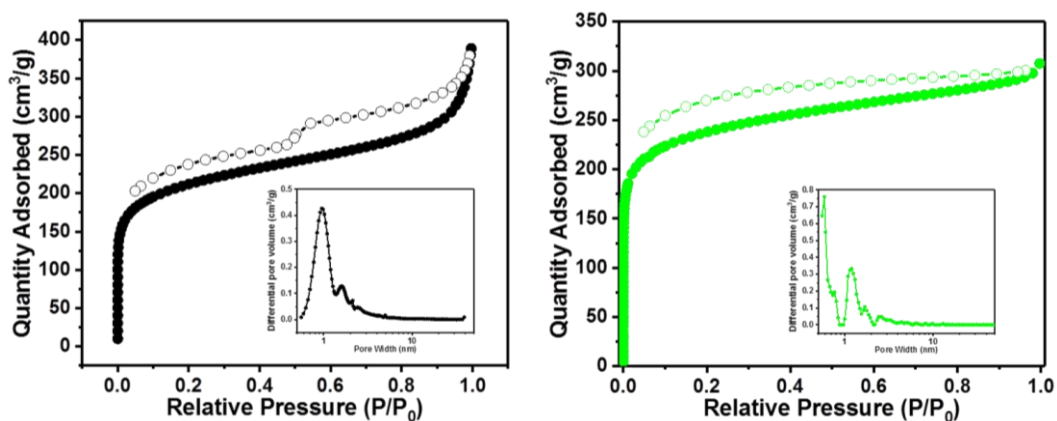


Figure 3.2 Full nitrogen isotherms of triphenylmethanol (left) and BINOL (right) networks. Inset is the pore size distribution.

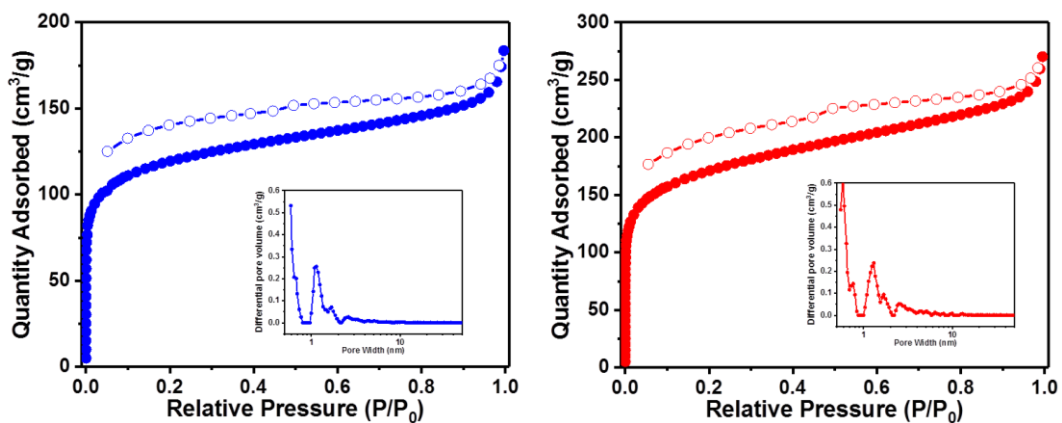
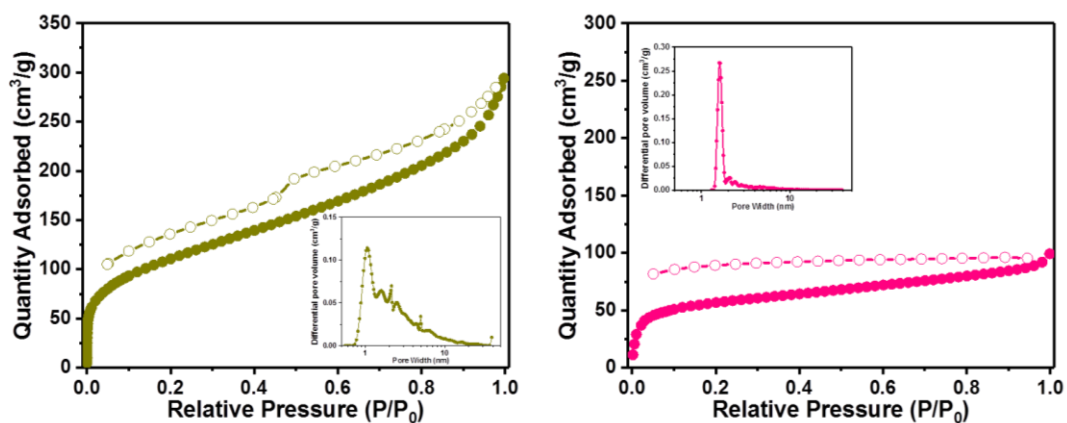


Figure 3.3 Full nitrogen isotherms of carbazole (left) and triphenylamine (right) networks. Inset is the pore size distribution.



**Figure 3.4** Full nitrogen isotherms of dibenzyl ether (left) and fluorobenzene (right) networks. Inset is the pore size distribution.

### Carbon Dioxide uptake data

All data obtained from experiments with CO<sub>2</sub> such as rate tests and pressure related uptake tests are presented in this section.

**Table S4** The amount of sample used to determine the rate of uptake (kinetic tests) for each network

Polymer network	Quantity (g)
Poly(styrene)	1.670
Triphenylmethanol	1.005
BINOL	1.631
Triphenylamine	1.799
Carbazole	1.011
Diethyl ether	2.797
Fluorobenzene	2.789

**Table S5** The  $t_{90}$  values obtained for polymer networks at 40 °C at 10 bar

Material	$T_{90}$ at 10 bar and 40 °C (seconds)	
	10 bar	20 bar
Poly(styrene)	< 10	< 10
Triphenylmethanol	103	48
BINOL	186	85
Carbazole	175	29
Triphenylamine	30	14
Dibenzyl ether	102	< 10
Fluorobenzene	23	12

### High pressure gas adsorption data

Once the kinetic tests had been carried out and told us the times at which each networks were fully saturated with CO<sub>2</sub> the next step was to determine how varying pressures of gas affected uptake. Each network was exposed to either CO<sub>2</sub> or N<sub>2</sub> at different pressures for a 5 minute adsorption period after which the material was weighted in order to determine sorption amounts. The data is presented both graphically and in tabular form in this section.

### CO<sub>2</sub> Uptake

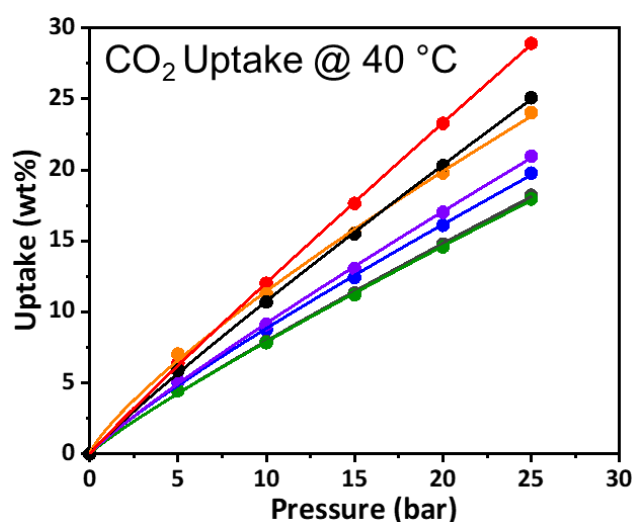


**Figure S4** CO<sub>2</sub> uptakes at 40 °C for each network as a function of pressure. HCPs are coded as follows: Poly(styrene), triphenylmethanol, BINOL, carbazole, triphenylamine, dibenzyl ether, and fluorobenzene

## N<sub>2</sub> Uptake

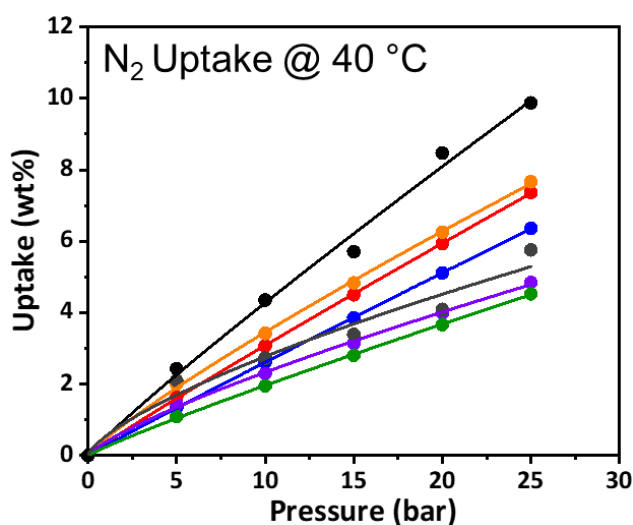


**Figure S5** N<sub>2</sub> uptakes at 40 °C for each network as a function of pressure. HCPs are coded as follows: Poly(styrene), triphenylmethanol, BINOL, carbazole, triphenylamine, dibenzyl ether, and fluorobenzene

## Pressure swing gas adsorption data

After testing of the materials with pure gases the next step was to examine the performance of select materials *via* a pressure swing methodology. This involved exposing the polymer to a mixture of CO<sub>2</sub>:N<sub>2</sub> and then seeing how the material fared at separating the two gases out as the pressure is lowered from 20 bar to 1 bar. The data seems to indicate that the most promising materials, i.e. triphenylmethanol and carbazole seem to have better separation abilities at elevated temperatures. This is good when it comes to applying these materials to industrial processes given that 40 °C is a more realistic working temperature.

**Table S6.1** Observed CO<sub>2</sub> concentrations after the polymers were exposed to a 20% CO<sub>2</sub> stream at 20 bar for 5 minutes before the pressure was dropped to 1 bar and the output stream analysed for CO<sub>2</sub> content at 40 °C

Polymer	% CO <sub>2</sub> detected	
	Input	1 bar
Triphenylamine	20.00	44.89
Carbazole	20.00	55.45
Triphenylmethanol	20.00	58.51
Poly(styrene)	20.00	60.41

**Table S6.2** Observed CO<sub>2</sub> concentrations after the polymers were exposed to a 50% CO<sub>2</sub> stream at 20 bar for 5 minutes before the pressure was dropped to 1 bar and the output stream analysed for CO<sub>2</sub> content at 40 °C

Polymer	% CO <sub>2</sub> detected	
	Input	1 bar
Triphenylamine	50.00	84.20
Carbazole	50.00	89.97
Triphenylmethanol	50.00	84.25
Poly(styrene)	50.00	72.05

### Recyclability

In order to determine whether the materials show any loss in performance over time recyclability studies were carried out through cycling the material from 25 bar to 1 bar and measuring the uptake. Recyclability studies were carried out on both the triphenylmethanol network and the triphenylamine network. It was hoped that the uptake should remain more or less constant throughout and that only very small amounts of the gas would remain adsorbed at 1 bar. Should these criteria be met then the material would be considered viable in terms of its recyclability.

**Table S7.1** Table showing the recyclability data obtained for the triphenylmethanol derived network at 40 °C

Run	CO <sub>2</sub> adsorbed (wt. %)	
	20 bar	1 bar
1	27.25	1.49
2	27.63	1.74
3	28.49	2.23
4	29.49	2.73
5	28.49	3.10
6	29.11	3.23
7	29.61	3.35
8	28.87	2.61
9	28.87	2.23
10	29.49	2.61

**Table S7.2** Table showing the recyclability data obtained for the triphenylamine derived network at 40 °C

Run	CO <sub>2</sub> adsorbed (wt. %)	
	20 bar	1 bar
1	20.95	1.33
2	21.14	1.39
3	21.33	1.65
4	21.27	1.52
5	21.52	1.52
6	21.46	2.28
7	22.35	3.17
8	22.60	3.11
9	22.73	3.23
10	22.67	3.36

## Chapter 8. Conclusions

# **Chapter 8 - Conclusions**

## Chapter 8. Conclusions

### 8.1 Conclusions

A novel and versatile synthetic procedure towards the design of microporous polymers capable of being dispersed and utilised in solution has been described for the first time. In this approach, the controlled radical polymerisation of crosslinking monomers alongside functional co-monomers mediated by a macro-CTA allows for the synthesis of porous polymeric nanoassemblies (Figure 8.1). This approach is compatible with many different monomers and this allows for the design of materials with different chemical properties. Furthermore, the resulting materials are no longer limited to only the solid state and solution phase applications can now be studied.

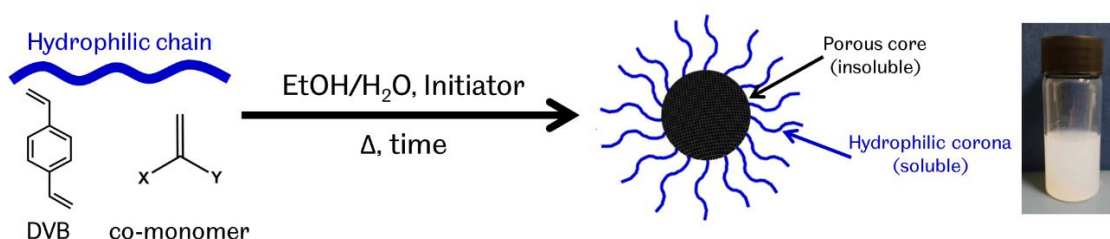


**Figure 8.1** General design principle of novel approach towards dispersible porous materials

The synthetic approach was fine-tuned through varying different chemical factors such as the solvent ratio, monomer ratio and targeted DP to fully understand the effect this has on the properties of the final material. Polymerisation of DVB and FN resulted in solution stable microporous dispersions with surface areas ranging from 244 – 409 m<sup>2</sup>/g. DLS and SAXS analysis gave great insight into the morphology of the resulting samples. Characterisation of the dispersions revealed that the samples are comprised of small individual particles which pack together to form larger aggregates which further agglomerate to form larger mass fractals. These mass fractals can be broken up *via* sonication, though the aggregates cannot be further broken down to yield individual particles suggesting that the crosslinking has linked some of the cores together.

The resulting porous DVB/FN materials were investigated for potential solution phase applications where it was found that the materials were capable of selectively sensing nitroaromatic compounds in solution. It was hypothesised that the interaction between the electron rich core of the material with the electron deficient nitroaromatics gives rise to the observed fluorescence quenching phenomenon which was exploited as the sensory mechanism. LoD of around 170 ppb for each sample calculated which are in line with those of other microporous materials used for the same application.

## Chapter 8. Conclusions

The versatility of the synthesis was demonstrated by replacing the fumaronitrile monomer with acrylic acid, which bears a carboxylic acid chemical moiety. Owing to the chemical stability of the final material, the sample could be post-synthetically modified to introduce new chemical properties into the final product. This was carried out in the form of an esterification reaction between the acrylic acid and 9-anthracenemethanol which allowed for anthracene units to be present in the core of the sample. The presence of anthracene within the core gave rise to blue emission in the visible region as confirmed by fluorescence emission spectroscopy. This emission could be exploited to produce white-light when the material is mixed with other fluorophore(s). The encapsulation of these organic materials ensured emission over the whole visible spectral range was accomplished which allowed for the production of white light emission in solution.

Chapter 6 and 7, present as journal manuscripts, focused on the design of more traditional microporous polymers for use in sustainable applications. Though these samples are not designed to be applied to solution-phase applications there are still applications for insoluble and stable porous materials. Hence, insoluble yet functional porous polymers were synthesised with specific end applications in mind.

Chapter 6 describes the design of a microporous polymer, synthesised *via* metal-free conditions containing pendant sulfonate groups present because of post-synthetic modification. This material was tested for its selective uptake capacity of both Sr and Cs with a view to be applied to remove radioactive isotopes from nuclear wastewater streams. It was found that the polymer, SHCP-1 that boasted a surface area of 850 m<sup>2</sup>/g, demonstrated a maximum uptake of 95.6 mg/g of Sr and 273 mg/g of Cs. Furthermore, this uptake was found to be selective towards these ions over other common ions found in these water streams such as Na and K.

In Chapter 7, the design of a range of microporous polymers containing different functional groups are reported and utilised towards CO<sub>2</sub> sequestration. In this work, a range of HCPs bearing different chemical moieties were synthesised through conventional hypercrosslinking chemistry using FeCl<sub>3</sub> as the catalyst. A pressure swing methodology was applied to separate CO<sub>2</sub> from dilute gas mixtures representative of industrial CO<sub>2</sub> point sources. Live IR monitoring of the output gas was carried out in order to follow the pressure-swing process and determine the CO<sub>2</sub> concentration of the final output stream. It was found that these materials were capable of turning a dilute CO<sub>2</sub> stream (20 %) into a much more concentrated CO<sub>2</sub> stream (> 80 %) after only two pressure-swing cycles.

## Chapter 8. Conclusions

### 8.2 Future Work

This thesis has described a novel synthetic approach towards the design of solution processable porous materials. In doing so it joins PIMs and a handful of other materials which are capable of being applied in solution whilst still retaining their porosity. As such, this work is at the forefront of a new boundary of materials combining the advantages of porosity with solution stability. This work is exciting and has obvious potential though there is still much work to be done. To put this into context, the first CMP was synthesised in 2007, yet the first soluble example was not reported until 2012. The first COF was reported in 2005 yet the first network to be based on something other than boron was reported in 2009. The first report of a HCP was reported in the 1970's yet example of the knitting method was developed in 2010. These examples highlight the potential for this work and what is yet to be achieved in good time. Some possible future research avenues for the near future are presented below.

#### Modifying the CTA

This work, though it has resulted in many new materials with two different solution phase applications has all been carried out using the same PEG-based macro-CTA. This CTA is cheap and easy to synthesise and is compatible with many different monomers which makes it convenient to use. However, this does limit the final material somewhat to having broadly quite similar solution-phase behaviour. In theory, it is possible to apply a wide range of different CTA to mediate the reaction of DVB and other monomers. Should this be applied it may be possible to design materials with a wide scope of new potential applications. For example, should the CTA be based on PNIPAM then the material would be thermoresponsive which could lead to quite interesting medicinal applications such as novel drug delivery systems. Likewise, it may also be possible to include PMDETA, which is a temperature responsive polymer and this could lead to other applications such as the uptake or release of a material which varies on the pH environment it is in. It may also be possible to switch the PEG to a PVA or AA polymer and this change could allow for better processability of the final product. PEG is unfortunately not able to form thin films and this limits the final product. However, PVA is particularly well known to form stable films thus a material which utilises PVA as the CTA may be able to form films which embeds the porous core within the film. This would be similar to a mixed matrix membrane but made of one material and could have applications in either gas or solution membrane separations. Thus, it is easy to see how much scope is possible from merely modifying one simple feature of the material. However, though this process seems simple it is important to remember that not all CTA are compatible with all monomers meaning some may not be able to include certain monomers. Thus, it is vital that the choice of both CTA and monomer are considered before attempting the synthesis.

## Chapter 8. Conclusions

### Varying the co-monomer

It has already been touched on in this work the huge difference replacing one monomer for another has on the properties of the final material. For example, by utilising FN as the co-monomer the final material was capable of sensing nitroaromatics yet replacing this with acrylic acid the final material could be used to produce white-light emission. Thus, the scope of applications by simply modifying this monomer is huge.

Usually homogeneous catalytic processes can be made heterogeneous through immobilisation of the catalyst onto a solid support, usually an insoluble material. This makes the removal and separation of the catalyst from solution simple though in doing so limits the rate of reaction as the catalyst can no longer mix as well with the solution. The materials discussed in this work have the unique benefit of having dual homo-/heterogeneous behaviour in that the samples are able to mix well with solution though can also be easily removed *via* centrifugation. Some work being carried out in collaboration with the Haynes group at the University of Sheffield has seen these materials applied as the catalytic support for the Monsanto acetic acid process.

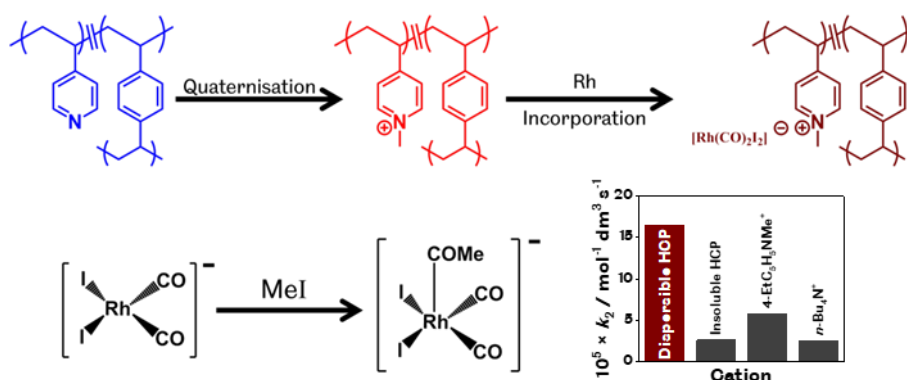


**Figure 8.2** Utilisation of a vinylpyridine system which can be act as a catalytic support for the Monsanto acetic acid process. Below is the rate limiting step of the reaction and how the catalyst compares to the heterogeneous and homogeneous analogues

In this work, microporous polymers capable of forming stable dispersions were synthesised using vinylpyridine as the co-monomer. This monomer was quaternised before encapsulation of the catalyst was achieved through ionic interaction of the negatively charged catalyst and positively charged nitrogen atoms present within the core (Figure 8.2). This material was found to have a faster rate of reaction than both the purely insoluble catalyst as well as the homogenous soluble catalyst. This is owed to the ability of the material to mix well with the solution as well as having the porous core, which allows the organic compounds present in solution to diffuse into the pores and interact with the catalyst. It is hoped that this work will

## Chapter 8. Conclusions

inspire others to consider these materials as supports for catalytic processes given their excellent properties. This work is being prepared as a manuscript and it hoped to be submitted in the coming months.

It is possible to vary the monomer further to yield other exciting applications. One such project was investigated by a recent master's student in the group who designed porous dispersions using pentafluorostyrene. This material is super hydrophobic and as such could be utilised to remove organic pollutants from aqueous solution given that oils and other organic pollutants are hydrophobic in nature. Likewise, it is also possible to take inspiration from other porous materials and design a material containing sulfonate groups embedded within the core which may be useful for removal of metal ions from solution. This design concept could be readily achieved through polymerising DVB with a sulfonated styrene monomer.

Through varying the co-monomer it is possible to synthesise a vast array of different materials which vary in end application. Most of the suggestions investigated have been based on monomers similar to styrene as this should polymerise at a similar rate as DVB. However, this does not have to be the case and as we have seen with FN and AA it is possible to apply non-styrenic monomers towards this synthetic procedure. It is also possible to vary both the crosslinking monomer and the co-monomer too, which could yield new and interesting applications resulting from the different chemical and physical properties of the sample.

### Further Characterisation

In addition to varying the materials used it may also be sensible to try other characterisation techniques to study these materials. Currently both SAXS and DLS have been applied to characterise the morphology of the materials in the solution phase with these results being corroborated with SEM/TEM images. What may be interesting is to apply other solution-phase which may reveal further insight into the morphology of the material. One technique which may be of interest is a LUMiSizer which gives information not only on particle size but also insight into whether sedimentation is occurring and other insight. These results may be interesting to compare to the DLS results and the UV-Vis results which give insight into the solution stability of the material.

Other techniques of interest may be rheology to determine if the solution is viscous as this may hinder some applications. It may also be of interest to further fine-tune the UV-Vis spectroscopy study which gives a more quantitative insight into dispersion stability. The longest a sample was analysed for was only 48 hours and it may be useful to study a samples for months to see if any change occurs, though this would be difficult as it is imperative that the sample is kept undisturbed for the period and the solvent level cannot change.

## Chapter 8. Conclusions

### Future Sustainability

Though this thesis demonstrates the potential of porous polymers in the field of sustainability there is much scope for improvement. In the work discussed in Chapter 6 though the sulfonated material shows great selective uptake towards the targeted ions more work needs to be undertaken to better understand the sorption properties of the material. For example, to be applied in the discussed context it is imperative that the ions can be removed from the polymer so they can be safely stored and thus far this body of work does not discuss the desorption properties of the material. Furthermore, scalability of the material needs to be examined if it is to be used in this context and any scalability needs to be achieved in a way which does not hinder the properties of the material (i.e. reduce surface area or degree of sulfonation).

In Chapter 7, a pressure-swing adsorption system was discussed and applied to evolve concentrated streams of CO<sub>2</sub> from dilute mixes of N<sub>2</sub>:CO<sub>2</sub>. This work demonstrates the potential for functionalised porous materials in this area and also highlights the potential benefits of switching from the conventional temperature-swing approach adopted by industry for many years. However, this work is still in its advent and many issues need to be overcome. One of which is the need to test these materials on a larger scale and further implement more realistic industrial conditions. For example, though some industries do produce flue gas stream at around 15 % CO<sub>2</sub> the partial pressure of that gas would not be 10 – 20 bar. Hence, it would be more appropriate to study the CO<sub>2</sub> uptake at more dilute conditions. Also, the scale-up of the porous polymers needs to be attempted so larger amounts of sample can be studied. Furthermore, gases of high purity need to be replaced with gases containing water vapour to see the full effect water vapour has on overall uptake and selectivity given that flue gas often contains large amounts of moisture.